University of Southampton
Faculty of Engineering and the Environment
Institute of Sound and Vibration Research

Inverse Methods in Cochlear Mechanics

Luyang Sun

A thesis submitted for the degree of

Doctor of Philosophy

December 2016

UNIVERSITY OF SOUTHAMPTON

ABSTRACT

FACULTY OF ENGINEERING AND THE

ENVIRONMENT

INSTITUTE OF SOUND AND VIBRATION

RESEARCH

Doctor of Philosophy

Inverse Methods in Cochlear Mechanics

by Luyang Sun

Cochlear modelling is used to provide insight into the physical mechanics of the cochlea. The complicated, three dimensional geometry of the fluid chambers in the cochlea is often represented in models of its mechanics by a box with a uniform area along its length. The first part of this thesis is concerned with the development of a tapered box model of the cochlea, in which the geometry of the cochlea is assumed to vary in a linear way along its length. Previous measurements of the variation in area of the two fluid chambers along the length of the cochlea in various mammals has been used to calculate a linear fit to the variation in the "effective area" that determines the 1D fluid coupling. The width of the basilar membrane is also assumed to vary linearly along the length of the model. The analytic form of the 1D fluid pressure distribution due to elemental BM motion is derived for this tapered box model, together with the added mass due to near field acoustic coupling. The coupled response in the 1D and 3D, uniform and tapered box model of passive cochlea can then be readily calculated. Although the form of the fluid coupling are very different in the uniform and tapered box models, the distribution of the basilar membrane vibration in the coupled models are very similar.

The second part of the thesis is concerned with deriving the parameters of cochlear models from measured data using inverse methods. Previous inverse methods are first reviewed before a novel direct method is introduced, based on modelling the poles and zeros of the micromechanical response. This is compared with other inverse methods,

using previously measured data on basilar membrane vibration in the cochlea, and relatively simple models are shown to provide a good fit to the data.

Contents

List of Figures

List of Tables

Symbols and Abbreviations

General Symbols

Re( )/ Im( ): Real/imaginary part of a complex variable

I: Unit matrix

ω: Angular frequency [radian/s]

f: Frequency [Hz]

ρ: Density [kg/m^3]

k: Wavenumber [m^{-1}]

F: fluid-coupling matrix

H: height of fluid chamber[m]

W: width of fluid chamber[m]

B: basilar membrane width[m]

h: effective height[m]

i: $\sqrt{-1}$

L: length of the cochlea [m]

ℓ : cochlear length scale [m]

$\mathbf{Y_{BM}}$: admittance matrix

N: number of cochlear elements

p : matrix of pressure

x: longitudinal position [m]

Δ: thickness of a cross-sectional element of the cochlear model [m]

γ : micromechanical feedback gain

Y_{BM}: "measured" BM admittance

$\hat{Y}_{BM}$: estimated BM admittance

V_{BM} : "measured" BM velocity

$\hat{V}_{BM}$: estimated BM velocity

Ω : normalised natural frequency of pole and zero

Q : Q factors of pole and zero

Q_0: Q factors in 1D fluid coupling

Abbreviations

1-D: one-dimensional

3-D: three-dimensional

FFT: Fast Fourier Transform

BM: Basilar Membrane

CF: Characteristic Frequency

CP: Cochlear Partition

IHC: Inner Hair Cell

OHC: Outer Hair Cell

SV: Scala Vestibuli

ST: Scala Tympani

TM: Tectorial Membrane

TW: Travelling Wave

WKB: Wentzel-Kramers-Brillouin approximation

SPL: Sound Pressure Level

DOF: Degree of Freedom

NMSE: normalized mean square error

Declaration of Authorship

I, Luyang Sun,

declare that the thesis entitled

Inverse methods in cochlear mechanics

and the work presented in the thesis are both my own, and have been generated by me as the result of my own original research.

I confirm that:

- this work was done wholly or mainly while in candidature for a research degree at this University;
- where any part of this thesis has previously been submitted for a degree or any other qualification at this University or any other institution, this has been clearly stated;
- where I have consulted the published work of others, this is always clearly attributed;
- where I have quoted from the work of others, the source is always given. With the exception of such quotations, this thesis is entirely my own work;
- I have acknowledged all main sources of help;
- where the thesis is based on work done by myself jointly with others, I have made clear exactly what was done by others and what I have contributed myself.

Signed :……..

Date :…….....

Acknowledgements

I would like to thank Steve Elliott and Ben Lineton for their help, espetially Steve, he is always patient to teach and guide me how I should think and solve problems, and lets me gradually have so much passion for research, which means a great deal to me in my future career.

I also would like to thank Dr Guangjian Ni, he is always patient to give me the feedback of my thesis over and over again, and teach me how I should express my thought and outcomes by writing, and my writing ability has been improved so much.

I also would like to thank David Simpson and Frank Boehnke, they gave me so many sensible suggestions about my thesis.

I would not be who or where I am today without my parents. My mother always cheers me up and let me have huge passion for my life, she is my idol, and my father always let me enjoy my life.

I also would like to thank my wife, Huajian Wang. She gives me huge support through my PhD career, she always let me be happy and relax for my life. I always feel lucky to be with her every day. This year, she gives me a most important gift, our baby, who was born in August of 2016, which gives me much power to finish my final work.

Thank everyone who loves me around.

Chapter 1

Introduction

Sensing sound, selecting frequencies, and hearing in different environments demonstrate the ability of the auditory system. This system's front end, the cochlea, transforms acoustic pressure into neuronal spikes in the auditory nerve, and it can analyse the mixture of frequencies, amplify low-level sound, and compress high-level sound. In the mammalian cochlea, the basilar membrane (BM) vibrates due to fluid pressure difference in the fluid chambers, which can provide broad frequency tuning. Within the cochlear partition of living animals, there is also the cochlear amplifier, which enhances active cochlear behaviour. Thus, the action of the cochlear geometry detects and filters sound signals and the cochlear amplifier selectivity amplifies the BM's responses, resulting in nonlinear active cochlear behaviour (Wen, 2006).

Many researchers, who want to uncover the mechanism of the cochlea, have either made physiological measurements of the cochlear response or mathematical models of its mechanics. Although many aspects of the cochlear mechanics have been revealed, there is still much which is unknown. The mechanics of the cochlea can be divided into its micro-mechanics and its macro-mechanics, where "micro-mechanics" refers to the interaction between elements of the organ of Corti, and "macro-mechanics" refers to the mechanics of fluid in the cochlea. The mechanical response of the cochlea at high levels or in the post-mortem cochlea would need to be modelled by the passive macro-mechanics alone. The mechanical response of the cochlea at low levels would need to be modelled by the active mechanics. Some researchers have attempted to match the coupled response of cochlear models to measurements made in the real cochlea. Viergever (1980) attempted to match the transfer functions generated by a two-dimensional box model with one degree of freedom system to the passive measurement of Johnstone (1975) using realistic parameters; he failed to find a simultaneous match of both the amplitude and phase of the BM response. Viergever and Diependaal *et al.* (1986) corrected some of the deficiencies of Viergever's (1980) approach and achieved a good match to the measurement data of Johnstone and Yates (1974) with a single degree of freedom, two-dimensional model, using the Wentzel-Kramers-Brillouin (WKB) method. However, their model did not use a realistic size (Fenmandes, 1952, Steven and Davies, 1938), and when these. dimensions are corrected, the transfer function of

the model cannot match the measurement data. Mammano and Nobili (1993) used a realistic model with parameters derived from measurement of the guinea pig to predict the coupled response. However, the “passive” output of this model fails to match measurements made in the guinea pig. Brass (1999) developed a model that is similar to the one used by Mammano and Nobili (1993), in which the parameter values used were more carefully chosen and realistic, and the new model matches passive mechanical data quite well. One purpose of this thesis is to propose a tapered box models of the cochlea, whose parameters are obtained from measurement data, in order to derive more realistic coupled responses. Relatively few people have tried to match the active cochlear model response to the measurement data from *in vivo* species, Zweig (1991) attempted to use an inverse method to match an active model to the *in vivo* measurement data, but the deficiency of this model is that it is a I/O transmission line model and the eatimated coupled response using this model will not fit to the *in vivo* measurement data around the peak area of cochlear response, where 3D fluid effects are known to be important. Different inverse methods have been developed by other authors. The other purpose of this thesis is to compare these and to investigate a new inverse method, the direct method, combined a new micromechanical model and the realistic geometry of fluid chamber from measurement, by optimization methods to match the measurement data with sound pressure level (SPL),which includes the conditions of the passive and the active cochlea.

1.1. The auditory system

1.1.1. Anatomy of the ear

The anatomy of the ear consists of three components: the outer ear, the middle ear, and the inner ear. A cross-sectional picture of the human ear is shown in Figure 1.1. The pinna and the ear canal constitute the outer ear, which provide directional hearing due to their scattering properties, although the head and the body also have an influence. The ear canal is a short curved tube which spreads from the pinna to the eardrum. The outer ear thus provides a protective interface to the environment and can locate sound sources (de Boer, 1980). The middle ear apparatus lies in an air-filled tunnel just beyond the eardrum, which embedded in the temporal bone. Acoustic vibrations of the eardrum are transmitted through the middle ear by means of three small bones: the malleus, the incus, and the stapes, and the air pressure can be equalized across the eardrum. The middle ear provides mechanical impedance matching between the air vibration of the outer ear and the fluid vibration of the inner ear. The inner

ear consists of the cochlea, the vestibule, and the semi-circular canals, these structures are embedded within the temporal bone. The semi-circular canals are oriented in three, orthogonal, spatial planes and serve the sense of spatial orientation (de Boer, 1980). The cochlea is the sensory organ for hearing; it receives the acoustic signals delivered by the stapes and distributes sound information to the individual auditory nerve fibres.

The cochlea is the principle sensory organ of the mammalian auditory system; it is a tapered spirally coiled tube, which forms a fluid-filled cavity, embedded in the temporal bone. The cochlear chamber is divided into three ducts by a thin bony shelf called the spiral lamina, and the stiff basilar membrane, and by a more compliant Reissner's membrane. The right panel of Figure 1.1 shows a cross-section of the cochlea and identifies the three cochlear ducts. The upper duct is called the scala vestibuli, the lower duct is called the scala tympani. The scala tympani and scala vestibuli are filled with a liquid called perilymph and communicate with each other at the apical end of the cochlea through an opening called the helicotrema. The central duct, the scala media, is filled with a different liquid called endolymph, which provides nutrients to the sensory hair cells and has a different ionic composition than perilymph. Reisssner's membrane provides a chemical barrier between scala media and scala vestibuli, but is probably not important mechanically (de Boer, 1980).

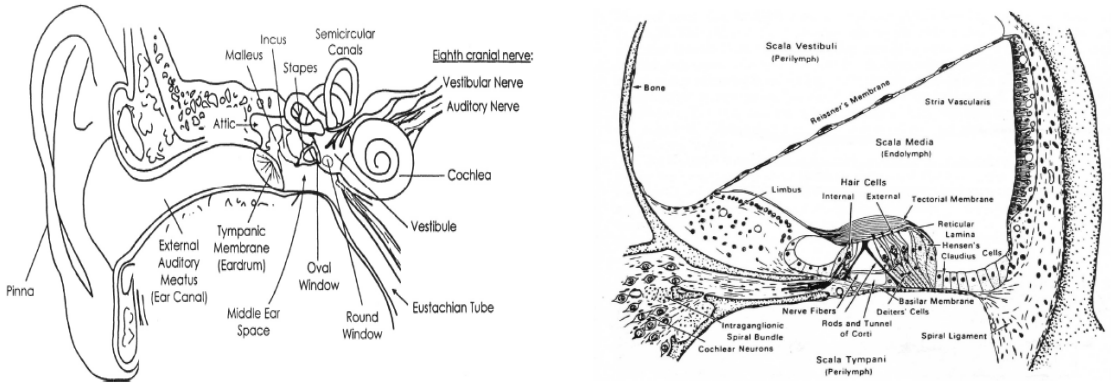

Figure 1.1 Left panel: The cochlea in relation to the outer and middle ears. Right panel: Cross-section of the cochlea. Reproduced from 'Hearing : an introduction to psychological and physiological acoustics,' by S.A. Gelfnd, copyright (1998), with permission from Marcel Dekker.

The oval window, which is open to the middle ear, is covered by the footplate of the stapes and an annular ligament. In the scala tympani, the corresponding opening is called the round window, which is covered simply by a thin membrane.

The basilar membrane extends from the stapes to the helicotrema. It is mechanically tuned, and varies from being light and stiff near the stapes to progressively more compliant toward

the apex. Within the cochlear partition, lying on the basilar membrane is the organ of Corti. The organ of Corti contains the tectorial membrane, the reticular lamina and the final receptor cells, the hair cells. These hair cells are innervated by nerve fibres which originate in the spiral ganglion.

1.1.2. The physiology of the auditory system

Sound waves travel into the canal, which vibrate the ear drum of the middle ear. The middle ear serves as an impedance transformer from the low-pressure high-velocity sound in the air to the high-pressure low-velocity sound in the fluid of cochlea. The vibrations of the ear drum are coupled into the stapes by means of this transformer, which vibrates the oval window of the cochlea. The vibration of the oval window leads to the generation of a traveling wave of fluid pressure along the length of the cochlea, which displaces fluid (Dallos, 2002). This fluid wave causes the physical motion of the organ of Corti including the basilar membrane (Geisler, 1998).

As the wave moves from the base to the apex, its velocity reaches a peak where the characteristic frequency of the basilar membrane and the organ of Corti matches the frequency of the incoming wave (Dallos, 2002). This gives rise to the well-known frequency-place mapping, in which the characteristic frequency decreases approximately exponentionally towards the apex (Greenwood, 1990), some examples of an exponentional fit to the characteristic frequency distribution along the cochlea in different species is shown in Figure 1.2, in which the deviation from the exponentional fit near the apex of the cochlea has been ignored.

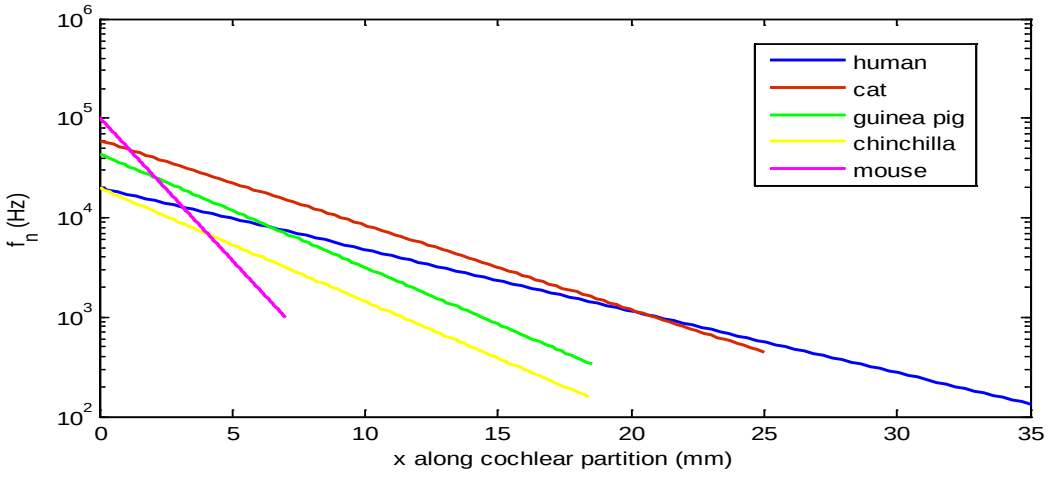

Figure 1.2 The characteristic frequency, f_n, distribution along cochlear partition for five species.

The motion of the cochlear partition stimulates the stereocillia, which protrudes from the top of each hair cell. The shearing motion between the reticular lamina and tectorial membrane bends the stereocilia, creates a corresponding intracellular potential change in the inner hair cells, and causes the release of synaptic vesicles in the vicinity of the afferent nerve fibre synapses, and the sensory hair cells transmit information about the motion to the auditory nerve (de Boer, 1980).

1.1.3. Measurements in the cochlea

Helmholtz (1874) put forward a resonance theory of hearing, in which the cochlear partition is considered as a series of tuned resonators. This resonance theory was questioned by von Bekesy (1960), who made the measurements, and observed the wave motion of the cochlear partition for the first time. Much of what we know about the physical mechanism of the ear is from Bekesy's experimental findings, in which the displacement of the cochlea in response to a sinusoidal tone was observed. The next significant step in the direct observation of the basilar membrane displacement was the introduction of the Mossbauser technique by Johnstone and Boyle (1967), which enabled measurements in living animals. This technique was refined by Rhode (1971), who was able to measure both amplitude and phase of basilar membrane displacement in living squirrel monkeys. The peak in the frequency response was found to be much sharper in these living preparations than they had been in the dead ones. Rhode and Robles (1974) also observed non-linearity in the displacement for the living squirrel monkey, which was not present once the monkey died. Recently, Lee *et al* (2015) used volumetric optical coherence tomography vibrometry to derive the measurement data, and can get the ratio of the BM velocity to the stapes velocity directly, this technique overcomes some limitations (e.g. that the data are limited to point measurements of BM vibration and opening of the cochlea may alter its function) by providing depth-resolved displacement measurements at 200 kHz inside a 3D volume of tissue with picometer sensitivity within the unopened cochlea.

The measurements described above are called direct measurements. Another way to measure the mechanics of cochlea is the indirect method, which involves measuring the response of the auditory nerve fibre, although this response consists of spikes, rather than a linear waveform (de Boer, 1977). de Boer (1977) provided a technique, which is called reverse-correlation technique, to derive the responses recorded from auditory nerve fibre. He concluded that for wide-band noises and single-tone signals, the firing probability is

predominantly controlled by a linearly filtered version of the acoustical stimulus, which constitutes the principle of specific coding. van Dijk (1994) proposed a new method of obtaining the frequency responses from primary auditory nerve fibres in the American bullfrog, which is called Wiener Kernel analysis. He provided a model for the function of the inner ear (1994), so that he could derive the linear response from a nonlinear auditory nerve fibre. Recio-Spinoso, *et al* (2005) used a second order Wiener-Kernel analysis to measure the response to noise of chinchilla auditory-nerve fibres, which provides the BM response.

Besides measuring the BM velocity to investigate the mechanics of the cochlea, some researchers also measure some other important parameters. Olson (2001) made pressure measurement for *in vivo* animals, and Dong and Olson (2009) made impedance measurement for *in vivo* animals.

Although many measurements have been made to investigate the mechanics of cochlea, the interpretation of data is often difficult. Modelling cochlear mechanics is a good way to obtain physical insight from measurement data. Cochlear modelling can be classified as either forward or inverse modelling. Forward modelling can be defined as predicting cochlear response using a given model and is different from inverse modelling, which fits model's properties from measurement data.

1.2. Forward modelling efforts for mechanics of the cochlea

The first successful and consistent mathematical model of the wave motion in the cochlea was formulated by Zwisloki (1948), who derived Bekesy's waves from classical theory of hydrodynamics. Early models assumed 1D fluid coupling (long-wave) and passive micromechanics, for which an analytic solution was derived firstly by Steele (1974) using the WKB method. Zweig *et al* (1976) developed a closed-form WKB solution for a 1D long-wave model. Following the 1D cochlear model, 2D and 3D fluid couplings in the cochlea were considered by Steele and Miller (1980), Steele and Taber (1979), and Taber and Steele (1981), respectively. The WKB solutions for the 2D and 3D cochlear models, which have passive mechanics show good agreement with the experimental results, except for the peak area. However, these methods are limited to a model of constant geometry along its length. Therefore, Allen introduced a generalized method, whose form involves a matrix equation with a "full" matrix using Green's function (Allen, 1977; Mammano and Nobili, 1993), which means the geometry of the cochlear model along the length can be varied.

Kim *et al* (1980) proposed an active cochlear model using negative damping, which means that the organ of Corti would contain elements that vibrate with the cochlear waves in such a way that they produce acoustical energy (or power) instead of only absorbing it. Neely and Kim (1986) then derived the solution of an active cochlear model using the finite difference method. This type of model has been developed by others, e.g. Geisler (1991, 1993), Neely (1993), de Boer (1992, 1993), and Hubbard (1993). Elliott *et al.* (2007) used a state space model to analyse the stability of a linear model of the active model, which was based on the Neely and Kim model. This model can also investigate the presence of instabilities due to random spatial inhomogeneities (Ku *et al*., 2008).

The mechanics can be idealised as an axial array of locally-reacting single or multiple-degree-freedom micromechanical systems, which are longitudinally coupled via the fluid. Precise anatomical data for the axial distribution of model parameters are lacking, however, and one typically has to make “educated” guesses of their values. The problem is more complicated with multiple degree-of-freedom models, where it is not clear which parts of the structure should be lumped together to constitute the different degrees of freedom. There is thus a general problem of deciding what parameter values should be used in such a model. Rather than estimate the physical mechanical parameters, such as the mass, stiffness and damping in a lumped parameter model, the poles and zeros of such a micromechanical model could be estimated by fitting to the coupled response, as proposed below. To narrow the gap between cochlear measurements and cochlear models, a number of inverse methods have previously been used to calculate the properties of the coupled response.

1.3. Backward modelling effort for the mechanics of the cochlea: Inverse methods

A forwards cochlear model, that allows the response of the basilar membrane to be predicted from the model and its parameters, is relatively straightforward to implement. The “inverse” problem is one of going from the measured response back to the physical parameters, If the response of the cochlea (e.g. the BM velocity) is given from measurement data, it may be possible, for example, to calculate the wavenumber, BM impedance, pressure, or other properties by backward solution (inverse method) of the equations used in models of cochlea. The difficulty with inverse models is partly because the physical parameters being estimated will depend on the assumptions of the cochlear model being used. It may assume either 1D or 3D fluid coupling, for example, and the inferred BM mass may will thus either include the

additional mass due to the fluid coupling, if 1D fluid coupling is assumed, or not, if 3D fluid coupling is assumed. Since 1986, there have been a number of attempts to use inverse method. A brief review of different inverse methods is given below, although only the final three methods are implemented in the thesis.

1.3.1. Diependaal's method

In order to validate the possibility that there are active elements in the BM impedance, and also explain the measurement data on the vibration of the BM, Diependaal (1986) suggested a method of calculating the BM impedance function from a given BM velocity in response to a sinusoidal input at the stapes. A 1D cochlear model, which uses long-wave fluid coupling, was assumed. The inverse problem is solved by integrating this formulation with a set of measured BM vibration data. Using scaling methods, this response can be transformed from the frequency domain to the spatial domain. The 1D fluid coupling fails around the peak area due to appearance of short wave, although the model could be extended to 2D fluid coupling. This inverse method was validated (Diependaal, 1986) by selecting a reference impedance and calculating the BM velocity, using the forward method, and then using the inverse model to calculate the impedance using this data, as shown Figure 1.3.

Figure 1.3(a) shows the response of a passive cochlea, since the real part of the BM impedance is always positive. While, Figure 1.3(b) shows an active cochlea, which means that the real part of the impedance is negative over a small region. It can also be seen that the velocity amplitude peak in the active case is only about 5 dB higher than that in the passive case. A higher amplitude peak can be realized by making the real part of the impedance more negative. However, it is difficult to realize a higher amplitude peak in a long-wave model, since the 1D fluid coupling assumption fails around the peak area.

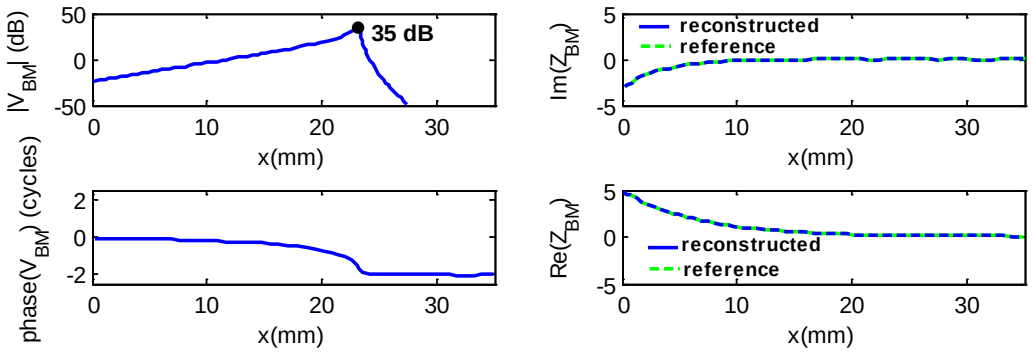

(a)

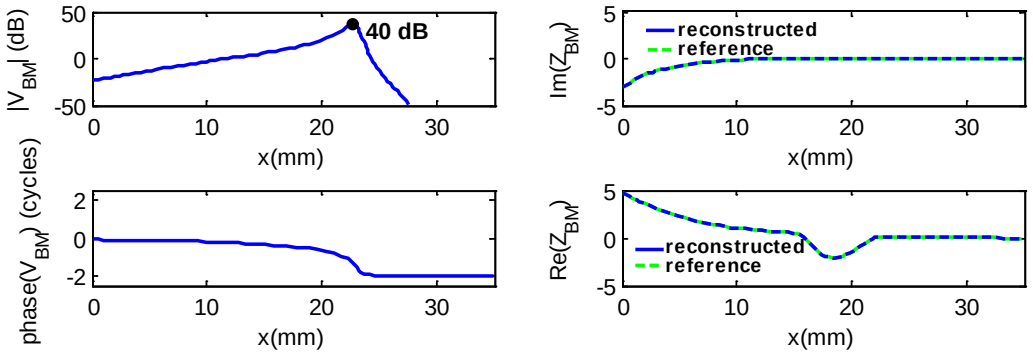

(b)

Figure 1.3 Comparison of reconstructed impedance function to reference impedance function for a 1 kHz tone. (a) passive response, (b) active response. Right panels: blue solid lines: real and imaginary parts of reconstructed impedance function, green dashed lines: real and imaginary parts of reference impedance function. Re-drawn from The Journal of the Acoustical Society of America, 80(1), 124-132., Diependaal (1986), "Are active elements necessary in the basilar membrane impedance?", with permission of The Journal of the Acoustical Society of America.

In general, the shortcoming of many inverse methods is that small changes in the BM velocity cause very large errors of the estimated BM impedance, which was originally illustrated by Diependaal (1986). Transforming the velocity data from the frequency domain into the spatial domain is one reason of these errors, which is also a common limitation among the other inverse methods described below.

Diependaal also calculated the energy flux into and out of cochlea from measured data, in order to determine whether the model was active or not. The cubic spline interpolation method, the least-squares and cubic spline smooth methods are used to fit experimental data and avoid numerical errors, due to the fact that there are too few and noisy data points in original experimental data, and the impedance function is very sensitive to small disturbances in BM velocity.

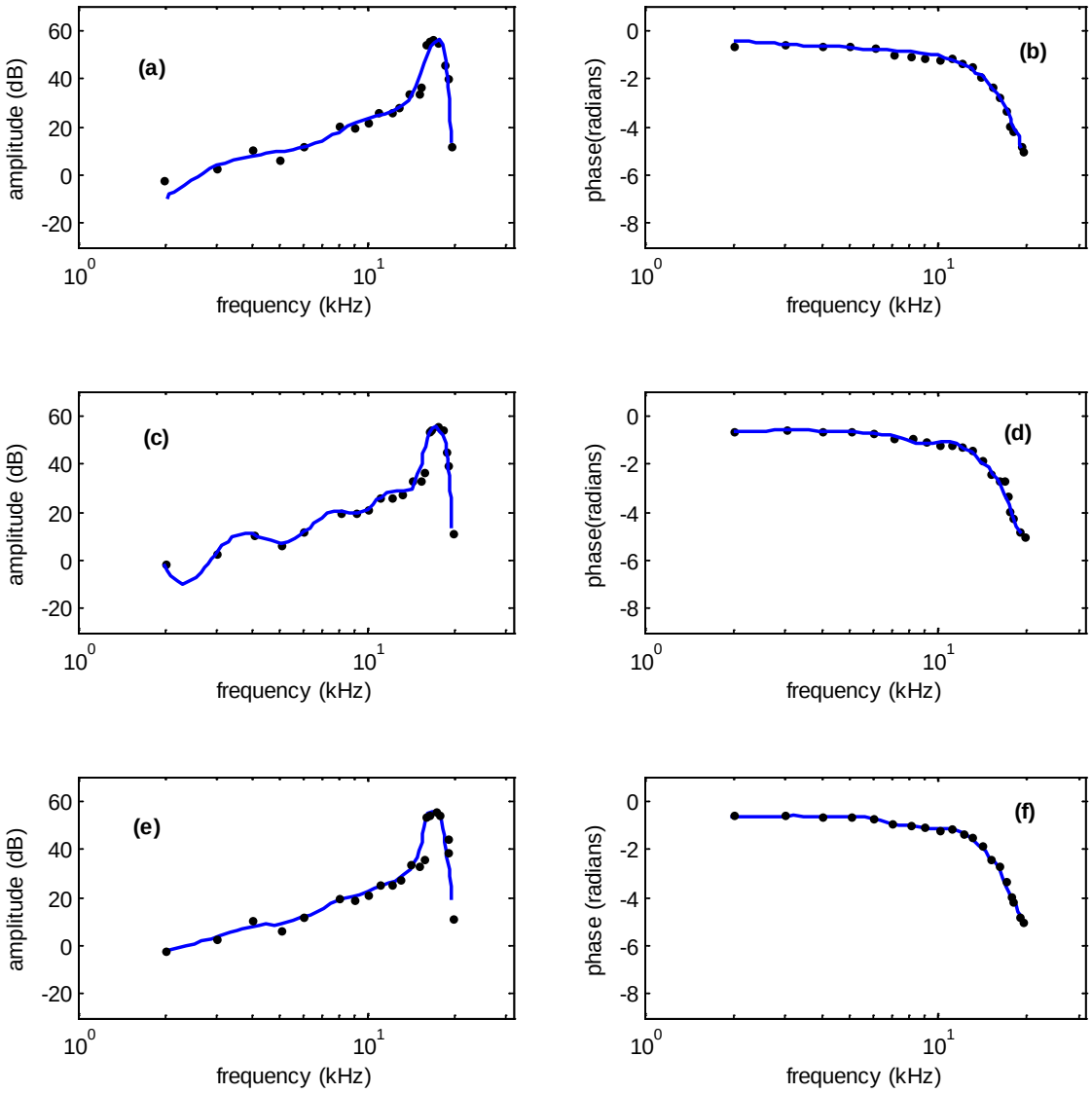

Figure 1.4 The BM velocity after interpolation and smoothing as a function of frequency. (a), (c) and (e) are the amplitude of the BM velocity. (b), (d) and (f) are the phase of the BM velocity. (a) and (b): least square interpolatation and smoothing method, a polynomial of the 6^{th} degree. (c) and (d): least square interpolatation and smoothing method, a polynomial of the 11^{th} degree. (e) and (f): cubic spline interpolatation and smoothing method. Re-drawn from The Journal of the Acoustical Society of America, 82(3), 917-926., Diependaal (1986), "Cochlear power flux as an indicator of mechanical activity", with permission of The Journal of the Acoustical Society of America.

It can be seen from Figure 1.4 that the results using different smoothing methods can appear to be similar, but the final results using the inverse method with those smoothed results can be very different, as described by Diependaal (1986).

The BM velocity in experiments is often measured as a frequency response curve, so that a transformation from the frequency domain to the spatial domain is needed. However, this transformation will add same error into the inverse method. Diependaal improved the transformation, as described in his paper (Diependaal, 1986).

1.3.2. Zweig's method

Zweig (1991) used an inverse method to estimate the wavelength and the impedance of the organ of Corti. He assumed that if the organ of Corti consists of a one-dimensional array of coupled elements, and its individual mechanical characteristics are unknown, then it is possible to use measurements of BM response to estimate the properties of those elements. The long-wave model is used, even though the 1D fluid coupling fails around the peak area due to appearance of short wave. The wavenumber is derived by an iteration procedure related to the BM response. If there is measurement error in the BM response, it increases the errors with each iteration, the iteration converges only if the BM response is smooth. A smoothing technique is developed that fits splines to the real and imaginary parts of the measurement data of the BM response (Zweig, 1991). The form of the derived wavenumber can show how the power flows to or from a harmonic traveling wave, which means that away from the characteristic frequency point, the cochlea is active and the traveling wave absorbs energy from the organ of Corti. Near the characteristic frequency point, the direction of energy flow is reversed and the wave no longer propagates. The calculated wavenumber is interpreted by showing that each section of the organ of Corti acts like a negative damped harmonic oscillator with negative feedback forces.

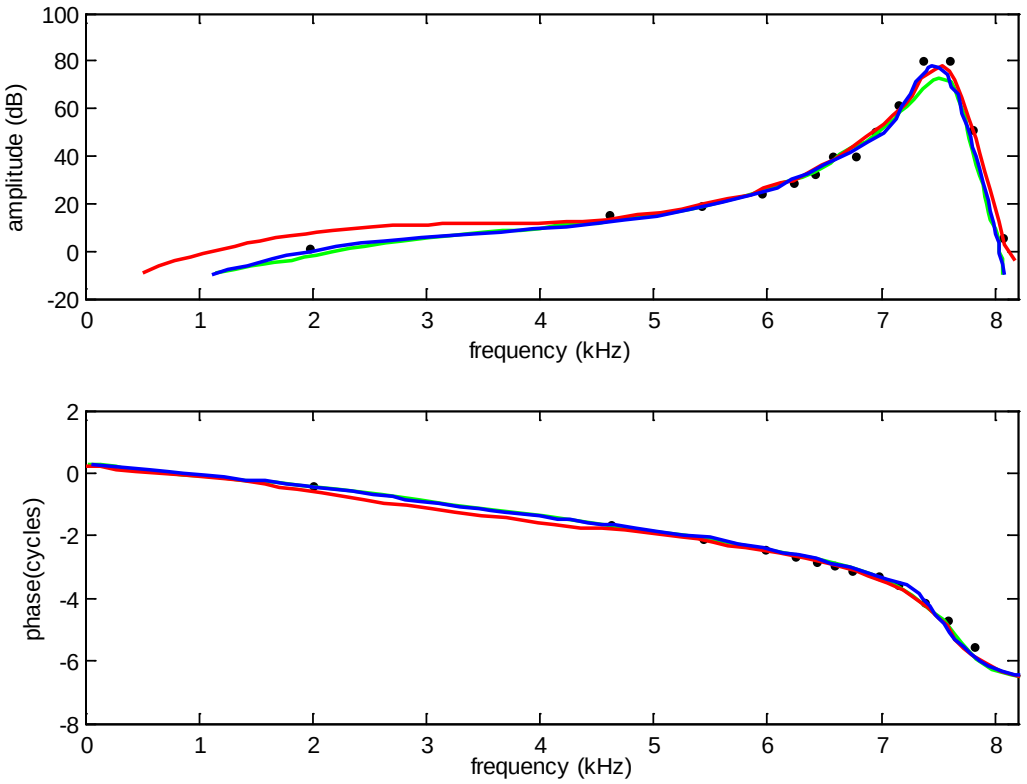

Figure 1.5 Comparison of BM velocity (amplitude and phase) in different situations as calculated by Zweig (1991). Black dotted dots: normalized BM velocity measured by Rhode (Rhode, 1973), blue solid line: reconstructed BM velocity from the wavelength derived via the inverse method by Zweig (1991), green solid line: the BM velocity derived from wavelength, red solid line: the BM velocity in a mechanical model. Re-drawn from The Journal of the Acoustical Society of America, 89(3), 1229, Zweig G. (1991), "Finding the impedance of the organ of Corti", with permission of The Journal of the Acoustical Society of America.

Figure 1.5 shows the measurement data, the fitted BM response, the estimated BM response derived from the estimated wavelength and another type of BM response using a simple mechanical model. It can be seen that the fitted BM response is in good agreement with the measurement data for both amplitude and phase. The BM response derived from the calculated wavelength is also in agreement with the measurement data, indicating the validity of the iteration procedure described above. Another type of BM response, using a simple mechanical model, is also in reasonable agreement with the measurement data, although not as accurate as the wavelength method.

1.3.3. de Boer's first method

de Boer (1995a) initially considered the inverse problem by following on from the methods of Diependaal (1986). The difference from Diependaal's is that the model is developed using a 3D uniform box model of the cochlea, which supports both the long and short waves. The WKB method was used to derive the approximate solution for the 3D model. In his method, the integral equation can be converted into an ordinary differential equation of third order. If

the BM velocity is known, the BM impedance can be calculated from the given BM velocity using this inverse method, as described in more detail in Chapter 2. The theoretical basis of the procedure is presented in (de Boer, 1995a), and an analysis is given for the validity of the method and errors involved. de Boer also discusses how very small errors in the BM velocity function produce unacceptably large errors in the results. Therefore, really well-smoothed data should be used, in order to avoid numerical errors.

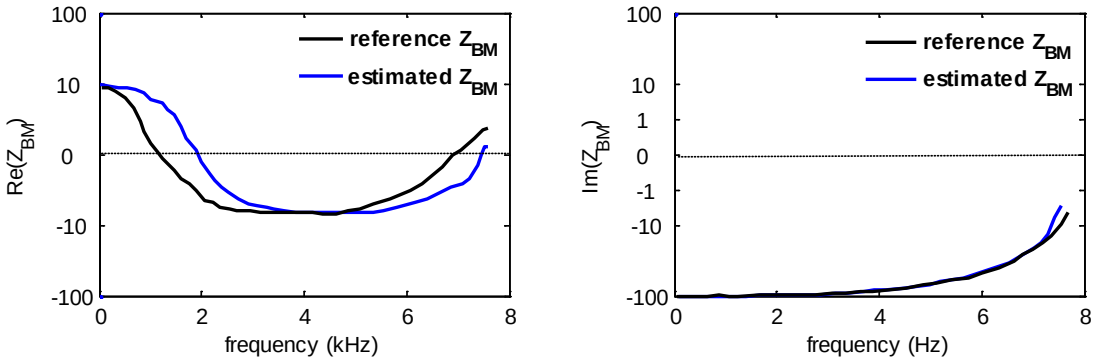

Figure 1.6 Real and imaginary part of the function $Z_{BM}(x)$ calculated for simulated data with and without a small error. The reference and the estimated functions can be distinguished. Re-drawn from The Journal of the Acoustical Society of America, 98(2), 896-903, de Boer (1995), "The 'inverse problem' solved for a three dimensional model of the cochlea. I. Analysis", with permission of The Journal of the Acoustical Society of America.

Initially, the BM velocity at a fixed frequency was simulated by de Boer using the 3D uniform box model of cochlea, which is taken as "measured" data, then, using de Boer's first inverse method, the estimated BM impedance was caclculated, and shown to fit with the reference BM impedance, even though there is small error for the phase. A different view of the same result is provided in Figure 1.6, which shows the real and imaginary parts of the BM impedance. The estimated impedance is in agreement with the reference ones, even when the real part of the estimated impedance is negative, the active cochlea (de Boer, 1995a).

Following the original paper (de Boer, 1995a), de Boer (1995b) applied the same inverse method to experimental data sets. The experimental data are interpolated and smoothed using method described by Diependaal (1986). Figure 1.7 shows the real and imaginary part of the BM impedance calculated from the measurement data. The real part of the BM impedance is seen to go from negative to positive, where the imaginary part remains negative and varies little, indicating an active cochlea.

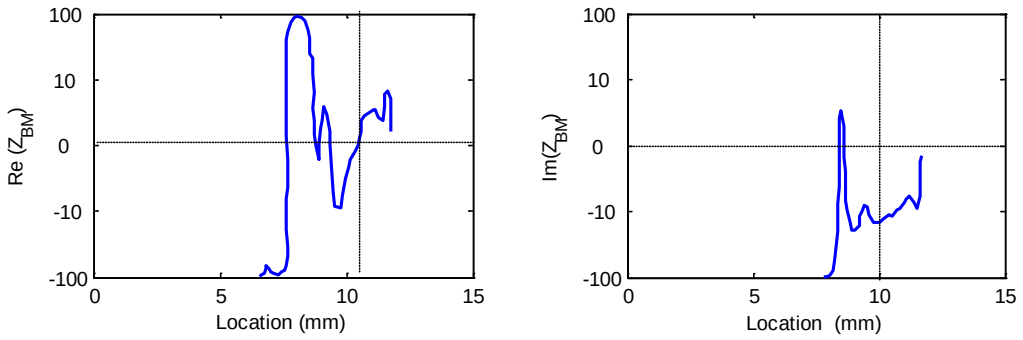

Figure 1.7 BM impedance function computed from a (regularized) measurement data set. Left panel: real part of the derived BM impedance from measurement data by using the inverse method. Right panel: imaginary part of the derived BM impedance from measurement data. Re-drawn from The Journal of the Acoustical Society of America, 98(2), 896-903, de Boer (1995b), "The 'inverse problem'solved for a three dimensional model of the cochlea. II. Application to experimental data sets", with permission of The Journal of the Acoustical Society of America.

1.3.4. de Boer's second method

de Boer (1999) described a more universal method compared with that described above, which could be used for models with arbitrary shape. This method will be investigated in Chapter 2. If the BM velocity, stapes velocity, and fluid coupling impedance are given, this method calculates the BM admittance using a simple matrix algebra. Also, the conservation of fluid volume is described, which leads to the concept of "virtual stapes velocity" that is used to calculate the stapes velocity using the measurement data of the BM velocity.

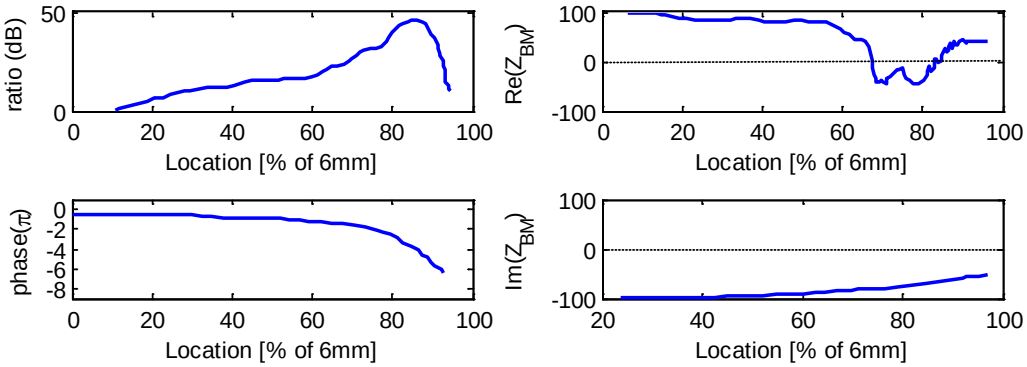

Figure 1.8 Left two panels: measurement data converted from the frequency domain to the spatial domain and slightly smoothed. Right two panels: real and imaginary part of the BM impedance derived from the measurement data using the inverse method. re-drawn from The Journal of the Acoustical Society of America, 105(6), 3410-3420, de Boer (1999), "The 'inverse problem' solved for a three-dimensional model of the cochlea. III. Brushing-up the solution method", with permission of The Journal of the Acoustical Society of America.

Figure 1.8 illustrates measurement data of BM response and the estimated BM impedance using de Boer's second inverse method, based the measured data. The left two panels show the amplitude and phase of the BM response in the spatial domain. The right two panels present real and imaginary parts of the BM impedance as estimated using a 3D model. The

real part of the BM impedance shows negative values (indicates an active cochlea) around characteristic position, and this occurs in the region where the response amplitude is rising most rapidly.

de Boer's second inverse method was also used to show the compression of the response, the reduction of frequency selectivity, the shift in peak frequency and most importantly, the preservation of timing in the impulse response, so that understanding the influence of cochlear nonlinearity on those cochlear features.

1.3.5. Shera's method

Shera (2007) followed the work of Zweig (1991) in calculating the properties of the wave, rather than the BM impedance, but assuming a complex wavenumber. Shera (2007) proposed an inverse method, which used measured BM velocity at a location along the *in vivo* cochlea in the frequency domain, to calculate the real and imaginary parts of wavenumber, using double integration.

He then went on to estimate the BM velocity distribution in the spatial domain to test the theory. This method gives a strong evidence of traveling wave amplification in the mammalian cochlea from measurements, which are based on the real and imaginary parts of the complex wavenumber shown in Figure 1.9, since the imaginary part of the complex wavenumber is seen to be positive at basal positions to the peak in the BM response, where the real part of the complex wavenumber is maximum.

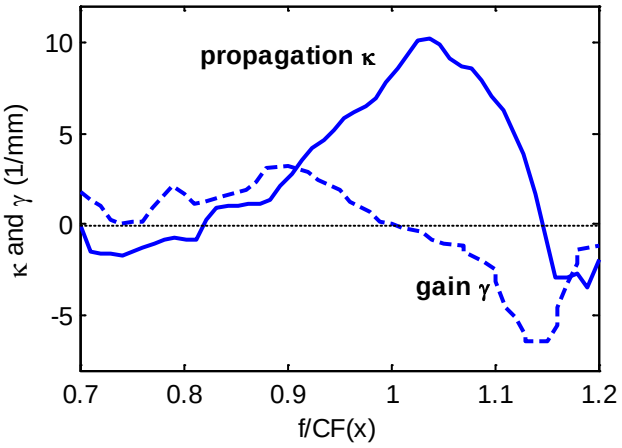

Figure 1.9 Derived propagation and gain functions, which are the real and imaginary part of the wavenumber derived from the measurement data of the BM velocity using the inverse method. Re-drawn from The Journal of the Acoustical Society of America, 122(5), 2738-2758, Shera, (2007), "Laser amplification with a twist: Traveling-wave Propagation and gain functions from throughout the cochlea", with permission of The Journal of the Acoustical Society of America.

1.4. "pole-zero" model of the cochlea: Silicon cochlea

All of the inverse methods described above were mainly used to confirm that there are active elements in the BM impedance, but not to investigate the mechanics of the BM impedance. A new formulation of the inverse method will be considered here, whose concept comes from the "pole-zero" model of the cochlea, as previously used in the silicon cochlea. This may provide further insight into the nature of the cochlear micromechanics.

Richard Lyon and Carver Mead (1988) created the first silicon cochlea, and there have been many variations and improvements since then. The challenge and attraction of building electronic cochlea lies in the design and implementation of a complex signal processing system that follows basic principles of the biological cochlea. In general, the filter models belong to three main families of filters (Lyon *et al.*, 2010): the rounded exponential, the gammatone / gammachip, and the filter cascade. Mandal *et al.* (2009) described a silicon cochlea, which used a transmission line model with micromechanical elements having two pairs of poles and one pairs of zeros model, to model the active cochlea. His model improved previous silicon cochlea designs, with sharper rolloff slopes and lower group delay than prior all-pole versions. The BM impedance of the silicon cochlea defined by pole and zero is shown in Figure 1.10. (Mandal *et al.*, 2009)

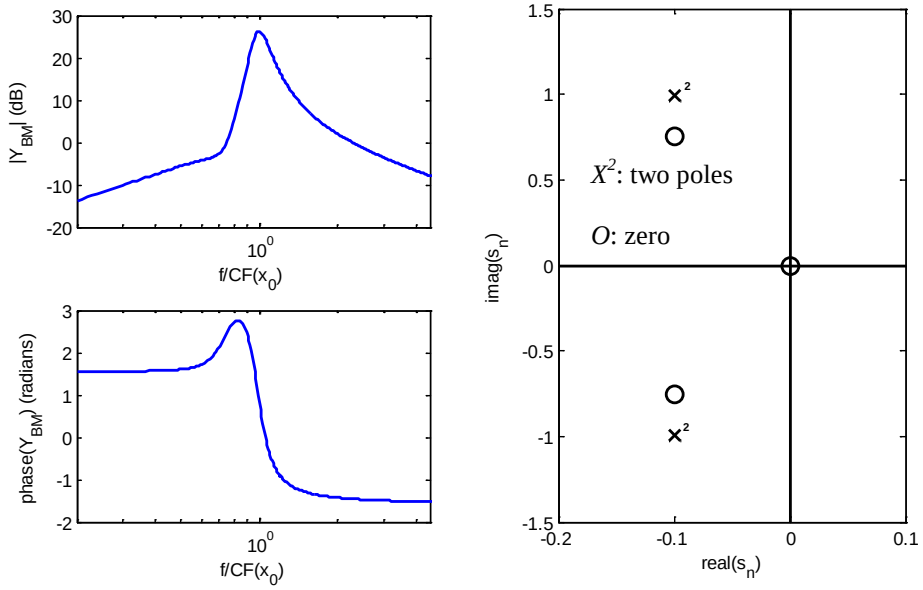

Figure 1.10 Left panel: normalized BM admittance, Y_{BM} , used in the silicon cochlea. Right panel: pole-zero plot for Y_{BM} , *O* stands for a zero at the origin or one pairs of zeros, X^2 stands for two pairs of poles (Mandal *et al.*, 2007).

1.5. Aims and structure

One aim of this thesis is to analyse the micromechanics of the cochlea according to different measurement data using a direct inverse method. It is hoped that these new findings would help to provide a new micromechanical model, and shed light on how the organ of Corti in the cochlea works and what is the relationship of the elements in the organ of Corti. Another aim of this thesis is to improve the current box model, with measurement data for the scalae dimensions. The uniform box model of the cochlea is described first, and different inverse methods are then validated using this uniform box model (Chapter 2). The uniform box model is then extended to a tapered box model for different species, for investigating the fluid coupling and the BM velocity, and the inverse methods are then also tested with this tapered box model (Chapter 3). Chapter 2 and Chapter 3 focus on the passive cochlear model, while Chapter 4 starts to investigate the active cochlea, using the Neely and Kim model (1986). The poles and zeros of the BM admittance are calculated with variations of characteristic position and sound pressure level, and a new formulation is suggested to optimise the required parameters. The results are compared with the parameters from the Neely and Kim model to investigate the performance of this direct inverse method. In Chapter 5, the performance of two different inverse methods, including the direct inverse method, are investigated, using measured BM velocity data to develop pole-zero structure of the micromechanics. Finally, findings of this research are summarized and discussed in Chapter 6, and suggestions made for futher work.

1.6. Contributions

The main contributions of this work are as follows:

1. The uniform box model is extended, to investigate the effect of tapering, on the BM velocity for different species with 1D and 3D fluid coupling. This tapered box model of cochlea is based on measured parameters. Other contributions made with this tapered box model are to investigate the difference between different species, and the influence of the near field fluid pressure on the coupled response of the cochlea.
2. Previous inverse methods for calculating the basilar membrane response from measurement data are investigated and their performances are compared systematically.

3. A new method, which is termed the “direct” inverse method, is proposed to calculate the poles and zeros of the organ of Corti directly from the measured BM response. These parameters are adjusted to minimise two objective functions, associated with the magnitude and phase, using multi-objective optimization.

Some of these findings were shared with the wider academic community through conference papers:

Sun, L. Y., Ni, G., Elliott, S. J. (2015) A tapered box model of cochlea, Mechanics of Hearing 2014, Cape Sounio, Greece.

Sun, L. Y., Elliott, S. J., Ni, G. (2016) Fitting pole-zero micromechanical models to coupled cochlear responses by direct optimization, *22th International Congress on Sound and Vibration,* Florence, Italy.

Two journal papers are currently under preparing concerning the tapered box model and the direct optimization results.

Chapter 2

The passive uniform box model

The cochlea is a fluid-filled organ with a spiral shape, which has almost immobile walls, since it is embedded in the temporal bone, which is very hard. The form of the cochlea, and the structure of the organ within it, is elegant and complicated. To investigate the basic mode of its function, we need to simplify the real structure of the cochlea initially using the uniform box model, as described by de Boer (1980), in which the spiral shape is uncoiled. The influence of the fluid chamber shape is first neglected, so that their cross-sectional shape is simplified to a rectangular one. The mechanical influence of Reissner's membrane is also neglected, so that the cochlear model contains only two fluid chambers instead of three. The upper chamber consists of both the scala vestibuli and the scala media, while the lower chamber consists of is the scala tympani. The cross-sectional area and shape of the two chambers are also assumed to be equal. The organ of Corti separates the two fluid chambers and is assumed to be passive. In this case, it can be modelled as a series of one degree of freedom systems. A uniform box model of the cochlea is used in this chapter to investigate the basic mechanics of the cochlea and also to test the inverse methods outlined in Chapter 1.

The mechanics of the cochlea can be thought as an interaction between the fluid inertia and the dynamics of the cochlear partition. The fluid coupling inside the cochlea can itself be divided into two components (Elliott *et al*., 2011b): one due to the plane wave component of the pressure in each chamber, also known as the 1D, or far field fluid component, and one due to the local pressure variations close to the BM, also known as the near field component, which, together with the plane wave go to make up the full 3D fluid coupling. The 1D component of the fluid coupling depends on the variation of a single "effective area" along the length of the cochlea (Peterson and Bogert, 1950; Elliott *et al.*, 2011b), which is a function of the area of the two fluid chambers, separated by the BM. The near field component of the fluid coupling, on the other hand, contributes a fluid added mass to the dynamics of the BM, which depends on the width and position of the BM relative to that of the fluid chamber. Since the near field pressure distribution is local to the BM, whose width is small compared with that of the cochlear partition over most of the cochlear length, then this component of the pressure is assumed not to be strongly dependent on the areas of the fluid chambers (Elliott *et al.*, 2011b).

2.1. Passive cochlear mechanics

2.1.1. One degree of freedom system

The cochlear partition is initially considered to be a single, passive entity and loosely termed the BM. One assumption is that the response of the BM is linear. In a linear system, movements at different frequencies can be added without influencing each other. A linear mechanical structure can be characterized by its mechanical admittance, defined as the ratio of velocity to pressure. The longitudinal coupling in the organ of Corti is neglected, so that it is a set of narrow bars that could move independently, as shown in Figure 2.1. In the case of passive cochlear, each bar is taken as a 1 degree of freedom (DOF) system including mass, stiffness and damping. The bar vibrates due to the average pressure difference over its width. The pressure divided by the vertical velocity yields the mechanical admittance of the bar; this admittance is a function of position, *x*, and the radian frequency, ω.

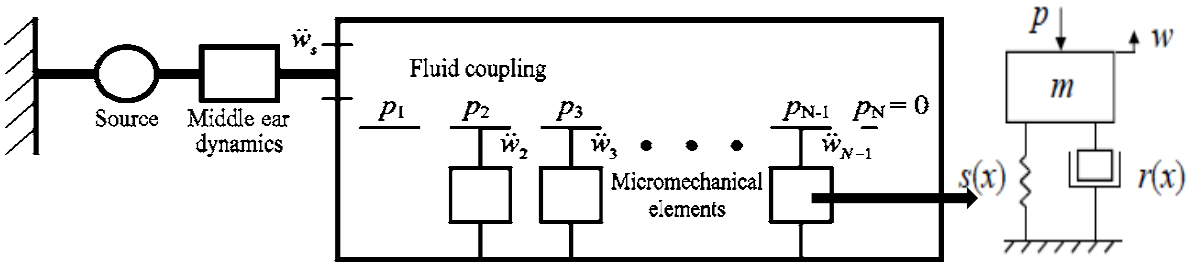

Figure 2.1 Left side: A uniform box model of the cochlea, in which the height of the fluid cochlear and the width of the cochlear partition and basilar membrane are constant along the length. Right side: 1 DOF system (one bar).

The admittance of the passive BM can be written as

$$Y_{BM}(x,\omega) = -\frac{v(x,\omega)}{p(x,\omega)} = \frac{i\omega}{i\omega r(x) + s(x) - \omega^2 m(x)}, \tag{2.1}$$

where $m(x)$, $s(x)$, $r(x)$ are the effective mass, stiffness, and damping of the BM at position *x*. Here, the mass is assumed to be independent of BM width, although it does depend on the BM thickness, which varies slowly along the length of the cochlea. This term should also include the mass due to fluid loading (Elliott *et al.*, 2011), the relative values are listed in Table 2.1.

The natural frequency of the BM is assumed to vary exponentially along its length as

$$\omega_n(x) = \omega_B e^{-x/l}, \tag{2.2}$$

where ω_B is the natural frequency at the base, and ℓ is the characteristic length. The distributions of the natural frequency, ω_n, for different species are shown in Figure 1.2.

The natural frequency $\omega_n(x)$ can also be expressed as $\sqrt{s(x)/m(x)}$. If the mass is constant all along the cochlea, m_0, the BM stiffness must vary exponentially as

$$s(x) = \omega_n^2(x) m_0 = \omega_B^2 m_0 e^{-2x/l}. \tag{2.3}$$

The damping can be represented by a *Q* factor of the system, which is assumed to be constant, Q_0, here, so that the damping term is given by

$$r(x) = \frac{\sqrt{s(x)m(x)}}{Q_0} = \frac{\omega_B m_0}{Q_0} e^{-\frac{x}{l}}. \tag{2.4}$$

2.1.2. 1D fluid coupling

1D fluid component (far-field component) is defined so that it obeys the equation derived from a one-dimensional analysis of the incompressible fluid as (Elliott *et al*., 2011)

$$\frac{\partial^2 p(x)}{\partial x^2} = -\frac{2i\omega\rho}{h} v(x). \tag{2.5}$$

The finite difference approach is used here to obtain a discrete representation, so that the spatial derivative of equation (2.5) can be written as

$$\frac{p(n-1) - 2p(n) + p(n+1)}{\Delta^2} = -\frac{2i\omega\rho}{h} v(n), \tag{2.6}$$

where Δ is the length of one element. The first and last elements, representing the boundary conditions at the base and apex, are assumed to have the same length as the BM elements, so that $\Delta = L/N$, where L is the assumed length of the cochlea.

The boundary conditions at the base and apex of the cochlea are assumed to be determined by the velocity of the stapes, corrected for the difference between the stapes and the chamber area, u_s, and a zero pressure difference condition at the helicotrema, as

$$\frac{\partial p(x)}{\partial x}\Big|_{x=0} = -2i\omega\rho u_s \text{ and } p(x)\big|_{x=L} = 0. \tag{2.7}$$

In the discrete representation, the finite difference method can be used to express these boundary conditions as

$$\frac{p(2)-p(1)}{\Delta} = -2i\omega\rho u_s \text{ and } p(N) = 0. \tag{2.8}$$

The complete discrete model of the 1D fluid coupling can thus be written in the matrix form as

$$\frac{h}{\Delta^2}\begin{bmatrix} -\frac{\Delta}{h} & \frac{\Delta}{h} & & & & & \\ 1 & -2 & 1 & & & & \\ 0 & 1 & -2 & 1 & & & \\ & & \ddots & & & & \\ & & & 1 & -2 & 1 \\ & & & 0 & 0 & \frac{\Delta^2}{h} \end{bmatrix}\begin{bmatrix} p(1) \\ p(2) \\ \vdots \\ p(N-1) \\ p(N) \end{bmatrix} = -2i\omega\rho\begin{bmatrix} 0 \\ v(2) \\ \vdots \\ v(N-1) \\ 0 \end{bmatrix} - 2i\omega\rho\begin{bmatrix} u_s \\ 0 \\ \vdots \\ 0 \\ 0 \end{bmatrix}. \tag{2.9}$$

The matrix above is simplified to an equation, which is given by

$$\mathbf{F}\mathbf{p} = -2i\omega\rho(\mathbf{v}+\mathbf{v}_s), \tag{2.10}$$

so that

$$\mathbf{p} = \mathbf{p}_s + \mathbf{Z}_{FC}\mathbf{v}, \tag{2.11}$$

where $\mathbf{Z}_{FC}$ is equal to $-2i\omega\rho\mathbf{F}^{-1}$ in this case denoting the 1D fluid coupling matrix, and $\mathbf{p}_s$ is equal to $-2i\omega\rho\mathbf{F}^{-1}\mathbf{v}_s$ denoting the pressure vector due to the stapes motion.

2.1.3. The 3D fluid coupling

The 3D fluid coupling, taken to include the full fluid coupling in the discrete model of Z_{FC}, can be defined that it includes both the far-field component and near-field component. Elliott *et al* (2011a) described the near-field component using the wavenumber analysis, as first developed by Steele and Taber (1979) in terms of an effective fluid chamber height, $Q_{3D}(k)$.

As described by Elliott *et al.* (2011a), if *k* is large, $Q_N(k)$ is equal to $1/k$, whatever the BM width, while if *k* is small, the near-field term becomes a constant, which can be interpreted as an effective fluid thickness, *T*, due to the fluid coupling. Apart from the physical mass per

unit area of the BM, fluid loading will provide some additional mass. In the 1D model of the cochlea, there is an effective additional thickness of the BM due to the fluid coupling, given by (Elliott *et al.*, 2011b)

$$T_f = \frac{8BH}{3\pi^2 W} + \sum_{n=1}^{\infty} \frac{4B}{n\pi^3} \coth\left(n\pi H / W\right) \left[\frac{1+\cos\left(n\pi B / W\right)}{1-n^2 B^2 / W^2} \right]^2, \tag{2.12}$$

where B is the width of BM, W is the width of chamber and H is the height of chamber and the BM is assumed to be located at the edge of the cochlear partition. In this case, B, W, H are constants along the cochlear partition, as listed in Table 2.1.

The near-field component of the fluid coupling impedance is equal to a constant, when kH is less than about unity. For such small values of k, $Z_N(k)$ can be written as $2i\omega\rho T$, where T is an effective fluid thickness. The near-field pressure contribution, for k=0, $p_n(0)$, is thus equal to $2i\omega\rho T v_0$. Using the properties of wavenumer transform, then $p_n(0)$ is also equal to the integral of the near-field component of the pressure in the spatial domain or equivalently, to sum of the elements of the discrete pressure distribution. A position-shifted sequence of these pressure distributions, normalised by the velocities of each element, can then be used to define the columns of the matrix $\mathbf{Z}_N$, which determines the fluid coupling due to the near-field coponents in the discrete model (Ni, 2012). The total distributions due to both the far and near-field fluid coupling by summing these two contributions and the part distribution only due to the far field fluid coupling are illustrated in Figure 2.2.

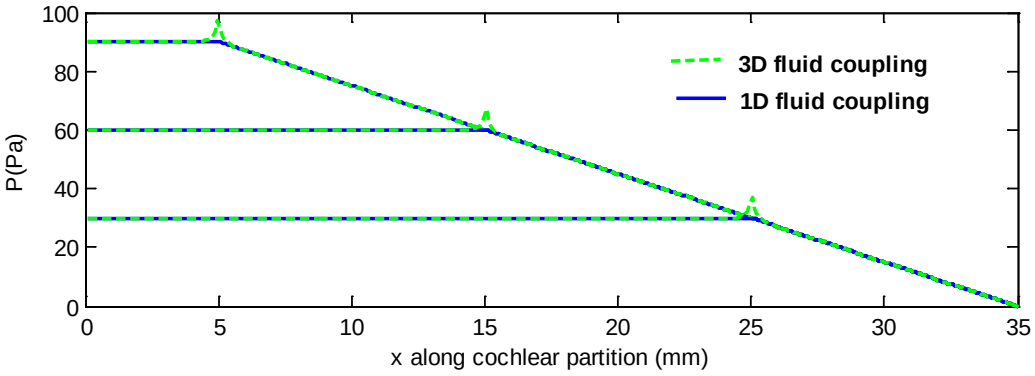

Figure 2.2 Distribution of the pressure with the 1D (far-field component) and 3D fluid coupling (far and near-field components) in the fluid coupling matrix along the length of the cochlea due to excitation of a single element on the BM at x = 5 mm, 15 mm and 25 mm with a velocity of 10 mm s^{-1} at a frequency of 1 kHz.

Table 2.1 Values of physical parameters used for the 1D and 3D uniform passive cochlear model for human.

Variable	Parameter	Value and unit
L	Length of cochlea	35 mm
W	Width of fluid chamber	1 mm
B	Width of basilar membrane	0.35 mm
H	Physical height of single fluid chamber	1 mm
h	Effective chamber height for 1D model	2.86 mm
ρ	Density of fluid	1,000 kg m^{-3}
N	Number of elements in discrete model	512
$\Delta = L / N$	Length of element	68 μm
m_{1D}	BM mass, 1D model	0.28 kg m^{-2}
m_{3D}	BM mass, 3D model	0.05 kg m^{-2}
f_B	BM natural frequency at base	20,000 Hz
ℓ	Natural frequency length scale	7 mm
Q_0	Q factor	2.5

2.1.4. Coupled response in a uniform box model

The coupled response of the cochlea in the box model can be calculated using the elemental approach (Elliott *et al*., 2011b), in which the fluid coupling and BM admittance are combined in a matrix formulation. The BM in the box model of the cochlea is divided into N discrete elements, as shown in Figure 2.1, each of which is coupled longitudinally only via the cochlear fluid.

Following the description in section 2.1.2, equation (2.1) can be rewritten as

$$v(n) = -Y_{BM}(n)\, p(n), \tag{2.13}$$

where n=2 to N-1, $v(1)=v_s$, is assumed to be unaffected by $p(1)$, and $p(N)=0$, these equations can be written in a matrix form as below

$$\begin{bmatrix} v(1) \\ v(2) \\ \vdots \\ \vdots \\ v(N-1) \\ 0 \end{bmatrix} = \begin{bmatrix} 0 & & & & \\ & Y_{BM}(2) & & & \\ & & \ddots & & \\ & & & Y_{BM}(N-1) & \\ & & & & 0 \end{bmatrix} \begin{bmatrix} p(1) \\ p(2) \\ \vdots \\ \vdots \\ p(N-1) \\ p(N) \end{bmatrix} + \begin{bmatrix} v_s \\ 0 \\ \vdots \\ \vdots \\ 0 \\ 0 \end{bmatrix} \tag{2.14}$$

This matrix equation can be written in a form of the BM velocity, given as

$$\mathbf{v} = \mathbf{v}_s - \mathbf{Y}_{\mathrm{BM}}\mathbf{p}, \tag{2.15}$$

where $\mathbf{v}_s$ is a vector whose first element is the stapes velocity and $\mathbf{Y}_{BM}$ is a matrix of the BM admittances. Substituting equation (2.11) into (2.15) gives the vector of the coupled BM velocities as

$$\mathbf{v} = \left[\mathbf{I} + \mathbf{Y}_{\mathrm{BM}}\mathbf{Z}_{\mathrm{FC}}\right]^{-1}\mathbf{v}_s, \tag{2.16}$$

where Z_{FC} can be calculated for either the 1D or 3D models of fluid coupling.

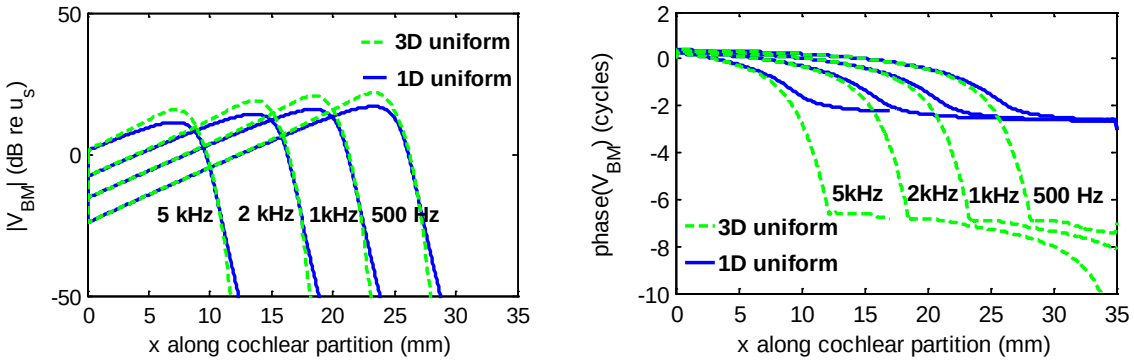

Figure 2.3 Amplitude and phase of the BM velocity with 1D and 3D fluid coupling at four fixed frequencies (500 Hz, 1 kHz, 2 kHz, and 5 kHz) as a function of position in a 1D and 3D uniform box model of the passive cochlea for human. Blue solid lines: 1D uniform box model; green dash lines: 3D uniform box model.

Figure 2.3 and Figure 2.4 show the BM velocity at fixed frequencies, as a function of position, and fixed positions, as a function of frequency, in the 1D and 3D uniform box models of the human cochlea, calculated using equation (2.16), which illustrates the basic mechanics of the cochlea. At the base of the cochlea, the stiffness dominates the dynamics of the BM, so the wave propagates quickly and there is little phase shift. The stiffness decreases exponentially along the cochlear partition, so that the wave slows down and the slope of the phase lag can be seen to increase. The amplitude of the BM velocity increases until it resonates, where a

peak is observed in the velocity curve. Finally, the mass dominates in the cochlear partition, the BM velocity decreases more rapidly. as seen in Figure 2.3. For different frequencies, the locations of the peak are different, and in Figure 2.4 for different positions, the frequencies of the peak are different as well, so that the cochlea model can map frequency to place that is shown in Figure 1.2. The parameters that are used for simulation are listed in Table 2.1.

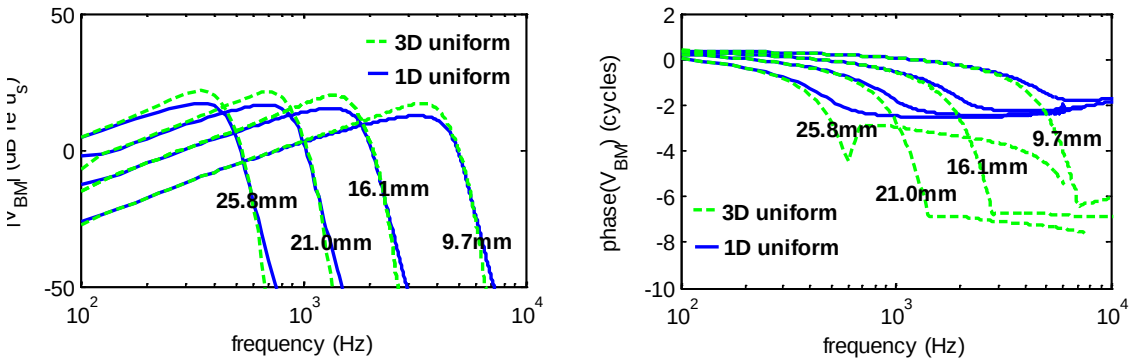

Figure 2.4 Amplitude and phase of the BM velocity with 1D and 3D fluid coupling at four fixed positions (25.8 mm, 21.0 mm, 16.1 mm, and 9.7 mm) as a function of frequency in a 1D and 3D uniform box model of the passive cochlea for human. Blue solid lines: 1D uniform box model; green dash lines: 3D uniform box model.

The BM mechanical response is a function of both distance from the stapes, x, and the driving frequency, f. In most experiment, the BM motions are measured at fixed positions, x_o, in the frequency domain, while the inverse methods, which are described later, are used in spatial domain. Therefore, the data should be transformed from the frequency domain to the spatial domain using transformation methods, which are related to the frequency-place mapping. In this chapter, de Boer's (de Boer, 1995b) and Shera's (Shera, 2007) transformation methods are described.

2.1.5. Transformation from the frequency domain to the spatial domain

Shera (2007) proposed a transformation method, which is similar as de Boer's method that is illustrated in Appendix A**,** following Zweig (1991). Local scaling symmetry can be used to convert $V_{BM}(x_o, f)$ at a fixed location x_o into an estimate of $V_{BM}(x, f_o)$ at a given frequency, f_o. The local scaling implies that $V_{BM}(x, f)$ depends on x and f in the form of a dimensionless combination, $f / CF(x)$, where $CF(x)$ is the characteristic frequency. In other words, $V_{BM}(x_o, f)$ can be plotted against $f / CF(x_o)$ in the frequency domain, while $V_{BM}(x, f_o)$ will be plotted against $f_o / CF(x)$ in the spatial domain, which means that this form of $V_{BM}(x, f_o)$ can be distributed evenly as a function of position derived from

$V_{BM}(x_o, f)$ using this transformation method. The details of the transformation method method is shown below.

For instance, the calculated BM velocity frequency response at 21 mm, is transformed in this way and shown in Figure 2.5 plotted against $f / CF(x_o)$. The BM distributions at a fixed frequency and at a fixed position are illustrated in a same figure using local scaling symmetry. Figure 2.5 shows that the amplitudes and phases of the BM velocity obtained at a fixed position and a fixed frequency are almost the same when they are plotted against non-dimensional variable $f / CF(x)$, as expected in this theoretical case.

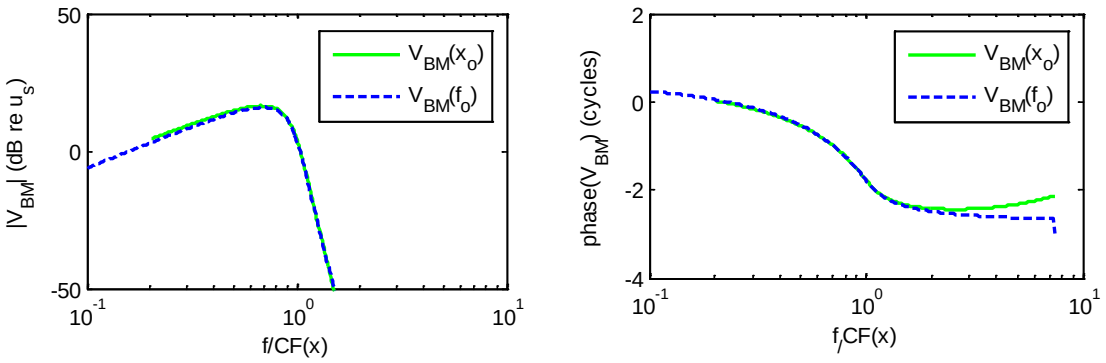

Figure 2.5 The amplitude and phase of BM velocity distribution of cochlear using the 1D uniform box model of the human cochlea at a fixed position and a fixed frequency, respectively. The logarithmic abscissa $f / CF(x)$ can express a frequency axis as a fixed position $f / CF(x_0)$ and a space axis as a fixed frequency $f_0 / CF(x)$, respectively.

Since $V_{BM}(x_o, f)$, as a function of $f / CF(x_o)$, is calculated at a fixed position, it needs to be transformed to be, in the form $V_{BM}(x, f_o)$, as a function of $f_o / CF(x)$, at a fixed frequency f_o and then needs to be sampled uniformly in the space domain. This is achieved using a linear interpolation method, as illustrated in Figure 2.6, where $y = V_{BM}$ is the function being interpolated, which is originally sampled uniformly in the frequency domain and then resampled in the spatial domain using the mapping $CF(x) f_B e^{-x/\ell}$, where f_B =20 kHz, ℓ =7 mm.

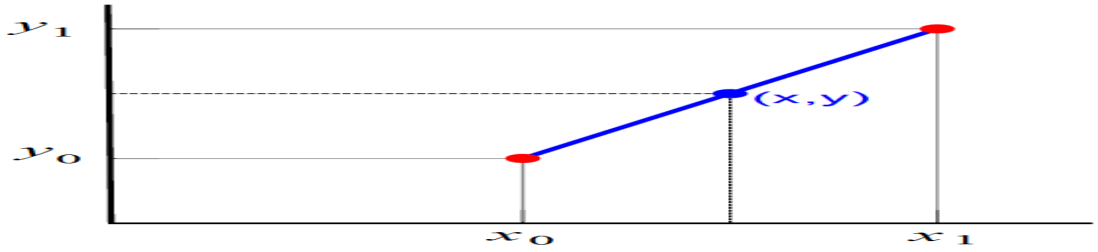

Figure 2.6 Illustration of linear interpolation. Red points are taken as two points within the given points of the V_{BM} as a function of $f/CF(x_0)$, blue point is taken as one point with the re-sampled points of the "new" V_{BM} as a function of $f_0/CF(x)$. x_0 and x_1 are two values of $f/CF(x_0)$, x is one value of $f_0/CF(x)$. y_1 and y_0 are two values of the magnitude of the V_{BM} as a function of $f/CF(x_0)$. y is one value of the magnitude of the "new" V_{BM} as a function of $f_0/CF(x)$.

Figure 2.6 shows the linear interpolation method, with the two know points given by the coordinates (x_0, y_0) and (x_1, y_1), the linear interpolation is the straight line between these points. For a value x in the interval (x_0, x_1), the value y along the straight line is given from the equation,

$$\frac{y-y_0}{x-x_0}=\frac{y_1-y_0}{x_1-x_0}, \tag{2.17}$$

and solving this equation for y, which is the unknown value at x, gives

$$y=y_0+(y_1-y_0)\frac{x-x_0}{x_1-x_0}, \tag{2.18}$$

which is the formula for linear interpolation in the interval (x_o, x_1).

According to this formula, the BM velocity, which is sampled uniformly as a function of frequency, is converted into the one that is sampled uniformly as a function of position, as illustrated for an example on an expanded scale in Figure 2.7 as a function of log frequency and linear position.

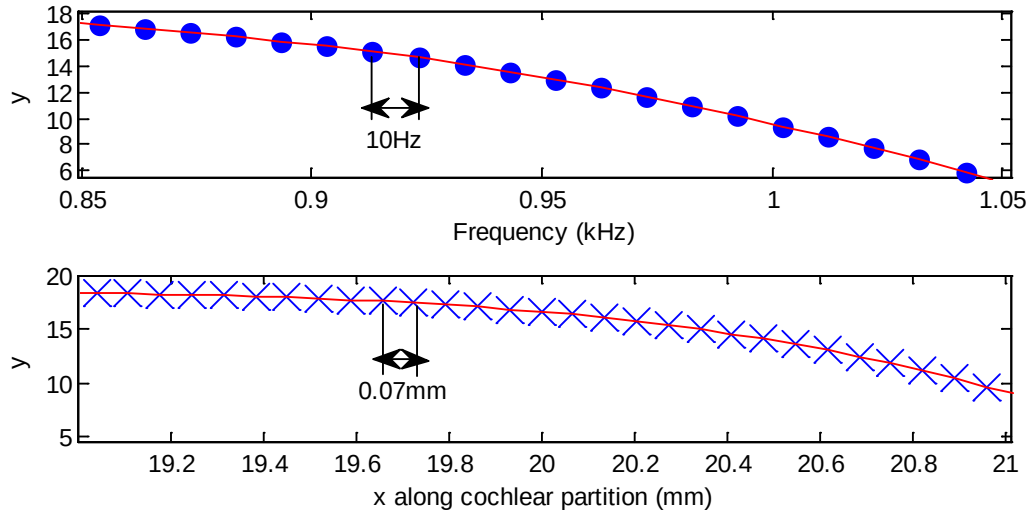

Figure 2.7 Parts of the magnitude of the BM velocity as a function of frequency at 21 mm and the derived BM velocity as a function of position at 1 kHz from $V_{BM}(x_0, f)$.

Figure 2.8 shows that each re-sampled point, which is marked as blue dot, is approximated between two consecutive points that are related to the re-sampled point within these given points, which are marked as green dot. The selection of the two points and the value of the re-sampled point depends on the values of $f_o / CF(x)$ and $f / CF(x_o)$. Also, the number of re-sampled points depends on the values of $f_o / CF(x)$ and $f / CF(x_o)$, because the selected values of $f_o / CF(x)$ should be in the range of $f / CF(x_o)$.

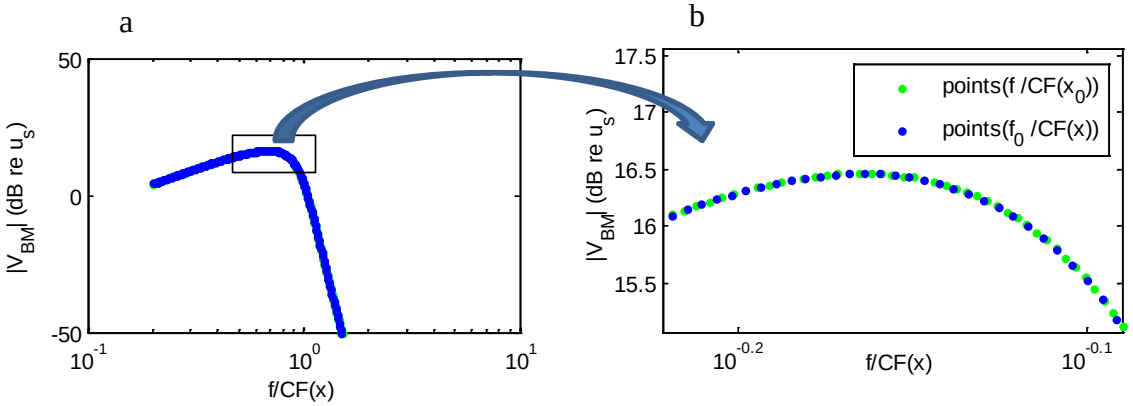

Figure 2. 8 Illustration of the interpolation method. (panel a) the points of V_{BM} as a function of $f / CF(x_0)$ and the re-sampled points of V_{BM} as a function of $f_0 / CF(x)$ are illustrated in the same figure. (panel b) enlarged rectangular part of the figure in panel a. Based on the initial points (green dot)of V_{BM} as a function of $f / CF(x_0)$, the re-sampled points (blue dot) are interpolated between some pairs of initial points, the re-sampled points are based on $f_0 / CF(x)$.

Figure 2.9 shows that the BM velocity distribution in the spatial domain obtained by converting the BM velocity calculated at a fixed position in frequency domain, the re-

sampled BM velocity is distributed uniformly along the cochlear partition. It can be seen that the converted BM velocity is almost the same as that calculated using the model at a fixed frequency. Therefore, the BM velocity is successfully converted from frequency domain into space domain.

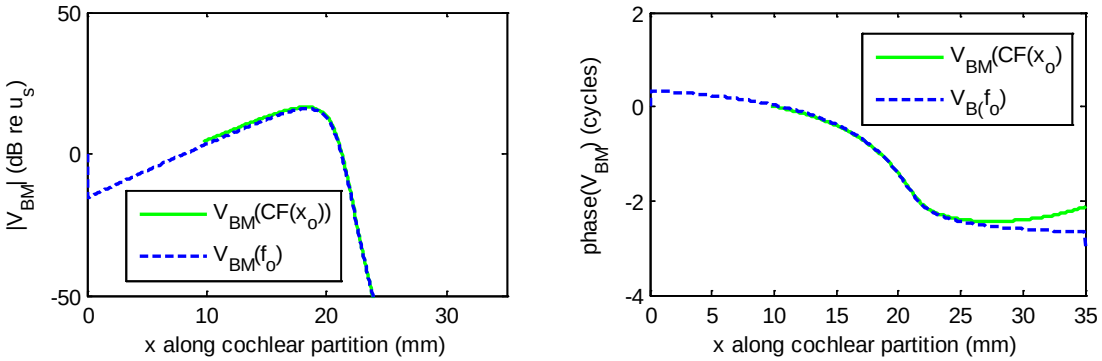

Figure 2.9. The magnitude and phase of $V_{BM}(CF(x_o))$ along the cochlear partition, which transformed from $V_{BM}(f_o)$ at a fixed position (21 mm) using the 1D uniform box model of human cochlea are denoted by black dashed line. The magnitude and phase of $V_{BM}(f_o)$ calculated at a fixed frequency (1 kHz) along the cochlear partition using the theoretical formula are denoted by blue solid lines.

Figure 2.10 shows the transformed BM response, which are derived from the frequency domain at four different fixed positions in 1D and 3D uniform box models of the passive cochlea for human in Figure 2.4, using the transformation method. It shows that low frequency responses are scaled to the right, which match the frequency-position mapping, for instance, the BM response of 25.8 mm in the frequency domain, is transformed into the position corresponsding to about 500 Hz in the spatial domain.

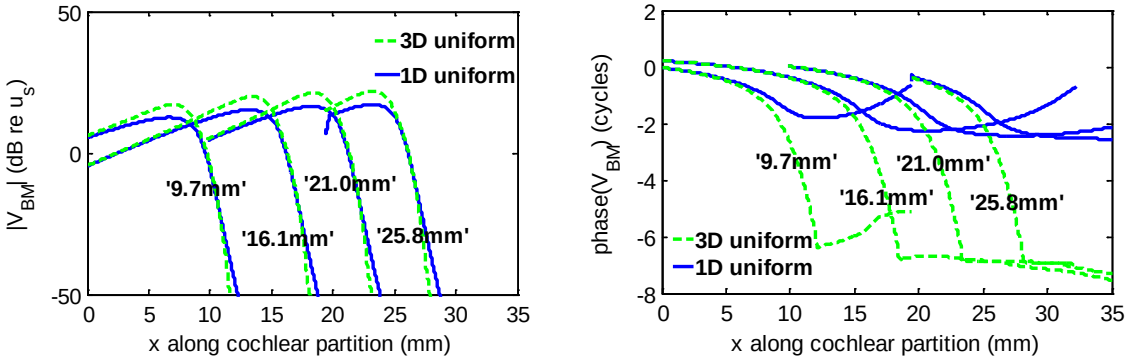

Figure 2.10 Amplitude and phase of the BM velocity as a function of position derived from the BM response at four fixed positions (25.8 mm, 21.0 mm, 16.1 mm, and 9.7 mm) in the frequency domain with Shera's method according to Figure 2.4. Blue solid lines: 1D uniform box model; green dash lines: 3D uniform box model. "25.8 mm": the original BM response at 25.8 mm in the frequency domain. "21 mm": the original BM response at 21 mm in the frequency domain. "16.1 mm": the original BM response at 16.1 mm in the frequency domain. "9.7 mm": the original BM response at 9.7 mm in the frequency domain.

2.2. de Boer's first inverse method in the 1D uniform box model

2.2.1. 1D uniform box model

de Boer (1995a) proposed his first inverse method and tested it in using a box model of cochlea, the details of this method are described in Appendix B. His formulation for the BM admittance is given here as

$$\hat{Y}_{BM}(x) = \frac{iV_{BM}(x)}{2\omega\rho F_0 \int_{x_0}^{x} \int_{x_0}^{x'} V_{BM}(x'')dx''dx'}. \tag{2.19}$$

where $\hat{Y}_{BM}$ is the estimated BM admittance, $V_{BM}(x)$ is the measured BM velocity, ω is the radian frequency, ρ is the fluid density, $F_0 = \frac{Bf_0}{WH}$, where B is the BM width, W is the width of fluid chamber and H is the physical height of a single fluid chamber.

Initially, the calculated BM response from our box model at 1 kHz in the spatial domain, as shown in Figure 2.3, is used as "measured" BM velocity, V_{BM}, to investigate de Boer's first inverse method, and will also be used for the other inverse methods. The results for the BM admittance, $\hat{Y}_{BM}$, are shown in Figure 2.11, and show very good agreement with that used in the box model, Y_{BM}.

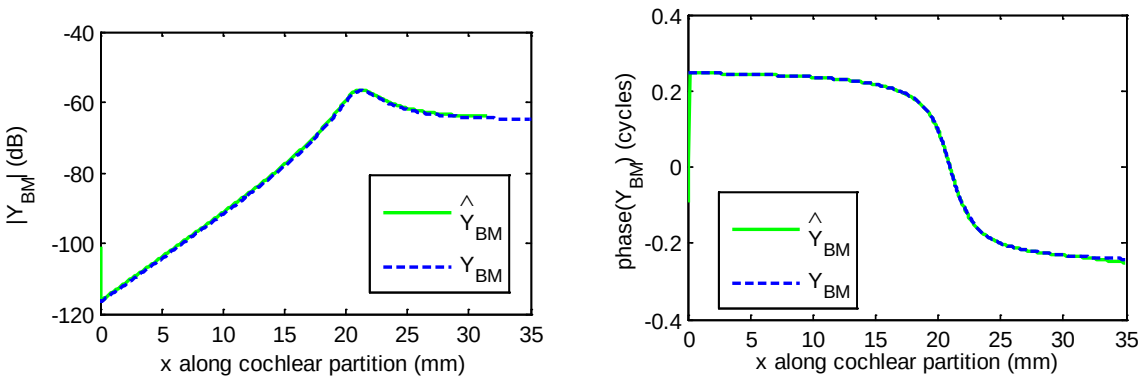

Figure 2.11 Comparison between the Y_{BM} at 1 kHz as a function of position in the 1D uniform box model and $\hat{Y}_{BM}$ derived using de Boer's first inverse method.

The BM frequency response at 21 mm , as shown in Figure 2.4, is then used to estimated this spatial data, as in Figure 2.10, and hence estimated the BM admittance. The results are shown in Figure 2.12, and indicate that $\hat{Y}_{BM}$ is again in reasonable agreement with Y_{BM}, although with some deviation towards the apex.

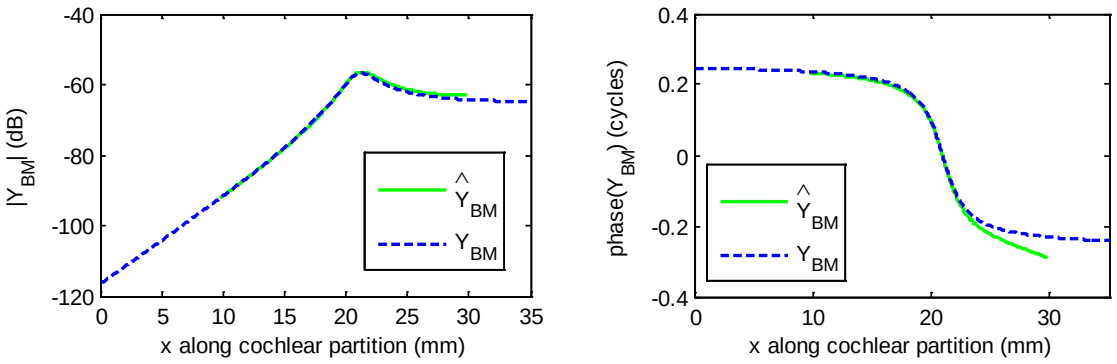

Figure 2.12 Comparison between Y_{BM} at 1 kHz as a function of position in 1D uniform box model and $\hat{Y}_{BM}$ derived using de Boer's first inverse method. Shera's transformation method is used.

2.2.2. 3D uniform box model

de Boer (1995a) also extended his first inverse method for a 3D uniform box model. The details of the procedure are described in Appendix B, but, in summary, the formulation of the estimated BM admittance is given as

$$\hat{Y}_{BM}(x) = \frac{iV_{BM}(x)}{2\omega\rho F_0 \left(\begin{array}{c} \int_{x_0}^{x} (x-x') \left[-\left(\frac{i}{D_0} \right) \int_{x_0}^{x} e^{\frac{-ix'}{D_0}} V_{BM}(x')dx' \right] \times e^{ix/D_0} dx' \\ -B_0 \left[-\left(\frac{i}{D_0} \right) \int_{x_0}^{x} e^{\frac{-ix'}{D_0}} V_{BM}(x')dx' \right] \times e^{ix/D_0} \end{array} \right)}, \tag{2.20}$$

where $B_0 = b_0 H^2$, $D_0 = d_0 H$, b_0 and d_0 are appropriately chosen dimensionless constants.

The spatial BM response at 1 kHz in a 3D uniform box model of cochlea for human is shown in Figure 2.3. de Boer's first inverse method is used to estimate the BM admittance using equation (2.20), and the results are shown in Figure 2.13.

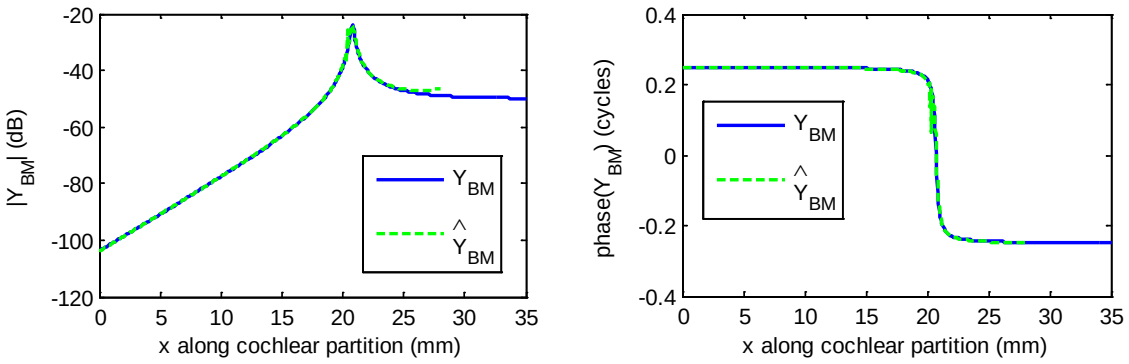

Figure 2.13 Comparison between Y_{BM} at 1 kHz as a function of position in 3D uniform box model and $\hat{Y}_{BM}$ derived from the BM response at 1 kHz as a function of position in 3D uniform box model using de Boer's first inverse method.

Figure 2.13 shows that in this case $\hat{Y}_{BM}$ is in good agreement with Y_{BM} particularly near the peak, there is missing data for $\hat{Y}_{BM}$ due to the transformation of BM velocity from the frequency domain to the spatial domain. Unfortunately the results are not so good at other excitation frequencies and, particularly when the spatial distributions are estimated from frequency response data.

2.3. de Boer's second inverse method

2.3.1. 1D uniform box model

de Boer (1999) proposed his second inverse method using a matrix formulation, details of which are described in Appendix B.

The vector of pressures along the cochlea, $\mathbf{p}$, is first calculated using the equation. $\mathbf{p} = \mathbf{Z}_{\mathbf{FC}}\mathbf{v}$, where $\mathbf{Z}_{\mathbf{FC}}$ is the 1D fluid coupling matrix. Assuming that the BM is responding only locally, the BM impedance at the nth position along the cochlea can be calculated as the ratio of the measured complex velocity, $v(n)$, and calculated complex pressure, $p(n)$, in equation (2.20).

$$\hat{Y}_{BM}(n) = \frac{v(n)}{p(n)}, \tag{2.21}$$

Initially, the BM response at 1 kHz in the spatial domain, as shown in Figure 2.3, is used to investigate de Boer's second inverse method. Through equation (2.21), $\hat{Y}_{BM}$ can be derived, as shown in Figure 2.14. Figure 2.14 shows that $\hat{Y}_{BM}$ is in so good agreement with Y_{BM} as

expected, since the assumption of de Boer's second method exactly match the way that the BM response was calculated in this case.

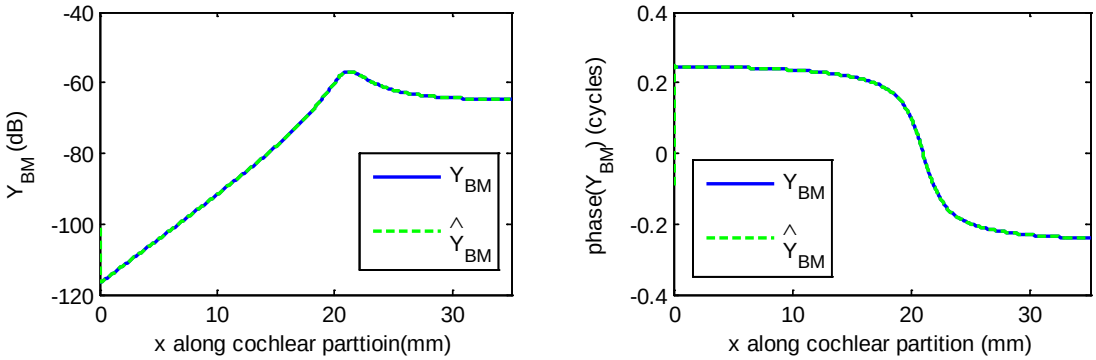

Figure 2.14 Comparison between $\hat{Y}_{BM}$ derived from the given BM velocity using inverse method and Y_{BM} using forward solution in a 1D uniform box model. The BM velocity is given at 1 kHz as a function of position.

When the BM velocity at a fixed position in the frequency domain is given as the "measured" data, a transformation needs to be made from the frequency domain to the spatial domain. If the transformation method is used, however, it is seen from Figure 2.10 that the derived BM velocity in the spatial domain does not cover the entire cochlear length. For instance, when the BM velocity at 21 mm is transformed from the frequency domain to the spatial domain, the derived distribution of the BM velocity starts from around 10 *mm* to the apex, the reason is that only a portion of the BM velocity as a function of position is duplicated by a portion of the BM velocity at a fixed position as a function of a frequency, which is shown in Figure 2.5. The difference becomes larger towards base and apex. Therefore, when the transformation is made by using the interpolation method, a portion of the BM velocity as a function of position can only be derived, however, for the de Boer's second inverse method, the "full matrix" is used, the whole BM velocity distribution needs to be derived, which means that the missing part of the transformed BM velocity needs to be estimated for deriving the BM admittance.

2.3.2. 3D uniform box model

The procedure and formulation of this inverse method is the same as the one in the 1D uniform box model, except for that Z_{FC} is the 3D fluid coupling. Initially, the BM response along the cochlea at 1 kHz, as shown in Figure 2.3, is used to investigate de Boer's second inverse method. Through equation (2.21), the BM admittance can be estimated, as shown in Figure 2.15, which shows that $\hat{Y}_{BM}$ is in good agreement with Y_{BM}, as again expected.

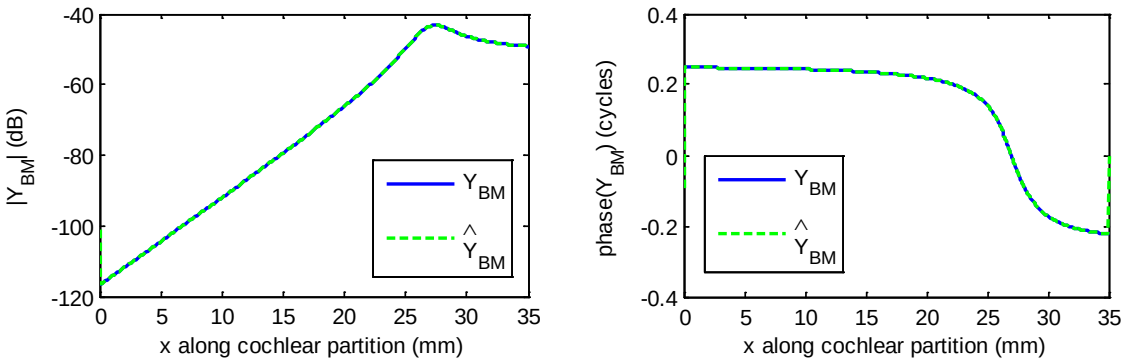

Figure 2.15 Comparison between $\hat{Y}_{BM}$ derived from the given BM velocity using inverse method and Y_{BM} using forward solution in a 3D uniform box model. The BM velocity is given at 1 kHz as a function of position.

When the BM velocity at a fixed position is given as the "measured" data, the "measured" data needs to be transformed from the frequency domain to the spatial domain. The transformation method is used, there will be the same problem as discussed above, which means that the derived BM velocity in the spatial domain does not cover correctly entirely along the cochlear length,

2.4. Shera's inverse method

2.4.1. 1D uniform box model

Shera (2007) proposed an inverse method to derive the spatial distribution of the complex wavenumber from basilar membrane (BM) responses. The real part of wavenumber determines the wavelength and the imaginary part of wavenumber characterizes the effects of energy gains or losses determining whether the wave amplitude is increased or decreased. The details of the procedure of Shera's inverse method is described in his paper (2007) and Appendix B, but in summary, the estimated wavenumber, $\hat{k}(x, f)$, is given by

$$\hat{k}^2(x, f) = -V_{BM}(x, f) \Big/ \int_x^L dx' \int_{x'}^L V_{BM}(x'', f) dx'', \tag{2.22}$$

where $V_{BM}(x, f)$ is the measured BM velocity, x' and x'' are dummy integration variables, and L is the cochlear length.

The WKB method is then used to validate the inversion procedure using the derived wavenumber to calculate the BM velocity distribution as

$$\hat{V}_{BM}(x, f) \propto \hat{k}^{3/2}(x, f) \exp[-i \int_0^x \hat{k}(x', f) dx']. \tag{2.23}$$

Initially, the BM velocity along our 1D uniform box model of passive cochlea for human at 1 kHz is given as the "measured" data, as shown in Figure 2.3.

Using 1D fluid coupling and local BM dynamics, the wavenumber can be given by

$$k = \sqrt{-2i\omega\rho / (h \times Z_{BM})}, \tag{2.24}$$

where, in this simulation, $Z_{BM} = j\omega m(x) + r(x) + s(x) / j\omega$, m is the mass per unit area of BM, r is the damping, s is the stiffness and ω is the excitation frequency.

So $\hat{k}$ calculated using the inversion formula, equation (2.22), can be directly compared with k calculated using the theoretical formula, as shown in Figure 2.16, and the two are seen to be in good agreement.

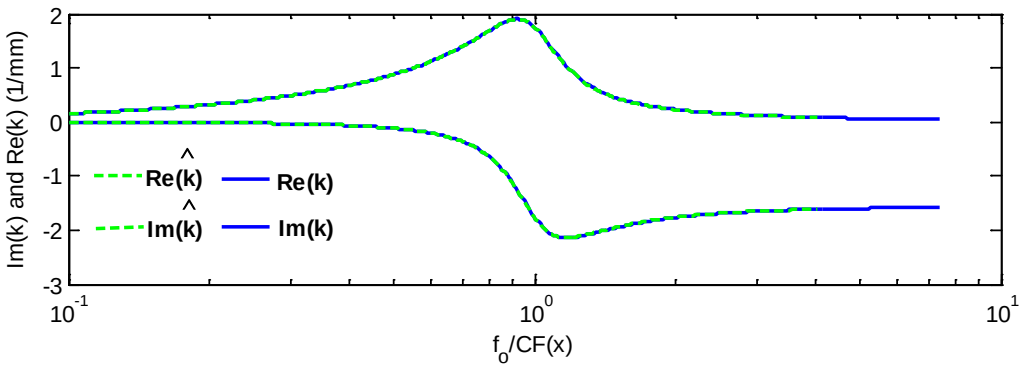

Figure 2.16 Comparison of Re($\hat{k}$) and Im($\hat{k}$) distributions between those using Shera's inverse method for the spatial BM distribution (green dash lines) and those using theoretical wavenumber formula (blue solid lines). Results were obtained at 1 kHz and plotted against logarithmic abscissa $f_0 / CF(x)$.

The WKB method is then used to estimated BM velocity, $\hat{V}_{BM}$, using $\hat{k}$ obtained from inverse method. Figure 2.17 shows that both the amplitude and phase of $\hat{V}_{BM}$ using the inverse method and these are in good agreement with V_{BM}.

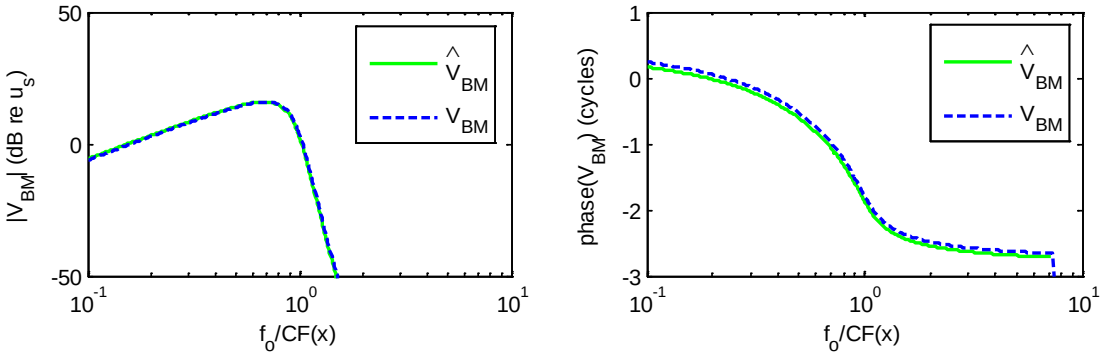

Figure 2.17 The BM velocity distributions that are either V_{BM} at a fixed frequency directly, or $\hat{V}_{BM}$ from the derived wavenumber, which is obtained from $V_{BM}(x, f_0)$ at a fixed frequency with using the WKB approximation are plotted against $f_0 / CF(x)$. The $\hat{V}_{BM}$ obtained based on $\hat{k}$ that is shown in Figure 2.23, is denoted by green solid lines. V_{BM} distribution is denoted by blue dashed lines. An overall complex scale factor is determined by matching the data at the peak.

Elliott *et al.* (2013) provided a method to derive the BM admittance from $\hat{k}$, the final form of the BM admittance is given here as

$$\hat{Y}_{BM} = \frac{\hat{k}^2(x)h}{-2i\omega\rho}, \tag{2.25}$$

$\hat{Y}_{BM}$ calculated using equation (2.25) is compared with Y_{BM} used in the simulations in Figure 2.16, and the two are seen to match very well in this idealised numerical example.

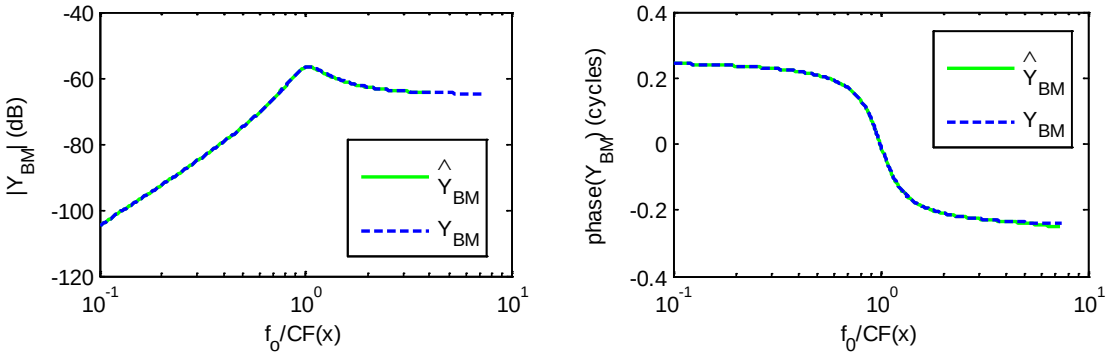

Figure 2.18 Magnitude and phase of $\hat{Y}_{BM}$ derived from $\hat{k}$ that is derived from the BM velocity at a fixed frequency (f=1 kHz) using Shera's inverse method (green solid line) and Y_{BM} at a fixed frequency (f=1 kHz) (blue solid line) in a 1D uniform box model of human cochlea are plotted against $f_0 / CF(x)$, where $f_0 = 1$ kHz.

Instead of having the BM velocity distribution at a single frequency available, in practice the frequency response at a single point is measured and scaling must be used to convert this data to that recognised. The calculated BM velocity frequency response at 21 mm, is transformed

using the transformation method and shown in Figure 2.9. Following this procedure, we can obtain $\hat{k}$ using inverse method based on the frequency response of the BM velocity obtained at a fixed position. Figure 2.26 shows a comparison of the real and imaginary parts of k, calculated at a fixed frequency in the spatial domain and $\hat{k}$ calculated based on the BM velocity obtained at a fixed position.

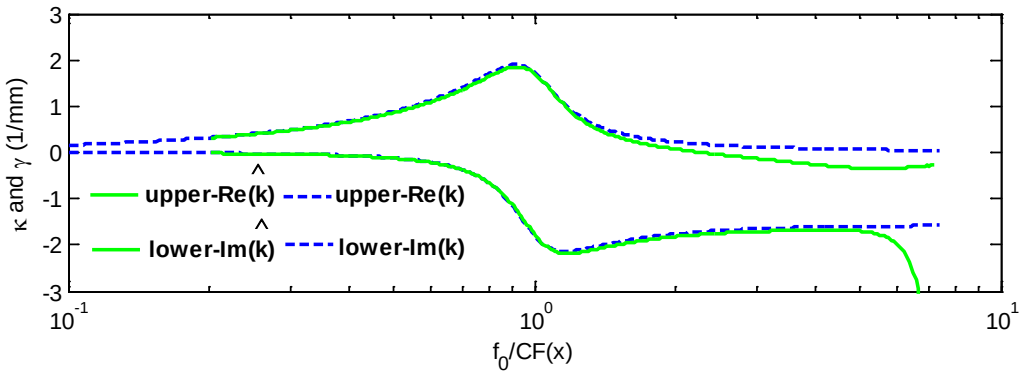

Figure 2.19 The real and imaginary part of between $\hat{k}$ (green solid line) and k (blue dashed line) calculated from the frequency response at are plotted against $f_0 / CF(x)$, where $f_0 = 1$ kHz.

It can be seen from Figure 2.19 that some parts of $\mathrm{Re}(\hat{k})$ and $\mathrm{Im}(\hat{k})$ are not entirely in good agreement with those from k. The reasons for these differences are not clear, since the theoretical model would appear to satisfy the requirements for local scaling symmetry perfectly, with the natural frequency distribution given by equation (2.2) and a BM response with a constant Q.

The WKB method can be used to estimate $\hat{V}_{BM}$ using $\hat{k}$ obtained from inverse method. Figure 2.27 shows that both the amplitude and phase of $\hat{V}_{BM}$ using the inverse method are in good agreement with those form V_{BM}, indicating that the deviations seen in the wavenumber in Figure 2.19 are perhaps not significant in determing the overall response.

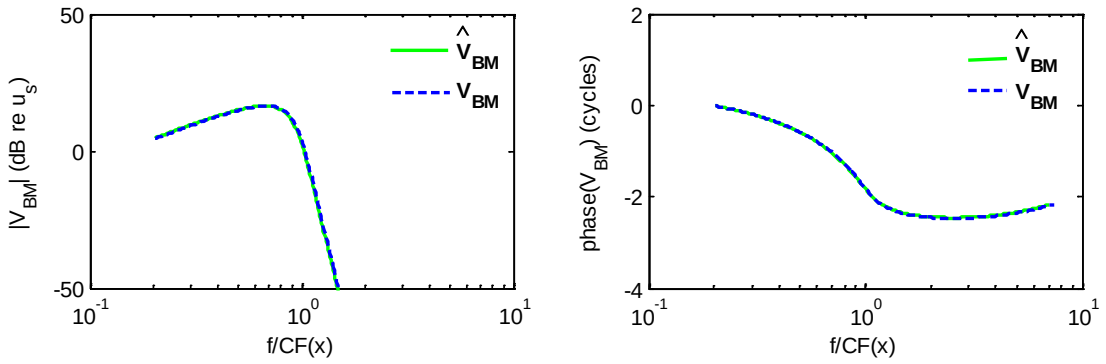

Figure 2.20 The BM velocity distributions that are either V_{BM}, or $\hat{V}_{BM}$ from the derived wavenumber, which is obtained from $V_{BM}(f_0, x)$ transformed from $V_{BM}(f, x_0)$ at a fixed position by using the WKB approximation are plotted against $f_0 / CF(x)$. $\hat{V}_{BM}$ based on $\hat{k}$ that is shown in Figure 2.19, is denoted by green solid lines. V_{BM} is denoted by blue dashed lines, as shown in Figure 2.5. An overall complex scale factor is determined by matching the data at the peak.

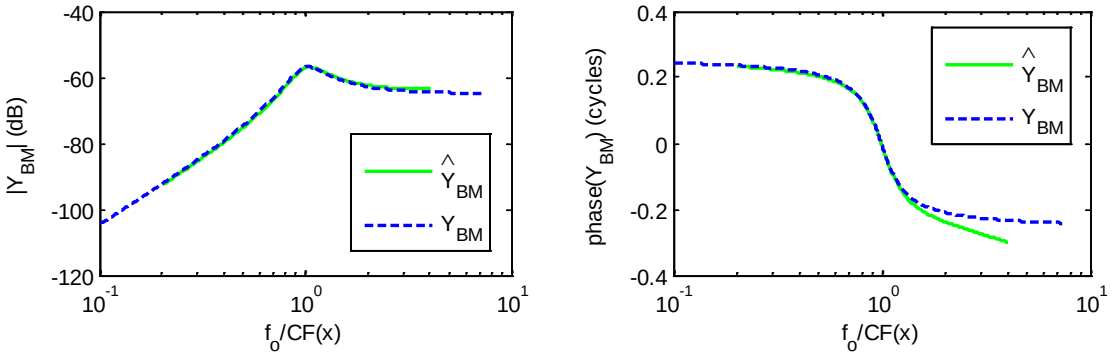

Figure 2.21 Magnitude and phase of $\hat{Y}_{BM}$ derived from $\hat{k}$ that is derived from the BM velocity at a fixed position (x=21 mm) using the inverse method that has been described before (green solid line) and Y_{BM} at a fixed position (x=21 mm) (blue solid line) in a 1D uniform box model of human cochlea are plotted against $f_0 / CF(x)$, where $f_0 = 1$ kHz.

Similarly, Figure 2.21 shows that $\hat{Y}_{BM}$ is also in reasonable agreement with Y_{BM} apart from the phase at higher frequencies.

2.4.2. 3D uniform box model

Shera's inverse method does not assume any particular form for the fluid coupling and so should also work on the data from 3D box model simulations.

Initially, the spatial distributions of BM velocity at 1 kHz in a 3D uniform box model is used, as shown in Figure 2.3, and the calculated distributions of Re($\hat{k}$) and Im($\hat{k}$) are shown in Figure 2.22, from which it can be seen that they are not in good agreement with the true

values. The reason is that there are some fluctuations of V_{BM} in the 3D uniform box model, which leads to errors of wavenumber using Shera's inverse method, which are similar to the problems encounted using de Boer's inverse method.

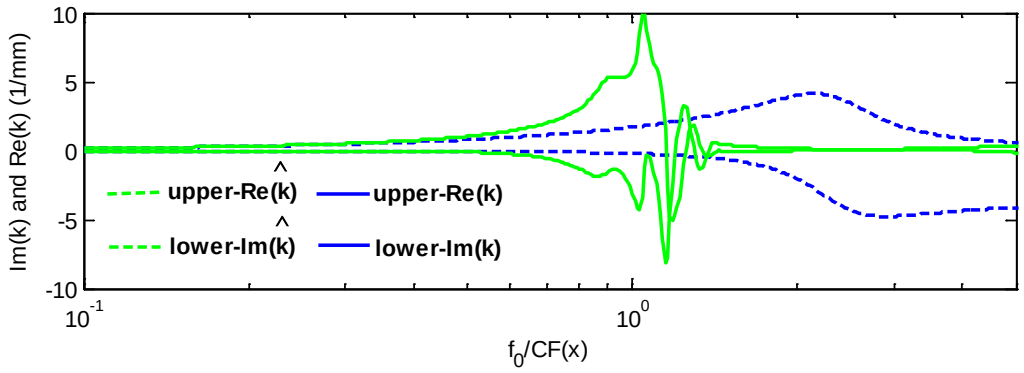

Figure 2.22 Comparison of real and imaginary part distributions between $\hat{k}$ using inverse method (green dash lines) and k using theoretical wavenumber formula (blue solid lines). Results were obtained at 1 kHz and plotted against logarithmic abscissa $f_0 / CF(x)$.

However, Figure 2.23 shows, surprisingly, that the reconstructed $\hat{V}_{BM}$, using the WKB method with these wavenumber distributions, is still in reasonable good agreement with V_{BM}.

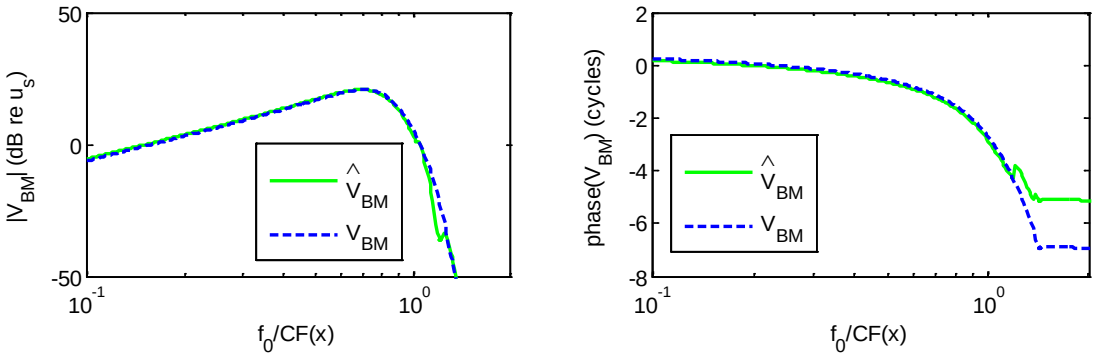

Figure 2.23 The BM velocity distributions that are either V_{BM} at a fixed frequency directly, or $\hat{V}_{BM}$ from $\hat{k}$, which is obtained from $V_{BM}(x, f_o)$ at a fixed frequency using the WKB approximation are plotted against $f_0 / CF(x)$. $\hat{V}_{BM}$ based on $\hat{k}$ that is shown in Figure 2.22, is denoted by green solid lines. V_{BM} is denoted by blue dashed lines. An overall complex scale factor is determined by matching the data at the peak.

The BM velocity at 21 mm in the 3D uniform box model, as shown in Figure 2.4, can also be used to calculate $\mathrm{Re}(\hat{k})$ and $\mathrm{Im}(\hat{k})$, and the results are shown in Figure 2.31, again indicating poor agreement, although again if these wavenumber distributions are used to reconstruct the BM velocities, as in Figure 2.6, the results are quite good. These results suggest that even

though this inverse method may appear to be working well, the wavenumber results may not be an accurate representation of the correct values.

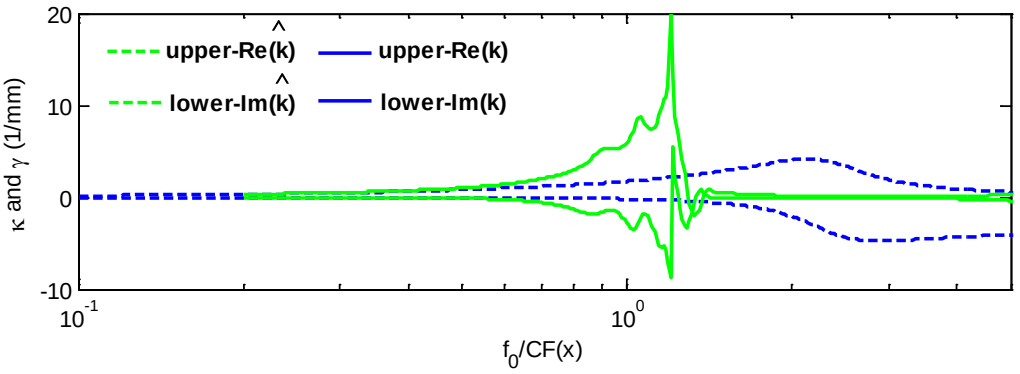

Figure 2.24 The real and imaginary part of $\hat{k}$ (green solid line) and k (blue solid line) calculated from the frequency response at 21 mm, but are plotted against $f_0 / CF(x)$, where $f_0 = 1$ kHz.

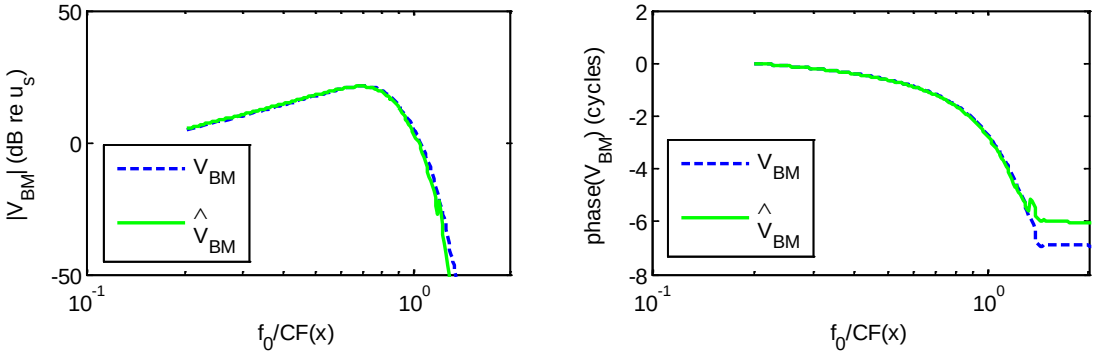

Figure 2.25 The BM velocity distributions that are either V_{BM}, or $\hat{V}_{BM}$ from the derived wavenumber, which is obtained from $V_{BM}(f_0, x)$ transformed from $V_{BM}(f, x_0)$ at a fixed position by using the WKB approximation are plotted against $f_0 / CF(x)$. $\hat{V}_{BM}$ obtained based on $\hat{k}$ that is shown in Figure 2.24, is denoted by green solid lines. V_{BM} is denoted by blue dashed lines. An overall complex scale factor is determined by matching the data at the peak.

2.5. The "Direct" inverse method

A new formulation of the inverse method is proposed here, using direct optimization methods and a description of the micromechanical model using poles and zeros.

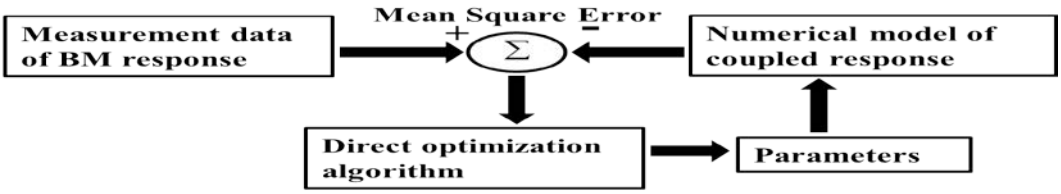

Figure 2.26 The procedure of the direct inverse method.

Figure 2.33 shows the procedure for the direct inverse method for finding the unknown parameters in the BM admittance. In order to test the procedure, the uniform box model of the cochlea is initially used.

The normalized mean square error is used to compare the estimated BM velocity with the "measured" BM velocity, as given by

$$NMSE = \frac{\sum_{n=1}^{N} \left| \hat{V}_{BM}(n) - V_{BM}(n) \right|^2}{\sum_{n=1}^{N} \left| V_{BM}(n) \right|^2}, \tag{2.26}$$

where n is the index of the elements along the length of the cochlea, N is the number of elements, $\hat{V}_{BM}(n)$ is the estimated complex BM velocity and $V_{BM}(n)$ is the "measured" complex BM velocity at the n-th element.

The constrained nonlinear minimization method (Marquardt, 1963) in the MATLAB 2012 Toolbox is used to adapt the parameters of the passive box model of cochlea, since separate simulations I made have shown that the NMSE in the passive model is a convex function of the parameters being optimized here.

The passive BM admittance at position x along the cochlea can be modelled, assuming local scaling symmetry, as a single degree of freedom system, and can be expressed in the Laplace domain as

$$Y_{BM}^{p}(x,s) = \frac{s}{m_0(s^2 + \Omega\omega_n(x)s/Q + (\Omega\omega_n(x))^2)}, \tag{2.27}$$

where $s = i\omega$, is the Laplace variable, m_0 is the BM mass, $\omega_n(x)$ is the natural BM frequency at position x, Ω is the normalised natural frequency and Q is the related Q factor. The three unknown parameters, which need to be optimized, are thus m_0, Ω and Q, which are assumed to be constant along the cochlea. In a 1D uniform box model of cochlea, assuming that the BM velocity is given, the BM admittance can be fitted directly by optimising the pole and zero positions and m_0 to ensure it is close to the given BM velocity.

2.5.1. 1D uniform box model

As an initial test of the direct inverse method, the distribution of BM velocity along the cochlea at a number of given frequencies is calculated using the 1D uniform box model of passive cochlea and then used as the "measured" BM response, V_{BM} . The underlying parameters of the micromechanical model are known, since they have been used to generate the "measured" data, and can be compared directly with the results from the "direct" inverse method.

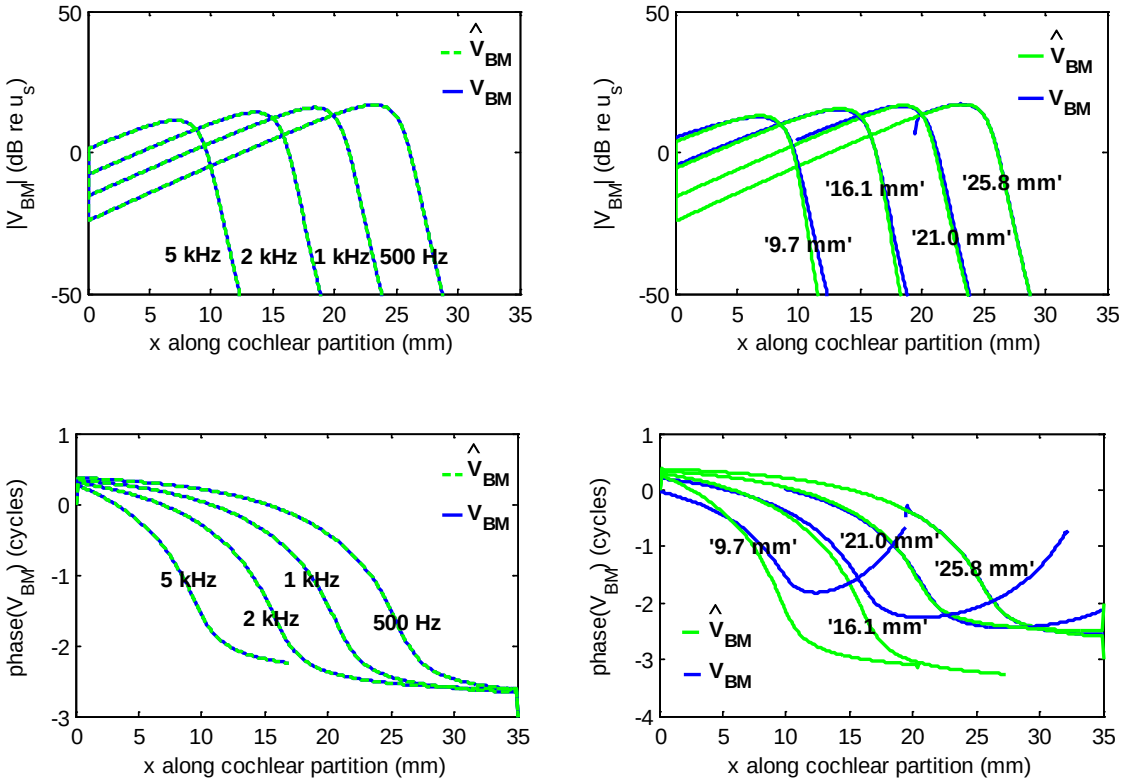

Figure 2.27 Left two panels: Amplitude and phase of V_{BM} and $\hat{V}_{BM}$ as a function of position in a 1D uniform box model of passive cochlea for human at 0.5, 1, 2, and 5 kHz. Right two panels: Amplitude and phase of V_{BM} derived from the BM velocity frequency responses at 9.7, 16.1, 21.0, and 25.8 mm and $\hat{V}_{BM}$ as a function of position at 0.5, 1, 2, and 5 kHz in a 1D uniform box model of passive cochlea for human. According to the position-frequency map for human, the position 9.7, 15.8, 21.0, and 25.8 mm are related to 5, ,2,1, and 0.5 kHz, respectively.

Figure 2.27 shows the true BM velocity distributions and those reconstructed using the parameters from the "direct" inverse method when the data used in the method was either calculated distributions of V_{BM} along the cochlea at given frequencies, or reconstructions of these from the frequency response of fixed positions, using Shera's method. It shows a so good estimation when using the spatial distribution data as expected. In the case of data reconstructed from the frequency responses, the agreement is a bit of worse than using the spatial distribution data, particularly the phase. The normalised mean square error is very

small in the two cases, as listed in Table 2.2, together with the values of Ω, Q, m_0 derived from the "direct" inverse procedure. The derived parameters are in good agreement with those used in the simulations when the spatial V_{BM} distributions are calculated directly, and are mostly in reasonable agreement when the frequency responses are used. In principle the frequency domain data does not need to be transformed into spatial distributions using the direct method, since the numerical model could be re-run at each frequency to directly predict the frequency response at a fixed position. This was found to involve a huge computational burden, however, since this whole set of response at each frequency needs to be calculated many times as the optimization algorithm adapts the parameters of the micromechanical model. the previous method of transforming frequency domain data into spatial distributions was thus employed, with the advantage that the results are consistent with the other inverse methods considered above.

Table 2.2 The optimized parameters for poles, Ω, Q, and m_0 of the micromechanical model obtained for a number of different conditions, together with the normalized mean square error, NMSE. The BM velocity is given at fixed frequencies and at fixed positions in a 1D uniform box model of the cochlea.

Direct inverse method: 1D uniform				
"measured data": 1D uniform (fixed frequencies)				
	Ω	Q	m_0	NMSE
500 Hz	1	2.5	0.28	3.72×10^{-29}
1 kHz	1	2.5	0.28	3.72×10^{-29}
2 kHz	1	2.5	0.28	3.72×10^{-29}
5 kHz	1	2.5	0.28	3.72×10^{-29}
"measured data": 1D uniform (fixed positions)				
	Ω	Q	m_0	NMSE
25.8 mm	1.13	2.59	0.11	0.032
21.0 mm	0.95	4.36	0.20	0.0067
16.1 mm	0.96	4.51	0.13	0.0058
9.7 mm	1.02	3.79	0.11	0.0184

2.5.2. 3D uniform box model

The direct inverse method is also tested using the 3D uniform box model of the passive human cochlea, using V_{BM} spatial distribution at four different frequencies and those inferred from the frequency response at four different positions transformed to the spatial domain using the transformation method. The constrained nonlinear minimization method is used to estimate the parameters of Y_{BM} and the results are plotted in Figure 2.35, estimated parameters are listed in Table 2.3.

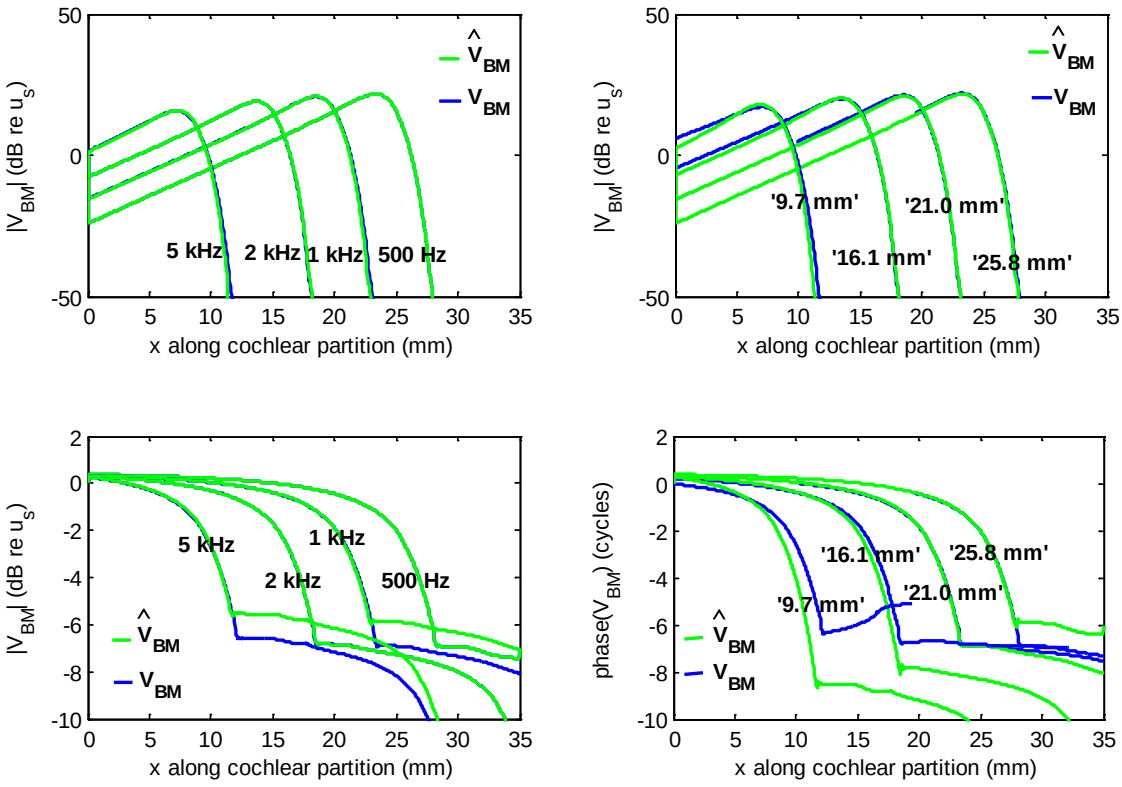

Figure 2.28 Left two panels: Amplitude and phase of V_{BM} and $\hat{V}_{BM}$ distribution as a function of position at 0.5, 1, 2, and 5 *kHz* in a 3D uniform box model of passive cochlea for human. Right two panels: Amplitude and phase of V_{BM} derived from the BM velocity frequency response at 9.7, 16.1, 21.0, and 25.8 mm and $\hat{V}_{BM}$ as a function of position at 0.5, 1, 2, and 5 kHz in a 3D uniform box model of passive cochlea for human. According to the position-frequency map for human, the position 9.7, 15.8, 21.0, and 25.8 mm are related to 5, 2, 1, and 0.5 kHz, respectively.

Figure 2.35 again shows an almost perfect estimation from the spatial distributions as expected, and those calculated from the frequency responses are also good. Table 2.3 shows the small values of NMSE derived by the optimization and the fitted values of Ω, Q, and m_0, which again are in reasonable agreement with the true values, of 2.1, 2.4, 0.05, in the model used to generate the data.

Table 2.3 The optimized parameters for poles, Ω, Q, and m_0 of the micromechanical model obtained for a number of different conditions. Together with the normalized mean square error, NMSE. The BM velocity is given at fixed frequencies and at fixed positions in a 3D uniform box model of the cochlea.

Direct inverse method: 3D uniform				
"measured data": 3D uniform (fixed frequencies)				
	Ω	Q	m_0	NMSE
500 Hz	2.37	2.11	0.05	2.50×10^{-7}
1 kHz	2.11	2.41	0.06	1.54×10^{-4}
2 kHz	2.42	2.06	0.05	1.79×10^{-5}
5 kHz	1.98	2.56	0.08	4.99×10^{-4}
"measured data": 3D uniform (fixed positions)				
	Ω	Q	m_0	NMSE
25.8 mm	2.21	2.25	0.06	0.0013
21.0 mm	2.29	2.27	0.06	0.0058
16.1 mm	2.29	2.57	0.05	0.0047
9.7 mm	1.76	4.05	0.07	0.0137

2.6. Discussion

The 1D and 3D uniform box models have been described, and then the results from those models used to test several inverse methods. de Boer's first inverse method is successful in the 1D uniform box model, but failed in the 3D uniform box model due to small errors of V_{BM}.

For de Boer's second inverse method, when the "measured" data is calculated in the spatial domain, it works well, but it does not work, if the "measured" spatial distributions are calculated from the frequency responses using scaling.

In Shera's inverse method, it works well in the 1D uniform box model, but again fails to give accurate values of wavenumber in the 3D uniform box model.

The "direct" inverse method gives good results for both 1D and 3D uniform box models, and the estimated results are in good agreement with the "measured" data, when the spatial distributions are calculated from the measured frequency responses using scaling.

These simulations demonstrate the sensitivity of most inverse methods to small errors in the "measured" data, but appear encouraging for the new direct methods.

Chapter 3

The passive tapered box model

Even in models in which that properties of the organ of Corti vary in the longitudinal direction (Ramamoorthy *et al.*, 2007), the cross-sectional area of the fluid chambers is often assumed to be uniform along the length of the cochlea. If the uniform box model represents a first approximation to the cochlea geometry, for the calculation of the fluid coupling, a sensible second approximation would thus appear to be one, in which the width and height of the fluid chambers are equal but linearly varying along the cochlear length, together with the width of the BM, as shown in the right part of Figure 3.1. Steele and Taber, (1979) noted that a physical model of the cochlea due to Cannell (1969) had a linearly varying height but constant width, although these authors only analysed another model with a constant height. More recently, Kim *et al*. (2011) analysed a finite element model of the cochlea in which the BM and cochlear partition width, together with the height of the fluid chambers appears to vary approximately linearly along the straight box model (Yoon *et al*., 2011).

There are several sources of information about the variation in the physical dimensions of the fluid chambers, along the length of the cochlea in different species, among many of which the database of Salt (2010) is perhaps the most comprehensive. Salt (2010) obtained these measurements from reconstructions of three-dimensional magnetic resonance images. The measured variations in chamber area and cochlear partition geometries in a number of species are used here to calculate variations in the effective area, the BM and cochlear partition width. It has previously been observed that the variation of the BM and cochlea partition width is approximately linear along the length of the cochlea. It is found that even though the variation of the areas of the individual fluid chambers along the cochlea can be rather complicated, the square root of the effective area, varies in a surprisingly linear way along the length of the cochlea. It is assumed that the cross-sectional shape of each fluid chamber is not crucially important for the 1D and 3D fluid coupling, and so it is convenient to assume that the cross section is square. Although the results demonstrated in this chapter are mostly for the human cochlea, details of other species can be found in Appendix C.

The analytic form for the 1D and the 3D fluid coupling, and the added mass on the BM due to the near-field pressure, are calculated here using a linearly varying tapered model. It is shown that the 1D pressure distribution and the 3D pressure distribution are significantly different

from that obtained with the uniform box model, which gives rise to different BM velocity distributions when the coupled response of the passive cochlea is calculated.

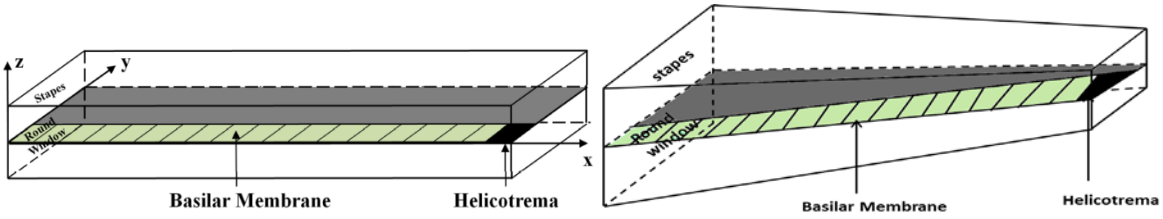

Figure 3.1 The uniform box model of the cochlea (left), in which the height of the fluid cochlear and the width of the cochlear partition and basilar membrane are constant along the length, and the tapered box model (right), in which the chamber height and width are equal, but decrease along the length, the width of basilar membrane increases along the length.

The "direct" inverse method will be applied in the tapered box model, results show that the geometry of the fluid chamber of cochlea has a minor influence on the estimated response.

3.1. Cochlear fluid chamber cross-sectional area

The geometrical feature that is important for the 1D fluid coupling is the effective area of each chamber, defined (Peterson and Bogert, 1950; Elliott *et al.*, 2011b) as

$$A_e(x) = \frac{2A_1(x)A_2(x)}{A_1(x)+A_2(x)}, \tag{3.1}$$

where x is the longitudinal position and $A_1(x)$ and $A_2(x)$ are the areas of the upper and lower fluid chambers. Although $A_1(x)$ and $A_2(x)$ vary in a complicated way with position, as shown in Figure 3.2 for the human (Salt, 2010), the variation of A_e, and particularly, the square root of this effective area is much smoother. The latter can be reasonably well approximated by a linear line in this case, as shown in Figure 3.3.

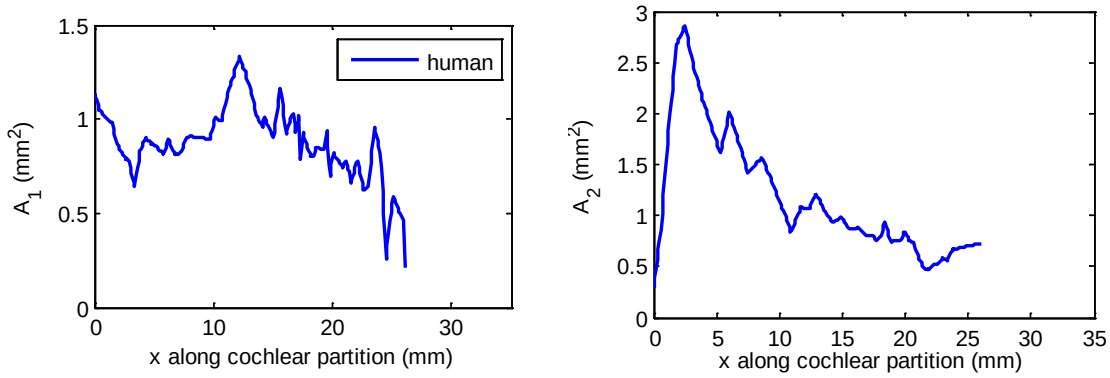

Figure 3.2 $A_1(x)$ (upper chamber) and $A_2(x)$ (lower chamber) for the human cochlea, (Thorne et al, 1999; Salt, 2010).

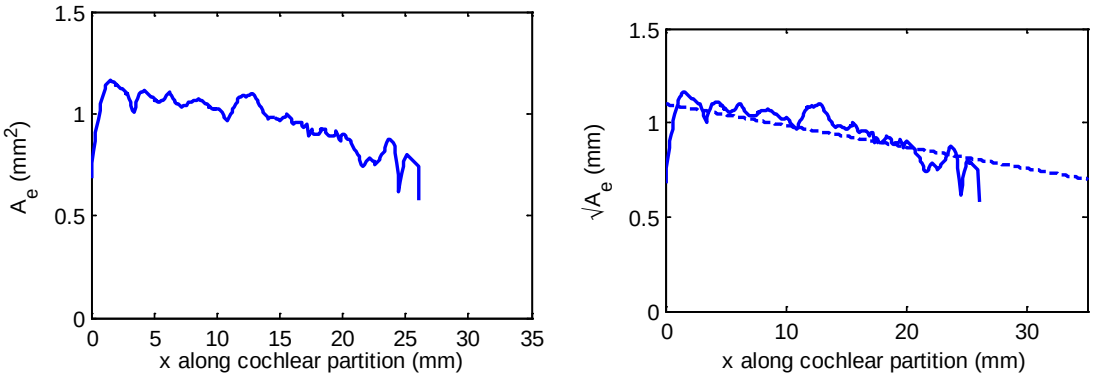

Figure 3.3 Effective area of the fluid chambers (Left panel) for the human cochlea and its square root (right pael).

The equivalent width and height of each fluid chamber, W_{eq} and H_{eq}, are thus assumed to be equal and can be given by

$$H_{eq}(x) = W_{eq}(x) = \sqrt{A_e(x)}. \tag{3.2}$$

The least squares method is used here to fit a linear variation for the square root of the effective area, as also shown in Figure 3.3. The linear variation is a reasonable fit to the square root of the effective area, although it overestimates the true value by about 14% near the apex where the 3D geometry is known to be complicated. The linear curve is assumed to extend over the entire length of the cochlea, 35 mm in this case, even though the experimental measurements of Salt (2010) only extended to about 30 mm.

The linearized variations of W_{eq} and H_{eq} with position along the cochlea, W_l and H_l, can be defined as

$$H_l(x) = H_B - \frac{H_B - H_A}{L} x, \tag{3.3}$$

$$W_l(x) = W_B - \frac{W_B - W_A}{L} x, \tag{3.4}$$

where L is the length of the cochlea, H_B and H_A are the equivalent height at the base and apex, W_B and W_A are the equivalent width at the base and apex, respectively.

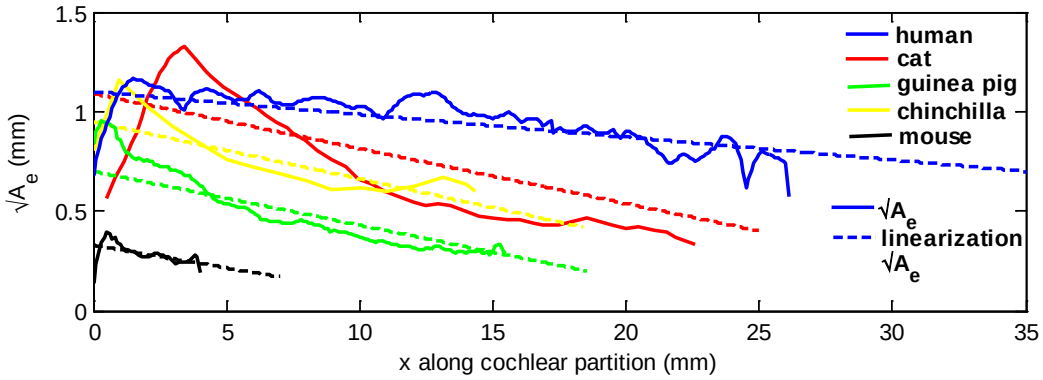

Figure 3.4 Variation of square root and corresponding fit of the cochlear effective area along cochlear length for five species.

Figure 3.4 shows the variation of the square root of the equivalent cochlear chamber area and its linear approximation for five species, calculated from the measured areas (Salt, 2010), as described in the appendix C. The values of H_B and H_A for these linear approximation are given in Table 3.2.

The correlation coefficient for the least squares form is given by

$$r = \left| \frac{\sum_{i=1}^{n} (X_i - \bar{X})(Y_i - \bar{Y})}{\sqrt{\sum_{i=1}^{n} (X_i - \bar{X})^2} \sqrt{\sum_{i=1}^{n} (Y_i - \bar{Y})^2}} \right|, \tag{3.5}$$

where X_i are the sampled points along the cochlea and Y_i are the sample points of H_e and W_e, $\bar{X}$ and $\bar{Y}$ are their average value, as illustrated in Figure 3.5.

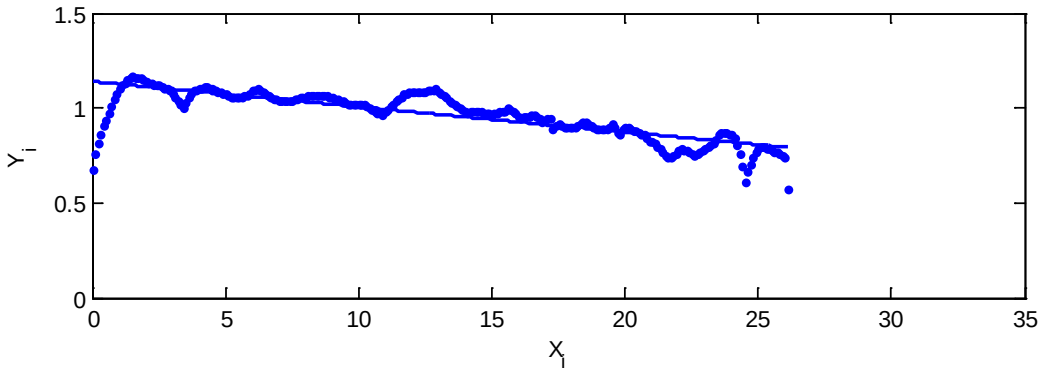

Figure 3.5 An example of the method of calculating the correlation coefficient for linear fits. x_i corresponds to the x along the cochlear partition, the y_i corresponds to the square root of effective cochlear cross-sectional area. Solid line stands for the curve fitting for the square root of effective cochlear cross-sectional area with least square method.

The calculated correlation coefficients for five species are also listed in Table 3.2. It can be seen from the correlation coefficients for the linear fit that the linear variation works better approximation in some cases, e.g. the human, guinea pig, chinchilla, mouse, than others, e.g. cat, which means that the variation of measured data for cat can not be fitted well using linear approximation, other approximations should be investigated, e.g. polynomial approximation.

3.2. Variation of BM width and characteristic frequency

3.2.1. Variation of BM width

Figure 3.6 shows the variation of the BM width measured along the length of the cochlea (from the base to the apex), $B(x)$, for human (Femandes, 1952). The results for other species are taken from references listed in the Figure 3.7 caption. A linear approximation to $B(x)$, based on values at the base and apex, is given by

$$B_l(x) = B_B + \frac{(B_A - B_B)}{L} x. \tag{3.6}$$

The effective width of the tapered fluid chamber in the guinea pig and cat cochlea has been constrained to be no less than the BM width at the apex.

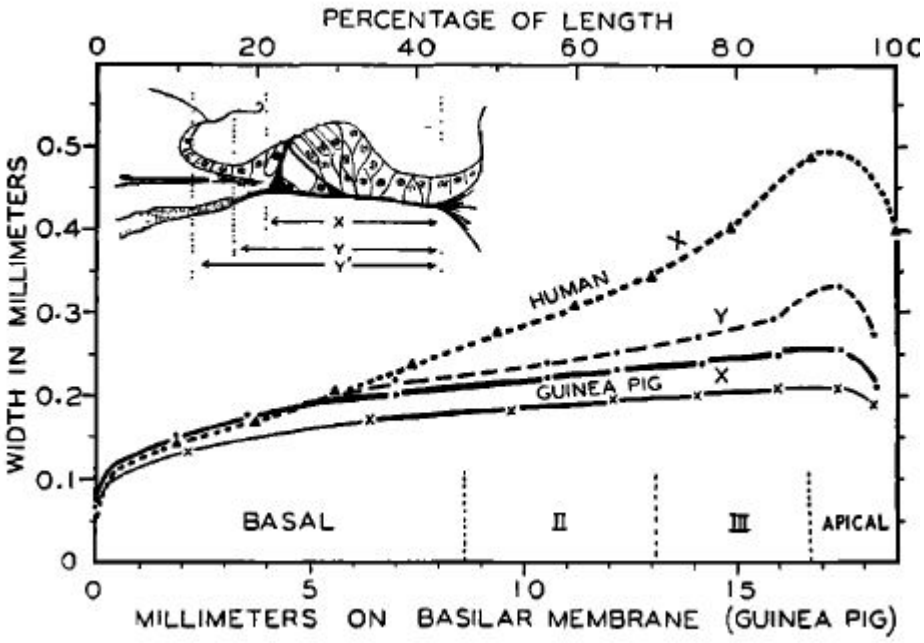

Figure 3.6 The basilar membrane width in the human and guinea pig cochlea. X and Y represent measurements made according to the criteria shown in the sketch. Y is used in the upper turns where the bony spiral lamina does not extend beyond the limbus. The lowest curve, x–x, represents Guild's data (Guild, 1927) for the guinea pig measured from spiral ligament to the spiral lamina. The upper curve (human) shows Wever's measurements. For these data use the scale for percentage of length (at the top). To convert these percentages into millimetres multiply by the factor 0.315. (Fernandez, 1952) "Dimensions of the cochlea (guinea pig)", with permission of The Journal of the Acoustical Society of America.

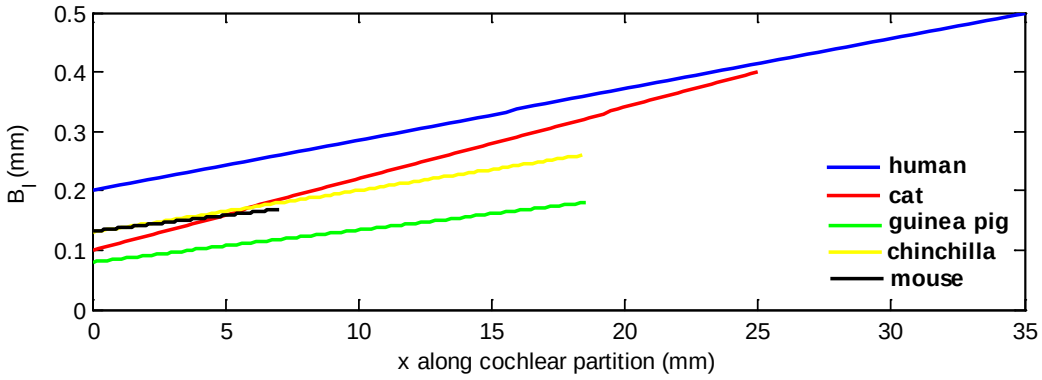

Figure 3.7 Linear approximations of the BM width variation along the cochlear partition in different species. The BM width for human is derived from Elliott *et al.*, 2011b, for cat: Cabezudo, 1977, for guinea pig: Fernandez, 1952, for chinchilla: Dallos, 1970, for mouse: Keiler *et al.*, 2001.

The near-field fluid loading depends on the ratio $B(x)/W(x)$ (Ni, 2012), which is plotted for various species in Figure 3.8, assuming that both $B(x)$ and $W(x)$ vary linearly along the cochlea, which will be used below.

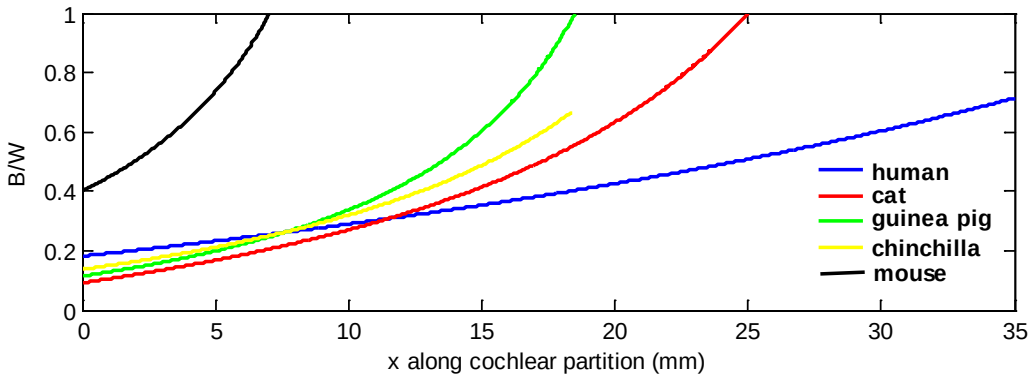

Figure 3.8 The ratio of the BM width to the width of fluid chamber area along cochlear partition for five species, where both widths are assumed to vary linearly along the cochea.

3.2.2. Variation of characteristic frequency

The mechanism underlying the function of the inner ear is believed to be similar in most mammals. There is, however, a wide range of physical sizes of the cochlea in different species, resulting in differences in the frequency range over which mammals can hear.

Greenwood (1990) developed a function that relates the characteristic frequency, CF, to distance away from the cochlea base, x, as

$$\mathrm{CF} = A(10^{\frac{\alpha(L-x)}{L}} - k), \tag{3.7}$$

where A is a constant that controls low frequency limit, equal to the CF at the apex, α is the constant that controls the slope of the map, L is the length of the cochlea, and k is a constant that controls low frequency behaviour.

Greenwood (1990) derived the coefficients for the cochlear frequency–position function for several species. For example, Figure 3.9 describes the frequency versus cochlear position in human cochlea.

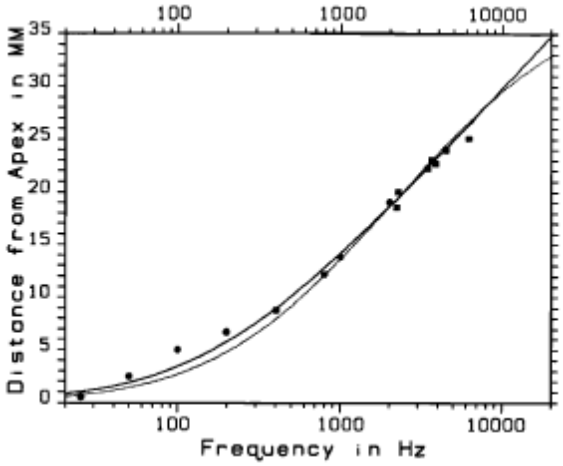

Figure 3.9 Characteristic frequency versus cochlear position in the human cochlea. Békésy's human curve is nearly parallel to the line from about 5 to 12 mm from apex and displaced about 1.9 mm basally on the ordinate. The curve is given by equation (3.7) $\mathrm{CF} = A(10^{\frac{\alpha(L-x)}{L}} - k)$, in which A=0.165(kHz), α=2.1 and k=0.85 (Greenwood, 1990). "A cochlear frequency position function for several species-29 years later.", with permission of The Journal of the Acoustical Society of America.

The relevant parameters for different species, taken from Greenwood (1990), are listed in Table 3.1.

Table 3.1.Parameters for calculating the CF of different species (Greenwood, 1990).

Species	$A \approx f_{apex}$ [Hz]	α	L [mm]
Human	165	2.1	35
Cat	456	2.1	25
Guinea pig	350	2.1	18.5
Chinchilla	163.5	2.1	18.4
Mouse	960	2.04	7 (6.8)

In this study, the focus is the variation at the base of the cochlea, and so the factor k above is ignored, in which case the characteristic frequency can be taken as

$$CF = f_o e^{-x/\ell}, \tag{3.8}$$

where f_o is the characteristic frequency at the base, which equals to $A10^{\alpha}$, and ℓ is the characteristic length, which equals to $x/\log 10(\alpha x/L)$, $0 < x \le L$.

Using equation (3.8) and the parameters in Table 3.2, the upper and lower frequency limit along the basilar membrane can be calculated, as also shown in Table 3.2.

Table 3.2 The parameters of the tapered box model of the passive cochlea in 5 different species, together with the references from which they are chosen (a) Cabezudo, 1977, (b) Dollos, 1970, (c) Elliott *et al.*, 2011b, (d) Fernandez, 1952, (e) Greenwood, 1990, (f) Keiler *et al.*, 2001, (g) Liberman, 1982, (h) Salt, (1995–2010), (i) Stefan *et al.*, 2002, (j) Wysocki, 2001.

Species / Parameters	Human	Cat	Guinea Pig	Chinchilla	Mouse
L (mm)	35(e)	25(g)	18.5(e)	18.4(e)	7(e)
f_B (kHz)	20(e)	60(g)	44(e)	20(e)	105(e)
f_A (kHz)	0.14(e)	0.45(g)	0.34(e)	0.16(e)	0.99(e)
$H_B = W_B$ (mm)	1.1(h)	1.1(j)	0.8(h)	0.95(i)	0.33(h)
$H_A = W_A$ (mm)	0.7(h)	0.4(j)	0.20(h)	0.42(i)	0.17(h)
Correlation coefficient	0.90	0.60	0.90	0.80	0.80
B_B (mm)	0.2(c)	0.1(a)	0.08(d)	0.13(b)	0.132 (f)
B_A (mm)	0.5(c)	0.4(a)	0.2(d)	0.28(b)	0.169(f)
ℓ (mm)	7	5.1	3.8	3.8	1.5
Q	2.5	2.5	2.5	2.5	2.5
L / ℓ	5	5	4.7	4.8	4.6

A uniform box model has also been used below, to calculate results for comparison with the tapered box model. The parameters of the uniform box model, H_{av}, H_{av} and B_{av} are taken to be the average of values listed in Table 3.3, together with the effective thickness of the organ of Corti and the BM, T_t, and the added thickness due to the fluid in this case, T_f, as discussed in Section 3.3.

Table 3.3 Parameters of the uniform box model of the passive cochlea in 5 different species, together with the references from which they are chosen (a) Bohne *et al.*, 1979, (b) Elliott *et al.*, 2011b, (c) Fernandez, 1952, (d) Greenwood, 1990, (e) Keiler *et al.*, 2001, (f) Liberman, 1982, (g) Neely, 1986.

Species / Parameters	Human	Cat	Guinea Pig	Chinchilla	Mouse
L (mm)	35(d)	25(f)	18.5(d)	18.4(d)	7(d)
f_B (kHz)	20(d)	60(f)	44(d)	20(d)	105(d
f_A (kHz)	0.14(d)	0.45(f)	0.34(d)	0.16(d)	0.99(d)
$H_{av}=W_{av}$ (mm)	0.9	0.75	0.45	0.7	0.25
B_{av} (mm)	0.35	0.25	0.14	0.2	0.15
h (mm)	2.86	2.8	1.8	2.93	0.51
T_t (μm)	50(b)	30(g)	85(c)	62(a)	30(e)
T_f (μm)	230	180	115	160	70
m_{3D} ($\mathrm{kg\times m^{-2}}$)	0.05	0.03	0.085	0.062	0.03
m_{1D} ($\mathrm{kg\times m^{-2}}$)	0.28	0.21	0.2	0.22	0.1
ℓ (mm)	7	5.1	3.8	3.8	1.5
Q	2.5	2.5	2.5	2.5	2.5
L/ℓ	5	5	4.7	4.8	4.6

In addition to parameters for the uniform box model, Table 3.3 also lists the BM mass and Q value. It is striking that the ratio of the cochlea length, L, to the CF decay length, ℓ, is always about 5, implying, from equation (3.7), that the frequency range of the cochlea in each species is always about 7 octaves.

3.3. Fluid Coupling

The linear behaviour of the cochlear dynamics can be represented by matrix representations of two separate phenomena (Elliott *et al.*, 2011b). First, the way that the pressure distribution is determined by the fluid coupling within the cochlear chambers when driven by the BM velocity, and second, the way in which the BM dynamics responds to the imposed pressure distribution. This kind of representation was used, for example, by Neely and Kim (1986), to simulate an early model of the active cochlea, and has been used by many authors since then. Elliott *et al.* (2011b) further developed this method to study the fluid coupling and the coupled response in the cochlear box model, in which the modal pressure difference and the modal BM velocity are a function of a single longitudinal variable. Ni (2012) analysed the effects of the tapered in the fluid chambers and proposed expressions which take all these variations into account. In this chapter, the elemental method described by Elliot *et al.* (2011b)

and the fluid coupling expressions, described by Ni (2012), are used to analyse the fluid coupling in a box model of the cochlea with linearly-varying geometric parameters.

A one-dimensional analysis can be used to derive the far-field component of the pressure in each of the fluid chambers for a box model of the cochlea with uniform and tapered fluid chambers and hence the far-field contributs to the pressure difference. The near-field components of the pressure are not very sensitive to the shape of the cochlear chambers (Elliott *et al.*, 2011b), so they will continue to be approximately equal and opposite in the two chambers and can be calculated using the wavenumber approach for a uniform cochlea, as described by Elliott *et al*. (2011b). An example is given of the calculated pressure difference for assumed variations of the chamber volumes in different species. The effect of this modified fluid coupling on the coupled response of the passive cochlear model is calculated in the following section.

3.3.1. Far-field pressure

Ni (2012) described the procedure for deriving the fluid coupling expressions in a tapered box model of cochlea. Details of this procedure can be found in Appendix B, but the final form of the far-field pressure is given by

$$\begin{aligned} p_{\mathrm{F}}(n)\big|_{0<n<n_0-1} &= -16i\omega\rho\Delta^2 v_0 \sqrt{\frac{B_l(n_0)W_l(n_0)B_l(n)}{W_l(n)}} \sum_{n'=n_0}^{N} \frac{1}{H_l^2(n')}, \\ p_{\mathrm{F}}(n)\big|_{n_0<n<N} &= -16i\omega\rho\Delta^2 v_0 \sqrt{\frac{B_l(n_0)W_l(n_0)B_l(n)}{W_l(n)}} \sum_{n'=n}^{N} \frac{1}{H_l^2(n')}, \end{aligned} \tag{3.9}$$

where $n_0 = x_0/\Delta$, B_l, W_l, and H_l are the linear approximations of varying BM width, fluid chamber width, and fluid chamber height, as listed Table 3.2. Equation (3.9) can be used to calculate the far-field pressure component in the tapered cochlea due to varying fluid chambers. These results are also compared with the results for the uniform box model, in which all the geometric parameters are constant, which are the averages of those listed in Table 3.3. Figure 3.10 shows the far-field pressure distributions along the cochlea in several species when excited by the BM vibration at a single point, x=5 mm, calculated using either the uniform or tapered box model. The curvature in the pressure difference distribution for x greater than x_0 is due to the reduction of the effective area with distance, as shown in Figure 3.4, and is also seen in Fig. A1 of Shera *et al.* (2004), for example, which was calculated for a tapered cochlea using a Green's function approach.

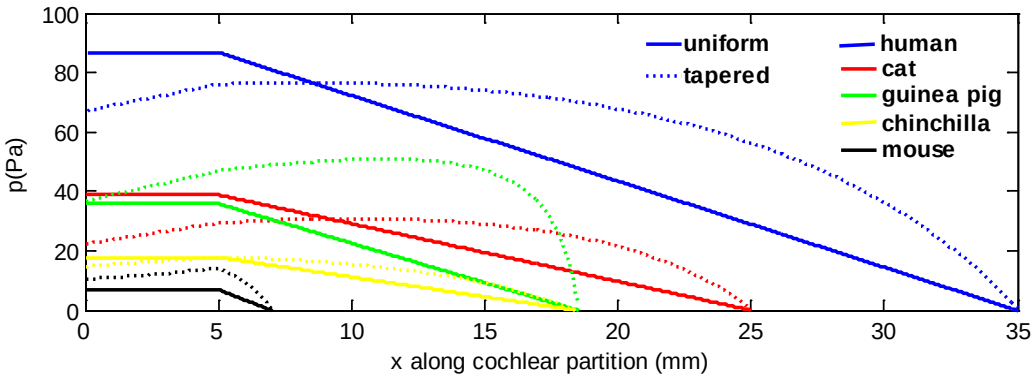

Figure 3.10. The calculated variation of the modal pressure difference due far-field component for the model of a tapered cochlea, due to the difference in chamber areas, CP width, *W*, and BM width, *B*, when only a single element of the discrete BM at x = 5 mm is driven sinusoidally with a velocity of 10 mm·s^{-1} at a frequency of 1 kHz, together with results for the uniform cases in dashed lines

3.3.2. Near-field pressure

Although the near-field component is assumed to be unaffected by the size of the fluid chambers (Elliott *et al.*, 2011a), the magnitude of the pressure does depend on the ratio, B/W, as described by Elliott *et al.* (2011b),

The distribution of the modal pressure difference with both far and near-field components, due to BM excitation by a single element of the BM at 5 mm is shown in Figure 3.11

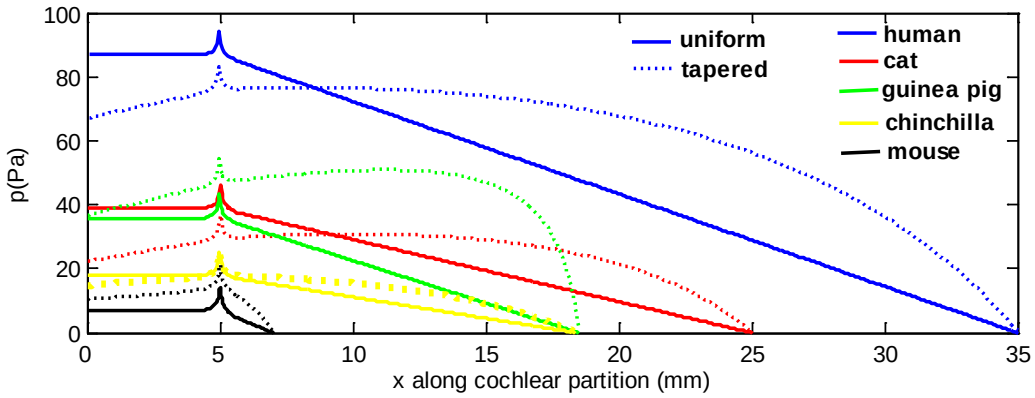

Figure 3.11 The calculated total variation in the modal pressure difference due to both far and near-field components for the tapered cochlear model, when only a single element of the discrete BM at x = 5 mm is driven sinusoidally with a velocity of 10 mm·s^{-1} at a frequency of 1 kHz, together with results for the uniform cases in dashed line.

3.3.3. Near-field fluid loading

Apart from the physical mass per unit area of the BM, fluid loading will also provide some additional mass. In the 1D model of the cochlea, there is an effective additional thickness of the BM due to the fluid coupling, given by equation (2.12). If $W(x) = H(x)$, as assumed here,

and the width of BM is normalised by the cochlear partition, so that $\beta(x)$ is to $B(x)/W(x)$, equation (2.12) can be written as

$$T_f(x) = H(x)\left(\frac{8}{3\pi^2}\beta(x) + \sum_{n=1}^{\infty}\frac{4}{n\pi^3}\beta(x)\coth(n\pi)\left[\frac{1+\cos(n\pi\beta(x))}{1-n^2\beta^2(x)}\right]^2\right), \qquad (3.10)$$

Equation (3.10) is plotted as a function of β for various values of H in Figure 3.12. For the tapered box model, both H and the ratio B/W vary with position along the cochlea. The cross points on the curves show the values of B/W that correspond to the different values of H, as this varies linearly along the length of the tapered box model of the human cochlea. It is interesting that although the effective thickness changes considerably if either H or B/W vary independently, the combination of their variations in the tapered box model gives an effective thickness which is more independent of the position along the cochlea. The added BM thickness due to the fluid coupling is shown in Figure **3.13** as a function of position along the human cochlea, and other species.

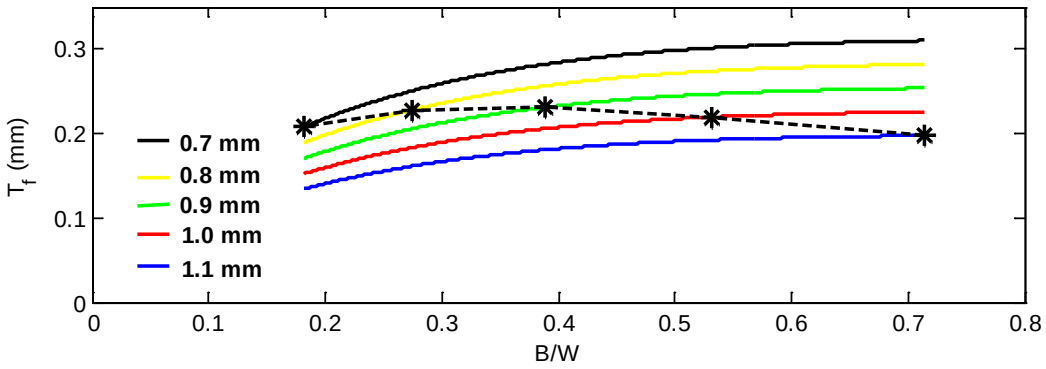

Figure 3.12 Effective thickness of fluid due to the near-field loading as a function of B/W for various values of H. Cross points correspond to values of B/W as H varies along the length of the human tapered box model.

The total BM mass per unit area for the 1D model is thus given by

$$m(x) = \rho\left(T_t + T_f(x)\right), \qquad (3.11)$$

where T_t is the sum of the physical thickness due to the organ of Corti, T_{OC}, and the BM, T_{BM}, and T_f is the effective thickness due to the fluid coupling. Since it is found that T_t is significantly less than T_f, its variation along the cochlea has not been calculated and an average value has been used, as listed in Table 3.3. The physical thickness of the organ of Corti and the BM can be given by

$$T_{\mathrm{OC}} = \frac{A_{\mathrm{OC}}}{B}, \qquad T_{\mathrm{BM}} = \frac{A_{\mathrm{BM}}}{B}, \tag{3.12)(3.13}$$

where A_{OC} is the average area of organ of Corti per mm, A_{BM} is average area of basilar membrane per mm, B is average BM width.

In the 3D human cochlear model, the physical BM mass is taken as 0.05 kg m^{-2}, corresponding to an average BM and organ of Corti thickness of 50 μm (Elliott et al., 2011b). In order to achieve an accuracy of 0.1 dB, 140 terms need to be used in the calculation of the additional thickness due to fluid coupling, T_f, using equation (2.12) with average values of $B(x)$, $W(x)$ and $H(x)$. The resulting average value of T_f for the human is about 230 μm, so that the total average BM mass in the human cochlea for the 1D uniform box model is 0.28 kg m^{-2}, as shown in Table 3.3. The variation of the total BM mass in the tapered box model, calculated for linear variations in $B(x)$, $W(x)$ and $H(x)$, and the value of T_t noted below, can be seen shown in Figure 3.14.

In the 3D cat cochlear model, the average value of the physical BM thickness, T_t, is about 30 μm (Neely and Kim, 1986). In the 1D uniform cat cochlear model, the value of T_f is about 180 μm according to equations (2.12) and (3.11), so that the total BM mass is about 0.21 kg m^{-2} for the uniform box model and the variation for the tapered box model is shown in Figure 3.14.

In the Guinea pig (Fernandez, 1952), the thickness of the BM is about 7.4 μm at the base and 1.34 μm at the apex, so the average value T_t is 4.4 μm. However, Fernandez also gives the area of the organ of Corti as 0.012 mm which gives an effective thickness of about 85 μm with the assumed width of BM, 0.14 mm. The total effective thickness is about 85 μm and thus the physical BM mass is about 0.085 kg m^{-2}. In the 1D Guinea pig cochlear model, according to equations (2.12) and (3.11), the value of T_f for the uniform model is about 115 μm, so that the total average BM mass for the uniform box model is increased to about 0.2 kg m^{-2}, Figure 3.14 shows the variation of the total BM mass for the tapered box model.

According to Bohne et al (1979), the area of organ of Corti in the chinchilla is from about 0.017 mm^2 at the base to 0.007 mm^2 at the apex, so the average value is 0.012 mm^2. The thickness of BM is about from about 0.004 mm at base to about 0. 0001 mm at the apex (Yoon et al, 2011), so the average value is 0.002 mm. The total effective thickness, T_t is about 62 μm and thus the BM mass in 3D model is about 0.062 $kg \times m^{-2}$. In the 1D chinchilla cochlear model, according to equations (2.12) and (3.11), T_f is about 160 μm, so that the BM mass for the uniform box model is about 0.22 $kg \times m^{-2}$; the variation for the tapered box model is also shown in Figure 3.14.

In the 3D mouse cochlear model, the area values of the BM and the organ of Corti are given by Keiler and Richter (Keiler and Richter, 2001), the total average area is assumed to be 4765 μm^2, so that the total thickness, T_t is about 30 μm and so the physical BM mass is about 0.03 kg m^{-2}. In the 1D mouse cochlear model, according to the equation (2.12) and (3.11), T_f is about 70 μm, so that the total average BM mass is increased to about 0.1 kg m^{-2} for the uniform model, Figure 3.14 also shows the variation of the total BM mass for the tapered box model of mouse.

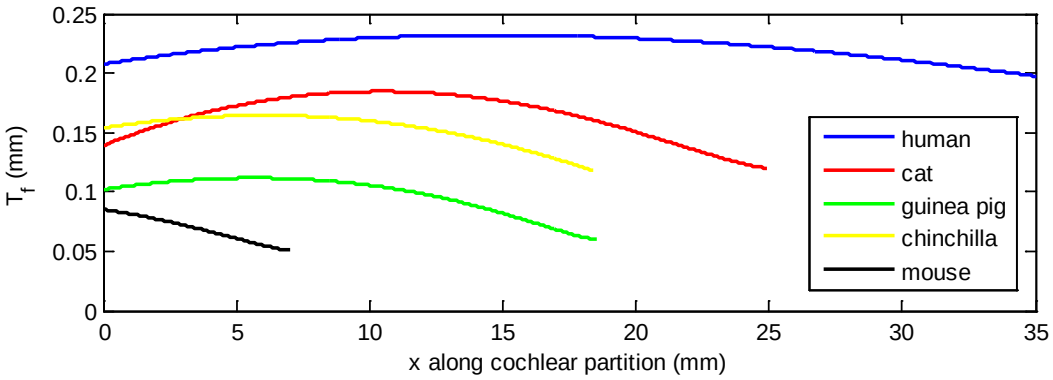

Figure 3.13 The added BM thickness due to fluid loading for five species, assuming linear variations in the geometry parameters.

By adding the assumed physical BM thickness values, T_t, estimated above, and listed inTable 3.3, and the values for T_f, shown in Figure 3.13, the total effective BM mass for a 1D model can be calculated, whose value, on a logarithmic scale is shown in Figure 3.14. It is striking how uniform the overall BM mass is along the cochlea for this tapered model, considering the large variations in fluid chamber dimensions and BM width assumed, as in Table 3.4 and Figure 3.7.

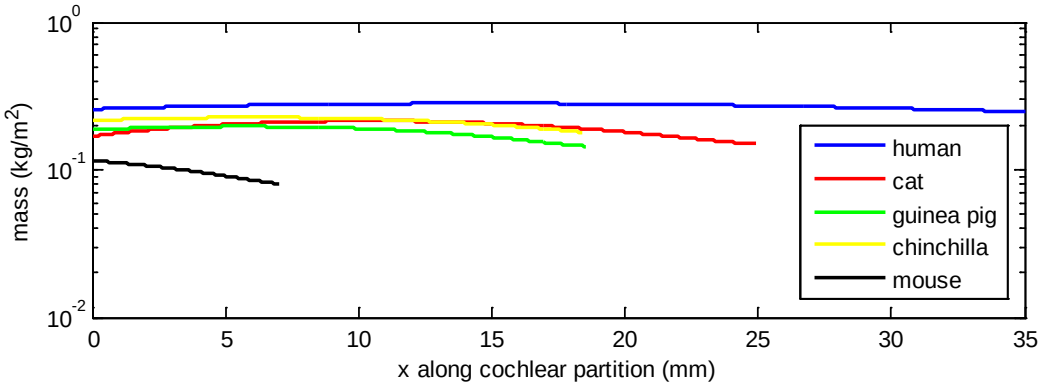

Figure 3.14 Variations of the total mass along the cochlear partition, including added fluid mass, for five species.

3.4. Coupled Response

In order to apply the "direct" inverse method to the data obtained from the 1D and 3D tapered box models of the human cochlea, the coupled responses in the 1D and 3D tapered box models of cochlea are calculated and will then be used as "measured" data. The coupled BM velocity is calculated by combining the passive BM dynamics with the fluid coupling results calculated above, and are shown in Figure 3.10, for 1D fluid coupling, and Figure 3.11, for 3D fluid coupling. The BM velocities at four frequencies and positions are shown in Figure 3.15 and Figure 3.16. According to the frequency-position map for human, 0.5, 1, 2, 5 kHz are related to 25.8, 21.0, 16.1, 9.7 mm, respectively. The coupled responses do not look very different from those in the uniform model described in chapter 2, although the results from the tapered model are about 6 dB higher. The roll-off of the tapered model is somewhat greater than that of the uniform model close to the characteristic place. The tapering has a greater effect on the changes in the wavelength of the BM motion as it approaches the characteristic place, since the effective area of the cochlear chambers becomes smaller than that at the base. There is then a reduction in longitudinal fluid flow due to reflection and an increase in the local mass loading, slowing the wave and increasing the phase accumulation. When the box model is extended from 1D to 3D fluid coupling, these changes become more obvious, which means that the amplitude of the BM response of the 3D tapered model is higher than that in the 1D model. Comparison of the coupled response in the uniform and tapered box models for all species is shown in Appendix D for reference.

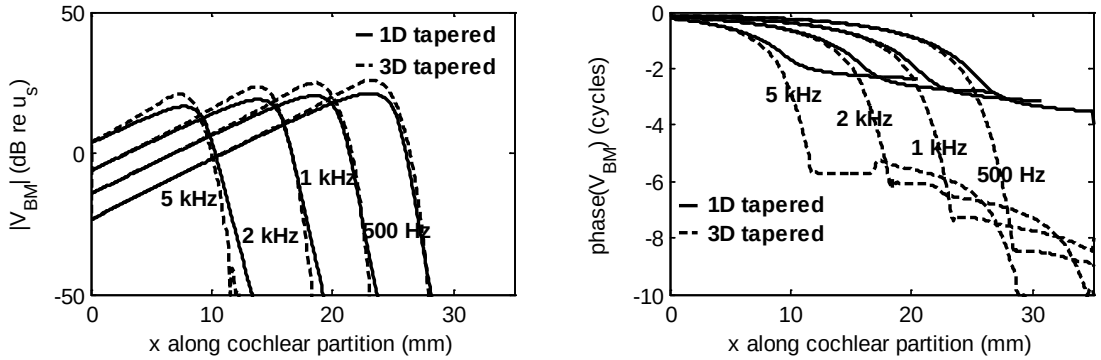

Figure 3.15 Amplitude and phase of the BM velocity at four fixed frequencies (500 Hz, 1 kHz, 2 kHz, and 5 kHz) as a function of position in the 1D and 3D tapered box models of the passive cochlea for human. Solid lines: 1D tapered box model and dashed lines: 3D tapered box model.

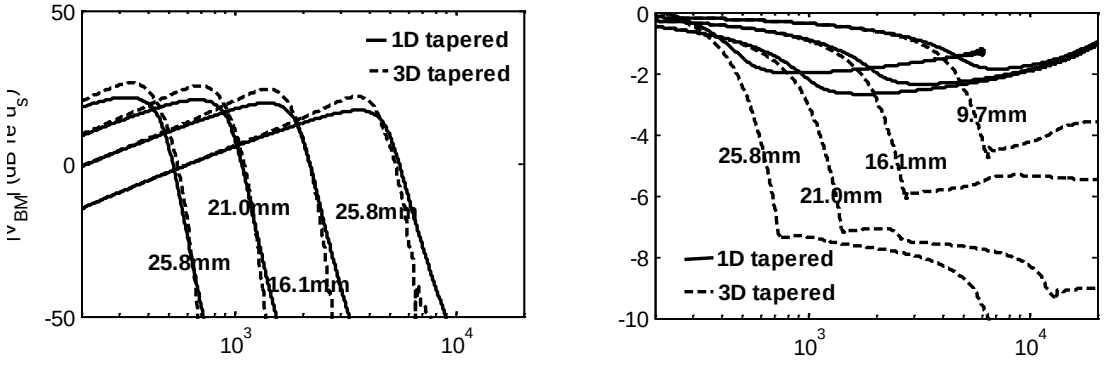

Figure 3.16 Amplitude and phase of the BM velocity at four fixed positions (25.8 mm, 21.0 mm, 16.1 mm, and 9.7 mm) as a function of frequency in a 1D and 3D tapered box models of the passive cochlea for human. Solid lines: 1D tapered box model and dash lines: 3D tapered box model.

3.5. The "direct" inverse method in the tapered models

The "direct" inverse method has been tested using the results from the passive uniform box model in the previous chapter, and the estimated response, $\hat{V}_{BM}$, is found it fits well with the "measured" data, V_{BM}. The same procedure is used here, but for the responses calculated using the tapered models.

3.5.1. 1D tapered box model

The BM velocity distributions along the cochlea, as calculated from the 1D tapered model, has been taken as the "measured" data at four different frequencies, as shown in Figure 3.15. The passive 1D tapered box model assumes that m_0, Q, Ω are constants along the cochlear partition, and are given by 0.28 $\mathrm{kg \cdot m^{-2}}$, 2.5 and 1, respectively. The constrained nonlinear minimization method, as described in Chapter 2, again with the fluid coupling calculated using the 1D uniform box model, is then used to estimate these parameters and the estimated

responses with these fitted parameters are plotted in Figure 3.17. A good fit is observed for the case where V_{BM} is directly taken as the spatial distribution at four different frequencies, although the phase of $\hat{V}_{BM}$ has more cycles than those of V_{BM}, presumably since the dimensions of the tapered box model are changing relatively slow along the cochlea, and it has been found that values of m_0, Q and Ω are not close to those used to generate V_{BM}, as listed in Table 3.4, but the normalised mean square error is very small.

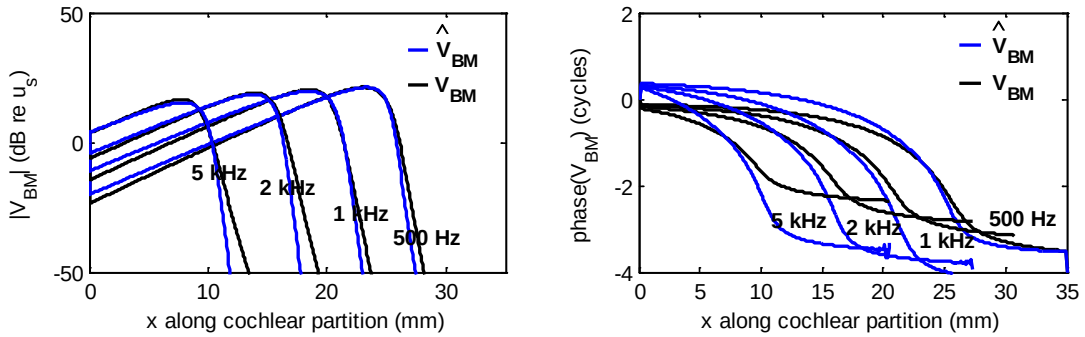

Figure 3.17 Amplitude and phase of V_{BM} and $\hat{V}_{BM}$ as a function of position at 500 Hz, 1 kHz, 2 kHz, 5 kHz in the 1D tapered box model of passive cochlea for human..

Table 3.4 Optimized parameters for poles, Ω, Q, and m_0 of the 1D tapered model obtained at different frequencies.

Direct inverse method: 1D uniform				
"measured data": 1D tapered (fixed frequencies)				
	Ω	Q	m_0	NMSE
500 Hz	0.97	3.76	0.16	0.002
1 kHz	1.09	3.24	0.11	0.005
2 kHz	1.04	4.01	0.13	0.002
5 kHz	1.11	3.74	0.13	0.010

3.5.2. 3D tapered box model

The direct inverse method has also been tested using data as V_{BM}, shown in Figure 3.15, at four different frequencies from the 3D tapered box model, where it is assumed that m_0, Q, Ω are constants along the cochlear partition, given by 0.05 kg×m^{-2}, 2.1 and 2.4, respectively. The constrained nonlinear minimization method, again with the fluid coupling calculated using the 3D uniform box model, is then used to estimate these parameters and the results are also plotted in Figure 3.18. The amplitude of $\hat{V}_{BM}$ is almost the same as V_{BM}, although the

phase of $\hat{V}_{BM}$ has more cycles than those of V_{BM}. It has been found that values of m_0, Q and Ω are not close to those used to generate V_{BM}, while the normalised mean square error is small, as listed in Table 3.5.

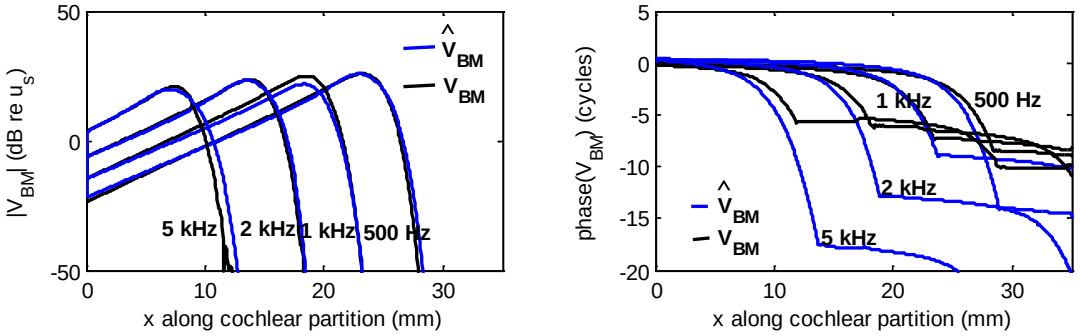

Figure 3.18 Amplitude and phase of V_{BM} and $\hat{V}_{BM}$ as a function of position at 500 Hz, 1 kHz, 2 kHz, 5 kHz in the 3D tapered box model of passive cochlea for human.

Table 3.5 Optimized parameters for poles, Ω, Q, and m_0 of the 3D tapered model obtained at different frequencies.

Direct inverse method: 3D tapered				
"measured data": 3D tapered (fixed frequencies)				
	Ω	Q	m_0	NMSE
500 Hz	2.21	4.02	0.04	0.003
1 kHz	2.60	2.20	0.04	0.088
2 kHz	1.93	5.13	0.05	0.004
5 kHz	2.80	3.71	0.02	0.020

3.6. Discussion

A simple modification of the widely used box model can be used to take into account the observed longitudinal variation of the fluid chamber areas and the BM width. At first, a 1D tapered box model of cochlea is created, in which case the passive coupled response is similar in the uniform and tapered box models, although the peak BM velocity is increased by about 10 dB using the tapered model. Then the 1D tapered box model is extended to include 3D fluid coupling, which gives a fluid added BM mass, decreasing along the cochlear length.

The robustness of the direct inverse method is then tested by fitting "data" from the tapered box model to the model that only incorporates the uniform box model. the fit is still good, although the phase of the fit has more cycles than the "data" around the characteristic place,

probably indicating that it is only the dimensions of the cochlea close to the characteristic place that significantly determines the BM response.

Chapter 4

The active cochlea

The cochlea works as the front-end of the auditory system, turning incoming sound signals into neural impulses transmitted along the auditory pathway for further processing. The cochlea does not just transmit mechanical sound into electrical impulses; but also processes and amplifies sound using its unique structure and the physical properties. Rhode (1971) measured the basilar membrane response in living squirrel monkeys and found that the frequency response was much sharper than that in the dead ones, which confirmed that the cochlea is active in living animals.

The cochlea exhibits remarkable acoustic sensitivity, high frequency selectivity and high level compression in processing sound signals. The significant differences in the response amplitude and frequency tuning between the dead and living cochlea is due to an amplification mechanism, namely, the cochlear amplifier, which exists within the organ of Corti and provides mechanical energy to the BM locally, thus enhancing the frequency tuning of the cochlea (de Boer, 1991). However, details of the cochlear amplifier still remain largely unknown as it is not clear how precisely the OHC motile forces act on the BM to amplify its motion in a frequency-selective way (Wen and Boahen, 2009).

Many researchers have modelled the active cochlea, and some results are in reasonably agreement with measurement data (Neely and Kim, 1987; Zweig, 1991; Mammano and Nobili, 1992). However, each active model is built to fit specific measurement data from specific species and cannot be changed arbitrarily to match different measurement data. Among many of the active cochlear models, the Neely and Kim model **(**1986**)** was the first attempt to explain the cochlear response by introducing active feedback elements based on physical principles, anatomical characteristics, and observed responses of the cochlea.

4.1. Neely and Kim model

In 1986, Neely and Kim published a mathematical model of the cat cochlea which included the cochlear amplifier. This model is an idealisation of the cochlea, the motions of the BM and TM are assumed to be linear, and the physical characteristics of the CP are lumped into local mass, stiffness and damper as a function of longitudinal position.

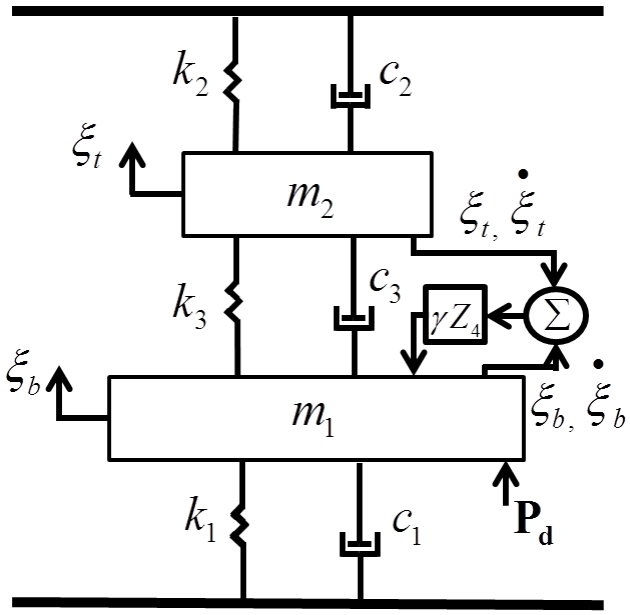

Figure 4.1 Neely and Kim micromechanical model of the cochlea

The Neely and Kim model is a two degrees of freedom system, which consists of two masses, three springs and three dampers, as shown in Figure 4.1. The mass m_1 represents the BM mass which is attached to rigid bone by stiffness and damping components k_1 and c_1. The mass m_2 represents the TM mass which is attached to rigid bone by stiffness and damping coponents k_2 and c_2. The two masses are coupled by stiffness and damping components k_3 and c_3. p_d is the pressure difference cross the BM (Ku, 2008). ξ_b and ξ_t stand for the the maximum displacement over the width of the BM and TM, respectively, $\dot{\xi}_b$ and $\dot{\xi}_t$ stand for the BM velocity and TM velocity, respectively. Each local micromechanical model represents the averaged motion of that slice cochlea in the radial direction. The main parameter symbols are listed in Table 4. 1, and the parameters used to calculate the coupled response are listed in Table 4.2.

Table 4. 1 Symbols of physical parameters used for the active cochlear simulations of Neely and Kim model (1986) for cat.

P_a	Pressure source in OHC	ξ_b	Average z displacement of BM
ξ_c	Shear displacement between TM and RL	ξ_t	Component ξ_c due to TM displacement
Z_1	Impedance associated with ξ_b	Z_2	Impedance associated with ξ_t
Z_3	Impedance associated with ξ_c	Z_4	Impedance associated with P_a

Table 4.2 Values of physical parameters used for the active cochlear simulations of Neely and Kim model (1986) for cat.

Variable	Parameter	Value
$k_1(x)$	Stiffness component of Z_1	$1.1\times10^{10}e^{-400x}$ N×m^{-3}
$c_1(x)$	Damping component of Z_1	$200+1500e^{-200x}$ N×s×m^{-3}
$m_1(x)$	Masscomponent of Z_1	3×10^{-2} kg×m^{-2}
$k_2(x)$	Stiffness component of Z_2	$7\times10^{7}e^{-440x}$ N×m^{-3}
$c_2(x)$	Damping component of Z_2	$100e^{-220x}$ N×s×m^{-3}
$m_2(x)$	Mass component of Z_2	5×10^{-3} kg×m^{-2}
$k_3(x)$	Stiffness component of Z_3	$1\times10^{8}e^{-400x}$ N×m^{-3}
$c_3(x)$	Damping component of Z_3	$100e^{-80x}$ N×s×m^{-3}
$k_4(x)$	Stiffness component of Z_4	$6.15\times10^{9}e^{-400x}$ N×m^{-3}
$c_4(x)$	Damping component of Z_4	$100e^{-80x}$ N×s×m^{-3}
γ	feedback gain	1
g	BM to IHC lever gain	1
b	Ratio of ζ_b to ζ_p	0.4
L	length of cochlear partition	0.025 m
H	Height of cochlear chamber	0.001 m
ρ	Density of cochlear fluid	1000 kg/m^3
N	Number of elements in discrete model	251

4.1.1. Micro-mechanics

Neely and Kim define b as the ratio of the average displacement across the width of the CP, ξ_p, to the maximum displacement over the width of the BM, ξ_b, so that

$$\xi_p(x) = b\xi_b(x) \tag{4.1}$$

The Neely and Kim micromechanical model is driven by an active mechanism which represents the contribution of the outer hair cells. An active impedance, Z_4, is included to provide a frequency-dependent phase shift between the active pressure source and the relative motion between the BM and TM,

$$p_a(x) = -\gamma Z_4(x)\dot{\xi}_c(x) \tag{4.2}$$

where Z_4 consists both real and imaginary components, p_a the pressure generated by the outer hair cells, the term γ denotes feedback gain, where $\gamma = 0$ generates a passive response, and $\gamma = 1$ generates a fully active response, and $\dot{\xi}_c$ is defined as the difference between the TM and BM velocities as

$$\dot{\xi}_c(x) = g\dot{\xi}_b(x) - \dot{\xi}_t(x) \tag{4.3}$$

where g is the BM to IHC lever gain. The real component of Z_4 primarily serves to reduce the damping of the CP, the imaginary component provides a shift in frequency relative to the passive resonances. The feedback function takes the difference in displacements and velocities of the BM and TM as its input. The output is the pressure generated by the outer hair cells, p_a.

As the input to the system is the local pressure difference, p_d, it is instructive to calculate the BM velocity for a given pressure; the ratio of output velocity to input pressure is defined as admittance, or mobility function. The transfer function of the active BM admittance, $\frac{\dot{\xi}_b(x)}{p_d}$, as given by Neely and Kim, has the form of

$$Y_{BM} = \frac{\dot{\xi}_b(x)}{p_d} = \frac{1}{g[Z_1(x) + Z_2(x)(\frac{Z_3(x) - \gamma Z_4(x)}{Z_1(x) + Z_2(x)})]} \tag{4.4}$$

in which,

$$\begin{aligned} Z_1(x) &= \frac{k_1(x)}{s} + c_1(x) + sm_1(x), \\ Z_2(x) &= \frac{k_2(x)}{s} + c_2(x) + sm_2(x), \\ Z_3(x) &= \frac{k_3(x)}{s} + c_3(x), \\ Z_4(x) &= \frac{k_4(x)}{s} + c_4(x). \end{aligned} \tag{4.5}$$

If we define that $s = j\omega$, the admittance in Neely and Kim model in terms of Laplace variable can be described as

$$Y_{BM}(s) = \frac{b\left(Z_2(s) + Z_3(s)\right)}{g\left\{Z_1(s)\left[Z_2(s) + Z_3(s)\right] + Z_2(s)\left[Z_3(s) - \gamma Z_4(s)\right]\right\}}, \tag{4.6}$$

Figure 4.2 shows the magnitude and phase of the BM admittance, calculated in the fully active case, with $\gamma = 1$, at four different frequencies and at four different postions. It can be seen that the BM admittance grows gradually until it reaches a peak, after which, the magnitude begins to decrease. The peak of the admittance increases along the cochlear position, and it decreases with increase of frequency. For the phase of the admittance, there is a peak around the characteristic frequency and then decrease until a certain value. The phase decreases along the cochlear partition or increases with an increase of frequency after finish increasing to about 0.25 cycles, so that the real part of the admittance is negative and the model can supply energy into the wave propagating along the cochlea.

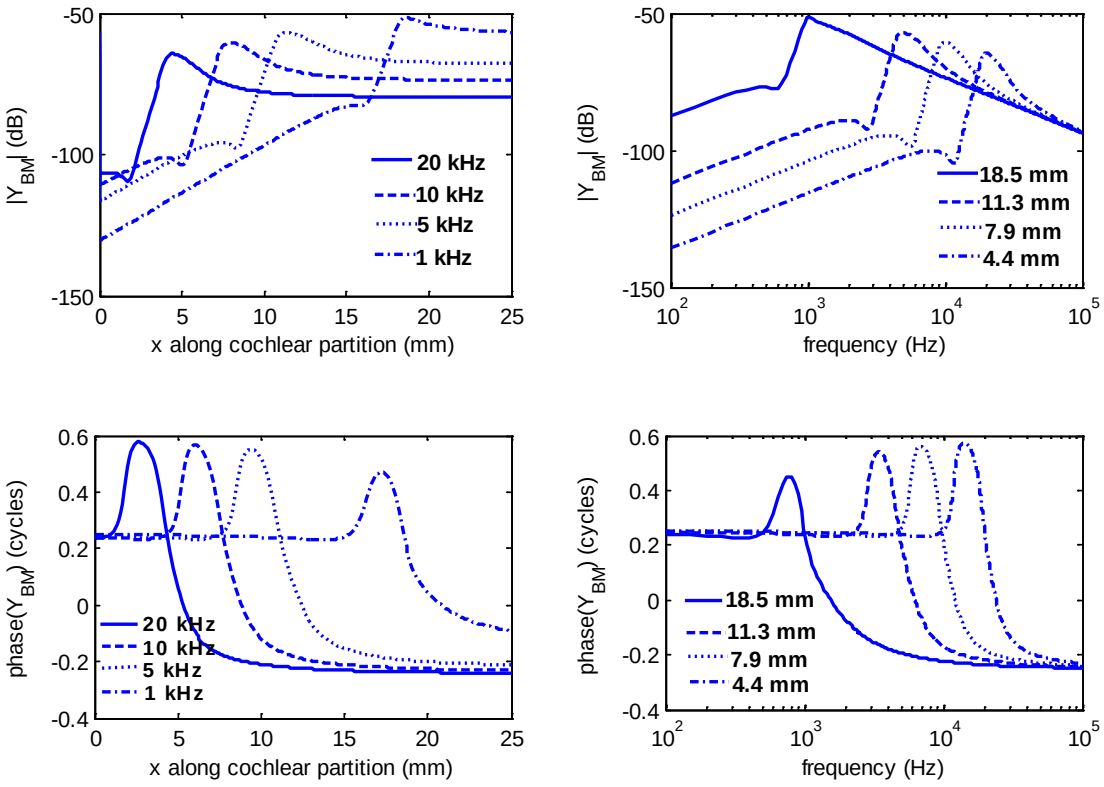

Figure 4.2 Amplitude and phase of the BM admittance at four different fixed frequencies (left panel) and four different fixed positions (right panel) in the Neely and Kim model of cat cochlea when the cochlea is active ($\gamma = 1$). The four fixed frequencies are 1 kHz, 5 kHz, 10 kHz, and 20 kHz, respectively. The four fixed positions are 18.5 mm, 11.3 mm, 7.9 mm, and 4.4 mm away from the base.

By setting the denominator and numerator of quation (4.6) to zero and solving for the values of *s* that satisfy these equations, the positions of poles and zeros at those four frequencies and positions have been calculated and are shown in Figure 4.3. This shows that from the base to the apex, the poles and zeros move towards to the origin, and there are always two pairs of poles and one pairs of zeros.

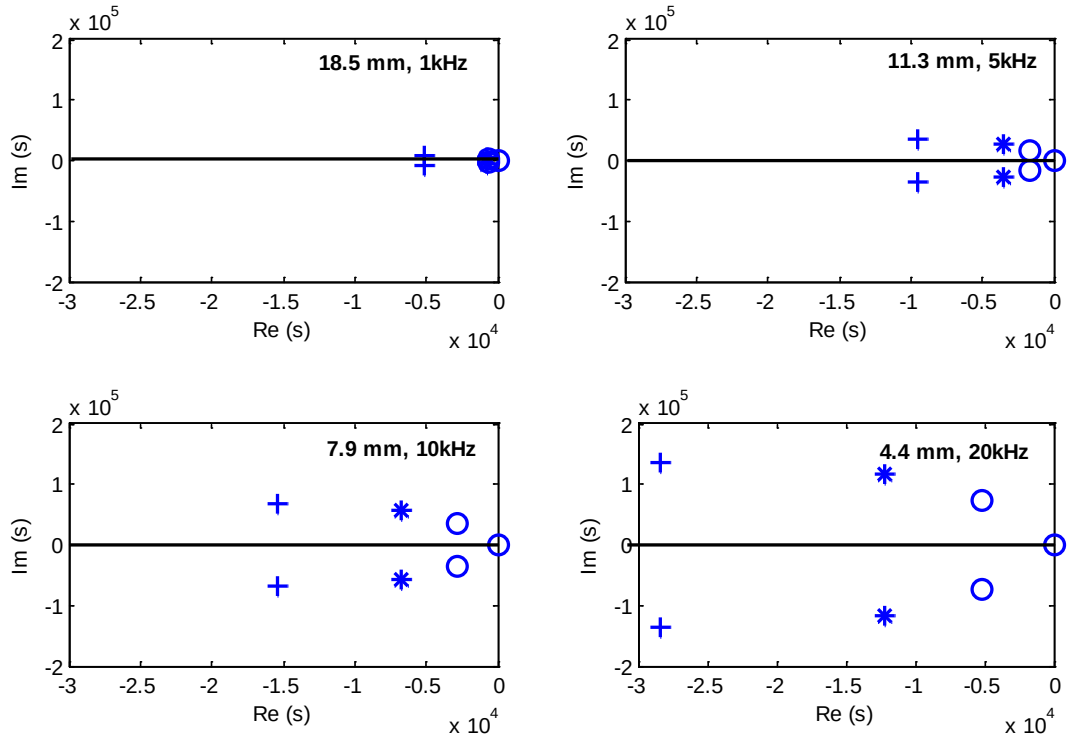

Figure 4.3 Position of pole/zero at four different positions and frequencies in the Neely and Kim model. According to the frequency-position map for cat, 18.5 mm is related to 1kHz, 11.3 mm is related to 5 kHz, 7.9 mm is related to 10 kHz, 4.4 mm is related to 20 kHz.

Figure 4.4 shows the variation of the BM admittance at a fixed frequency (1 kHz, left panel) and a fixed position (18.5 mm, right panel) with four different values of γ between $\gamma = 0$ (passive) and $\gamma = 1$ (fully active), which reveals that the peak of amplitude and phase for the BM admittance become higher, and the phase cycle gets larger when γ increases.

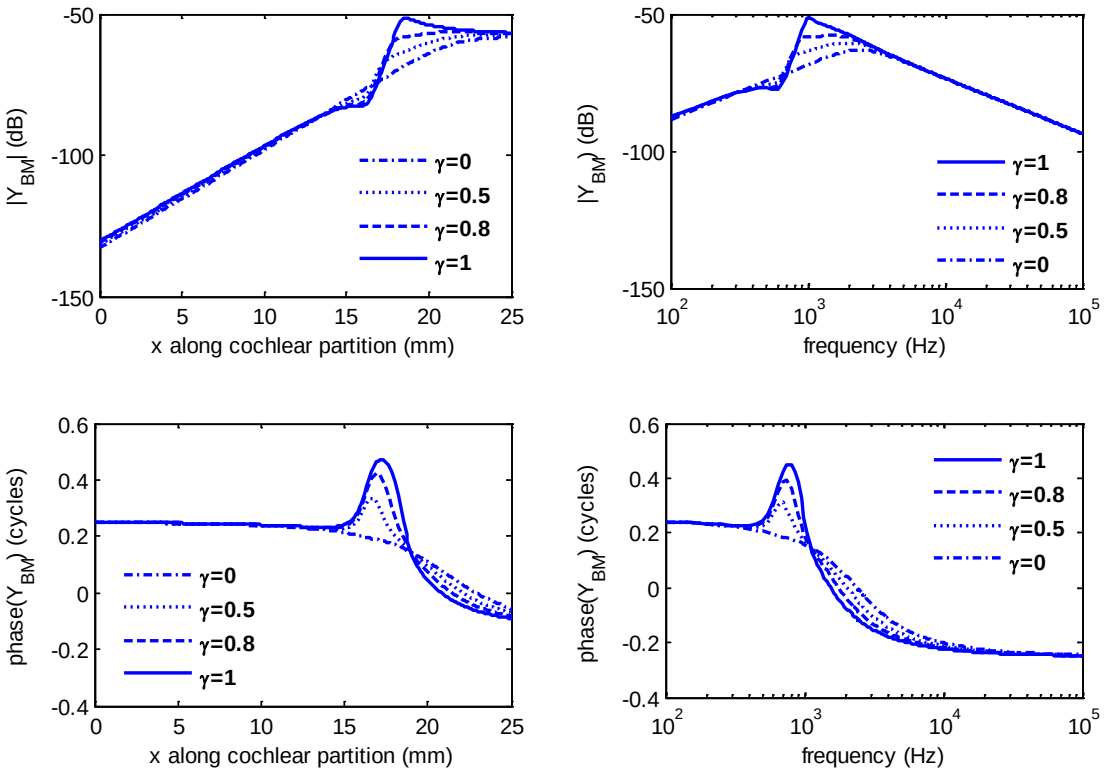

Figure 4.4 Amplitude and phase of the BM admittance at 1 kHz (left panel) and at 18.5 mm (right panel) with four different γ in the Neely and Kim model of cat cochlea. The four different γ is 0, 0.5, 0.8, and 1.

The positions of the poles and zeros at 18.5 mm (1 kHz) with those four different values of γ are then shown in Figure 4.5. As γ varies from $\gamma = 1$ to $\gamma = 0$, which means from being fully active to being fully passive, one pairs of poles moves towards to one pairs of zeros, so that they cancel each other when the cochlea becomes fully passive.

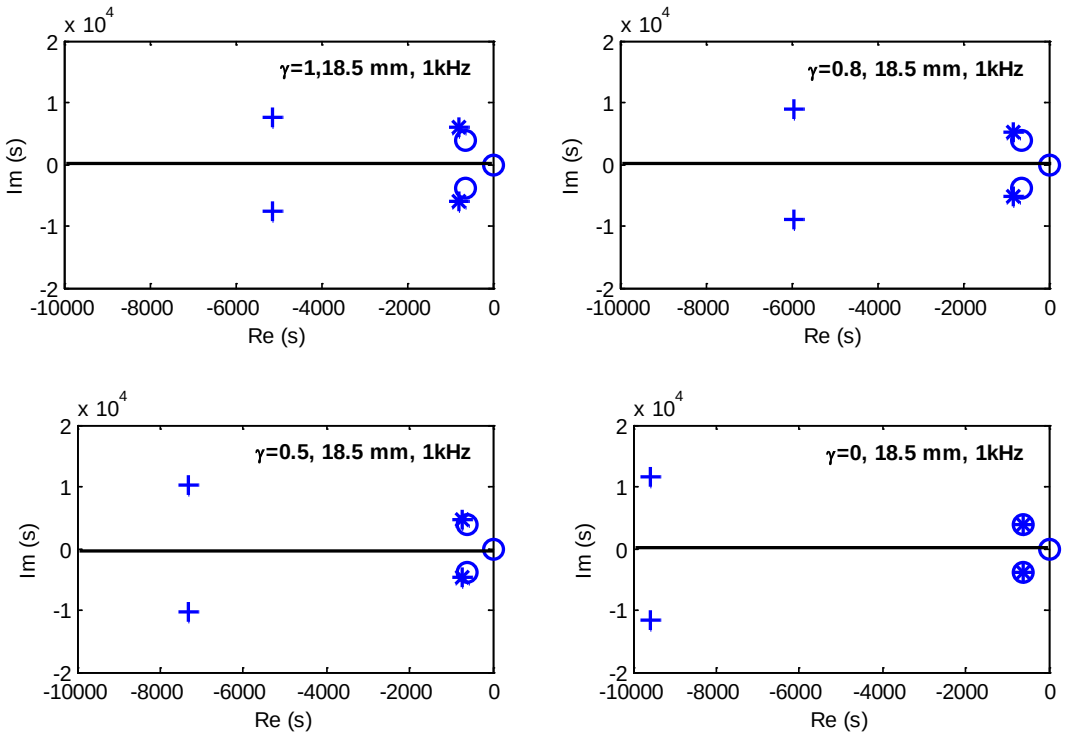

Figure 4.5 Position of pole/zero at 18.5 mm (1 kHz) with four different γ (1, 0.8, 0.5, 0) in the Neely and Kim model.

4.1.2. Coupled response

The finite difference method is used to calculate the coupled response of the Neely & Kim model, as described in Chapter 2. The effect of the active elements on the basilar membrane response is clearly shown in Figure 4.6 from the coupled response at a fixed frequency (1 kHz, left panel) and a fixed position (18.5 mm, right panel) with four different values of the feedback gain parameter γ. As γ varies from 0 to 1, the peak BM velocity increases and the tuning becomes sharper.

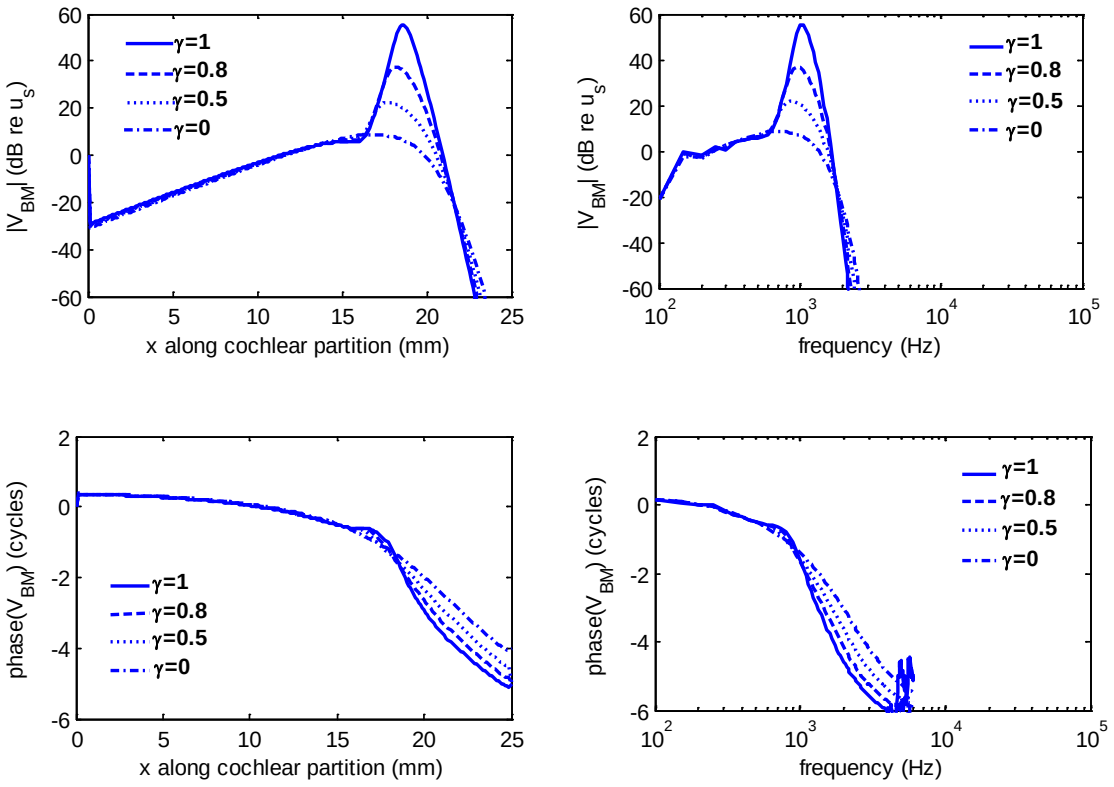

Figure 4.6 Amplitude and phase of the BM velocity with four different γ (γ=0, 0.5 0.8 and 1) at 1 kHz and 18.5 mm as a function of position and as a function of frequency, respectively, in the Neely & Kim model of the cat cochlea.

4.2. Optimization methods for the "direct" inverse method

4.2.1. A new formulation of the active BM admittance

The Neely and Kim model is used here to provide the "measured" data for the active cochlea. For the passive cochlear model (one degree of freedom system), there was only one pair of poles in the BM model, and the estimated passive BM admittance was given by equation (2.27). While for the Neely and Kim model (two degree of freedom with feedback control system), there are two pairs of poles and one pairs of zeros. Based on equation (2.27) and (4.6), the estimated active BM admittance can be written as

$$Y_{BM}^{a}(x,s)=\frac{s(s^2+\Omega_1\omega_n(x)s/Q_1+(\Omega_1\omega_n(x))^2)}{m_0(s^2+\Omega_2\omega_n(x)s/Q_2+(\Omega_2\omega_n(x))^2)(s^2+\Omega_3\omega_n(x)s/Q_3+(\Omega_3\omega_n(x))^2)}, \quad (4.7)$$

where Ω_1 and Q_1 are the normalised natural frequency and Q factor of the pair of zeros and Ω_2, Ω_3, Q_2, Q_3 are the normalised natural frequencies and the Q factors of the two pair of poles, and m_0 is again the BM mass, which are all assumed to be independent of x.

The active natural frequency of the BM at position *x* is given by $\omega_n(x)$, which is assumed here to be $\omega_n(x) = \omega_B e^{-x/\ell}$, where in this case $\omega_B = 2\pi \times 60$ kHz, and $\ell = 5.1$.

If $s \to \infty$, equation (4.7) can be changed to $Y_{BM}^a \Rightarrow 1/sm_0$ in pole/zero model, according to equation (4.5), $Z_1 \Rightarrow sm_1$, $Z_2 \Rightarrow sm_2$, $Z_3 \Rightarrow 0$, and $Z_4 \Rightarrow 0$, equation (4.6) can be changed to $Y_{BM}\big|_{s\to\infty} = b/sm_1 g$, so $m_0 = m_1 g/b$.

According to equation (4.6) in the Neely and Kim model, it has 11 variables including 2 masses, 4 stiffnesses, 4 dampings and 1 constant (*g*/*b*), while according to equation (4.7) it has 7 variables including 2 pairs of poles, 1 pairs of zeros and 1 constant (m_0). Therefore, the parameters that should be adjusted are reduced. Since Y_{BM} is completely defined by equation (4.7), the tuning of the Neely and Kim mechanical velocities is not unique for given response.

According to equation (4.7), poles and zeros can be derived by solving the following equations

$$\begin{aligned}
&(s^2 + \Omega_1\omega_n(x)s/Q_1 + (\Omega_1\omega_n(x))^2) = 0,\\
&(s^2 + \Omega_2\omega_n(x)s/Q_2 + (\Omega_2\omega_n(x))^2) = 0,\\
&(s^2 + \Omega_3\omega_n(x)s/Q_3 + (\Omega_3\omega_n(x))^2) = 0,
\end{aligned} \tag{4.8}$$

so that,

$$\begin{aligned}
s &= \frac{-\frac{\Omega_i\omega_n}{Q_i} \pm \sqrt{(\frac{\Omega_i\omega_n}{Q_i})^2 - 4(\Omega_i\omega_n)^2}}{2}\\
&= \frac{-\frac{\Omega_i\omega_n}{Q_i} \pm \Omega_i\omega_n\sqrt{(\frac{1}{Q_i})^2 - 4}}{2},
\end{aligned} \tag{4.9}$$

where $i = 1, 2, 3$. Based on equation (4.6), the poles and zeros can be given as

$$poles \quad or \quad zeros = a + bi \tag{4.10}$$

where

$$a = -\frac{\Omega\omega_n}{2Q}, b = \frac{\Omega\sqrt{4-(\frac{1}{Q})^2}}{2}\omega_n, \tag{4.11}$$

so that

$$Q = \frac{\sqrt{\frac{b^2}{a^2}+1}}{4}, \Omega = \frac{\sqrt{a^2+b^2}}{2\omega_n}. \tag{4.12}$$

4.2.2. Investigation of Q and Ω in the Neely and Kim model

Based on parameters in Table 4.2, the theoretical pole/zero positions in the active Neely and Kim model can be derived at each position along the cochlea using equation (4.12), as shown in Figure 4.7.

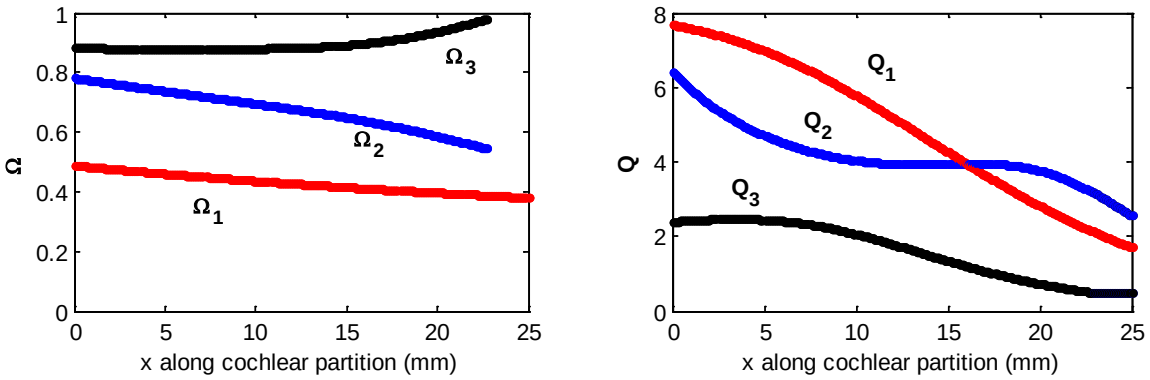

Figure 4.7 Ω and Q distribution along the cochlear partition using the parameters in Neely & Kim model, together with the parameters obtained from fitting the "measured" data at different fixed frequencies, black star for Ω_3 and Q_3, blue star for Ω_2 and Q_3 red star for Ω_1 and Q_1, for $\gamma = 1$.

It can be seen in Figure 4.7 that Ω_1 and Ω_2 decrease while Ω_3 increases at each position, and Q_1, Q_2 and Q_3 decrease at each position.

The Neely and Kim model can also be changed from being fully active to fully passive by varying the parameter, γ, the variation of Ω_n and Q_n along γ at a CF of 1 kHz are shown in Figure 4.8.

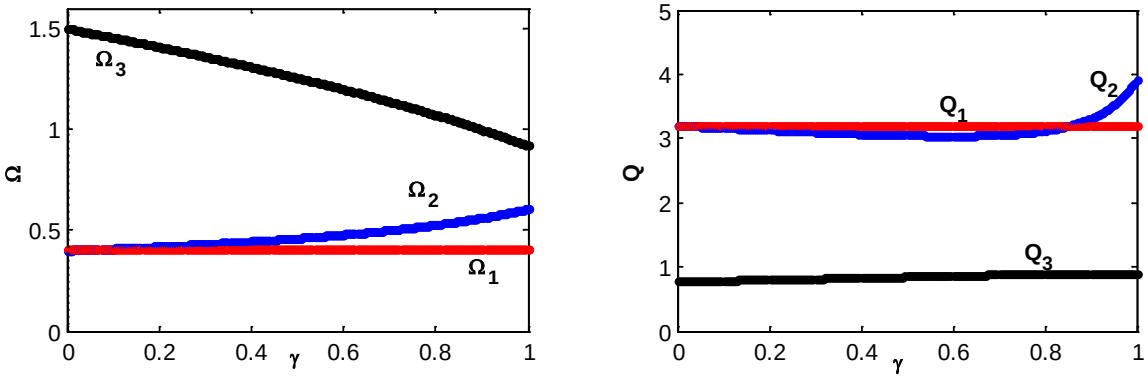

Figure 4.8 Variation with the feedback gain parameter γ of the normalised natural frequencies Ω, and Q factors of the zero, Ω_1, Q_1, and poles, Ω_2, Q_2, Ω_3, Q_3 of the Neely and Kim model at 1 kHz. $\gamma = 0$ corresponds to a passive cochlea and $\gamma = 1$ corresponds to a fully active cochlea, black star for Ω_3 and Q_3, blue star for Ω_2 and Q_2, red star for Ω_1 an Q_1.

It is seen from Figure 4.8 that the Q factor and Ω of one pair of poles are very similar to those of the zeros at $\gamma = 0$, so that the effects of this pole/zero pair is cancelled, indicating that there is effectively only one pairs of poles when the cochlea is passive. As γ increases, the Q and Ω of this pole moves away from those of the zero, confirming that there are two separate pairs of poles and one pairs of zeros when the cochlea is active.

4.2.3. One objective optimization

The normalized mean square error is initially used to compare the matching between the estimated BM velocity, $\hat{V}_{BM}$, and the "measured" BM velocity, V_{BM}, with the formulation of the normalized mean square error is the same as equation (2.26). The one objective optimization using genetic algorithm (Deb, 2001), which is *ga-Genetic Algorithm* for solver in the MATLAB optimization Toolbox was chosen to adapt the parameters of the passive box model of cochlea.

Initially, V_{BM} at four different fixed frequencies, were calculated using the Neely and Kim model when the cochlea is fully active ($\gamma = 1$). The direct inverse method using one objective optimization was then used to estimate $\hat{V}_{BM}$ which is compared with the "measured" V_{BM} shown in Figure 4.9.

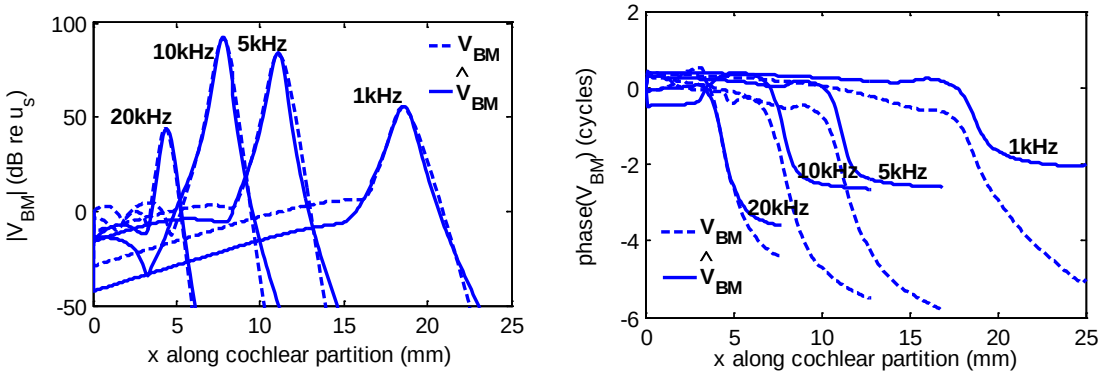

Figure 4.9 Amplitude and phase of V_{BM} and $\hat{V}_{BM}$ along cochlear partition at 1, 5, 10, and 20 kHz in the Neely & Kim model for cat. Dashed lines: the "measured" BM responses. Solid lines: the estimated BM responses. The estimated parameters are given in Table 4.3.

Figure 4.9 shows reasonable agreement between the modulus V_{BM} and that of $\hat{V}_{BM}$, although the phase of V_{BM} is 1 cycle more than $\hat{V}_{BM}$, which is still in phase and hence gives a small mean square error. There are some differences between the two responses, since m_0, Q, Ω are assumed to be constants in the estimated model, but varying with position in the Neely and Kim model, as seen in Figure 4.7.

The estimated parameters, as listed in Table 4.3, together with the "measured" data are shown in Figure 4.10, which shows that the estimated parameters of zeros (red) are quite close to the "measured" data, while the estimated parameters of poles (blue and black) are not in agreement with the "measured" data, taking parameters as constants in the active cochlear model can also be investigated in Appendix F, it shows bad results, which confirms that the parameters should vary along cochlear partition in the Neely and Kim model.

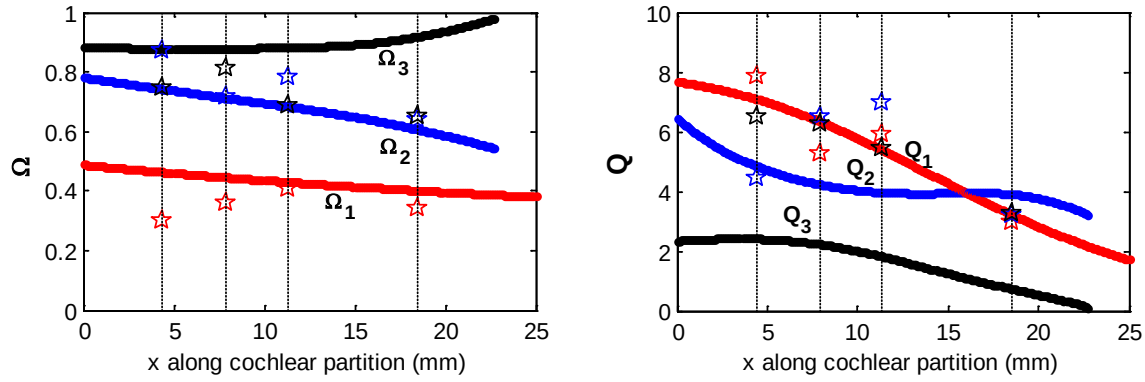

Figure 4.10 Comparison between estimated paramters derived from Figure 4.9 and "measured" data in Figure 4.7 along the cochlear partition using sigle objective optimization. Red stars stand for Ω_1 and Q_1, blue stars stand for Ω_2 and Q_1, black stars stand for Ω_3 and Q_3. The estimated paramters are listed in Table 4.3.

Table 4.3 The estimated parameters for the zero, Ω_1 and Q_1, and the poles, Ω_2, Ω_3, Q_2, and Q_3 of the micromechanical model obtained at fixed frequencies and positions in the Neely and Kim model of cat cochlea using single objective optimization, together with the normalised mean square error, NMSE.

Two objectives optimization								
Conditions $\gamma = 1$	Ω_1	Q_1	Ω_2	Q_2	Ω_3	Q_3	m_0	NMSE Amplitude
1 kHz	0.34	2.96	0.64	3.19	0.65	3.24	0.67	0.055
5 kHz	0.41	5.92	0.78	6.98	0.69	5.47	0.44	0.048
10 kHz	0.36	5.24	0.72	6.48	0.81	6.27	0.39	0.027
20 kHz	0.30	7.86	0.87	4.45	0.75	6.51	0.23	0.078

Next, V_{BM} is calculated using the Neely and Kim model, excited at 1 kHz with 4 different values of γ is given, as shown in Figure 4.6. The direct inverse method is used with the Neely and Kim data using one objective optimization with the results for $\hat{V}_{BM}$ shown in Figure 4.11.

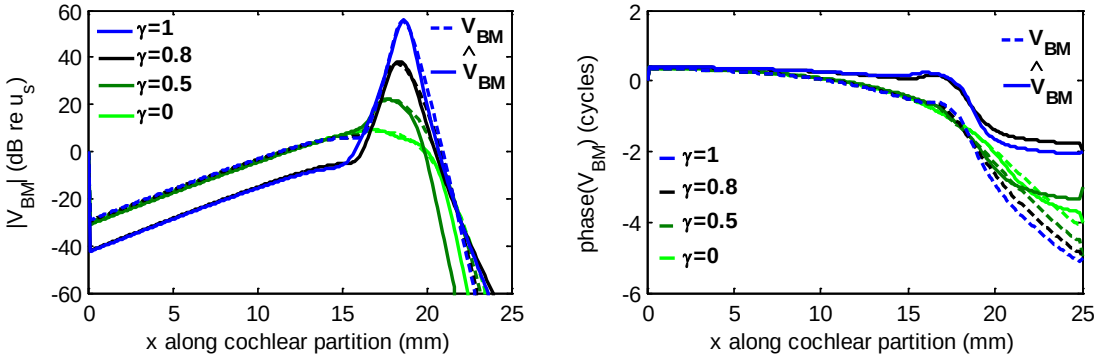

Figure 4.11 Amplitude and phase of V_{BM} and $\hat{V}_{BM}$ along cochlear partitional at 1 kHz with γ is equal to 0 (green lines), 0.5 (dark green lines), 0.8 (black lines), and 1 (blue lines) in the Neely and Kim model cat cochlea. The relative optimized pole-zero parameters are given in Table 4.4.

Again the magnitude is in reasonable agreement, although there are integer numbers of cycles of phase errors. The normalised mean square errors are relatively small, together with the eatimaed parameters, as listed in Table 4.4. The poles/zeros model is thus capable of smoothly making the transition from a fully active model to a passive model.

Table 4.4 The estimated parameters for the zero, Ω_1 and Q_1, and the poles, Ω_2, Ω_3, Q_2 and Q_3 of the micromechanical model obtained at 1 kHz and 18.5 mm with different feedback gains in the Neely and Kim model of cat cochlea for single objective optmization, together with the normalised mean square error, NMSE.

One objective optimization								
Conditions	Ω_1	Q_1	Ω_2	Q_2	Ω_3	Q_3	m_0	NMSE
1 kHz								
$\gamma = 0$	0.37	0.68	0.52	0.55	1.16	0.61	0.18	0.118
$\gamma = 0.5$	0.49	1.00	0.97	1.02	0.89	0.75	0.17	0.157
$\gamma = 0.8$	0.49	1.54	1.08	1.51	1.03	1.37	0.44	0.383
$\gamma = 1$	0.34	2.96	0.64	3.19	0.65	3.24	0.67	0.055

4.2.4. Two objectives optimization

In section 4.2, the one objective optimization is used, the results show that the amplitude of the estimated BM velocity, $\hat{V}_{BM}$, fits well with the "measured" data, V_{BM}, only around the peak area, while the phase of the "measured" data has an integer number of cycles more than the estimated BM velocity. With an integer number of cycles error in the phase, the complex value of $\hat{V}_{BM}$ can still be the same as V_{BM}, and so the single mean square error function can still be small. In order to improve the estimated phase, a new optimization method, based on having two objective functions (Deb, 2001), is investigated. The normalised mean square error is refined, and is now separated into the normalized mean square error of the BM velocity amplitude and the normalized mean square error of the BM velocity phase

$$NMSE_L = \frac{\sum_{n=1}^{N} (|\hat{V}_{BM}(n)| - |V_{BM}(n)|)^2}{\sum_{n=1}^{N} (|V_{BM}(n)|)^2},$$
$$NMSE_P = \frac{\sum_{n=1}^{N} (\angle\hat{V}_{BM}(n) - \angle V_{BM}(n))^2}{\sum_{n=1}^{N} (\angle V_{BM}(n))^2}. \quad (4.13)$$

Where n is the index of the elements along the length of the cochlea, N is the number of elements, which is 251 in this case, $\hat{V}_{BM}(n)$ is the estimated complex BM velocity at the nth element corresponding, $V_{BM}(n)$ is the "measured" BM velocity.

There are thus two objective functions for this optimization method, and the "Pareto distribution", which plots the results of the two objectives is used to find the best optimized parameters, as shown in Figure 4.12. In Figure 4.12, the best results to be chosen should be the spot that gives both a low $NMSE_L$ and a low $NMSE_P$, as indicated by the arrow. The selected sensible point is chosen manually by trying some points one the Pareto front to see the best fitted amplitude and phase of BM response by eye.

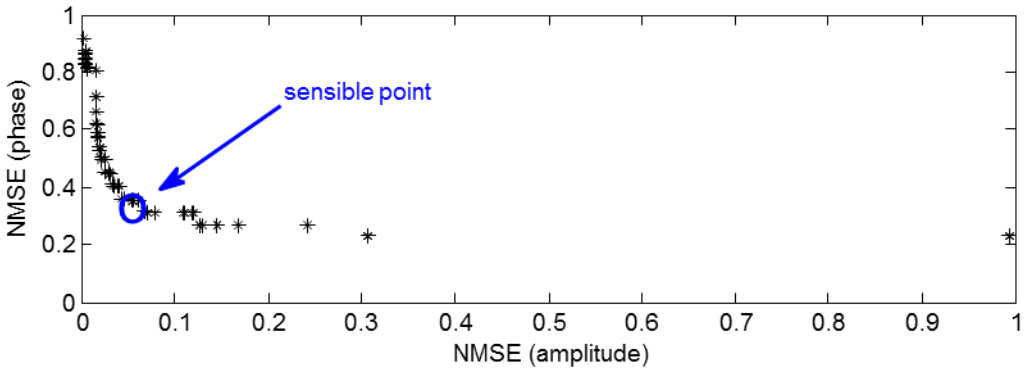

Figure 4.12 Pareto function for the multiple objectives optimization. The horizontal axis is one set of values of the normalized mean square error amplitude; the vertical axis is one set of the moralized mean square error phase.

Initially, using V_{BM} calculated along the cochlea at fixed frequencies, this new optimization method is used to give the results shown in Figure 4.13, with the estimated parameters listed in Table 4.4.

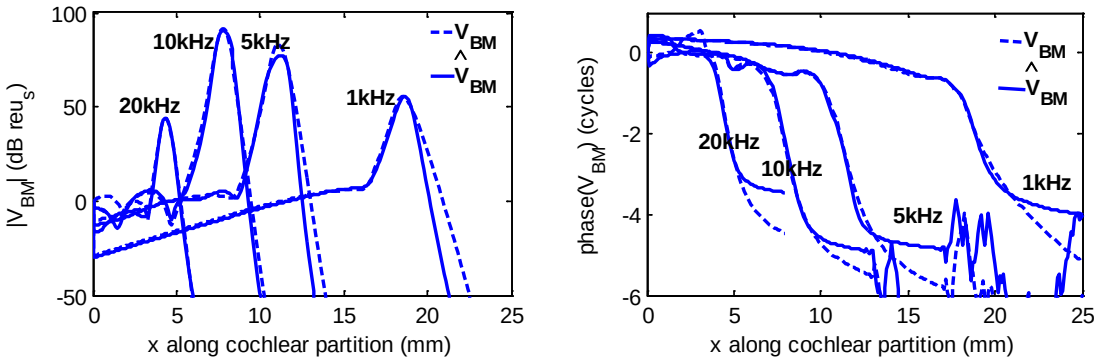

Figure 4.13 Amplitude and phase of V_{BM} and $\hat{V}_{BM}$ distribution along cochlear partition at 1, 5, 10, and 20 kHz in the Neely and Kim model cat cochlea using the two objective optimization. The estimated parameters are given in Table 4.5.

Figure 4.13 shows that not only is the amplitude of $\hat{V}_{BM}$ fitted well compared with V_{BM}, but now the phase of $\hat{V}_{BM}$ is also a good match.

The estimated parameters together with the parameters of the "measured" data are shown in Figure 4.14, which shows that the estimated parameters of the zeros (red) and poles (blue and black) are more close to those of the "measured" data, although the estimated values of the Q of pole/zero is not in such good agreement with the those of "measured" data (right panel), taking parameters as constants in the active cochlear model can also be investigated in Appendix F, it shows bad results, which certificate that the constants vary along cochlear partition in the Neely and Kim model.

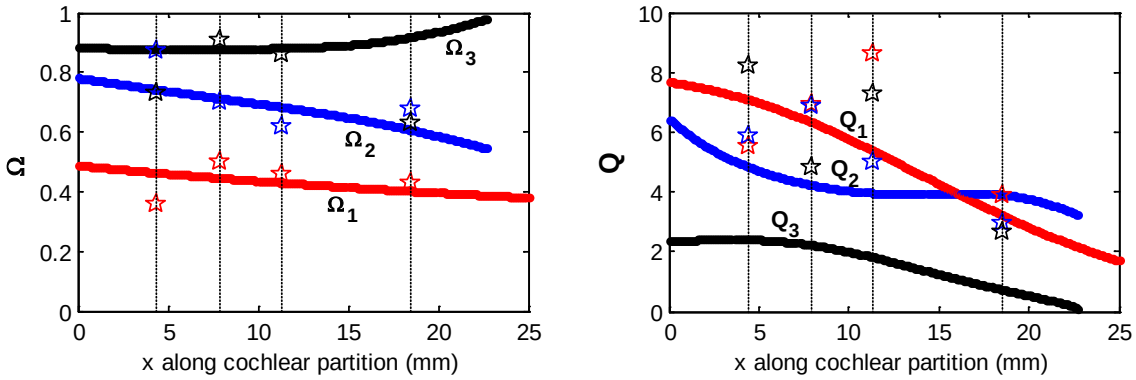

Figure 4.14 Comparison between estimated paramters derived from Figure 4.13 and "measured" data in Figure 4.7 along cochlear partition. Red stars stand for Ω_1 and Q_1, blue stars stand for Ω_2 and Q_1, black stars stand for Ω_3 and Q_3. The estimated paramters are listed in Table 4.5.

Table 4.5 The estimated parameters for the zero, Ω_1 and Q_1, and the poles, Ω_2, Ω_3, Q_2 and Q_3 of the micromechanical model obtained at fixed frequencies in the Neely and Kim model of cat cochlea, obtained using the two objective optimization together with the normalised mean square error, NMSE, for amplitude and phase, respectively.

Two objective genetic algorithm									
Condition $\gamma = 1$	Ω_1	Q_1	Ω_2	Q_2	Ω_3	Q_3	m_0	NMSE amplitude	NMSE phase
1 kHz	0.43	3.90	0.68	2.93	0.63	2.68	0.18	0.032	0.408
5 kHz	0.46	8.61	0.62	5.02	0.86	7.27	0.12	0.212	0.474
10 kHz	0.50	6.93	0.70	6.86	0.91	4.80	0.10	0.016	0.405
20 kHz	0.36	5.54	0.87	5.87	0.73	8.19	0.27	0.001	0.574

The direct inverse method using the two objective optimization is now used with V_{BM} calculated from the Neely and Kim model, excited at 1 kHz but with 4 different values of γ, with the results shown in Figure 4.16, where the estimated parameters are listed in Table 4.6.

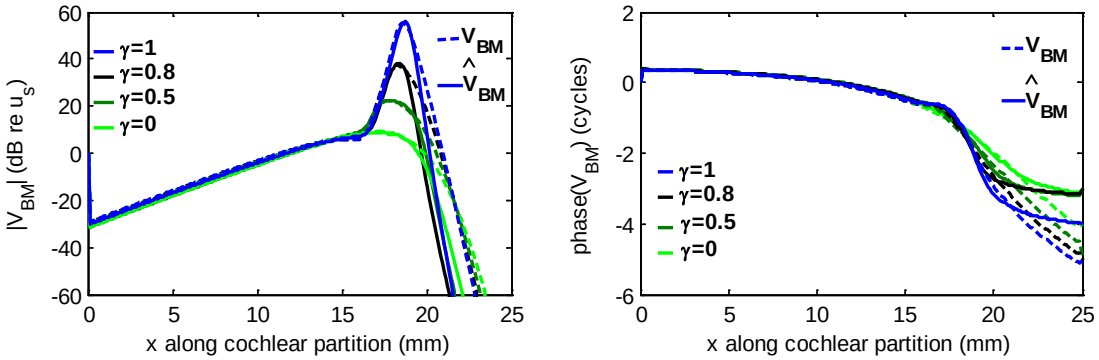

Figure 4.15 Amplitude and phase of V_{BM} and $\hat{V}_{BM}$ distribution along cochlear partitional at 1 kHz with γ is equal to 0 (green lines), 0.5 (dark green lines), 0.8 (black lines), and 1 (blue lines) in the Neely and Kim model cat cochlea using the two objective optimization.

Figure 4.15 shows better agreement of the phase between V_{BM} and $\hat{V}_{BM}$ than the one objective function optimization in Figure 4.11.

Table 4.6 The estimated parameters for the zero, Ω_1 and Q_1, and the poles, Ω_2, Ω_3, Q_2, and Q_3 of the micromechanical model obtained at 1 kHz with different feedback gains in the Neely and Kim model of cat cochlea, together with the normalised mean square error, NMSE, for amplitude and phase, respectively.

Two objectives optimization									
Conditions	Ω_1	Q_1	Ω_2	Q_2	Ω_3	Q_3	m_0	NMSE Amplitude	NMSE Phase
1 kHz									
$\gamma = 0$	0.93	0.79	0.91	0.89	0.89	1.44	0.27	0.011	0.309
$\gamma = 0.5$	0.43	4.37	0.46	4.64	0.80	2.88	0.28	0.010	0.555
$\gamma = 0.8$	0.44	4.34	0.54	3.27	0.68	3.76	0.29	0.081	0.585
$\gamma = 1$	0.43	3.90	0.68	2.93	0.63	2.68	0.18	0.033	0.408

4.3. Discussion

The pole-zero structure of the micromechanics in the classical active cochlear model of Neely and Kim (1986) has been initially investigated. It has been shown that when the cochlea is active, there are two pairs of poles and one pairs of zeros, and when the cochlea becomes passive, one pairs of poles is effectively cancelled each by the co-located zeros as that there is effectively only one pair of poles. The direct inverse method using the active pole/zero model in the 1D uniform box model is used to estimate the pole/zero parameters of the BM admittance formulation using the "measured" data simulated from the Neely and Kim model.

It is shown that there is a problem using the previous single objective optimization, using the squared modulus of the complex error, since this can be small even with integer numbers of cycles of error in the unwrapped phase. A new optimization approach is then developed that uses two objective function, the normalised mean square error for the magnitude and that for the phase. The algorithm is found to give a much better fit to the phase data from the active Neely and Kim model.

Chapter 5

Application of inverse methods using measurement data

In previous chapters, a number of inverse methods have been reviewed and tested on the BM response data obtained from cochlear models. This has tested the implementation of each of these methods and illustrated some "ill-posed" issues that result in their sensitivity to measurement noise. The true test of these inverse methods, however, is their behaviour in dealing with data actually measured in the cochlea, and this is the subject of the present chapter.

The most promising one among the previous inverse methods is Shera's method, which is used here to analyse the chinchilla auditory nerve data, originally used in Shera (2007). The sensitivity of the derived results using this method is tested, with different conditions that have been assumed in processing the experimental data. The estimated results using this method are shown to be reasonably robust with these conditions.

This chinchilla data is then analysed using the direct inverse method. The chinchilla data does not, however, include good samples of how the BM response changes with excitation level. So some recent mouse data (Lee *et al.*, 2015), is then investigated using the direct inverse method,which analyses the way that the response of the cochlea changes from being active to being passive, which allows an estimation of the variation of the estimated parameters of the micromechanical model.

5.1. Shera's inverse method with chinchilla data

Shera's method is used to estimate that the wavenumber is made for the BM click response obtained at a certain place along the chinchilla cochlea using the second–order Wiener-kernel analysis of auditory-nerve-fiber (ANF) response to noise (Recio-Spinoso *et al.*, 2005). A total of 193 files were obtained from the authors of this paper, as had originally been used by Shera (2007). Each file contains data of the mechanical BM click response at a fixed place. The 165^{th} file is initially chosen, which corresponds to the BM click response obtained around the place whose characteristic frequency is 9037 Hz. This file contains 256 samples for the time history of the BM click response.

Shera's estimate of the acoustic and synaptic transmission delay was 1.225 ms (Shera, 2007). Since the time interval between the two adjoining samples is 0.0227 ms, the number of

sampled due to the acoustic and synaptic transmission delay is $1.225/0.0227 \cong 54$. The most reasonable wavenumber distribution was, however, found to be derived with delays of 53 samples. Finally, 203 samples in total are kept for further use, as shown in Figure 5.2.

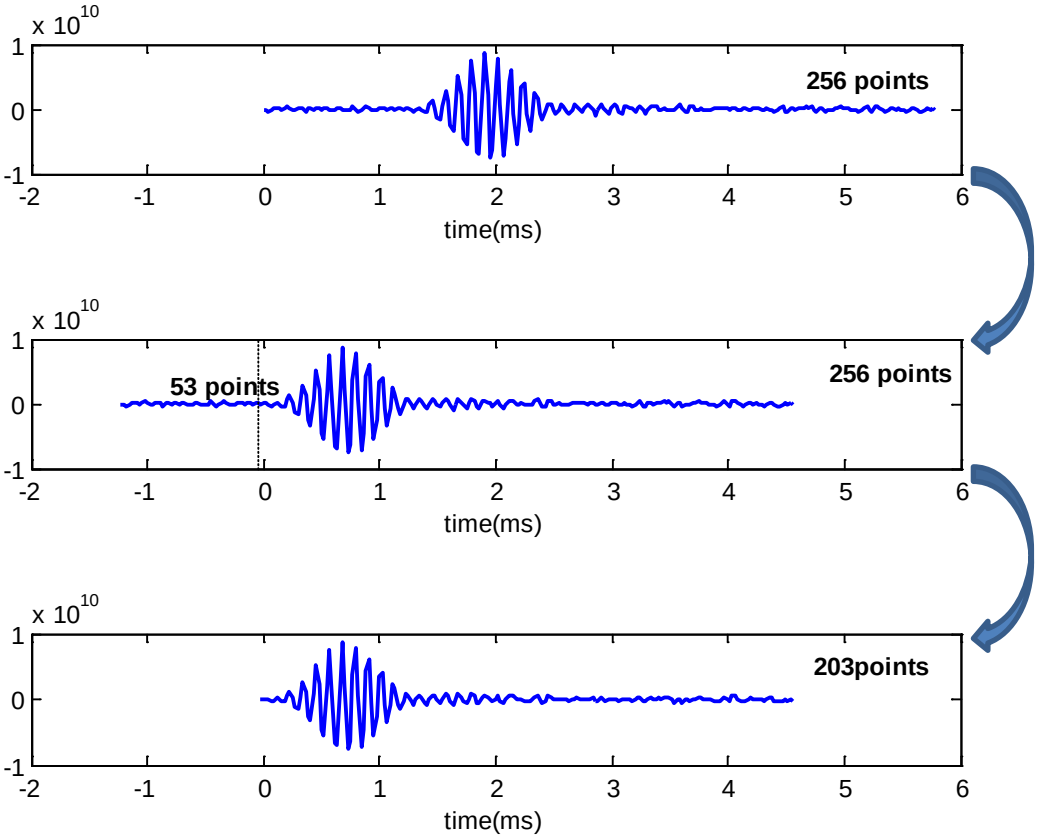

Figure 5.1 The mechanical BM click response $V_{BM}(x_0,t)$ at the cochlear location x_0 tuned to approximately 9 kHz in chinchilla in the time domain. Upper panel contains original data and lower panel contains rest data after removing data within the acoustic and synaptic transmission delays.

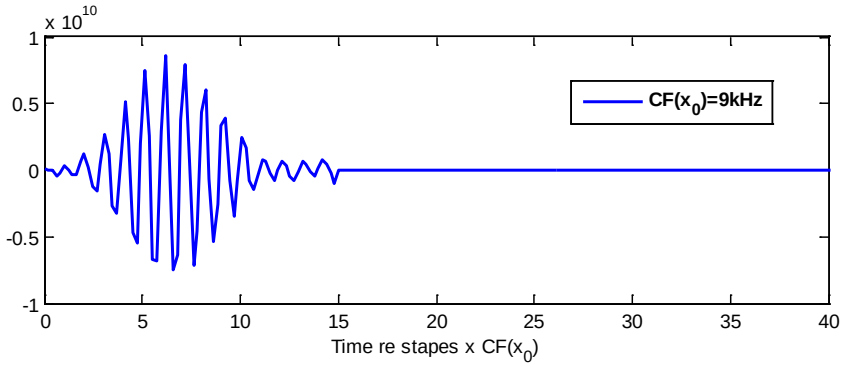

Figure 5.2 The mechanical BM click response used in this analysis, $V_{BM}(x_0,t)$, at the cochlear partition x_0 tuned to approximately 9 kHz in chinchilla (Recio-Spinoso *et al.*, 2005). The response estimate has been normalized by its peak value. Time, shown along the abscissa in units of the CF period as cycles, is measured relative to the approximate onset of stapes vibration by subtracting out estimates of acoustic and synaptic transmission delays amounting to a total of 1.225 ms (Temchin, *et al.*, 2005), and the result beyond 20 cycles is set to zero to reduce noise.

Initially, the BM response in the time domain is smoothed; this is achieved by setting the BM click response to zero after it is judged that the signal is negligible, which is after 15 cycles as shown in Figure 5.2, and then adding zeros to the response until it has 1024 points. The Fourier transform is then taken with a sampling resolution of the frequency domain data, 45 Hz, which is f_s / N_1, where $f_s = 1/0.0227 = 45$ kHz, $N_1 = 1024$.

Due to the symmetry of the Fourier transform, when the BM velocity is converted from the time domain to the frequency domain, only the half number of points is obtained, which gives only 512 points in the frequency domain. The local scaling for $V_{BM}(x_0, f)$ is then used to plot the results as a function of $f / CF(x_0)$, as illustrated in Figure 5.3.

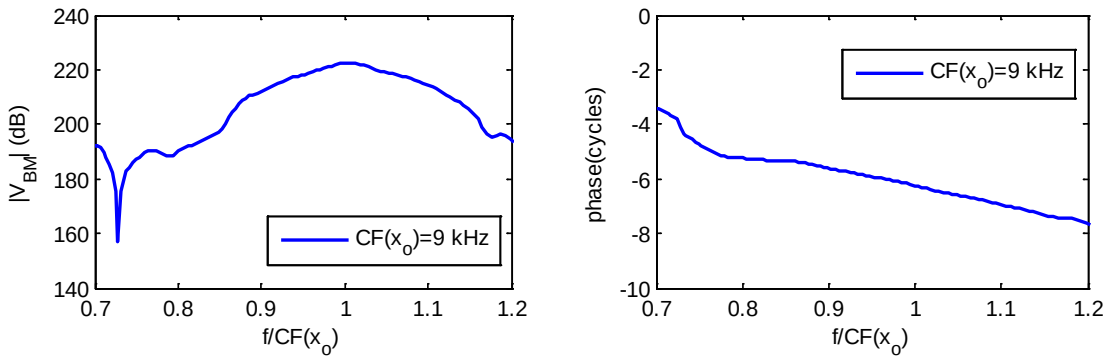

Figure 5.3 The amplitude and phase of the BM response are obtained from Fourier transform of $V_{BM}(x_0,t)$ and plotted against $f / CF(x_0)$.

The BM frequency response from the experiment at a fixed place can then be converted to that at a fixed frequency by logarithmically transforming from the frequency domain to the

spatial domain, and resampling those points. Initially, the BM velocity data is distributed uniformly from 165 Hz to 2.2 kHz and divided up into 512 parts linearly, the data is then re-sampled as a function of $f_o / CF(x)$ using the linear interpolation method to approximate the values of V_{BM} for non-given points, we assume that $CF(x) = f_{base} e^{-x/\ell}$, where f_{base} (20 kHz) is the natural frequency at the base of chinchilla cochlea, x is distributed uniformly along the cochlear partition from 0 mm to 18.4 mm by dividing it into 512 parts linearly, ℓ (3.8 mm) is the natural frequency length scale. The number of interpolated points depends on the range of the ratio of $f / CF(x_o)$ and the range of the ratio of $f_o / CF(x)$. In this case, the value of $f / CF(x_o)$ is from 0.0183 to 2.4344, which is divided by 512, the value of $f_o / CF(x)$ is from 0.4519 to 57.2656, which is divided by 1024, the selected values of $f_o / CF(x)$ should be in the range of $f / CF(x_o)$, therefore, 332 re-sampled points are derived. The real part, $\mathrm{Re}(\hat{k})$, and imaginary part, $\mathrm{Im}(\hat{k})$, of the estimated wavenumber, $\hat{k}$, can then be calculated using Shera's inverse method, as given by equation (2.22), and the results are shown in Figure 5.4.

These results are in broad agreement with those presented in Shera (2007) and show that the real part of the wavenumber increases along the cochlea, as the wave slows down, but the imaginary part goes from a positive value basal to CF, indicating that the wave is being amplified, to negative just before CF where the wave is being attenuated.

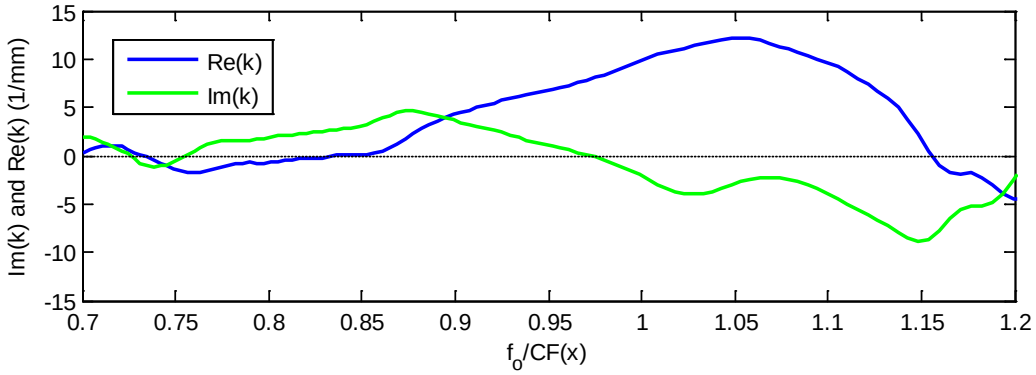

Figure 5.4 $\mathrm{Re}(\hat{k})$ and $\mathrm{Im}(\hat{k})$ are plotted against the generalized scaling variable, as were obtained by inversion of the estimate of $V(f_0 / CF(x))$ shown in Figure 5.3 (CF=9 kHz).

Figure 5.5 shows the amplitude and the phase of the BM response, $\hat{V}_{BM}$ reconstructed from the estimated wavenumber, using the WKB method, and it can be seen that $\hat{V}_{BM}$ and the measured response, V_{BM}, are in reasonable good agreement, as also observed by Shera (2009).

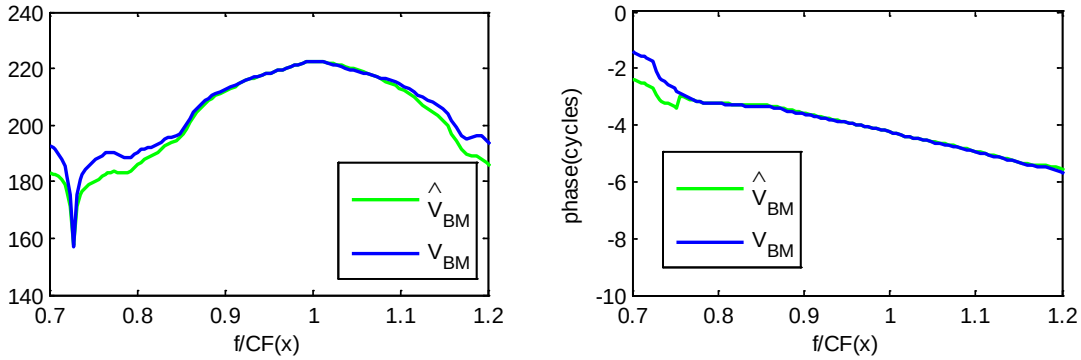

Figure 5.5 $\hat{V}_{BM}$ derived from $\hat{k}$ shown in Figure 5.4 using the WKB approximation (green solid line) and the original Wiener-kernel measurements (blue solid line) are plotted against local scale variable, as shown in Figure 5.3. An overall scale factor was determined by matching the data at the peak.

5.2. Sensitivity of the estimated results in Shera's inverse method

In this section, it is shown that although the estimated wavenumber distributions are somewhat sensitive to the assumed starting point of the impulse response, they do not depend strongly on the point of truncation in the time domain, and that consistant, but sparsely sampled distributions, are abtained if zero padding is not used.

5.2.1. Effect of start point

As discussed above, the number of sample that should be removed from the original measurement was originally assumed by Shera (2002) to be $1.225/0.0227 \cong 54$. In order to investigate the sensitivity of the results to this codition, the response was calculated starting at the 53^{th}, 54^{th} and 55^{th}.

Figure 5.6 shows the amplitude and phase of V_{BM} transformed from the time domain with different start points.

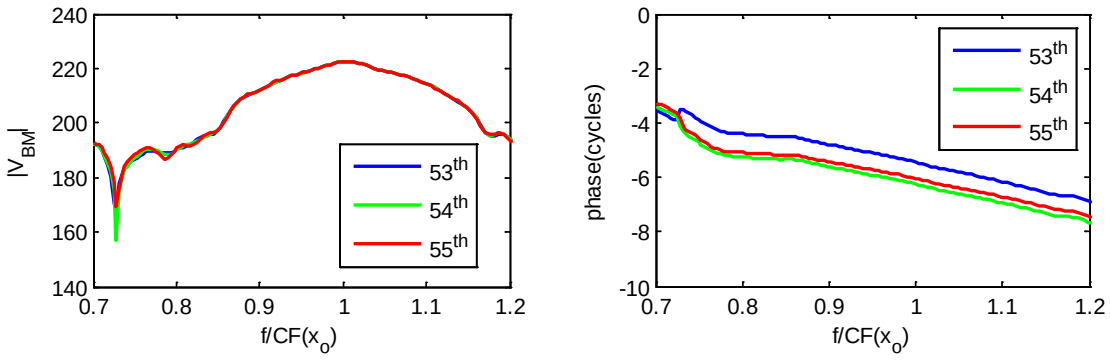

Figure 5.6 $V_{BM}(x_0, f)$, which has different delay points, is plotted against $f / CF(x_0)$ where CF (x_o) =9 kHz.

The inverse method is used to derive the distribution of Re($\hat{k}$) and Im($\hat{k}$) based on V_{BM} in the time domain with different start points, as shown in Figure 5.7. There appears to be quite a large variation in the Re($\hat{k}$) and Im($\hat{k}$) distributions for different starting points, although the amplitude and the phase of $\hat{V}_{BM}$ reconstructed from these wavenumber distributions, as shown in Figure 5.8, are all in reasonable agreement with V_{BM} for the three different of starting points. The sensitivity of the wavenumber distributions to this delay is a consequence of the ill-posed matter of the inverse problem involved in the estimation of $\hat{k}$.

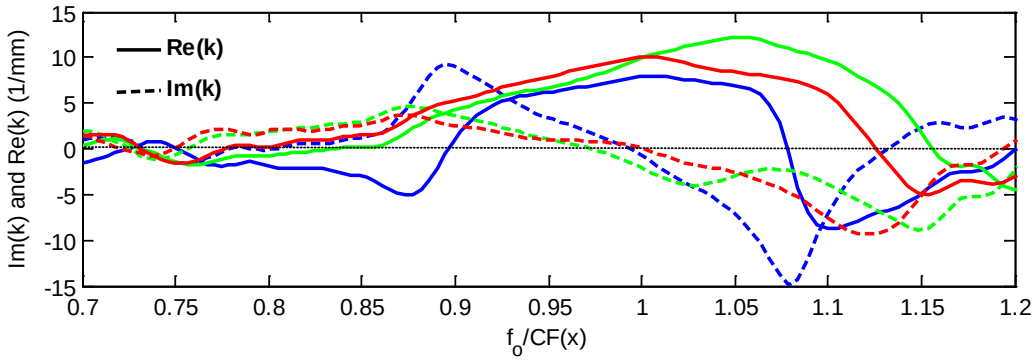

Figure 5.7 Re($\hat{k}$) and Im($\hat{k}$) for three different "delay points" derived from Fig 5.6. The data has been smoothed in time and frequency domain. Re($\hat{k}$) and Im($\hat{k}$) are plotted against the generalized scaling variable denoting by solid and dashed lines, respectively. The colours here correspond to those shown in Fig 5.6.

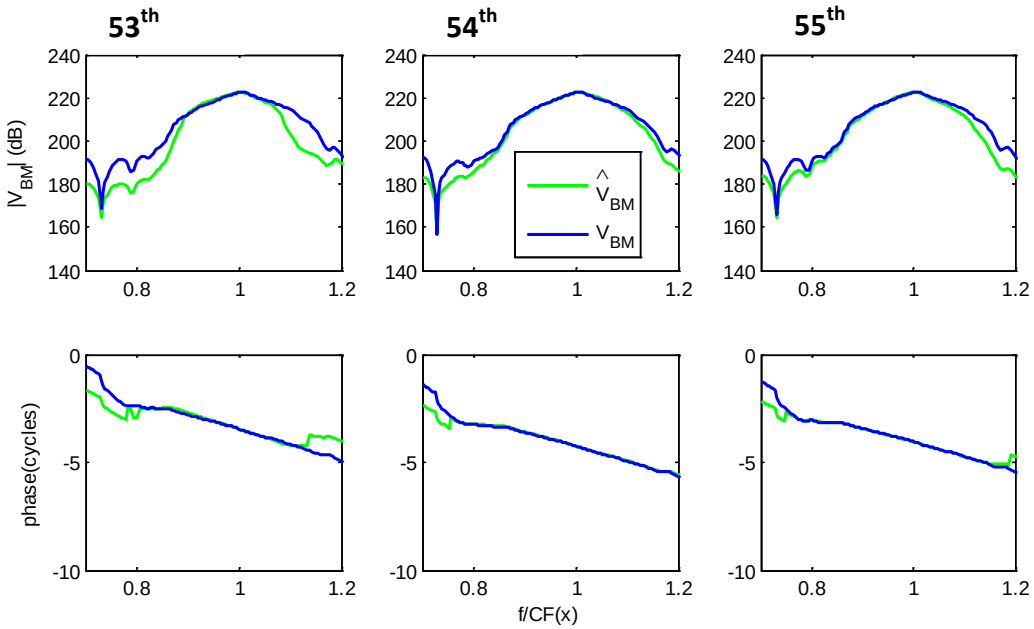

Figure 5.8 $\hat{V}_{BM}$ derived from $\hat{k}$ for three different "start points". using the WKB approximation (green solid line) and the original Wiener-kernel measurements (blue solid line) are plotted against local scale variable, as shown in Figure 5.6. $\hat{V}_{BM}$ was obtained from $\hat{k}$ in Figure 5.7. An overall complex scale factor was determined by matching the data at the peak.

5.2.2. Effect of truncation in the time domain

The BM click response above was set to be zero beyond 30 cycles in the time domain. In order to investigate the effect of truncation at different points, the truncation was systematically changed at 15, 20 and 30 cycles, respectively.

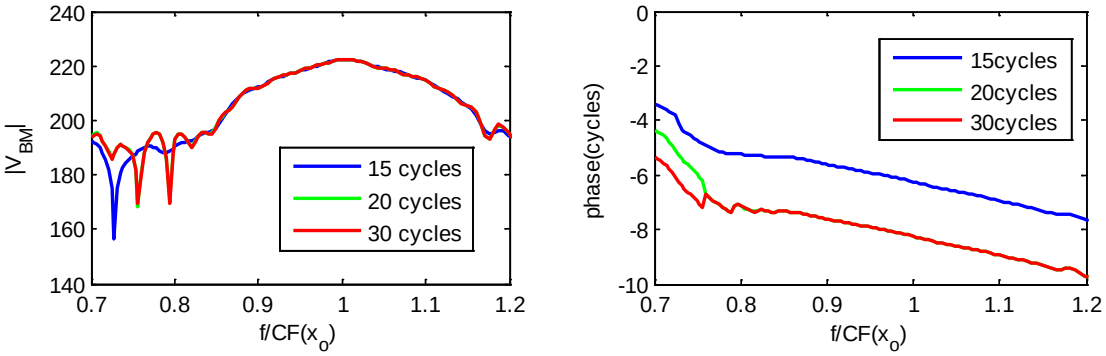

Figure 5.9 $V_{BM}(x_0, f)$, which has different truncation points, is plotted against $f / CF(x_0)$, where $CF(x_0)$=9 kHz.

Figure 5.9 shows that the magnitude of $V_{BM}(x_0, f)$ for different truncation points are almost the same around the peak, although there is some change in phase probably due to the

unwraping of noisy data. However, the estimated Re($\hat{k}$) and Im($\hat{k}$) are almost the same, as illustrated in Figure 5.10 below.

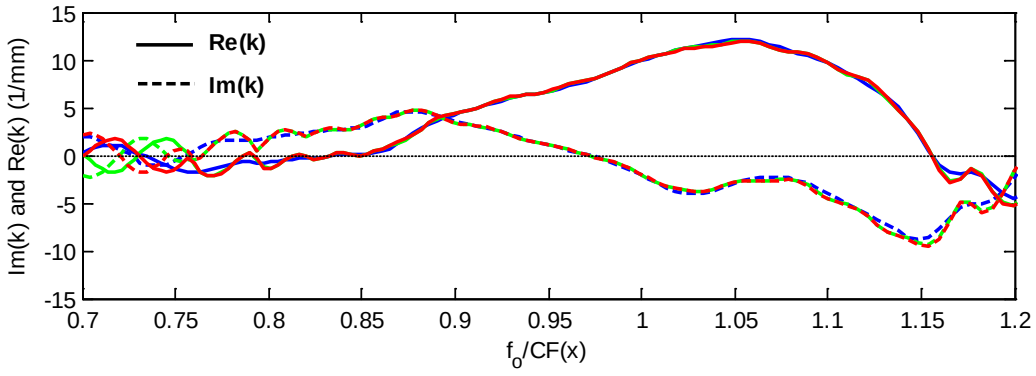

Figure 5.10 Re($\hat{k}$) and Im($\hat{k}$) for three different truncation points. The data has been smoothed in time and frequency domain. Re($\hat{k}$) and Im($\hat{k}$) are plotted against the generalized scaling variable denoting by solid and dashed lines, respectively.

Figure 5.11 shows that although the truncation points are different, good reconstructions of $\hat{V}_{BM}$ from the wavenumber distributions can again be derived.

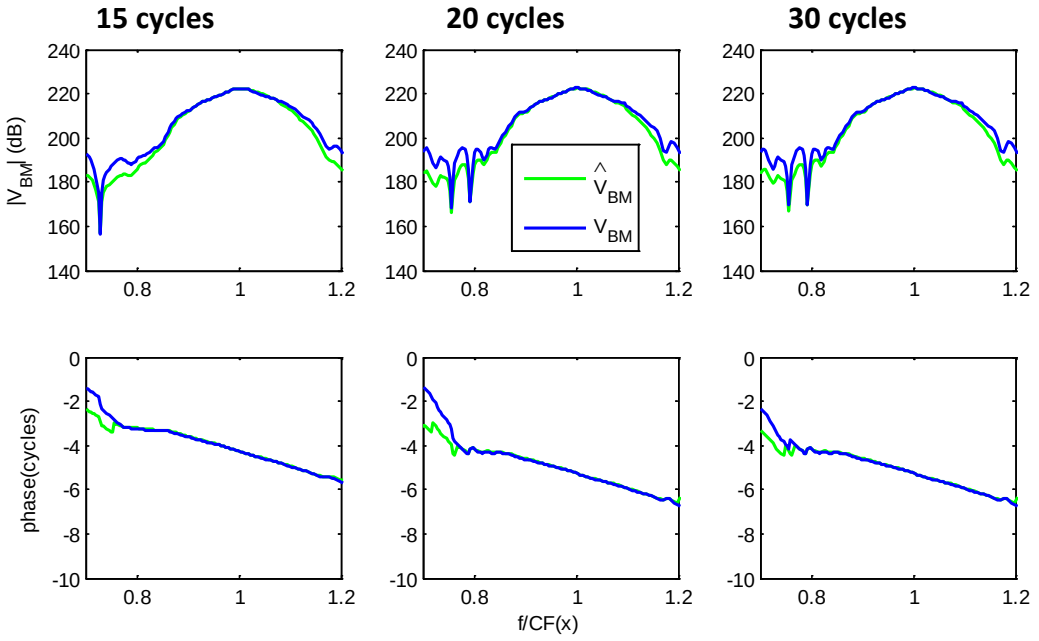

Figure 5.11 $\hat{V}_{BM}$ derived from $\hat{k}$ for three different truncation points. using the WKB approximation (green solid line) and V_{BM} (blue solid line) are plotted against local scale variable, as shown in Figure 5.9. $\hat{V}_{BM}$ was obtained from $\hat{k}$ in Figure 5.10. An overall complex scale factor was determined by matching the data at the peak.

5.2.3. Effect of zero padding the original measurement data

The original data in Figure 5.1 includes 203 sample points; if, instead of zero-padding, only these points are used to calculate the Fourier transform, and then the estimated $\mathrm{Re}(\hat{k})$ and $\mathrm{Im}(\hat{k})$ obtained using the inverse method are shown in Figure 5.12. Due to symmetry of Fourier transform, when V_{BM} is converted from the time domain to the frequency domain, only the half number of points is obtained, which gives only 102 points in the frequency domain. From Figure 5.12, it can be seen that the shape of the curves is similar to those in Figure 5.4, but the magnitudes are rather greater.

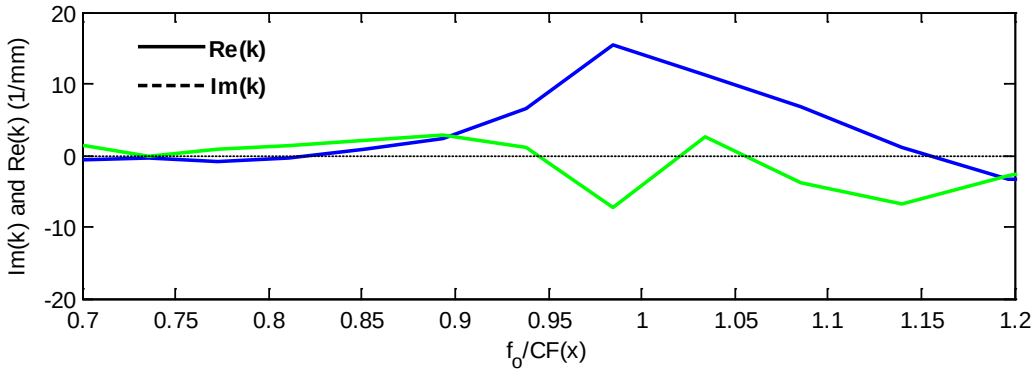

Figure 5.12 $\mathrm{Re}(\hat{k})$ and $\mathrm{Im}(\hat{k})$ using original measured data without smoothing process are plotted against the generalized scaling variable.

It can be seen from Figure 5.13 , however, that $\hat{V}_{BM}$ reconstructed from this wavenumber distribution is not in good agreement with V_{BM} in this case.

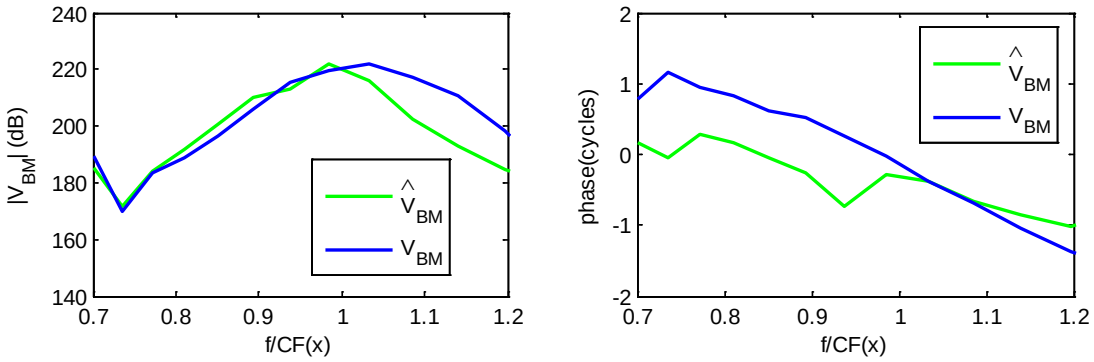

Figure 5.13 $\hat{V}_{BM}$ derived from the derived wavenumber, as shown in Figure 5.12.

5.3. Estimates of the wavenumber at different positions

The inversion and reconstruction procedures described above are now used on some of the other 193 near-threshold Wiener-kernel BM click responses supplied by Recio-Spinoso *et al.* (2005). The chosen BM positions are close to the characteristic places for frequency of 200 Hz, 500 Hz, 800 Hz, 1 kHz, 2 kHz, 5 kHz, 8 kHz, 9 kHz, 13 kHz and 15 kHz.

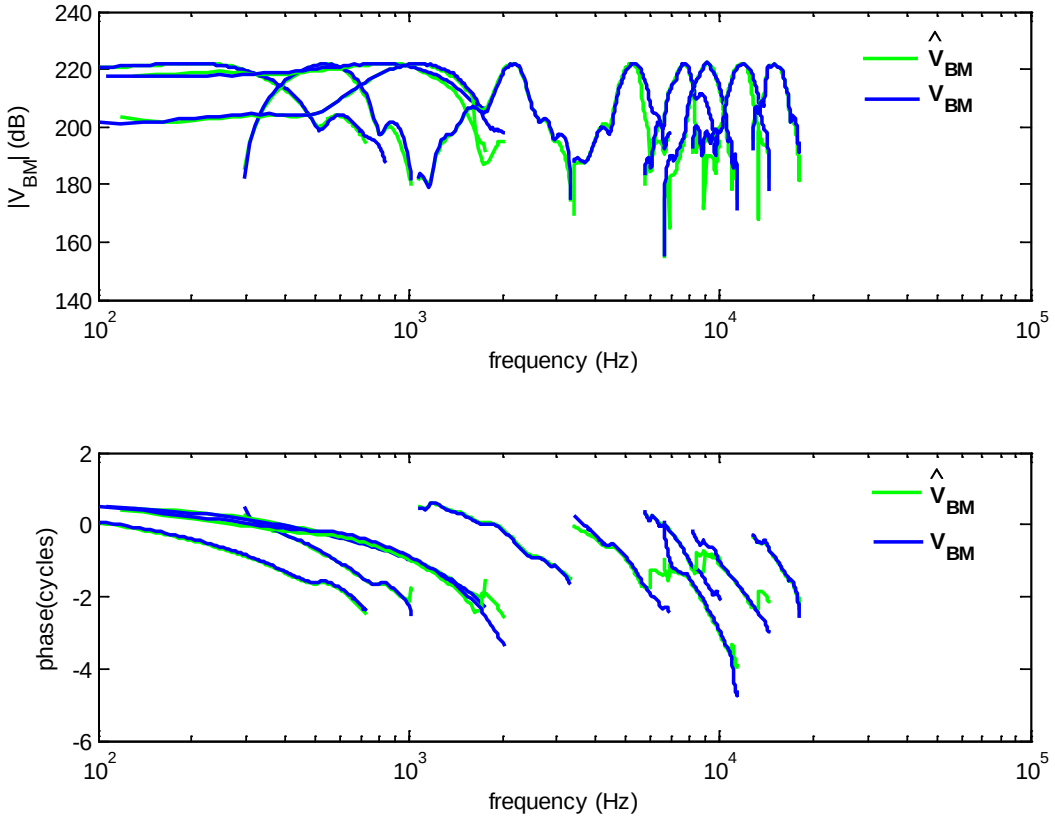

Figure 5.14 V_{BM} and $\hat{V}_{BM}$ derived from individual data sets of different locations throughout the chinchilla cochlea. Transfer functions are shown normalized to the same peak amplitude.

Figure 5.14 shows a generally good comparisons between some example V_{BM} responses and the reconstructed $\hat{V}_{BM}$, at different CFs places along the length of the chinchilla cochlea.

Figure 5.15 shows the wavenumber distributions Re($\hat{k}$) and Im($\hat{k}$) derived from nineteen individual Wiener-kernel estimates of V_{BM} together with their trend lines that capture the overall behaviour in the range 8-10 kHz. Other data sets for different positions on the cochlea can be found in Appendix F.

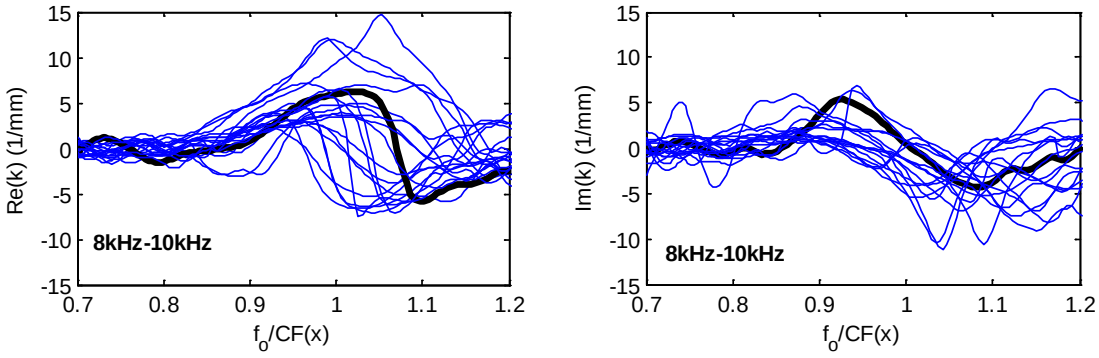

Figure 5.15 Re($\hat{k}$) and Im($\hat{k}$) derived from all nineteen Wiener kernels with CFs in the range 8-10 kHz. Blue lines shows individual functions Re($\hat{k}$) and Im($\hat{k}$); black lines show rends obtained by selecting a line that can shows the mean behaviour roughly.

The frequency range from 100 Hz to 20 kHz spans the whole length of the cochlea for chinchilla (Greenwood, 1990). This frequency span has been divided up into five sets of frequencies, which are 100 Hz to 2 kHz, 2 kHz to 5 kHz, 5 kHz to 8 kHz, 8 kHz to 10 kHz, 10 kHz to 15 kHz, respectively. Different groups have different number of Wiener kernels,but those judged to be typical distributions are chosen in each case, as shown in Figure 5.16, which are in broad agreement with the results shown in Figure 7 of Shera (2007).

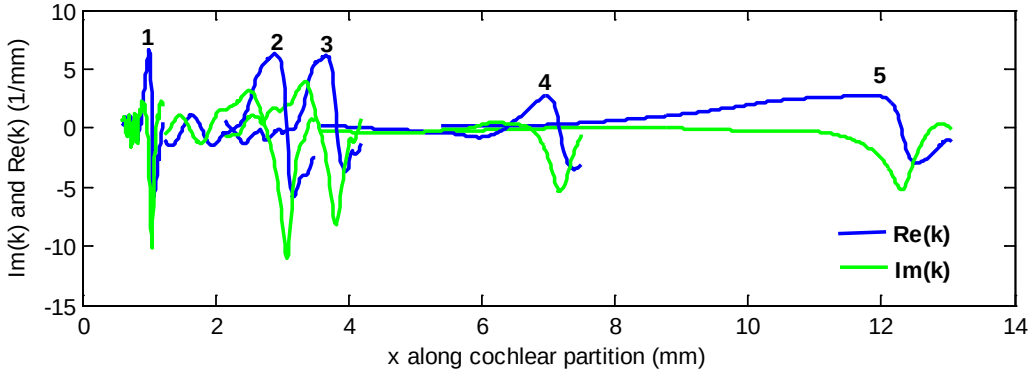

Figure 5.16 Re($\hat{k}$) and Im($\hat{k}$) trends throughout the cochlea. The figure shows trend functions Re($\hat{k}$) and Im($\hat{k}$) at five positions, x_n, spanning the cochlear partition. The satisfied Wiener Kernels were binned into five groups, with the bin edges of {16, 10, 8, 5, 2, 0.1} kHz. '1' for 10-16 kHz, '2' for 8-10 kHz, '3' for 5-8 kHz, '4' for 2-5 kHz, '5' for 0.1-2 kHz. Trend functions were derived by selecting a line that can shows the mean behaviour roughly in each group. The results are plotted on a spatial axis.

5.4. Estimates of wavenumber at different sound levels

Of the total of 193 Wiener kernels available, some have been collected at the same place but at different sound pressure level. The original data and Fourier transform of the original data

in these cases for different locations along the BM are shown in Appendix G. An example is shown in Figure 5.17.

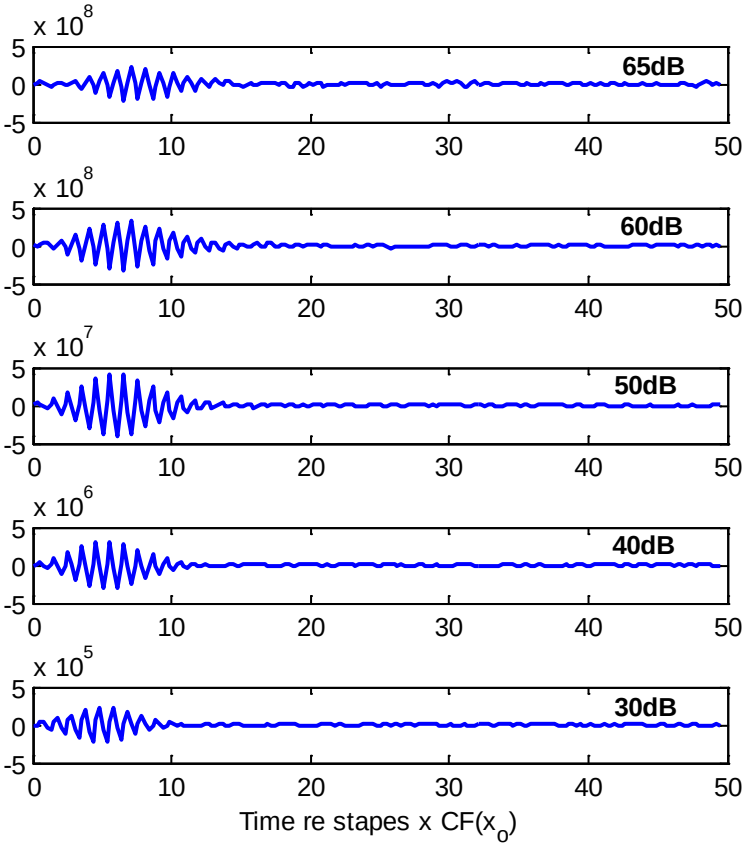

Figure 5.17 auditory-nerve based estimate of the BM click response, $V_{BM}(x_0,t)$, at the cochlear partition x_0 tuned to approximately 12 kHz in chinchilla at different sound pressure levels (SPLs), 65, 60, 50, 40 and 30 dB, respectively. Time, shown along the abscissa in units of the CF period, is measured relative to the approximate onset of stapes vibration by subtracting out estimates of acoustic and synaptic transmission delays amounting to a total of 1.225 ms.

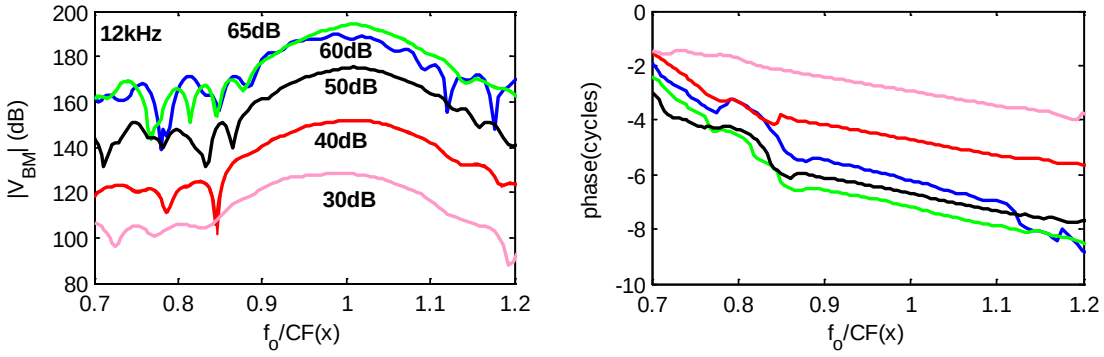

Figure 5. 18The amplitude and phase of V_{BM} at a fixed frequency are converted from them at a fixed position ($CF(x_0)$=12 kHz), which are obtained from Fourier transform of $V_{BM}(x_0,t)$ and plotted against $f_0/CF(x)$ at different SPLs of 65, 60, 50, 40 and 30 dB, respectively.

The wavenumber distributions have then been calculated at the same place but at both low and high levels, in order to try to investigate the variation in Re($\hat{k}$) and Im($\hat{k}$) from the active cochlea to the passive cochlea, with the results shown in Figure 5.19. The calculated Re($\hat{k}$) and Im($\hat{k}$) functions for 9 different CFs can be found in Appendix G. It is difficult to discern any particular trend with level on any of them, so that only one set, f_0=12.1 kHz, is shown here in Figure 5.19.

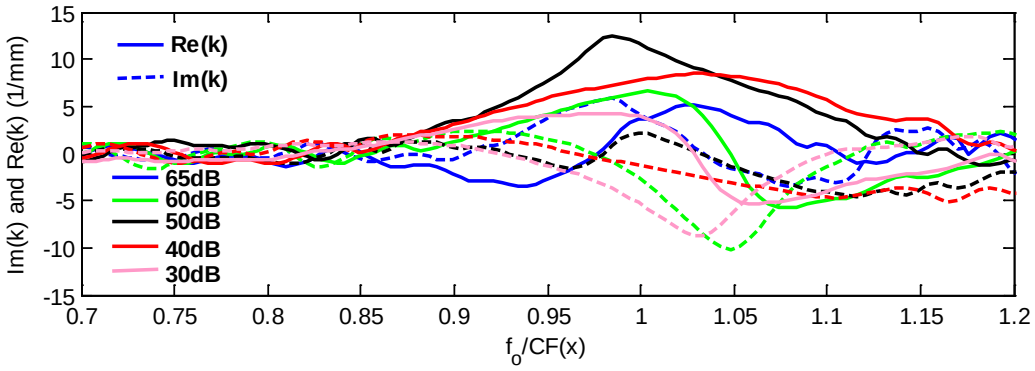

Figure 5.19 Re($\hat{k}$) and Im($\hat{k}$) are plotted against the generalized scaling variable using solid (propagation) and dash (gain) lines, respectively, the functions Re($\hat{k}$) and Im($\hat{k}$) were obtained by using the inverse method at the certain frequency place, which is 12.102 kHz, for different SPLs of 65, 60, 50, 40, 30 dB, respectively. $CF(x) = f_B e^{-x/\ell}$ where f_B =20 kHz, x=18.4 mm, ℓ =3.8 mm (the 183th, 184th, 185th, 186th, 187th files are selected).

There does not appear to be any systematic change in the wavenumber distributions with excitation level. This is rather surprising, since one might expect Re($\hat{k}$) to be higher at the lowest levels, when the cochlea is most active. The original impulse response data, does not, however, show the expected changes with level, as described by Robles and Ruggero (2001) for example, and so must be considered somewhat suspect.

5.5. The "direct" inverse method with measured chinchilla data

Details of the "direct" inverse method, tested with passive and active cochlear models, have been described in Chapter 2 and Chapter 4, respectively. Here, the chinchilla data, is used to derive the estimated parameters using the direct inverse method. The estimate of the BM click response at the position corresponding to a characteristic frequency of 9 kHz of the chinchilla cochlea as shown in Figure 5.3, is initially used. Since auditory nerve fibre instead of mechanical vibration is measured here, the absolute level of this response is unknown so that the scaling parameter m_0 cannot be physically interpreted. The BM frequency response,

V_{BM} , must again be transformed from the frequency domain to the space domain using the known distribution of characteristic frequency. Then the two objectives optimization, which is called *gamultiobj-Multiobjective optimization using Genetic Algorithm* in MATLAB Toolbox, is used to derive the parameters of the estimated model, whose response is shown in Figure 5.20. A two degrees of freedom model is assumed for the micromechanics.

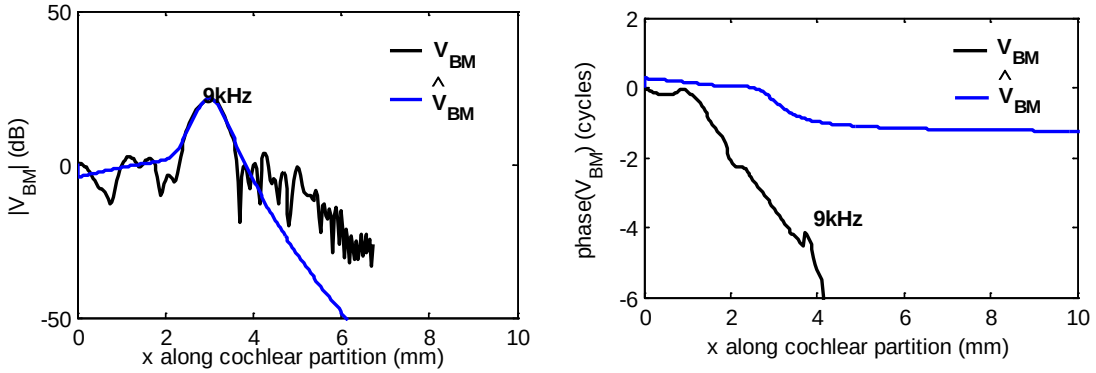

Figure 5.20 Amplitude and phase of the "measured" BM response, V_{BM} , for the Chinchilla data, and the estimated BM response, $\hat{V}_{BM}$, distribution along cochlear partition at CF(x_0)=9 kHz for the Chinchilla. The relative optimized parameters are given in Table 5.1.

It is seen from the left panels of Figure 5.20 that the amplitude of $\hat{V}_{BM}$ is fitted reasonably well around peak area; however, the phase of $\hat{V}_{BM}$ is much less than V_{BM} .

The two objectives optimization was also been used to fit for the response measured at different characteristic positions, $CF(x_0)$, using the same procedure, and the results are shown in Figure 5.21.

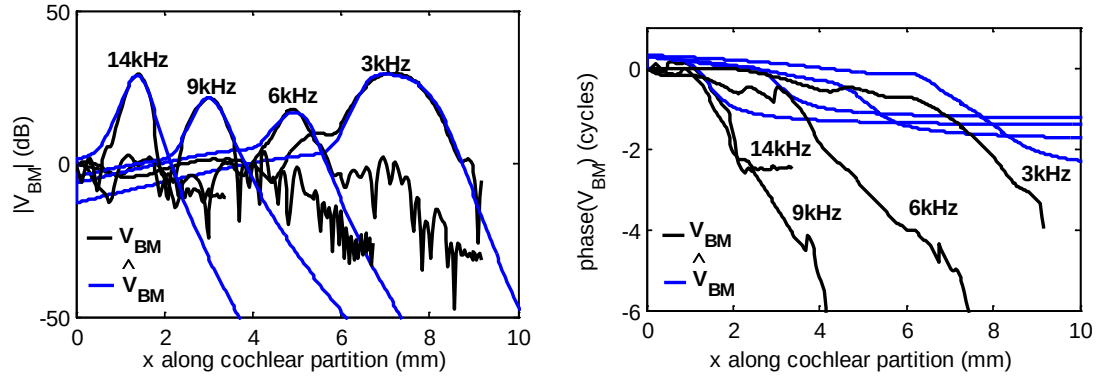

Figure 5.21 Amplitude and phase of V_{BM} for the Chinchilla data and $\hat{V}_{BM}$ distribution along cochlear partition at CF(x_0)=3, 6, 9, and 14 kHz, respectively for chinchilla. The optimized parameters are given in Table 5.1.

Figure 5.21 shows similar results to those in Figure 5.20: the amplitude of $\hat{V}_{BM}$ with two objectives optimization is fitted well around the peak are, but the phases of $\hat{V}_{BM}$ are still much less than V_{BM}, perhaps due to phase wrapping problems with the noise data from the original data.

The properties of the poles and zeros of the micromechanical models fitted to the measured data are also given in Table 5.1. It is interesting to note that the normalised natural frequency of the zero, Ω_1, is below the natural frequency of the two poles, Ω_2 and Ω_3, in all these cases, as was also observed in the simulations with the active Neely & Kim model. The positions of the two poles are also rather close together for the low level results at 9 kHz and 14 kHz, as previously seen in the model of Mandal (2009). The normalised mean square error for these results is relatively high, but the pole-zero model appears to capture the main features of the measured response.

Table 5.1 The optimized parameters for the zero, Ω_1 and Q_1, and the poles, Ω_3, Ω_3, Q_2 and Q_3 of the micromechanical model obtained for selected chinchilla data, together with the normalised mean square error, NMSE, for amplitude and phase.

Condition		Ω_1	Q_1	Ω_2	Q_2	Ω_3	Q_3	m_0	NMSE Amplitude	NMSE phase
Measurement Data Chinchilla CF(x_0)	3 kHz 40dB	0.69	4.48	0.84	4.69	1.34	2.61	0.24	0.0086	1.976
	6 kHz 50dB	0.90	4.78	1.19	4.17	0.97	3.21	0.44	0.086	1.959
	9 kHz 60dB	0.81	4.83	0.99	3.77	0.99	4.06	0.75	0.017	1.101
	14 kHz 40dB	0.81	4.52	1.02	4.73	1.01	4.03	0.42	0.017	1.578

The variation of the estimated BM admittance, $\hat{Y}_{BM}(x)$, can be calculated from the derived pole and zero parameters, using equation (2.25), and hence the wavenumber can also be calculated using equation $k(x) = \sqrt{-\frac{2i\omega\rho}{h} Y_{BM}(x)}$, where h is the effect chamber height of cochlea. Using the optimized parameters obtained for the results shown in Figure 5.20, the variation of wavenumber has been calculated and is shown in Figure 5.22.

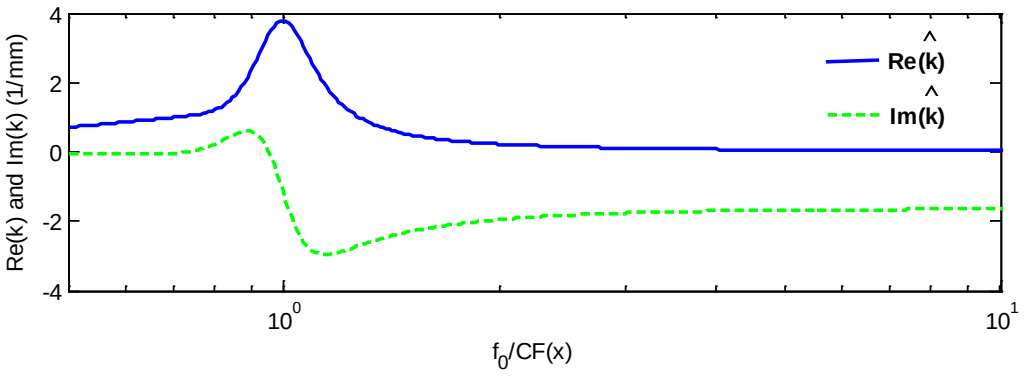

Figure 5.22 Re($\hat{k}$) and Im($\hat{k}$) are plotted against the generalized scaling variable using solid and dashed lines, respectively, the functions Re($\hat{k}$) and Im($\hat{k}$) were obtained using the optimized parameters in Figure 5.20 and wavenumber equation (just described above). (CF=9 kHz)

The wavenumber distributions are similar to those seen in Figure 5.4, derived using Shera's inverse method, with Re($\hat{k}$) increasing to a peak at the characteristic frequency ($f_0 / CF(x) = 1$), and then decreasing, while Im($\hat{k}$) is initially positive, below *CF* indicating an active behaviour, and then becomes negative.

5.6. The "direct" inverse method using mouse data

5.6.1. The mouse data

Four recent sets of measured BM response in the mouse Lee et al (2015) are used here to derive the estimated parameters at different excited locations. These are measured using volumetric optical coherence tomography vibrometry, a technique that overcomes some limitations of previous methods (including the fact that the cochlea does not need to be opened, which may alter its function and affect the findings) by providing depth-resolved displacement measurements at up to 200 kHz inside a 3D volume of tissue with picometer sensitivity with the unopened cochlea (Lee et al, 2015).

Initially, the four sets of mouse data at different excitation levels and measurement positions along the cochlea are used, obtained from the supplementarily measured in Lee *et al.* (2015), as shown in Figure 5.23 and Figure 5.24. Those are plotted as sensitivity ratios, which are the ratio of the BM velocity to the stapes velocity.

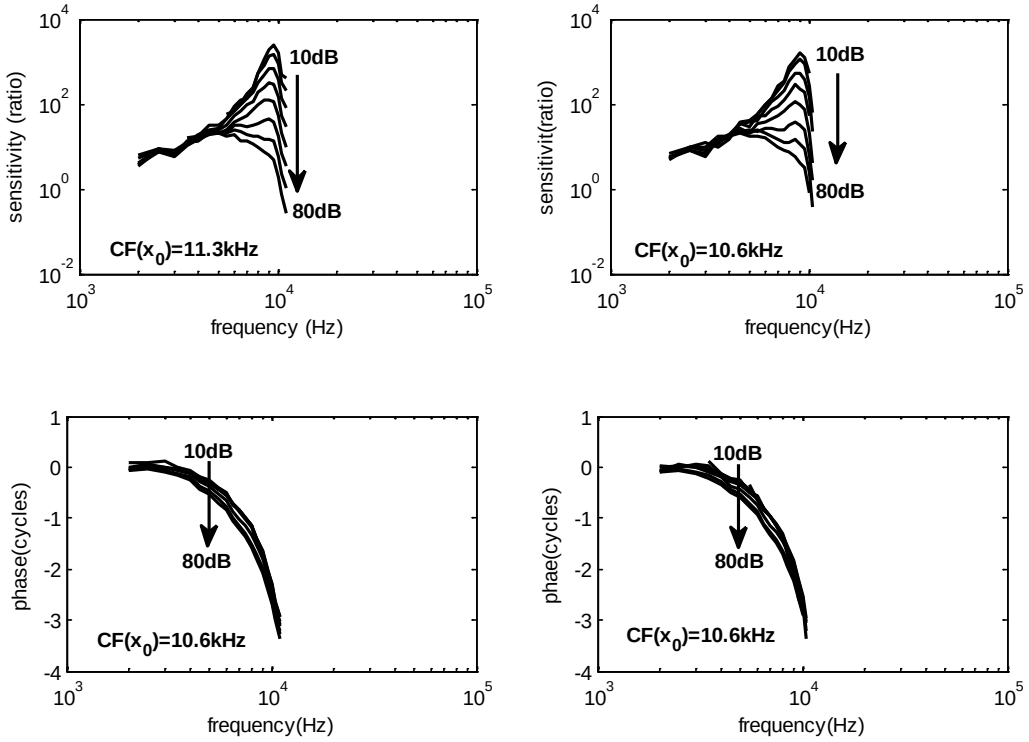

Figure 5.23 Sensitivity ratios (the displacement of the BM divided by the displacement of the middle ear ossicular chain) and phase measurements of the BM responses at CF(x_0) =11.3, 10.6 kHz. from SPLs of 10 dB to 80 dB.

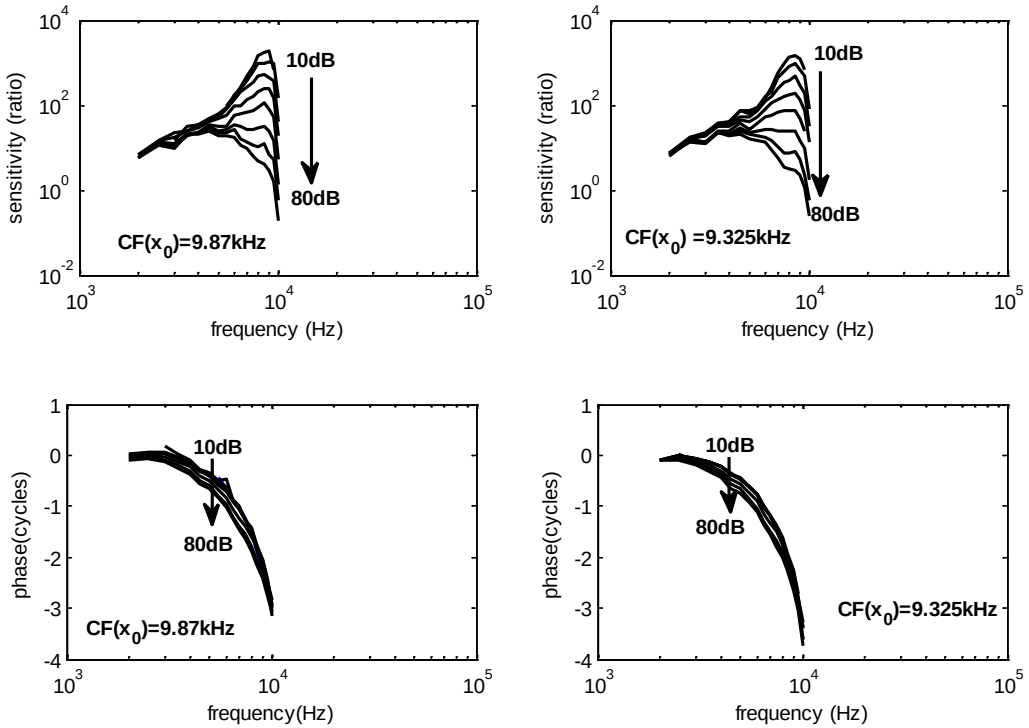

Figure 5.24 Sensitivity ratios (the displacement of the BM divided by the displacement of the middle ear ossicular chain) and phase measurements of the BM responses at CF(x_0)=9.87, 9.325 kHz. from SPLs of 10 dB to 80 dB.

The transformation from the frequency domain to the spatial domain has been performed here using Shera's method, as described above. The transformed results as a function of position along the cochlea, obtained using the frequency–place map for the mouse described in Chapter 2, are shown in Figure 5.25 and Figure 5.26.

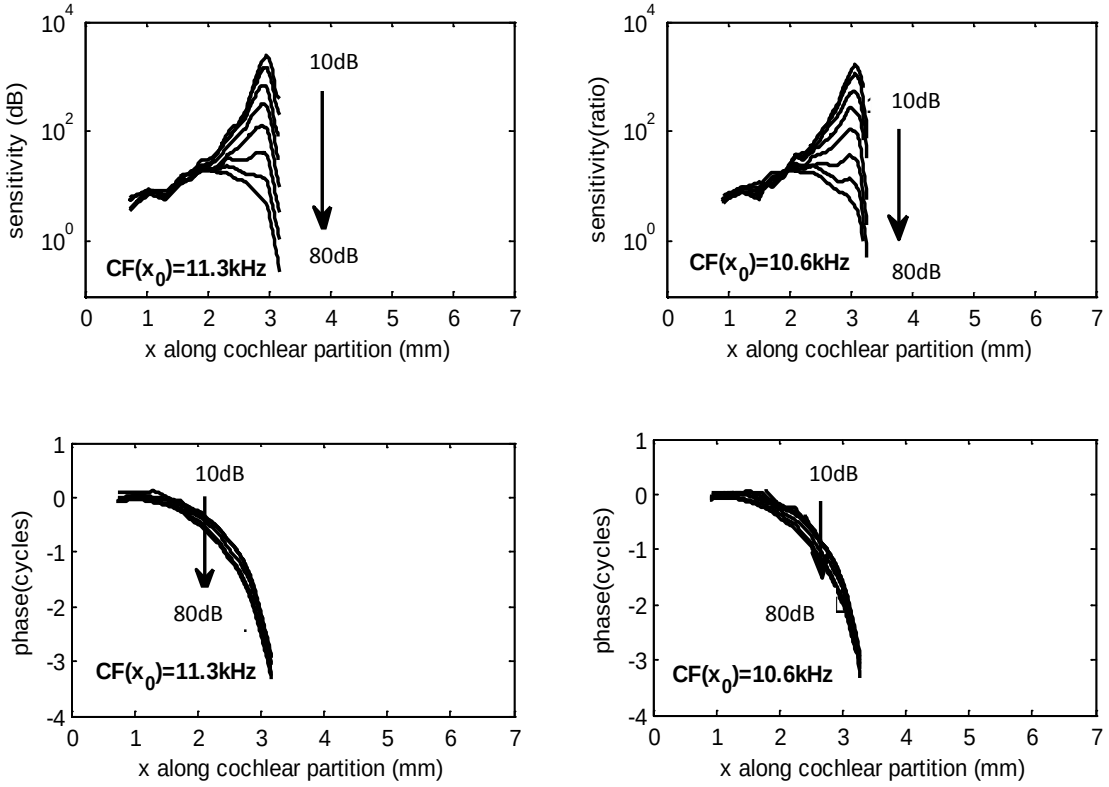

Figure 5.25 Sensitivity ratios (the displacement of the BM divided by the displacement of the middle ear ossicular chain) and phase measurements of the BM responses in the spatial domain transformed from BM responses in the frequency domain at CF(x_0)=11.3, 10.6 kHz. from SPLs of 10 dB to 80 dB.

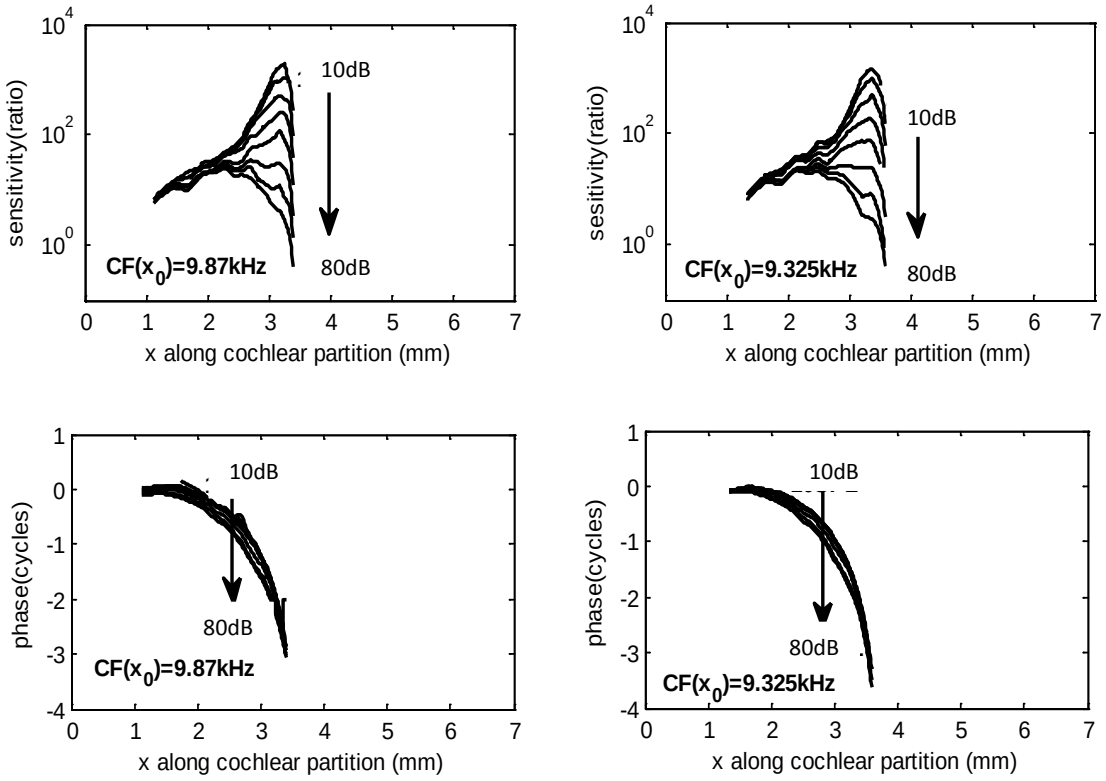

Figure 5.26 Sensitivity ratios (the displacement of the BM divided by the displacement of the middle ear ossicular chain) and phase measurements of the BM responses in the spatial domain transformed from BM responses in the frequency domain at CF(x_0)=9.87, 9.325 kHz. from SPLs of 10 dB to 80 dB.

5.6.2. Fitting the active response

The 1D uniform box model of active cochlea is used with the direct inverse method, optimized with two objective functions. The procedure of selecting the relatively reasonable estimated parameters is shown from Figure 5.27 to Figure 5.33. Based on the experiment data at CF(x_0)= 9.325 *kHz*, the estimated results at other characteristic positions also follow this selection method.

It can be seen in Figure 5.27 that the estimated NMSEs of phase are over 1 at SPLs of 10, 20, 30, 50 and 70 dB, which lead not to be in agreement with the mouse, but the estimated NMSEs of amplitude are always in a reasonable range. Therefore, three particular points in those pareto distributions are selected, it shows that black circles stand for the lowest value of NMSE for amplitude, while the highest value of NMSE for phase, green circles stand for the relatively reasonable values of NMSE for both of amplitude and phase, red circles stand for the lowest value of NMSE for phase, while the highest value of NMSE for amplitude, the estimated results using those points can be compared to decide the relatively best point.

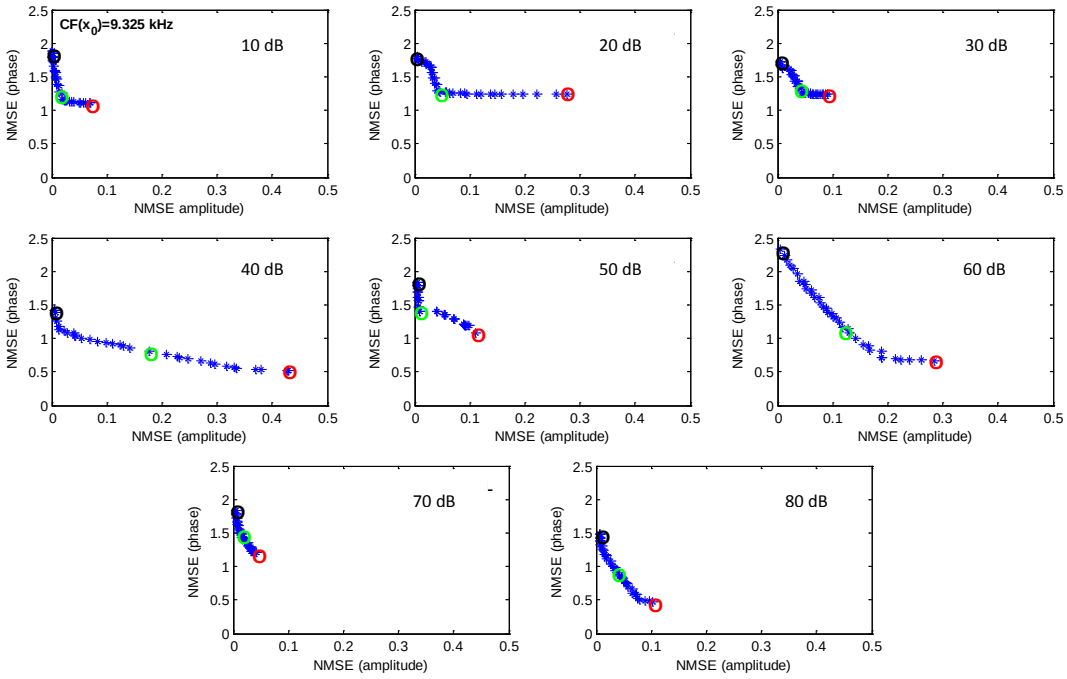

Figure 5.27 The values of normalised mean square error in the amplitude and the phase plotted at 9,325 *kHz* with SPLs of 10, 20, 30, 40, 50, 60, 70 and 80 dB in the 1D uniform box model of active cochlea for the population of solutions obtained using multi-objective optimization. The solution that is judged to give the best results is circled. Black cicles: the least value of NMSE for amplitude. Green circles: the relatively reasonable value of NMSE for both of amplitude and phase. Red circles: the least value of NMSE for phase.

For selecting the most reasonable parameters, initially, the estimated parameters are selected based on the smallest values of NMSE for phase, the red circles shown in Figure 5.27, at each SPL. It can be shown in Figure 5.28 that although the phases of the estimated results are in agreement with the measured data, the amplitudes of the estimated results are not in agreement with the measured data expect for the estimated results at SPL of 10 dB, those estimated amplitudes can not reach the peak of the measured data or have some gaps compared with the measured data.

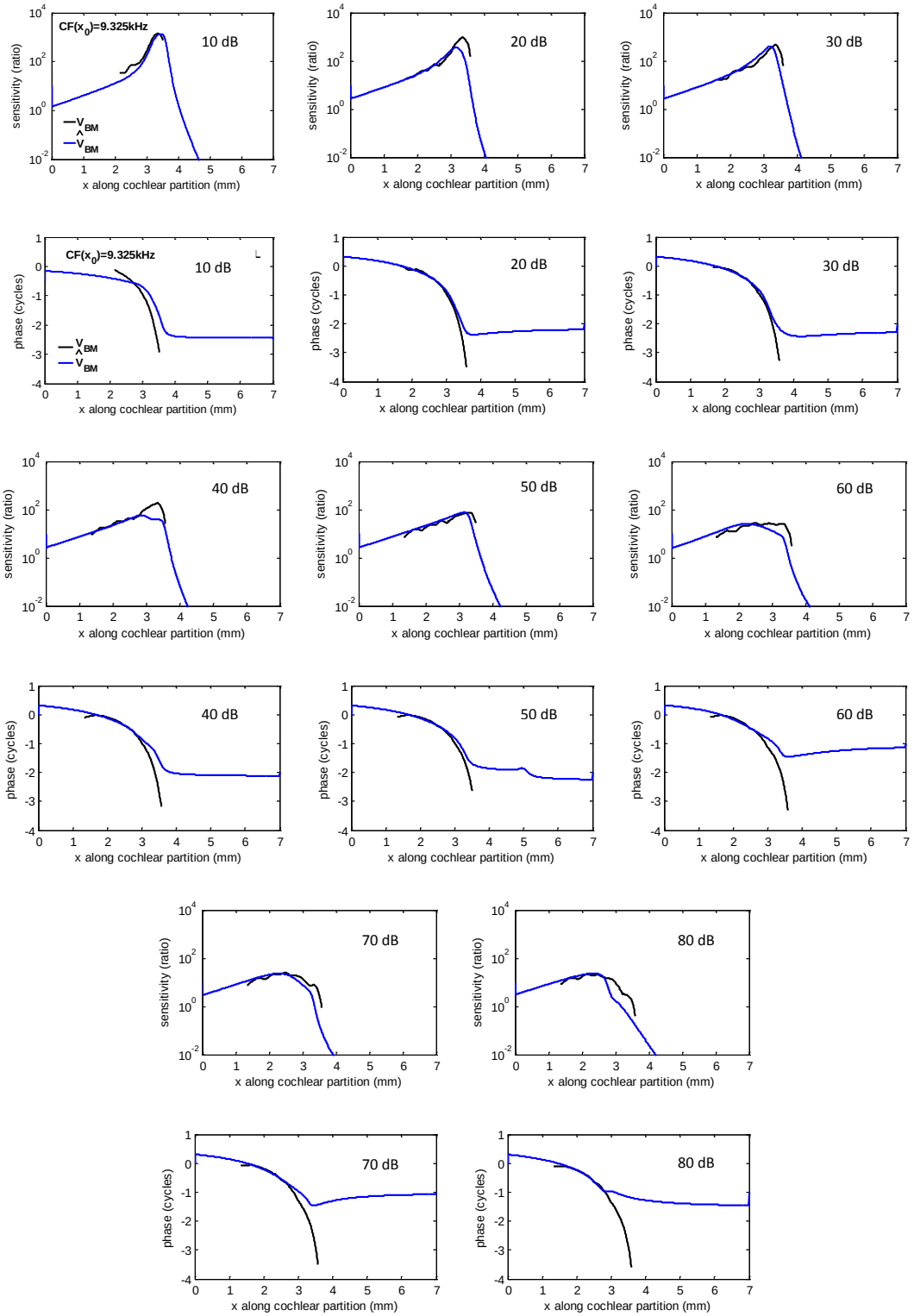

Figure 5.28 Comparison of amplitudes and phases of the BM responses measured by Lee *et al.* (2015) for a CF of 9.325 kHz and SPLs of 10, 20, 30, 40, 50, 60, 70 and 80 dB, black line, and the responses of a model with second order micromechanics and 1D uniform fluid coupling, obtained using multi-objective optimization to identify the micromechanical poles and zeros, blue lines. The estimated data selected are based on the smallest value of NMSE for phase.

Then, the estimated parameters are selected based on the relatively small values of NMSE for both of amplitude and phase, the green circles shown in Figure 5.27. It can be also seen in Figure 5.29 that the phase of the estimated results are again in reasonable agreement with the measured data, while the amplitudes of the estimated results are still not in agreement with the measured data except for the estimated results at SPLs of 10 dB and 30 dB, those estimated amplitudes also can not reach the peak of the measured data to have some gaps compared with the measured data.

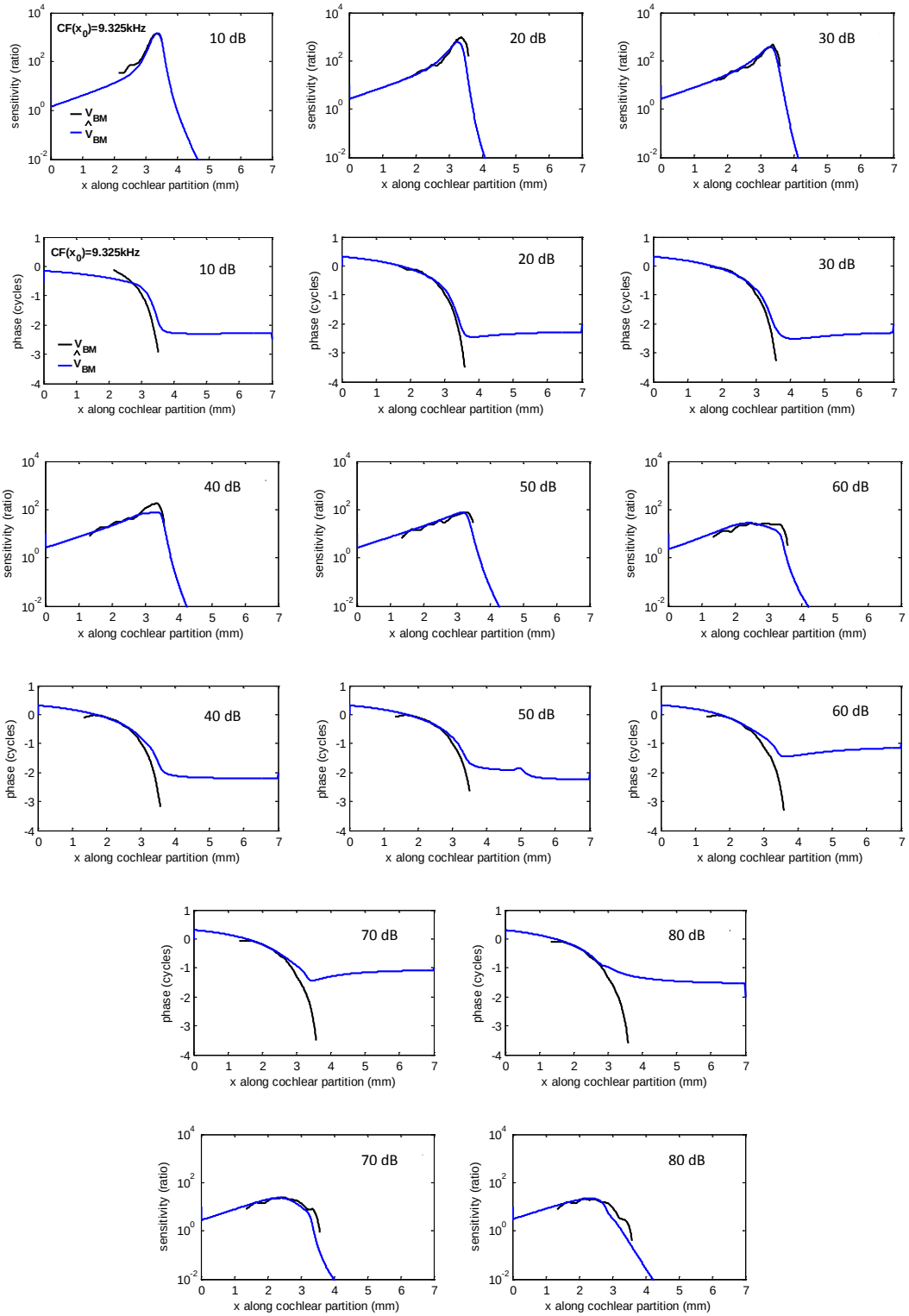

Figure 5.29 Comparison of amplitudes and phases of the BM responses measured by Lee *et al.* (2015) for a CF of 9.325 kHz and SPLs of 10, 20, 30, 40, 50, 60, 70 and 80 dB, black line, and the responses of a model with second order micromechanics and 1D uniform fluid coupling, obtained using multi-objective optimization to identify the micromechanical poles and zeros, blue lines. The estimated data selected are based on the relatively the reasonable value of NMSE for both of amplitude and phase.

Finally, the estimated parameters are selected based on the smallest value of NMSE for amplitude, the black circles shown in Figure 5.27, at each SPL. It can be shown in Figure 5.30.that the amplitudes of the estimated results are in much better agreement with the measured data, although the phases of the estimated results at some SPLs are worse that the previously estimated results using green circles or red circle shown in Figure 5.27, for instance, the estimated results at SPLs of 50, 60, 70 , 80 dB.

According to the analysis of the estimated results, the estimated parameters based on the smallest value of NMSE for amplitude, the black circles shown in Figure 5.27, should be chosen, because the estimated amplitudes are in so good agreement with the measured data and the estimated phases are reasonably fitted with the measured data. The estimated parameters with the amplitude and phase of NMSE are listed in Table 5.2. This selection method is also used in the following cases. Those estimated results are as similar as the results by Wang *et al.* (2016), their estimated results are also in agreement with the measured data, while the phase is fitted badly with the measured data, but the direct inverse method improve those estimated results, which means the estimated phases are reasonably fitted with the measured data.

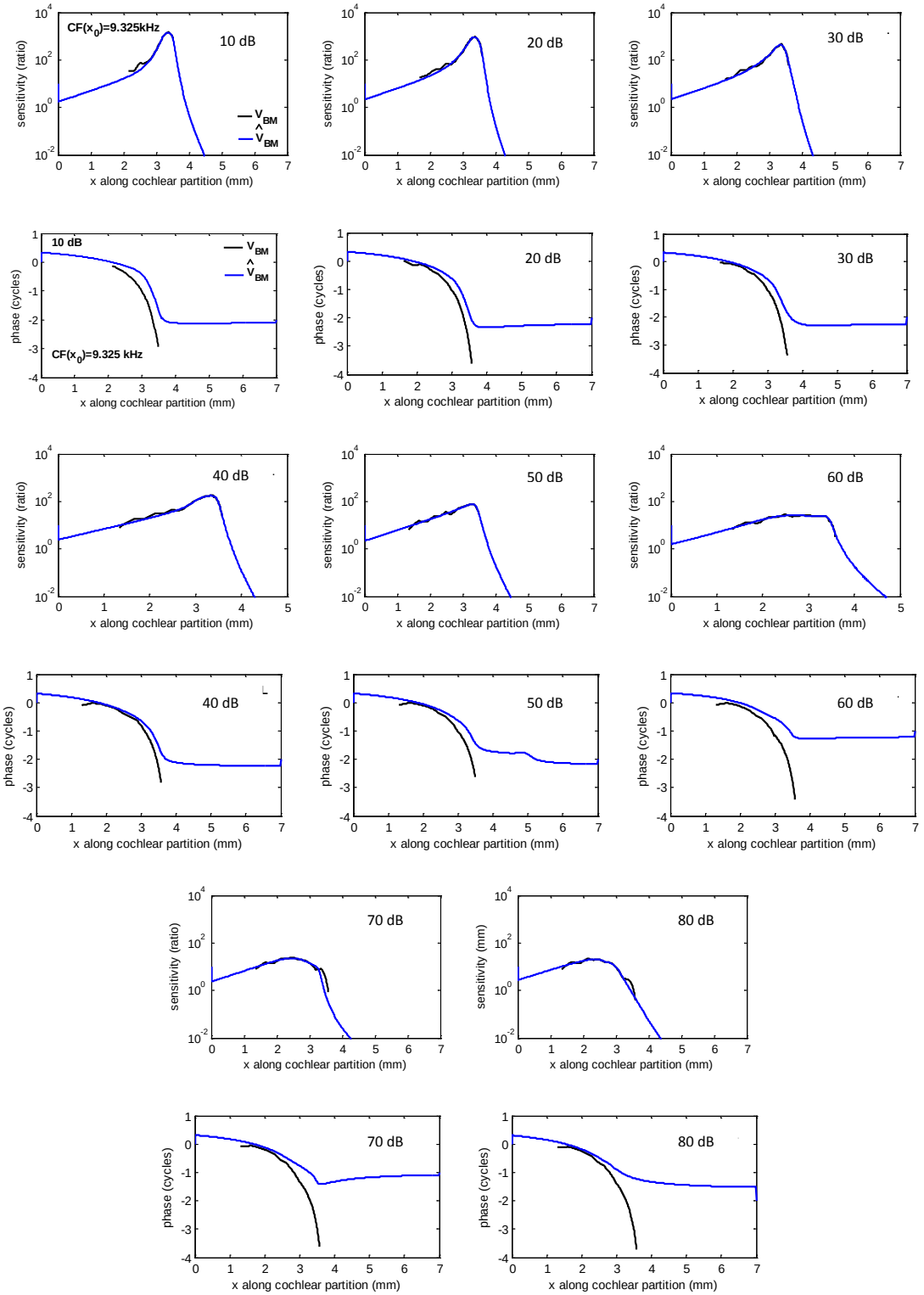

Figure 5.30 Comparison of amplitudes and phases of the BM responses measured by Lee *et al.* (2015) for a CF of 9.325 kHz and SPLs of 10, 20, 30, 40, 50, 60, 70 and 80 dB, black line, and the responses of a model with second order micromechanics and 1D uniform fluid coupling, obtained using multi-objective optimization to identify the micromechanical poles and zeros, blue lines. The estimated data selected are based on the smallest value of NMSE for amplitude.

It is also shown from Figure 5.31 to Figure 5.33 that the amplitudes of the estimated results at 9.87, 10.6, and 11.3 *kHz* are in good agreement with the measured data, the phases of the

estimated results are reasonably fitted with the measured data. The estimated parameters with the amplitude and phase of NMSE are listed in Table 5.2.

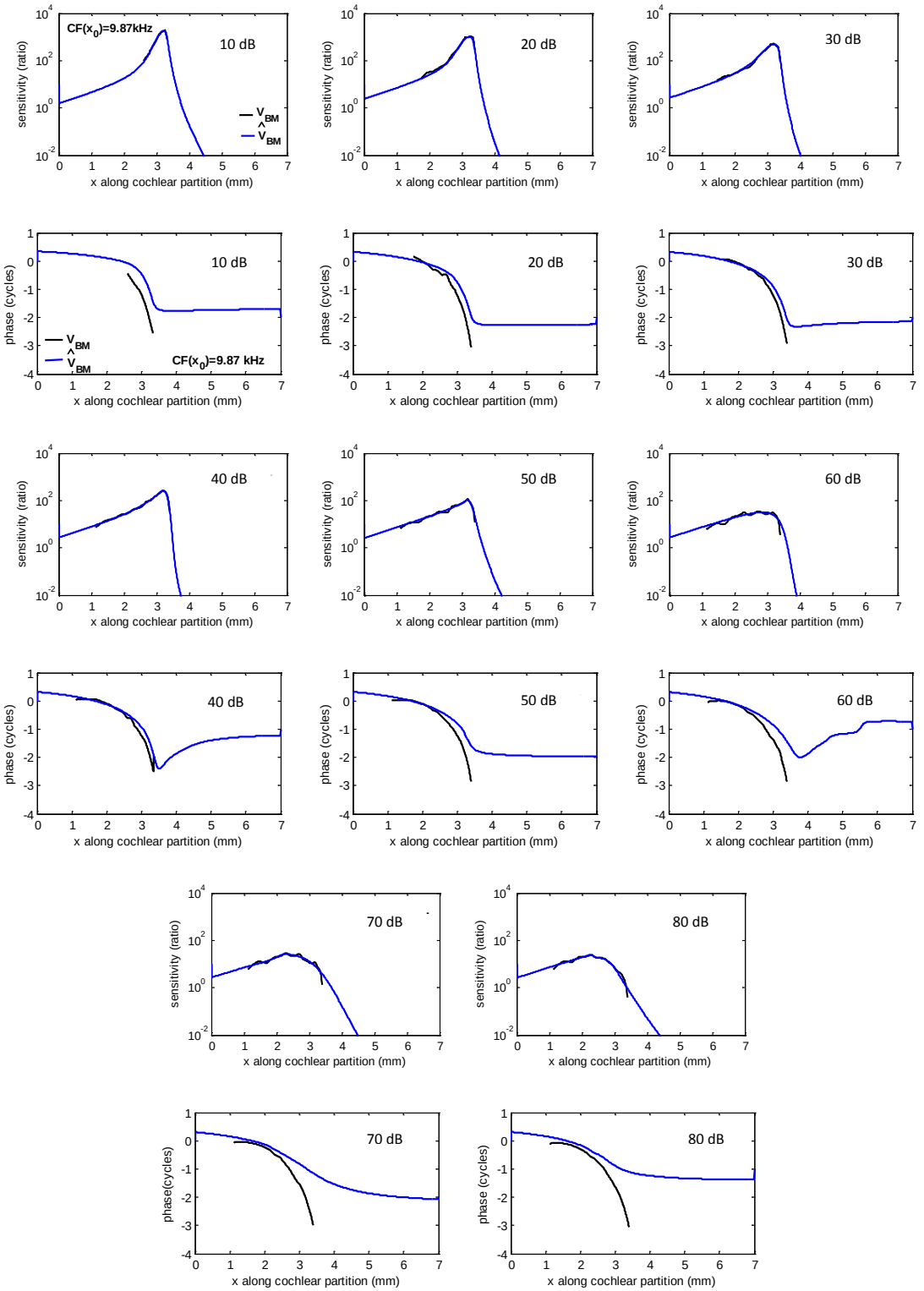

Figure 5.31 Comparison of amplitudes and phases of the BM responses measured by Lee *et al.* (2015) for a CF of 9.87 kHz and SPLs of 10, 20, 30, 40, 50, 60, 70 and 80 dB, black line, and the responses of a model with second order micromechanics and 1D uniform fluid coupling, obtained using multi-objective optimization to identify the micromechanical poles and zeros, blue lines. The estimated data selected are based on the smallest value of NMSE for amplitude.

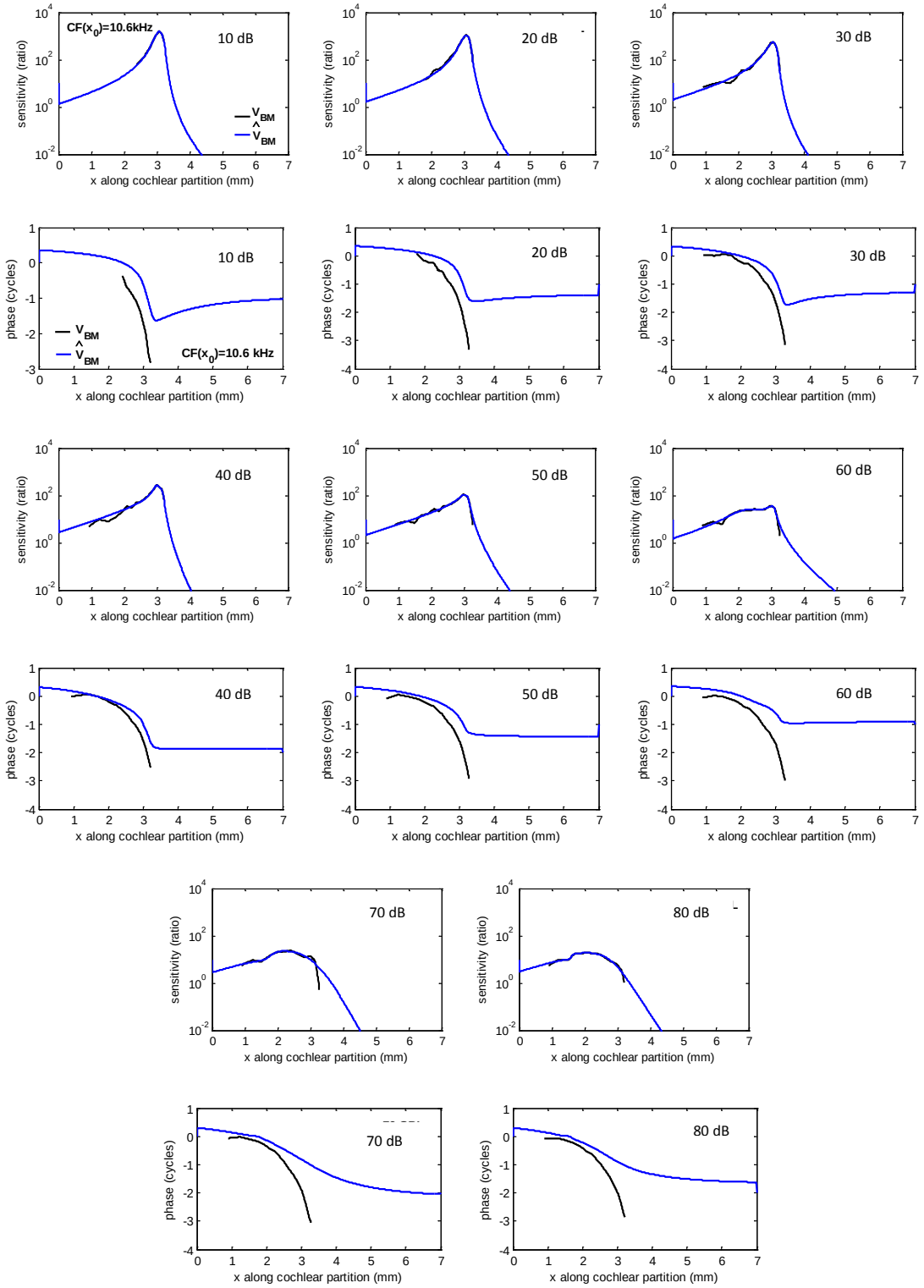

Figure 5.32 Comparison of amplitudes and phases of the BM responses measured by Lee *et al.* (2015) for a CF of 10.6 kHz and SPLs of 10, 20, 30, 40, 50, 60, 70 and 80 dB, black line, and the responses of a model with second order micromechanics and 1D uniform fluid coupling, obtained using multi-objective optimization to identify the micromechanical poles and zeros, blue lines. The estimated data selected are based on the smallest value of NMSE for amplitude.

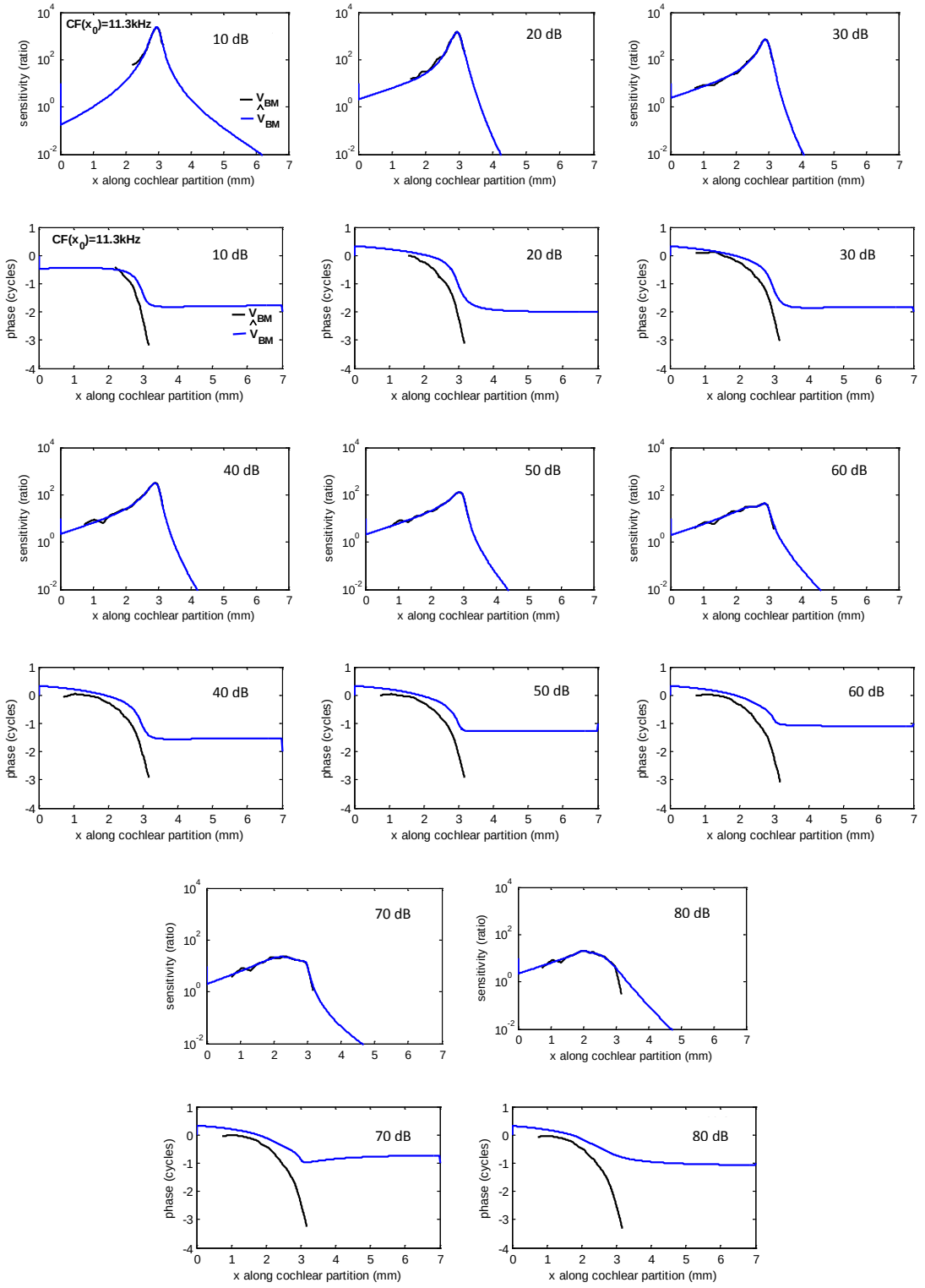

Figure 5.33 Comparison of amplitudes and phases of the BM responses measured by Lee *et al.* (2015) for a CF of 11.3 kHz and SPLs of 10, 20, 30, 40, 50, 60, 70 and 80 dB, black line, and the responses of a model with second order micromechanics and 1D uniform fluid coupling, obtained using multi-objective optimization to identify the micromechanical poles and zeros, blue lines. The estimated data selected are based on the smallest value of NMSE for amplitude.

Table 5.2 The estimated parameters for the zero, Ω_1 and Q_1, and the poles, Ω_2, Ω_3, Q_2 and Q_3 of the micromechanical model obtained in the 1D uniform box model of active cochlea for different characteristic positions with mouse data, together with the normalised mean square error, NMSE, for amplitude and phase.

Condition		Ω_1	Q_1	Ω_2	Q_2	Ω_3	Q_3	m_0	NMSE Amplitude	NMSE phase
Measurement data Mouse CF(x_0)=9.325 kHz SPL	10 SPL	0.62	1.54	0.92	7.86	0.74	3.27	0.12	0.008	1.85
	20 SPL	0.76	1.21	0.94	6.56	0.82	3.07	0.11	0.006	1.80
	30 SPL	0.87	0.93	0.87	4.38	1.02	1.87	0.10	0.005	1.73
	40 SPL	0.66	2.87	0.68	3.12	0.94	6.86	0.10	0.005	1.43
	50 SPL	2.17	4.28	2.53	3.63	0.88	5.43	0.11	0.005	1.84
	60 SPL	0.62	0.85	0.88	6.15	0.48	1.24	0.35	0.005	2.33
	70 SPL	0.99	0.91	0.54	1.17	0.90	9.93	0.43	0.006	1.83
	80 SPL	0.54	6.16	0.61	1.73	0.55	4.93	0.21	0.007	1.48
Measurement data Mouse CF(x_0)=9.87 kHz SPL	10 SPL	0.58	1.12	0.86	9.98	0.73	2.84	0.18	0.14×10^{-2}	2.04
	20 SPL	0.61	1.44	0.70	2.69	0.89	9.93	0.10	0.68×10^{-2}	1.31
	30 SPL	0.77	1.08	0.76	2.22	0.90	9.95	0.12	0.28×10^{-2}	1.58
	40 SPL	1.66	1.35	0.95	9.87	0.89	5.20	0.36	0.11×10^{-2}	1.56
	50 SPL	0.78	7.86	0.86	5.44	0.79	9.93	0.13	0.48×10^{-2}	1.70
	60 SPL	3.74	9.88	1.11	2.61	1.10	2.60	0.85	0.02	1.74
	70 SPL	0.37	2.28	0.86	0.96	0.39	2.75	0.11	0.01	2.04
	80 SPL	0.46	6.77	0.64	1.84	0.45	7.33	0.25	0.45×10^{-2}	2.05
Measurement data Mouse CF(x_0)=10.6 kHz SPL	10 SPL	0.93	0.55	0.89	9.74	0.79	5.05	0.56	6.98×10^{-4}	1.08
	20 SPL	0.72	0.96	0.85	8.37	0.77	3.55	0.28	9.86×10^{-4}	1.69
	30 SPL	0.93	1.12	0.86	9.97	0.79	4.46	0.32	0.16×10^{-2}	2.03
	40 SPL	0.75	4.05	0.85	9.95	0.74	7.33	0.14	0.25×10^{-2}	2.12
	50 SPL	0.77	9.66	0.81	9.97	0.76	9.96	0.25	0.27×10^{-2}	2.19
	60 SPL	0.51	0.99	0.43	1.75	0.79	8.04	0.63	0.54×10^{-2}	1.52
	70 SPL	0.31	2.92	0.34	2.60	0.86	0.77	0.11	0.91×10^{-2}	2.27
	80 SPL	0.29	5.85	0.30	5.55	0.68	1.07	0.18	0.24×10^{-2}	2.29

Condition		Ω_1	Q_1	Ω_2	Q_2	Ω_3	Q_3	m_0	NMSE Amplitude	NMSE phase
Measurement data Mouse CF(x_0)=11.3 kHz SPL	10 SPL	0.22	0.39	0.73	3.81	0.80	7.93	0.94	0.14×10^{-2}	1.52
	20 SPL	0.55	1.15	0.84	1.84	0.78	5.53	0.13	0.17×10^{-2}	1.64
	30 SPL	0.68	1.16	0.77	5.36	0.84	2.56	0.16	0.10×10^{-2}	2.05
	40 SPL	0.70	1.24	0.79	6.12	0.78	2.28	0.22	9.85×10^{-4}	2.25
	50 SPL	0.75	2.45	0.80	8.76	0.73	3.63	0.31	8.16×10^{-4}	2.04
	60 SPL	0.63	2.04	0.57	2.15	0.77	7.95	0.42	0.51×10^{-2}	1.82
	70 SPL	0.83	0.85	0.49	1.38	0.78	9.21	0.96	0.48×10^{-2}	1.95
	80 SPL	0.41	3.05	0.64	1.53	0.41	4.18	0.42	0.48×10^{-2}	2.22

The variations of the estimated parameters with different SPL excitation levels at each fixed position for the mouse data optimized to give the smallest NMSE for amplitude listed in Table 5.2, and these parameters are also shown in Figure 5.34 as a function of excitation level.

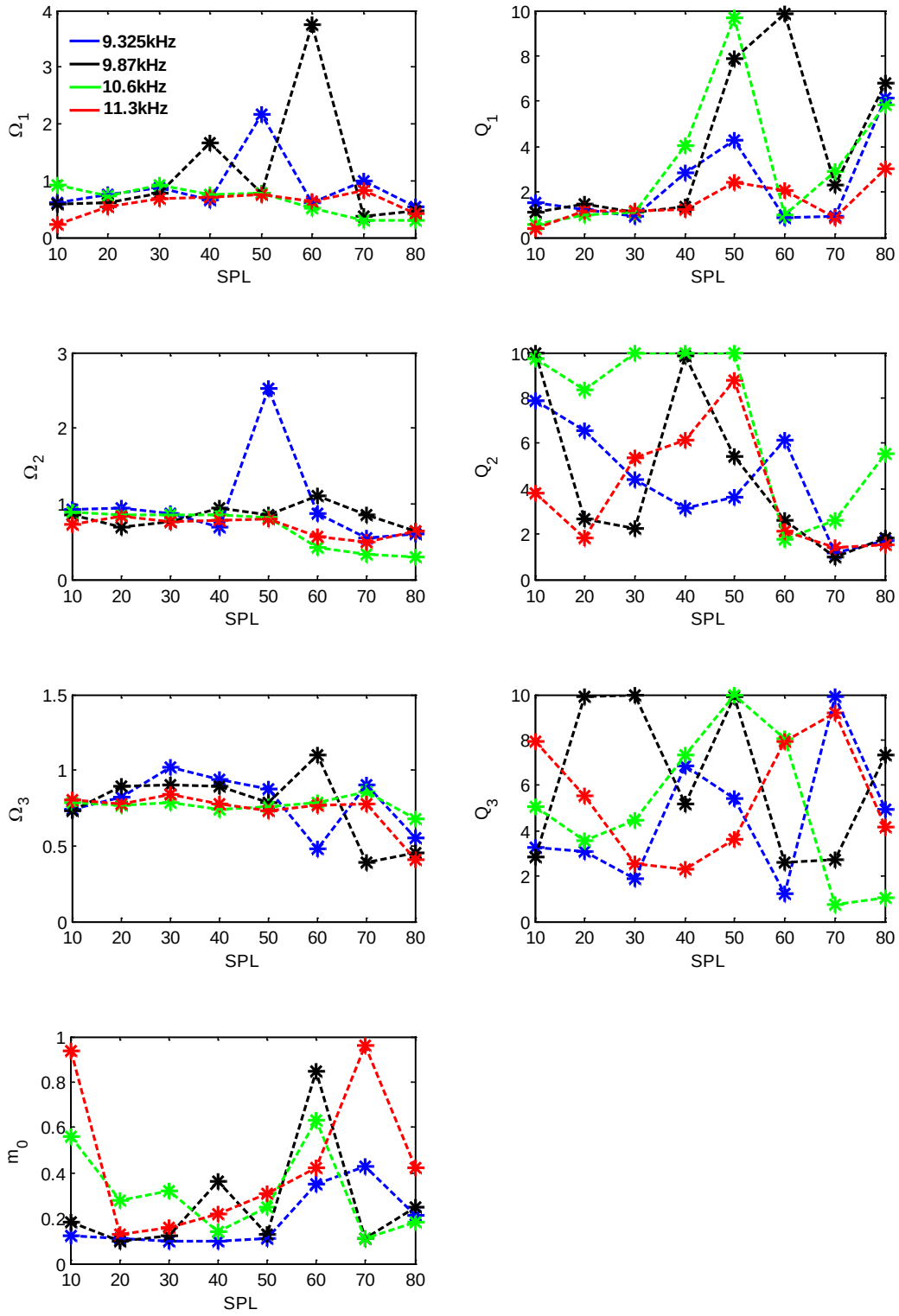

Figure 5.34 Variations of the estimated parameters for the zero, Ω_1 and Q_1, and the poles, Ω_2, Ω_3, Q_2 and Q_3 of the micromechanical model obtained at different fixed positions with variation of SPLs of 10, 20 30, 40, 50, 60, 70, and 80 dB for mouse data, blue mark: 9.325 kHz; black mark: 9.87 kHz; green mark: 10.6 kHz; red mark: 11.3 kHz.

Figure 5.34 shows that the variations of Ω and m are limited to a relatively narrow region, Q varies in a relatively wide region. The values of these parameters are averaged at each SPL,

as shown in Figure 5.35. The variations of average values of estimated parameter do not seem to have certain trend. Those average values of parameters are then used to calculate the real and imaginary part of poles and zeros, as shown in Figure 5.36.

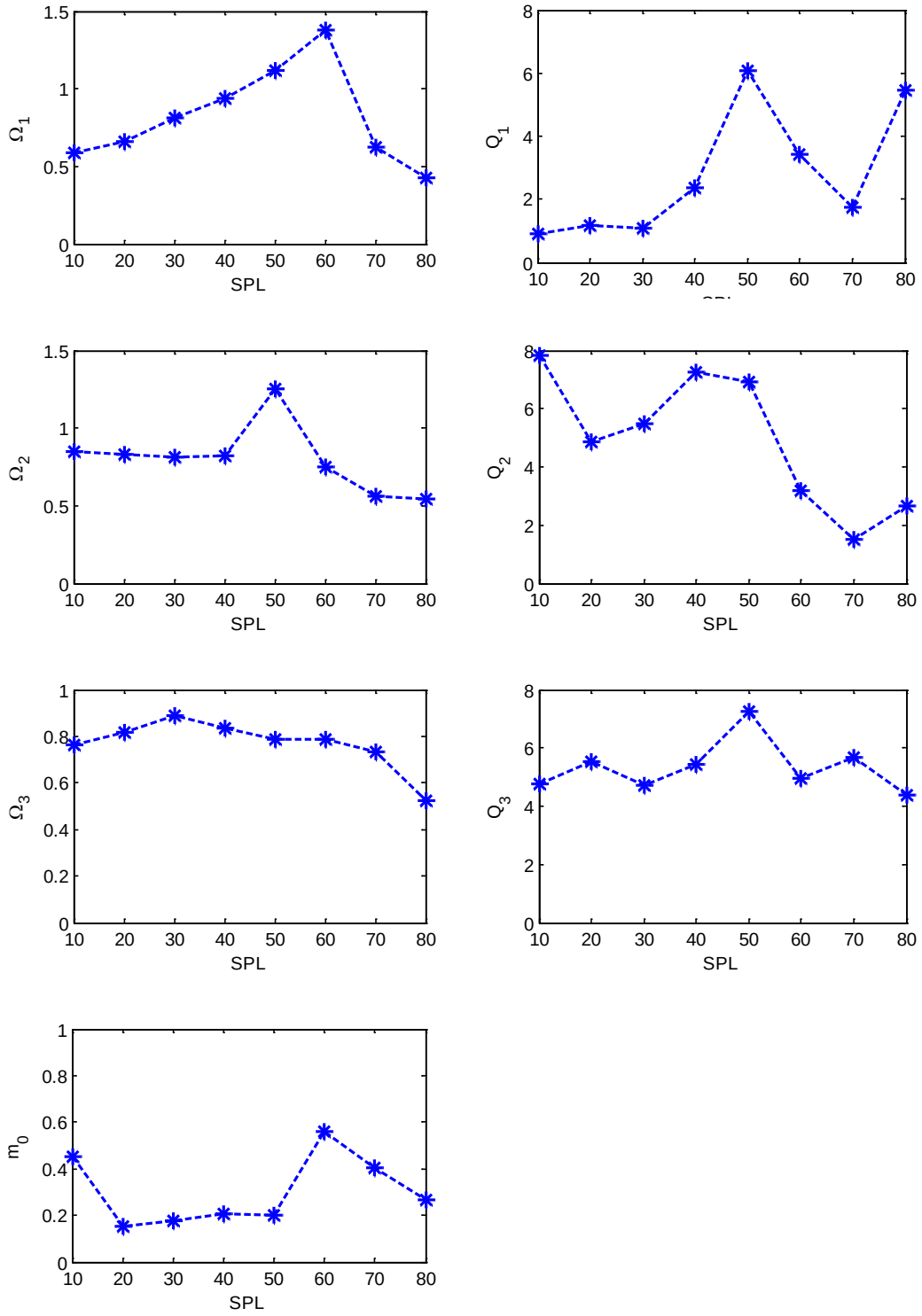

Figure 5.35 Variations of the average values of the estimated parameters with variations of SPLs of 10, 20, 30, 40, 50, 60, 70 and 80 dB.

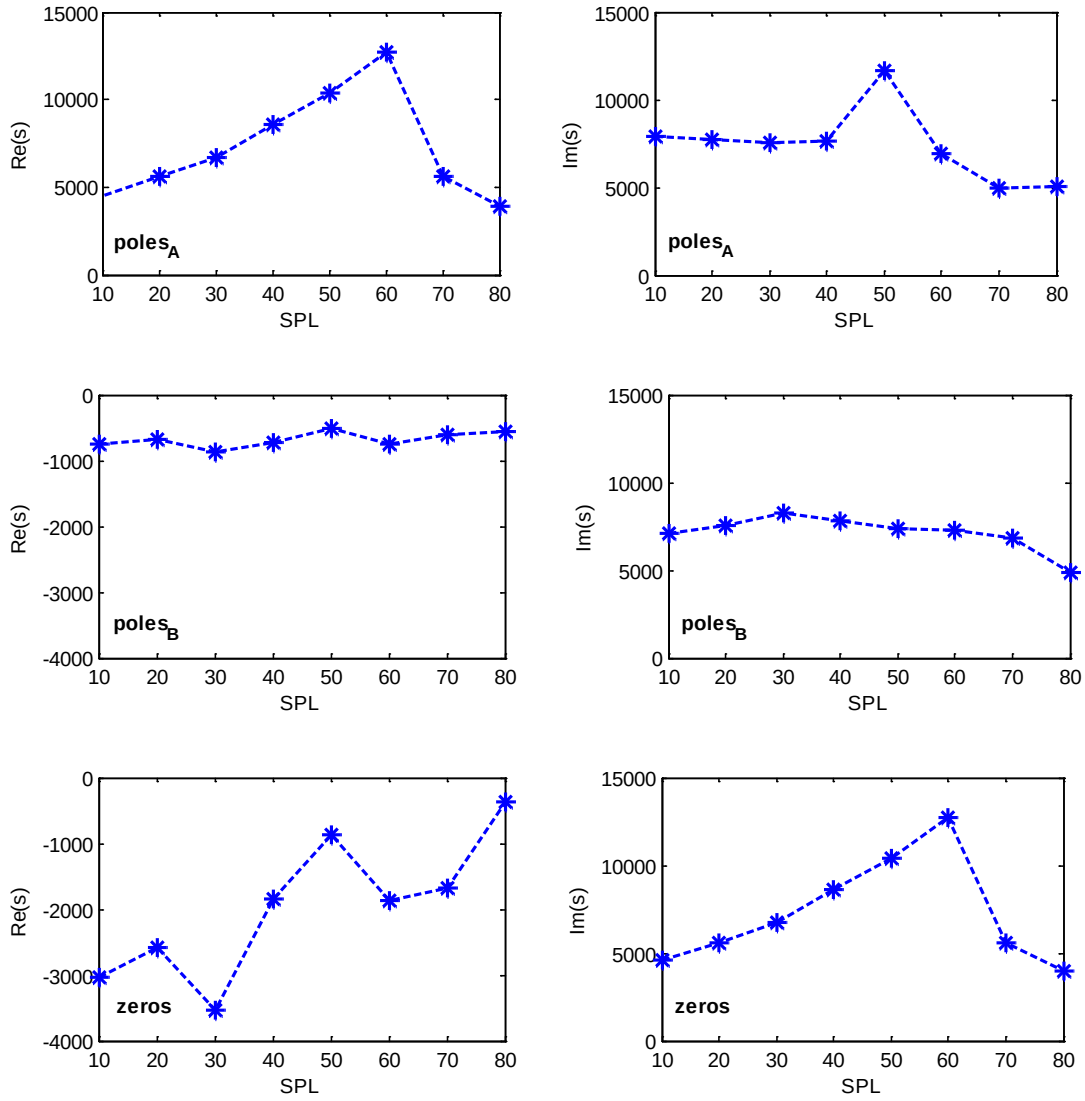

Figure 5.36 Variations of imaginary and real parts of poles and zeros with variations of SPLs of 10, 20, 30, 40, 50, 60, 70, and 80 dB.

It is shown in Figure 5.36 that there are no certain trends for the variations of real and imaginary part of poles and zeros with variation of SPLs.

The average values of estimated parameters are then used to determine the positions of the poles and zeros of Y_{BM} on the complex S plane, as shown in Figure 5.37.

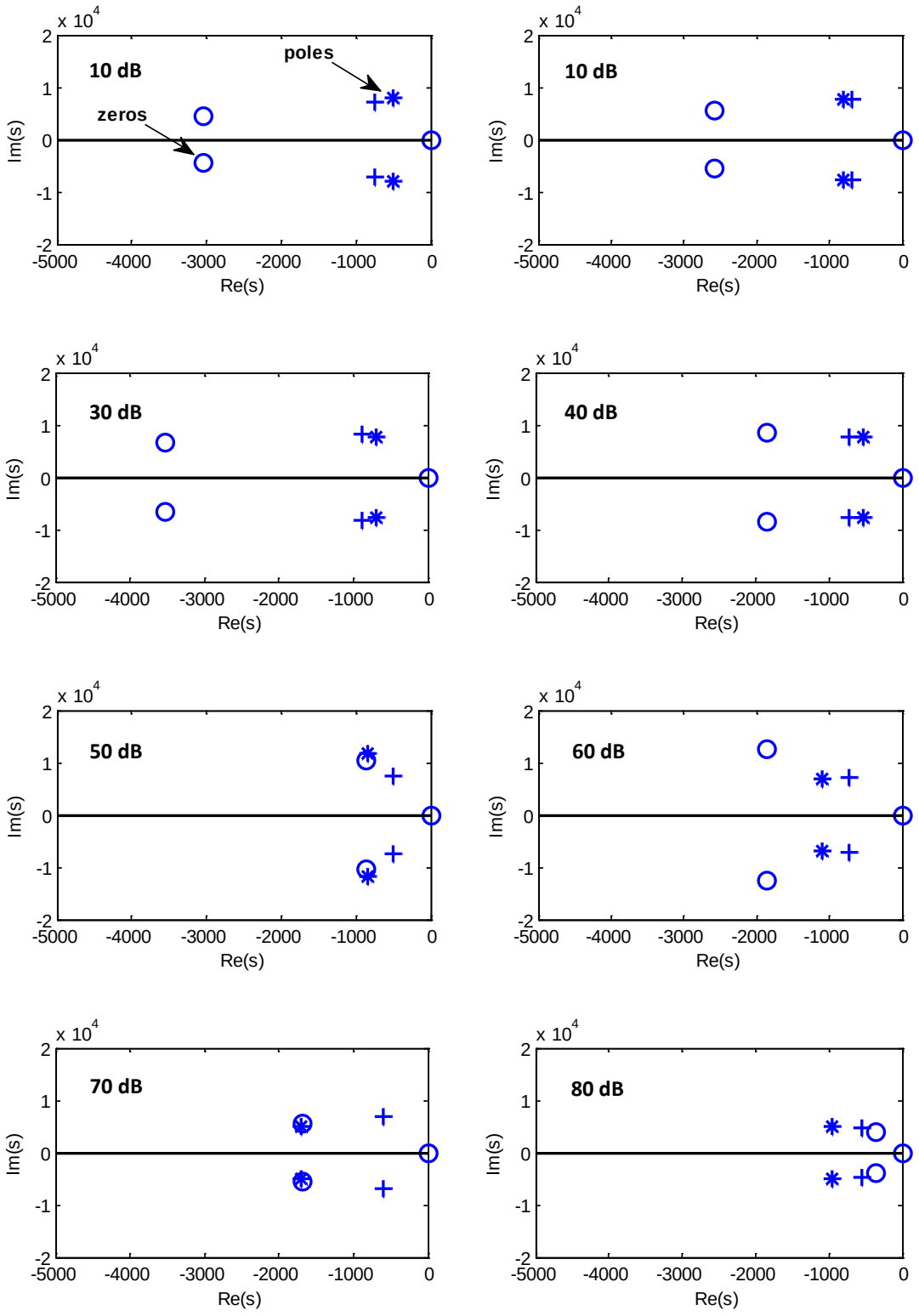

Figure 5.37 Positions of poles and zeros at CF(x_0) = 9.325 kHz, from SPLs of 10 dB to 80 dB in individual according to average values of estimated parameter.

The poles and zeros in Figure 5.37 express that two pairs of poles are always close to each other, and zeros are always complex values. The positions of poles and zeros are always varied according to different SPL. From SPLs 10 dB to 80 dB, one pairs of zeros seem to

move towards to one pairs of poles, so that the cochlea becomes from active to passive, as similar as the Neely and Kim model, this finding is also as similar as a silicon cochlear model created by Mandal (2009).

Due to the reason that the variations of average values of parameters, and real and imaginary part of poles and zeros calculated using those average values do not show certain distribution trends, the average values of real and imaginary part of poles and zeros using the estimated parameters at CF(x_0)=9.325, 9.87, 10.6 and 11.3 kHz and each set of these values at each characteristic position should be considered, as shown in Figure 5.38.

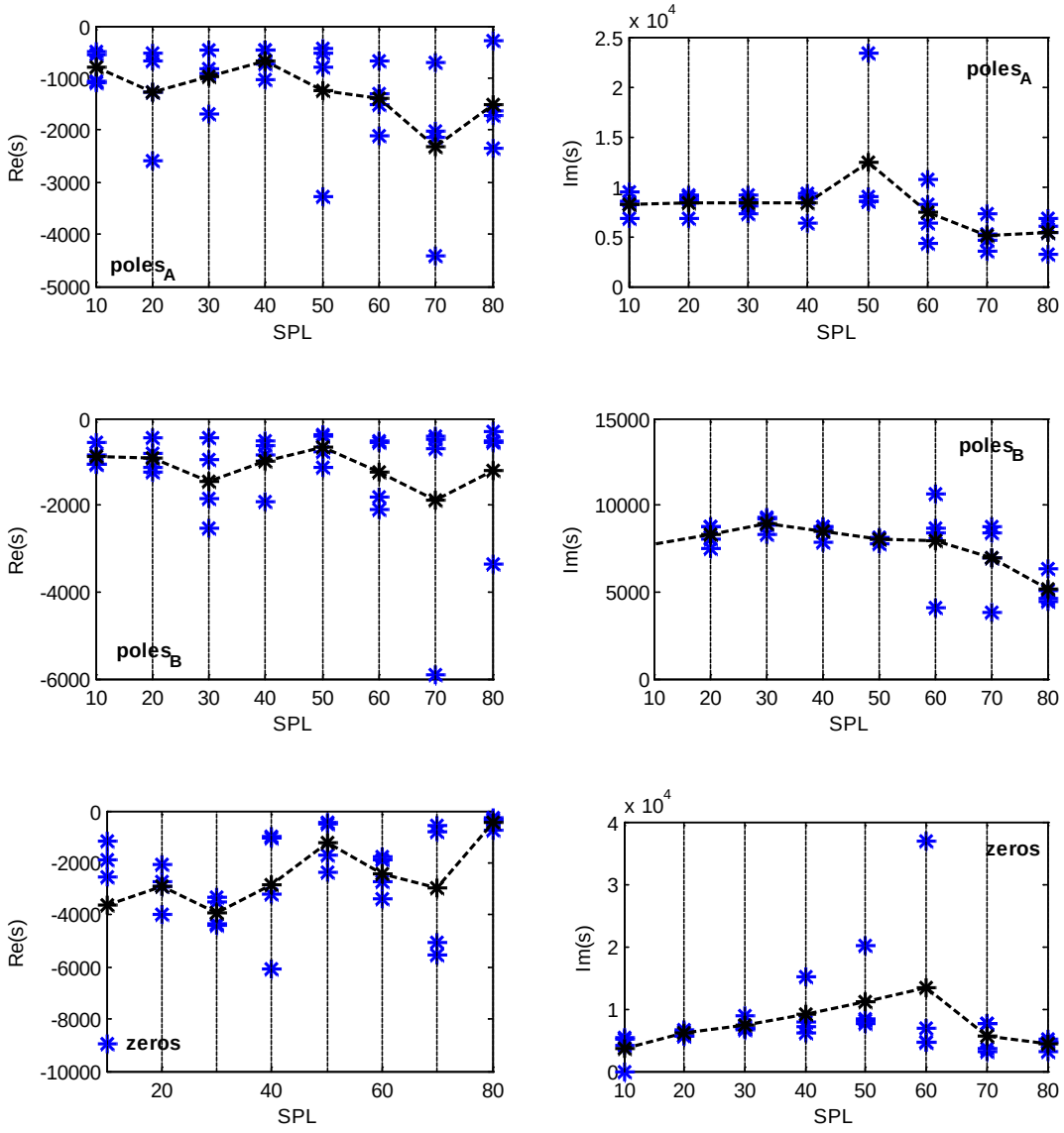

Figure 5.38 Comparison of variations of real and imaginary part of poles and zeros at CF(x_0)=9.325, 9.87, 10.6 and 11.3 kHz with SPLs, and variation anf average values of real and imaginary part of poles and zeros for the four characteristic positions with SPLs.

Figure 5.38 seems to show the reasonable distribution trends of variations of real and imaginary part of poles and zeros for the four characteristic positions. Those average values are used to calculate the positions of poles and zeros at each SPL shown in Figure 5.39.

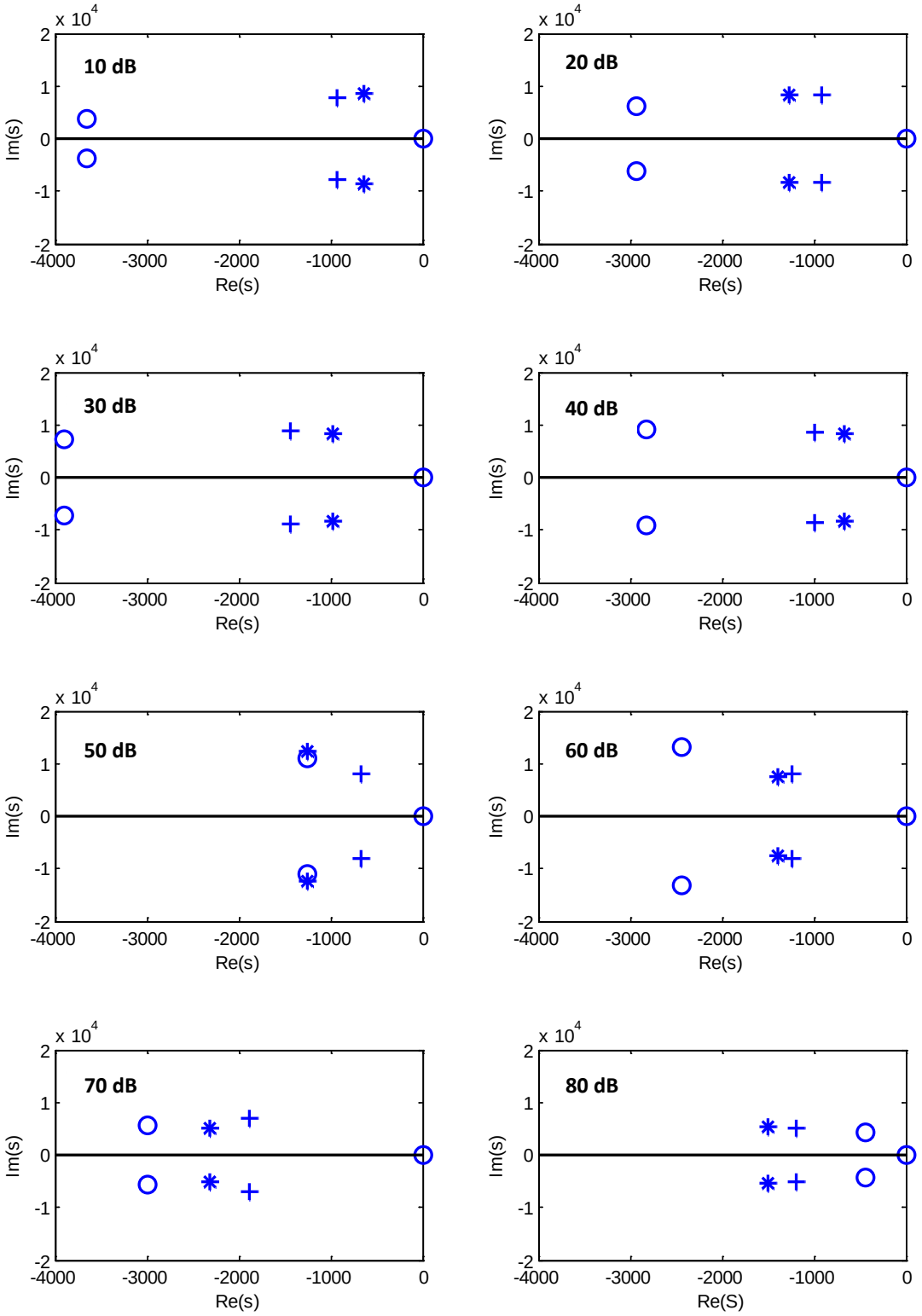

Figure 5.39 Positions of poles and zeros at each SPL of dB, oatained from the average values of real and imaginary part of poles and zeros for the four characteristic positions.

Figure 5.39 shows the similar results as those in Figure 5.37, two pairs of poles are always close to each other, and zeros are always complex values. The positions of poles and zeros are always varied according to different SPLs. From SPLs of 10 dB to 80 dB, one pairs of zeros seem to move towards to one pairs of poles, so that the cochlea becomes from active to passive.

Those average values of poles and zeros are chosen to reconstruct the local frequency response, $\hat{Y}_{BM}(i\omega, x_0)$, as shown in Figure 5.40, thus the coupled frequency response, $\hat{V}_{BM}(i\omega, x_0)$, can be calculated using the 1D uniform box model with this local response, $\hat{Y}_{BM}(i\omega, x)$, as shown in Figure 5.41. Figures 5.40 and 5.41 show the similar local and coupled responses with different SPLs as those in the Neely and Kim model as shown in Figures 4.4 and 4.5, which show the variation from being active to being passive when the SPL increases.

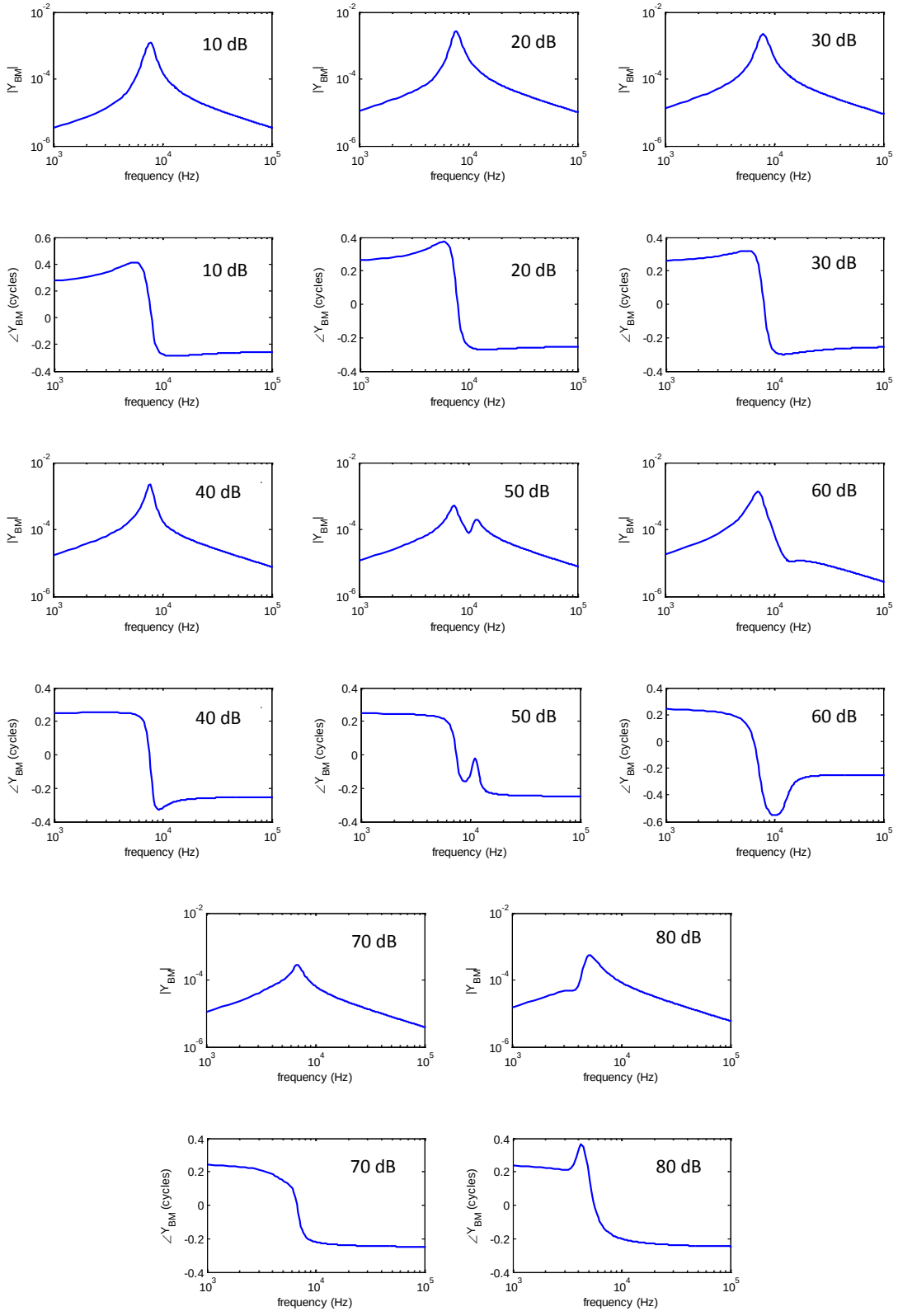

Figure 5.40 Amplitude and phase of the coupled responses of the cochlea, calculated using the 1D uniform box model with the distribution of BM admittance (second order micromechanics).

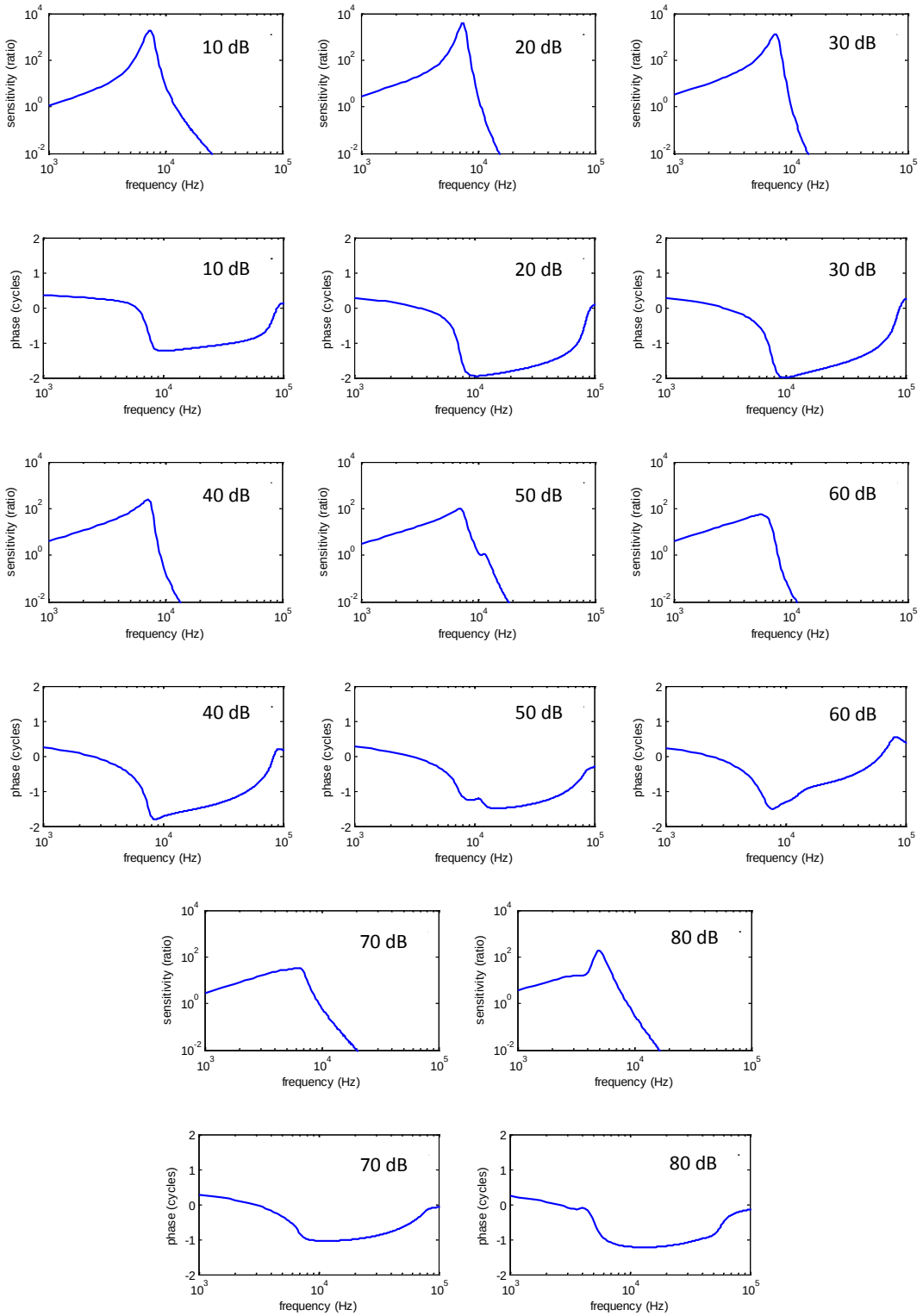

Figure 5.41 Amplitude and phase of the BM admittance calculated using the pole and zero locations shown in Figure 5.37.

The reconstructed wavenumber can also be calculated using the equation $k(x) = \sqrt{-\frac{2i\omega\rho}{h} Y_{BM}(x)}$, as shown in Figure 5.42. Figure 5.42 shows that the real part of the wavenumber,determining the wavelength, increases along the cochlea, as the wave slows

down, and it is higher at low SPL than that at high SPL around the characteristic place; the imaginary part of the wavenumber, characterizing the effects of energy gains or losses that determines whether the wave amplitude is increased or decreased, goes from a positive value basal to CF at low SPL, indicating the wave is being amplified, while at high SPL, this positive value gradually disappears, indicating the wave is not being amplified, then the imaginary part of the wavenumber goes to negative just before CF where the wave is being attenuated.

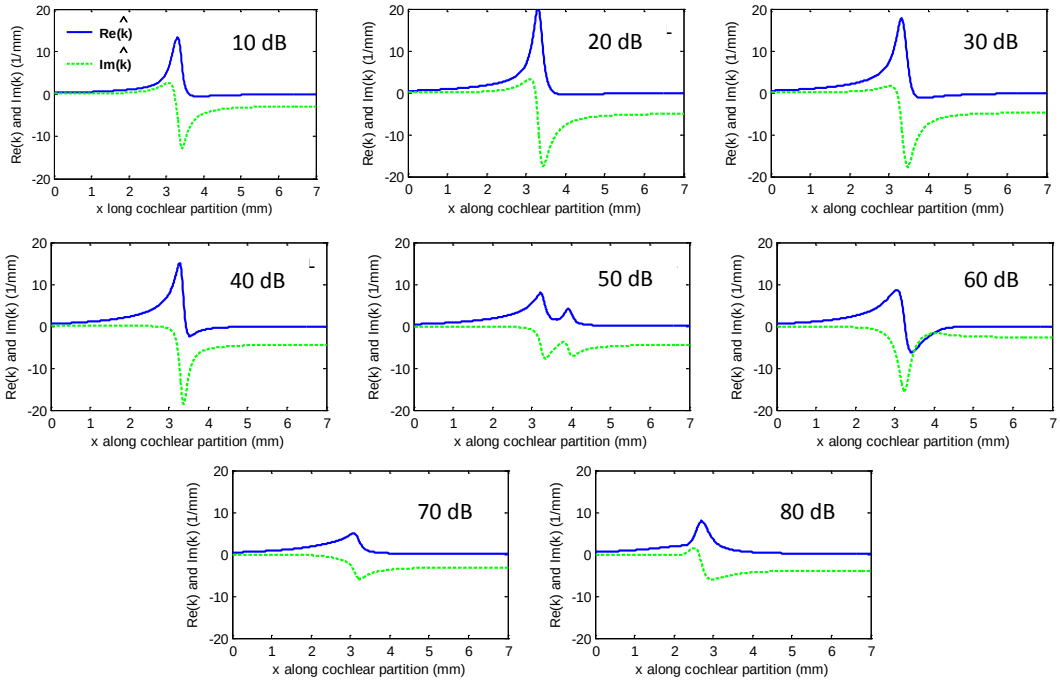

Figure 5.42 Real (blue solid lines) and imaginary (green dash lines) part of wavenumber distributions along cochlear partition calculated using the distribution of BM admittance shown in Figure 5.40.

5.6.3. Fitting the passive response

The response of the cochlea at high levels of excitation is expected to be passive, and so may be better filled with a single degree of freedom micromechanical result. Initially 1D uniform box model is used to estimate the parameters.

Figure 5.43 shows that although the fitted amplitudes of $\hat{V}_{BM}$ from SPLs 40 dB to 80 dB are in reasonable agreement with V_{BM}, from 10 SPL to 30 SPL, then the fitted BM velocity $\hat{V}_{BM}$ does not reach the measured peak values of V_{BM}. The phases of $\hat{V}_{BM}$ are a reasonable fit to V_{BM}. The eatimated parameters and NMSE of amplitude and phase are listed in Table 5.3.

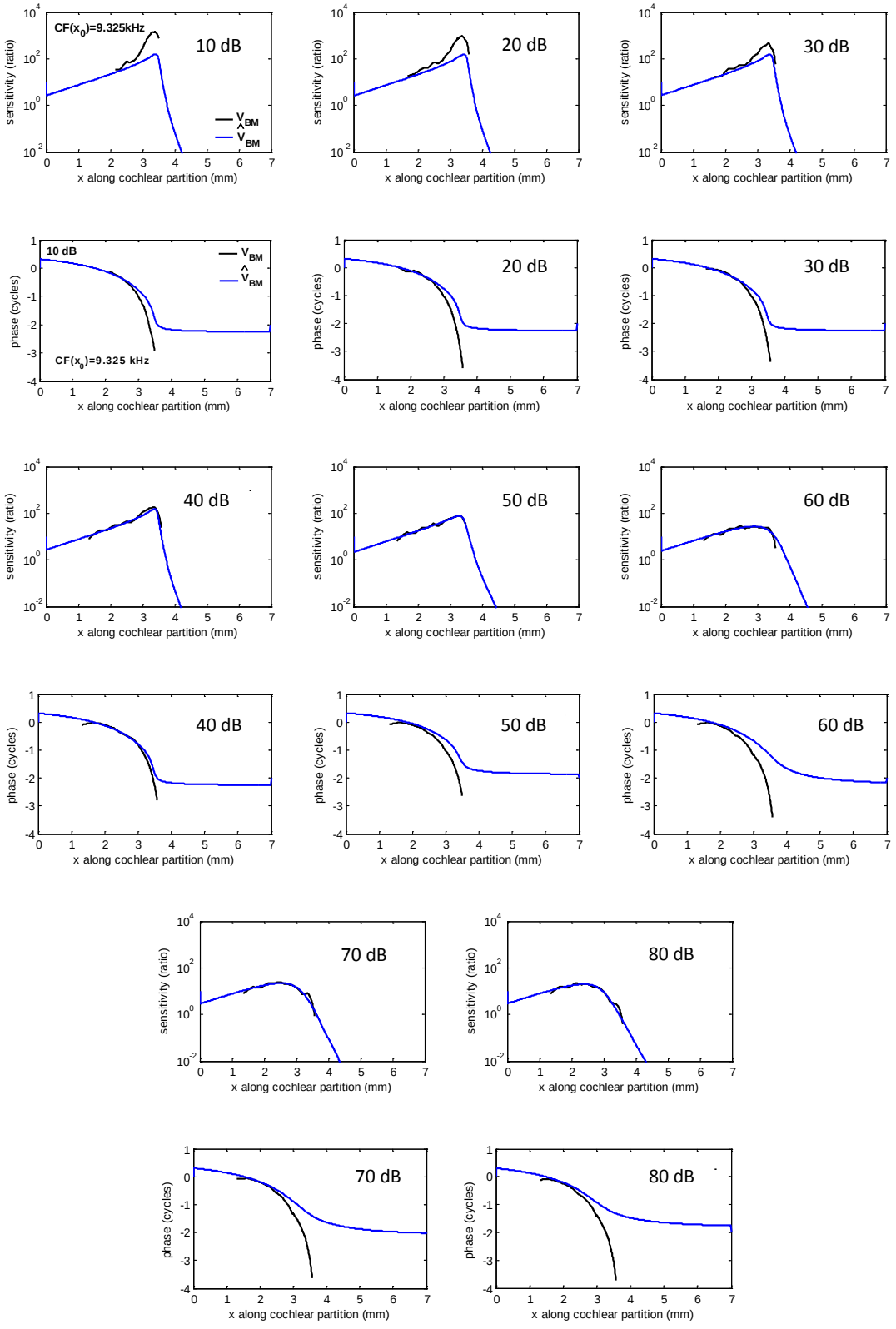

Figure 5.43 Comparison of amplitudes and phases of the BM responses measured by Lee *et al.* (2015) for a CF of 9.325 kHz and SPLs of 10, 20, 30, 40, 50, 60, 70 and 80 dB, black line, and the responses of a model with first order micromechanics and 1D uniform fluid coupling, obtained using multi-objective optimization to identify the micromechanical poles and zeros, blue lines. The estimated data selected are based on the smallest value of NMSE for amplitude.

Table 5.3 The estimated parameters for the zero, and, and the poles,and of the micromechanical model obtained in 1D uniform passive box model of cochlea at CF(x_0) = 9.325 kHz, together with the normalised mean square error, NMSE, for amplitude and phase.

1D uniform					
Passive	Ω	Q	m_0	NMSE Amplitude	NMSE phase
10 SPL	0.91	10.00	0.10	0.78	0.73
20 SPL	0.92	10.00	0.10	0.67	0.87
30 SPL	0.91	10.00	0.10	0.39	0.86
40 SPL	0.88	9.91	0.10	0.06	0.85
50 SPL	0.88	5.32	0.15	0.005	1.90
60 SPL	0.97	1.59	0.11	0.01	1.99
70 SPL	0.78	1.33	0.12	0.01	1.40
80 SPL	0.67	1.34	0.15	0.008	1.40

5.7. Effect of different cochlear box models on the optimization with mouse data

The 1D uniform box model of the active and passive cochlea for mouse has been used in the optimization model to estimate the parameters in Section 5.6. For the active model, the amplitudes of the estimated rsults fits well, for the passive model, those fits well at high sound pressure levels, but the phase only reasonably fits with mouse data in those two cases. The effect of the cochlear geometry on the fitted BM responses of the active and passive cochlea with the direct inverse method will be considered. Here, one set of measurement data, CF(x_0)=9.325 kHz, are selected to show the effect of different cochlear box models on the optimization.

5.7.1. Effect of tapering shape

Figure 5.44 shows the effect of using 1D the tapered box model of active cochlea, as described in Chapter 3, on the optimization method. The results do not appear to be significantly better than $\hat{V}_{BM}$ in the uniform box model, as shown in Figure 5.30. The normalized mean square errors are listed in Table 5.4 and show no significant improvement compared with the corresponding results for the uniform box model in Table 5.2. In particular, the tapered box model does not improve the phase of the estimated results. For the passive cochlear case shown in Figure 5.45, there is still no significant improvement of the estimated results, the normalised mean square errors listed in Table 5.4 do not also show better results compared with those listed in Table 5.2. It would appear that the tapered shape in the box model does not have large enough effect to markedly improve the estimated response.

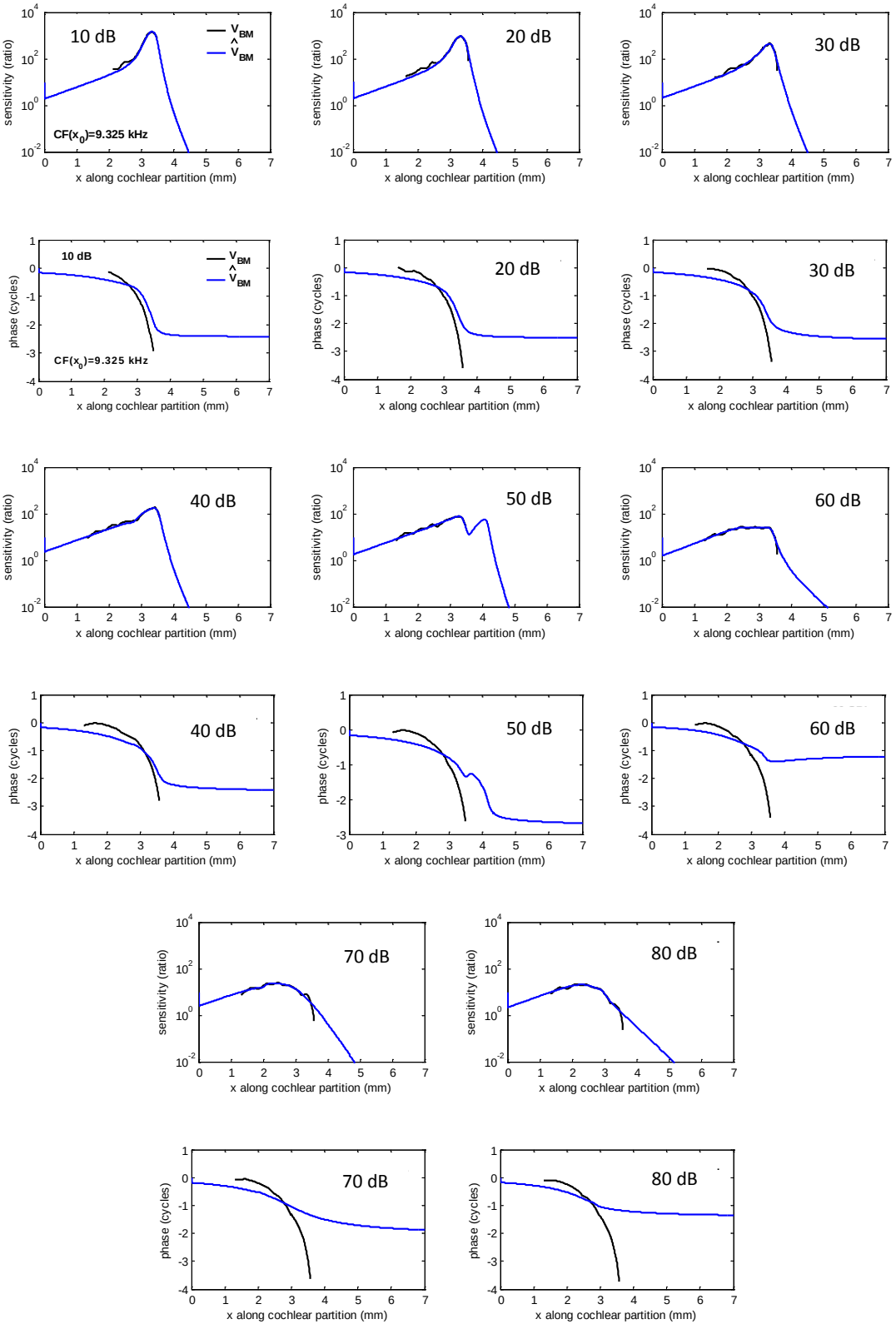

Figure 5.44 Comparison of amplitudes and phases of the BM responses measured by Lee *et al.* (2015) for a CF of 9.325 kHz and SPLs of 10, 20, 30, 40, 50, 60, 70 and 80 dB, black line, and the responses of a model with second order micromechanics and 1D tapered fluid coupling, obtained using multi-objective optimization to identify the micromechanical poles and zeros, blue lines. The estimated data selected are based on the smallest value of NMSE for amplitude.

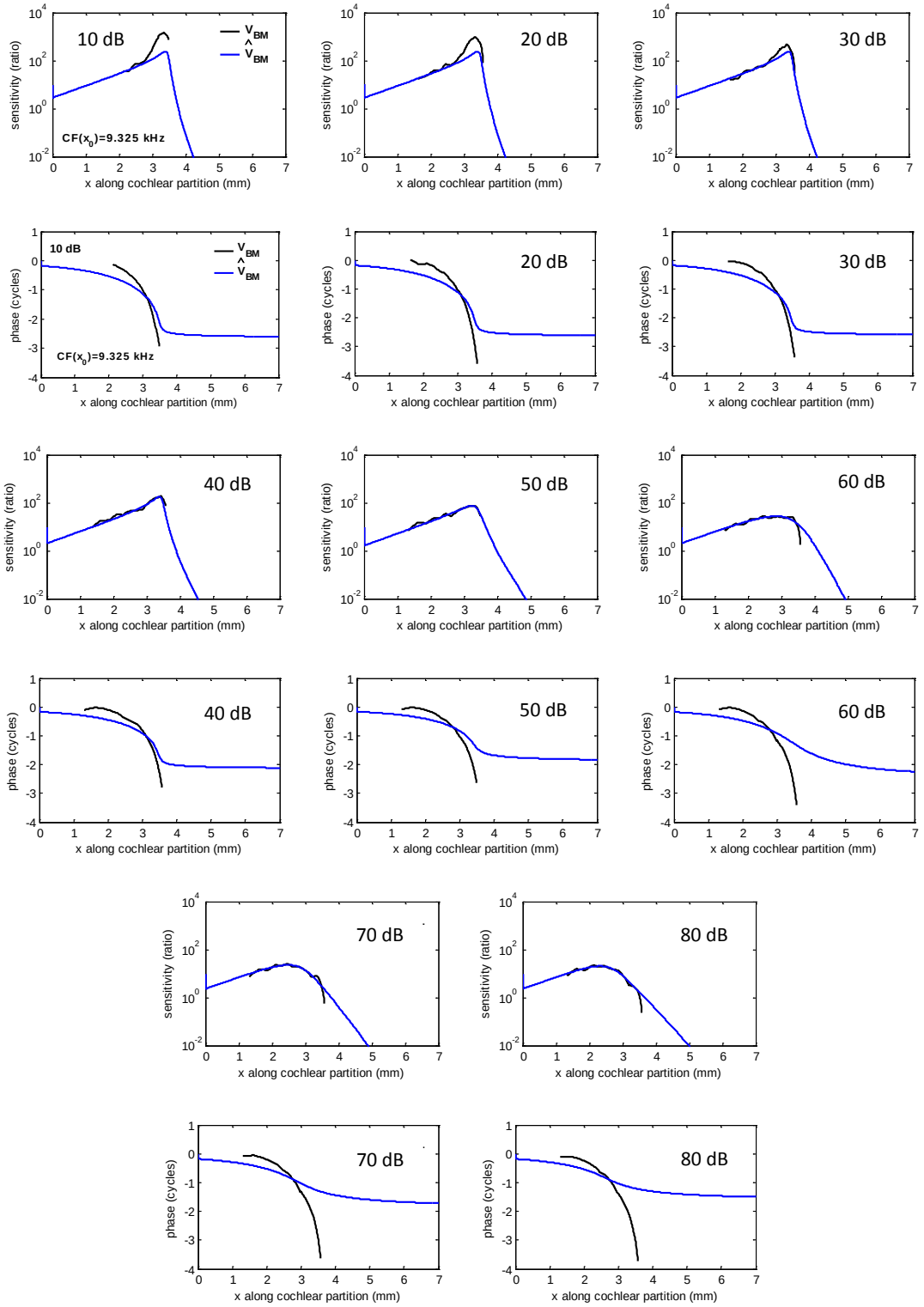

Figure 5.45 Comparison of amplitudes and phases of the BM responses measured by Lee *et al.* (2015) for a CF of 9.325 kHz and SPLs of 10, 20, 30, 40, 50, 60, 70 and 80 dB, black line, and the responses of a model with first order micromechanics and 1D tapered fluid coupling, obtained using multi-objective optimization to identify the micromechanical poles and zeros, blue lines. The estimated data selected are based on the smallest value of NMSE for amplitude.

Table 5.4 The estimated parameters for the zero, and, and the poles, and of the micromechanical model obtained in 1D tapered box model for the active and passive cochlea cases at $CF(x_0)$ = 9.325 kHz, together with the normalised mean square error, NMSE, for amplitude and phase.

1D tapered									
Active	Ω_1	Q_1	Ω_2	Q_2	Ω_3	Q_3	m_0	NMSE Amplitude	NMSE Phase
10 SPL	0.61	1.91	0.91	6.83	0.74	3.36	0.13	0.002	2.37
20 SPL	0.63	1.53	0.92	4.95	0.76	2.64	0.12	0.003	2.61
30 SPL	0.62	1.01	0.87	5.15	0.78	1.09	0.11	0.004	2.95
40 SPL	0.57	5.95	0.94	5.89	0.59	4.53	0.13	0.004	2.44
50 SPL	0.97	9.94	0.85	5.31	1.43	7.87	0.11	0.006	2.82
60 SPL	0.76	0.70	0.46	1.05	0.86	6.80	0.78	0.005	2.39
70 SPL	0.34	9.74	0.67	0.96	0.35	9.07	0.23	0.006	2.65
80 SPL	0.61	4.42	0.49	1.31	0.61	6.27	0.54	0.006	2.23
1D tapered									
Passive	Ω		Q		m_0			NMSE Amplitude	NMSE phase
10S PL	0.90		9.97		0.10			0.80	2.43
20 SPL	0.91		10.00		0.10			0.53	3.05
30 SPL	0.90		9.97		0.10			0.21	3.06
40 SPL	0.89		8.26		0.17			0.03	2.31
50 SPL	0.86		3.84		0.26			0.007	2.75
60 SPL	0.95		1.05		0.15			0.01	2.65
70 SPL	0.64		1.14		0.29			0.007	2.52
80 SPL	0.54		1.19		0.41			0.008	2.34

5.7.2. Effect of 3D fluid coupling

The direct optimization is again used to obtain results for the mouse data with $CF(x_0)$=9.325 kHz, but now with a 3D fluid coupling in the uniform box model together with a first and a second order micromechanical model, and the results are shown in Figures 5.46 and 5.47.

The amplitude of $\hat{V}_{BM}$ in Figures 5.46 and 5.47 again show good agreement with V_{BM}, but now the phase of $\hat{V}_{BM}$ appear to be closer to that of V_{BM} than in the 1D uniform box model for active and passive cochlea cases, ass shown in Figures 5.30 and 5.42. The normalized mean square errors are listed in Table 5.5 and same improvements in the phase errors can be seen compared with the 1D fluid coupling results in Tables 5.2 and 5.3.

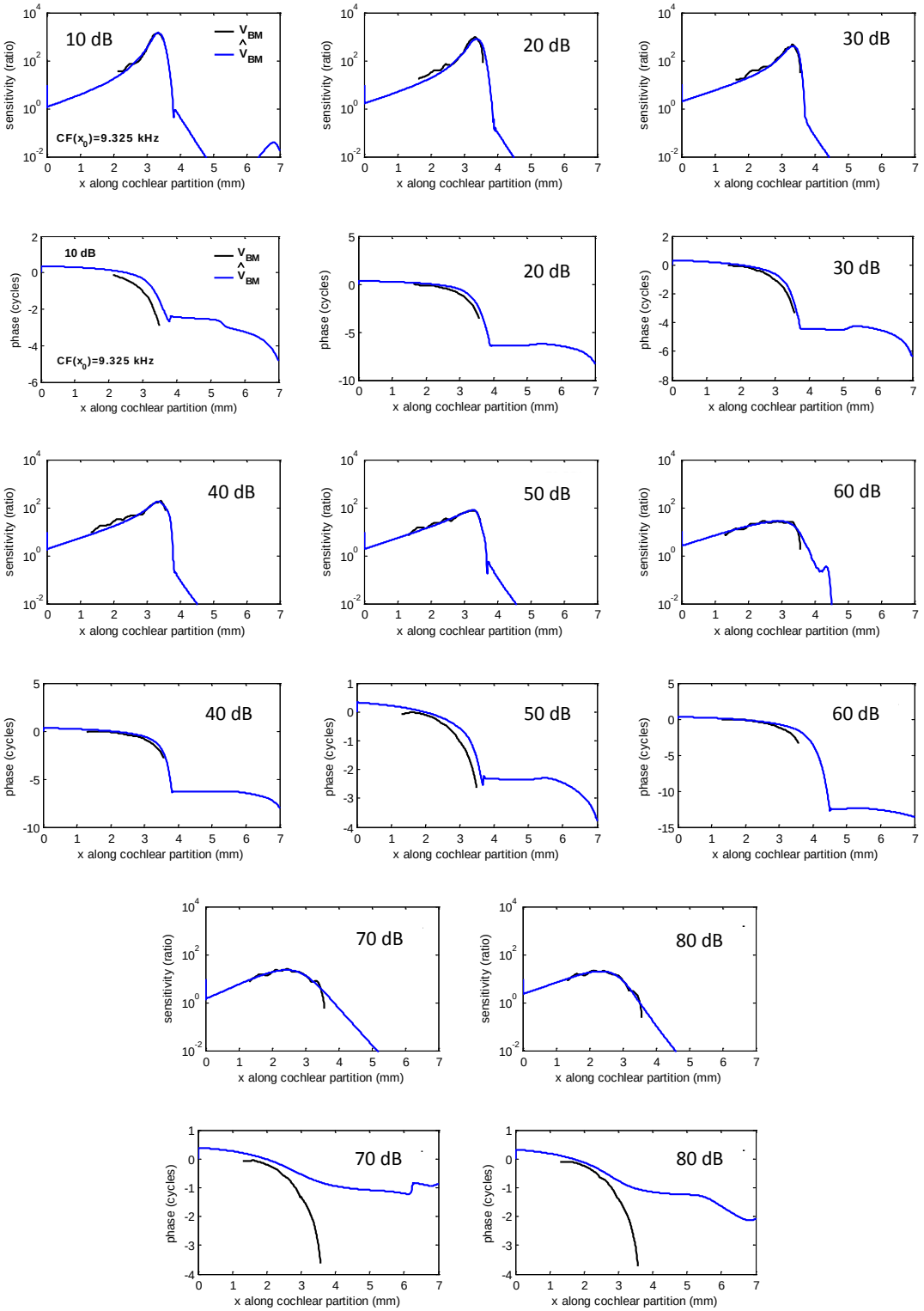

Figure 5.46 Comparison of amplitudes and phases of the BM responses measured by Lee *et al.* (2015) for a CF of 9.325 kHz and SPLs of 10, 20, 30, 40, 50, 60, 70 and 80 dB, black line, and the responses of a model with second order micromechanics and 3D uniform fluid coupling, obtained using multi-objective optimization to identify the micromechanical poles and zeros, blue lines. The estimated data selected are based on the smallest value of NMSE for amplitude.

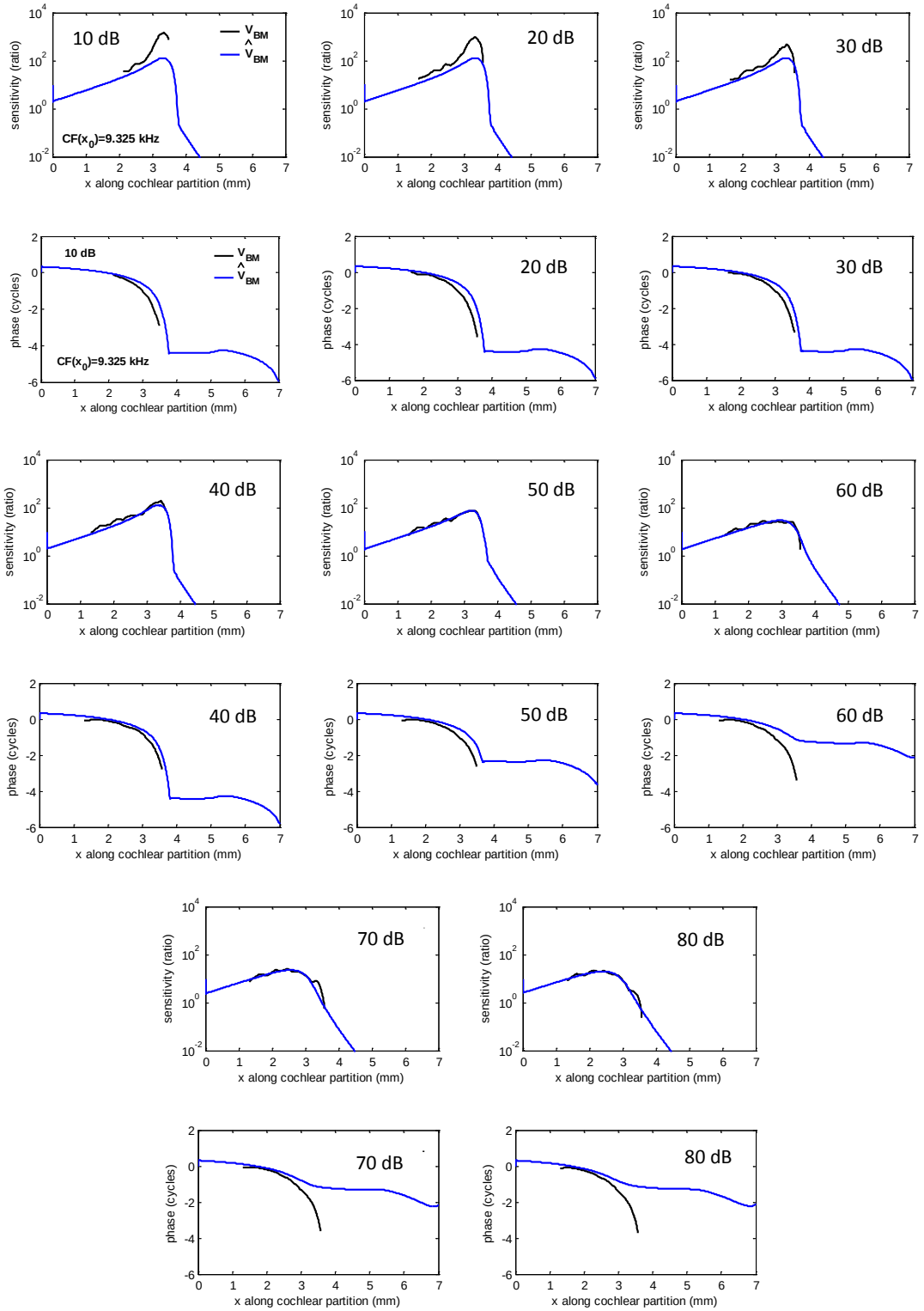

Figure 5.47 Comparison of amplitudes and phases of the BM responses measured by Lee *et al.* (2015) for a CF of 9.325 kHz and SPLs of 10, 20, 30, 40, 50, 60, 70 and 80 dB, black line, and the responses of a model with fisrt order micromechanics and 3D uniform fluid coupling, obtained using multi-objective optimization to identify the micromechanical poles and zeros, blue lines. The estimated data selected are based on the smallest value of NMSE for amplitude.

Table 5.5 The estimated parameters for the zero, and, and the poles,and of the micromechanical model obtained in the 3D uniform box model for the active and passive cochlea at CF(x_0) = 9.325 kHz, together with the normalised mean square error, NMSE, for amplitude and phase.

3D uniform									
Active	Ω_1	Q_1	Ω_2	Q_2	Ω_3	Q_3	m_0	NMSE Amplitude	NMSE Phase
10 SPL	2.39	0.16	3.06	2.83	0.90	1.76	0.22	0.004	1.80
20 SPL	2.00	0.34	1.00	1.51	1.41	7.23	0.36	0.048	1.93
30 SPL	1.98	0.80	1.00	2.91	2.06	7.69	0.13	0.023	2.16
40 SPL	0.89	4.27	0.88	4.64	1.09	9.96	0.13	0.011	1.72
50 SPL	0.85	9.14	0.85	9.96	1.13	3.97	0.16	0.007	1.96
60 SPL	9.08	0.13	1.72	9.83	4.84	0.13	0.11	0.013	1.92
70 SPL	0.55	0.14	0.92	0.56	0.66	0.33	0.28	0.007	2.33
80 SPL	0.75	0.24	0.54	0.43	1.16	0.75	0.17	0.007	1.94

3D uniform					
Passive	Ω	Q	m_0	NMSE Amplitude	NMSE phase
10S PL	1.15	10.00	0.10	0.79	1.82
20 SPL	1.16	10.00	0.10	0.68	1.93
30 SPL	1.14	10.00	0.10	0.41	1.68
40 SPL	1.11	10.00	0.10	0.06	1.90
50 SPL	1.14	4.84	0.11	0.007	2.12
60 SPL	1.23	1.48	0.10	0.03	2.19
70 SPL	1.00	1.16	0.10	0.02	1.77
80 SPL	0.92	1.04	0.11	0.01	1.75

5.7.3. Effect of combination of tapered shape and 3D fluid coupling

Figures 5.48 and 5.49 show the results of using the 3D tapered box model for the active and passive cochlea cases, although these do not appear to be significantly better than just using the 3D fluid coupling with uniform box model, as shown in Figures 5.46 and 5.47. The normalized mean square errors are listed in Table 5.6. Therefore, the combination and tapering shape and 3D fluid coupling in the box model does not further improve $\hat{V}_{BM}$ compared with $\hat{V}_{BM}$ in the 3D uniform box model.

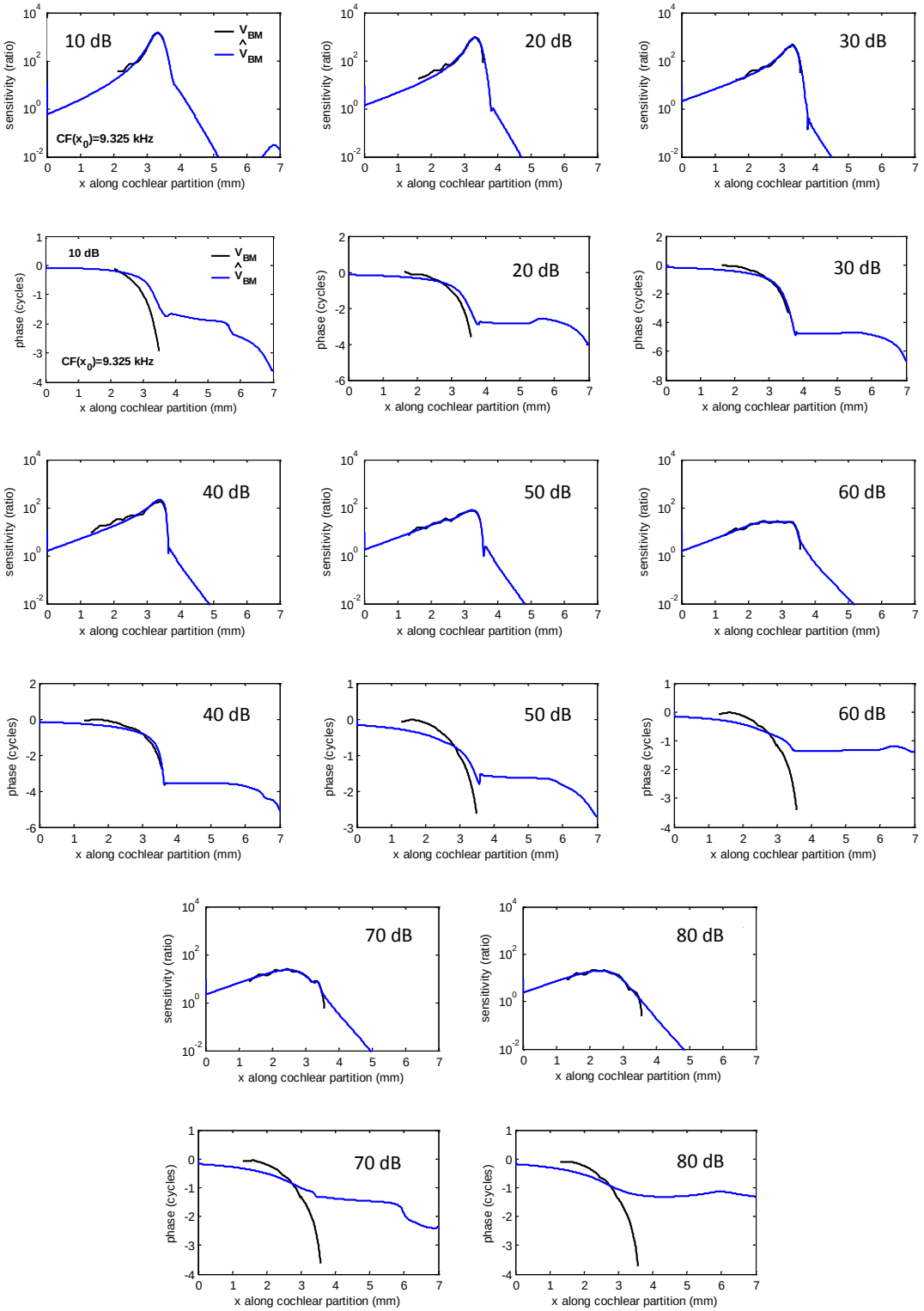

Figure 5.48 Comparison of amplitudes and phases of the BM responses measured by Lee *et al.* (2015) for a CF of 9.325 kHz and SPLs of 10, 20, 30, 40, 50, 60, 70 and 80 dB, black line, and the responses of a model with second order micromechanics and 3D tapered fluid coupling, obtained using multi-objective optimization to identify the micromechanical poles and zeros, blue lines. The estimated data selected are based on the smallest value of NMSE for amplitude.

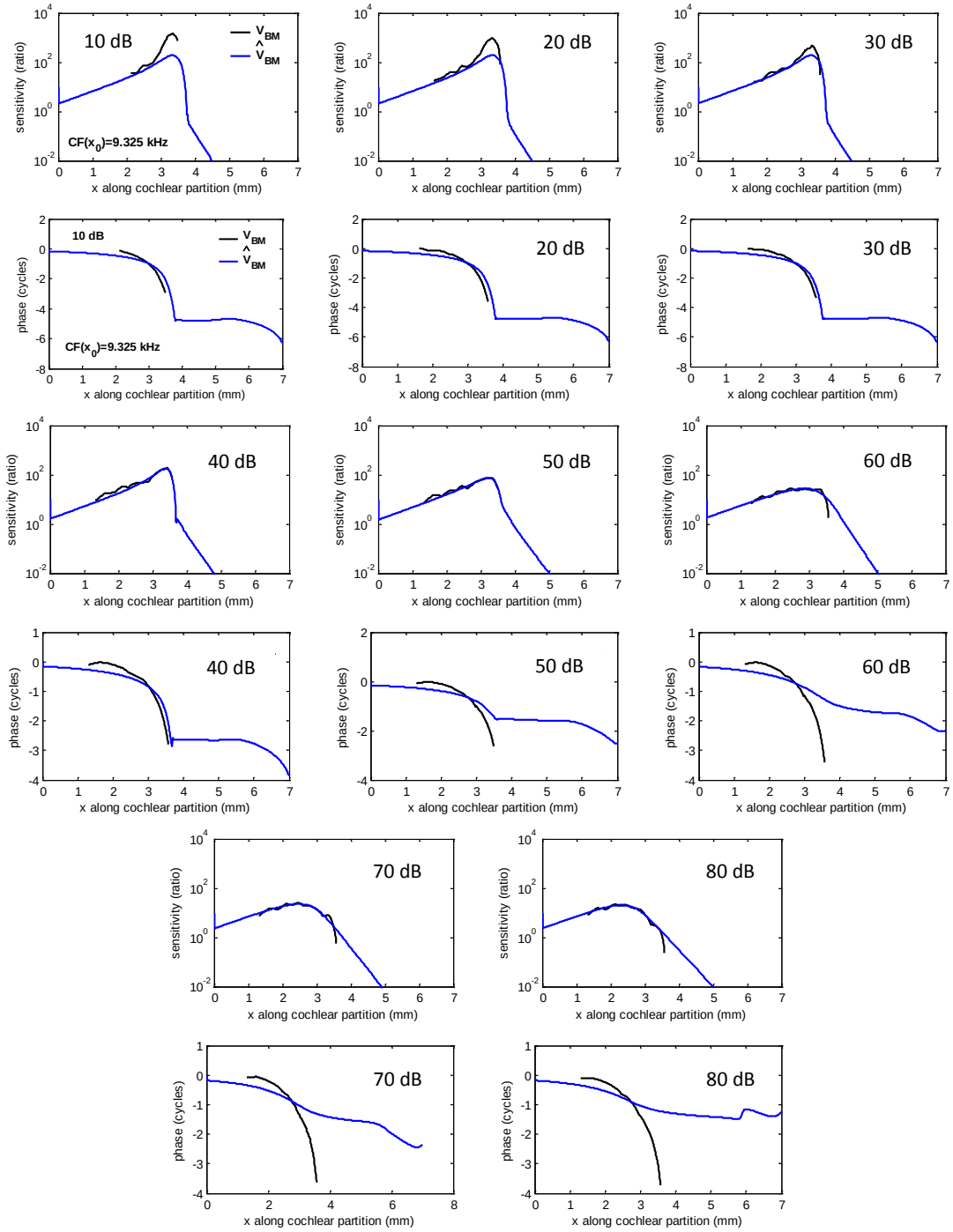

Figure 5.49 Comparison of amplitudes and phases of the BM responses measured by Lee *et al.* (2015) for a CF of 9.325 kHz and SPLs of 10, 20, 30, 40, 50, 60, 70 and 80 dB, black line, and the responses of a model with first order micromechanics and 3D tapered fluid coupling, obtained using multi-objective optimization to identify the micromechanical poles and zeros, blue lines. The estimated data selected are based on the smallest value of NMSE for amplitude.

Table 5.6 The estimated parameters for the zero, and, and the poles,and of the micromechanical model obtained in 3D tapered box model for the active and passive cochlea cases at CF(x_0) = 9.325 kHz, together with the normalised mean square error, NMSE, for amplitude and phase.

3D tapered									
Active	Ω_1	Q_1	Ω_2	Q_2	Ω_3	Q_3	m_0	NMSE Amplitude	NMSE Phase
10 SPL	1.37	0.14	0.83	2.07	2.84	3.86	0.28	0.001	2.16
20 SPL	1.47	0.40	1.96	7.66	0.90	1.84	0.17	0.007	1.16
30 SPL	1.00	1.52	0.91	2.45	1.23	6.77	0.11	0.006	3.04
40 SPL	7.80	8.07	6.50	8.52	1.00	9.90	0.30	0.032	2.01
50 SPL	0.51	4.06	0.50	3.57	1.05	3.54	0.16	0.004	3.02
60 SPL	0.65	1.03	0.94	8.44	0.48	1.18	0.46	0.005	2.35
70 SPL	0.83	5.84	0.72	1.03	0.86	9.95	0.23	0.006	2.44
80 SPL	2.39	0.48	0.91	0.84	0.92	0.88	0.95	0.007	2.39

3D tapered					
Passive	Ω	Q	m_0	NMSE Amplitude	NMSE phase
10S PL	1.15	9.95	0.10	0.71	2.82
20 SPL	1.17	9.93	0.10	0.56	2.98
30 SPL	1.20	9.94	0.20	0.23	3.17
40 SPL	1.07	9.90	0.17	0.008	1.94
50 SPL	1.04	3.48	0.20	0.008	2.42
60 SPL	1.30	0.82	0.10	0.02	2.44
70 SPL	0.86	0.86	0.16	0.008	2.52
80 SPL	0.66	0.98	0.27	0.007	2.34

5.8. Discussion

Measurement data is used to investigate the dynamics of the cochlea using inverse methods. Initially, Shera's method is investigated using chinchilla data and the estimated wavenumber confirms that there are active elements in the organ of Corti. Smoothing and interpolation in the time domain and the frequency domain have a large effect on the estimated results, which can reduce the error. There are, however, no clear indications from the real and imaginary parts of the wavenumber showing that the cochlea is changing from active to passive with different sound pressure levels.The direct inverse method is also tested using the chinchilla data, which shows good estimated results along the cochlear partition, although the phase of estimated response has less cycles than the measured data due to noisy data. Finally, mouse data, which can show good examples of how the BM response changes with excitation level, are used for the direct inverse method, the amplitudes of the estimated results show amazing agreement with measured data, even though the phases of the estimated results are only reasonably fitted with the measured data. It also seems that the tapering does not have significant effect on the estimated results in order to improve the estimation. It is interesting to find that, based on the values of NMSE, the 3D fluid coupling does not show significant

effect on the estimated results in order to improve the estimation either, but based on the figures, the 3D fluid coupling shows significant effect on the estimated results in order to improve the estimation. Also it is surprisingly found that the 3D fluid coupling has significant effect on improving the estimated results if another optimization method is used, which is given the details in Appendix H. The estimated parameters and poles/zeros show relative trends with variation of excitation level (from being active to being passive). The local and coupled response, calculated from pole/zero clearly show the variation from being active to being passive, which means that the peak response of BM gradually decreases, namely it can not have much energy (only absorbing energy when cochlea is passive, absorbing and generating energy when cochlea is active). Wavenumber calculated from the local response shows the presense of active element and the variation from being active to being passive with variation of SPL, which means that the imaginary part of wavenumber goes from a positive value (generating energy) when the cochlea is active, and this positive value gradually disappears when the cochlea gradually becomes passive. Those findings are also shown in the Neely and Kim model.

The one objective optimization method is also investigated in all cases, as described in Appendix H, the estimated results show that there are small gaps between the amplitude of the estimated BM response and mouse data from SPL of 60 dB to 80 dB, but the phases fit very well with mouse data. The estimated paramters and poles and zeros positions are also calculated to show relative trend along SPL. The local and coupled response, wavenumber calculated from pole/zero also clearly show the variation of from being active to being passive. The passive model derives bad results for the amplitude of BM response, but the phase is in good agreement with mouse data, the 3D fluid coupling can also improve the estimated results.

Chapter 6

Conclusions and future work

6.1. Conclusions

Inverse methods for modelling the cochlear mechanics have been explored for many years. Through those methods, some of the hypothesises about the action of the cochlea have been tested by connecting the cochlear models with experiments. However, some problems with these techniques have a significant effect on the results, with the most important shortcoming being the "ill-posed" problem. Therefore, it is worthwhile developing new inverse methods to get stable results by combining the more complicated cochlear models with experiment data, which is then used to get insight into the physical mechanics of the real cochlea.

A 1D and a 3D uniform box model of passive cochlea are first presented and different inverse methods are reviewed and tested on these models. de Boer's first inverse method is successful in the 1D uniform box model, no matter when the "measured" BM velocity, V_{BM}, is given at a fixed frequency or at a fixed position, which means that V_{BM} is calculated at a fixed frequency (1 kHz for instance) or at a fixed position (21 mm for instance) in the 1D uniform box model of passive cochlea, and this BM velocity is taken as the "measured" BM velocity, based on the theoretical investigation. This method can not be applied successfully in the 3D uniform box model, however, due to small errors of V_{BM}. de Boer's second inverse method is also investigated, this method can be successfully applied to the 1D and 3D uniform box model, when V_{BM} is given at fixed frequencies, however, when V_{BM} is given at fixed positions, the transformation method is used, there is missing data for the transformed V_{BM}, so that it cannot be used with de Boer's second inverse method. Shera's inverse method is also investigated in the 1D and 3D uniform box model. At first, this method is successful in the 1D uniform box model when the "measure" BM velocity is given at a fixed frequency. Then the transformation method is used to transform the BM velocity from the frequency domain to the spatial domain, even though there will be part of data of the BM responses missing, this inverse method works very well in the 1D uniform box model, from which can be derived the expected BM admittance, however, if V_{BM} is given in the 3D uniform box model, the wavenumber of BM admittance cannot be derived successfully using Shera's inverse method, which is due to small errors of V_{BM} in the 3D uniform box model. A direct

inverse method is then proposed, to estimate the poles and zeros of the micromechanical model to match the measurement data using optimization methods. At first, when this method is used in the 1D and 3D uniform box model of passive cochela, the estimated results can successfully match to the "measured" data given in the 1D and 3D uniform box model.

The uniform box model is then extended to be a tapered box model. Previous measurements of the fluid chambers area variations along the length of the cochlea for various mammals are used, to calculate variation of the effective area that determines the 1D fluid coupling. The square root of this effective area is found to vary surprisingly linearly along the cochlea length in mammalian species. Although the pressure distributions are very different between the uniform and tapered box models, the distribution of the coupled BM response are very similar, although the overall level of the response in the tapered model is about 10 dB greater than that in the uniform model. The direct inverse method is also tested in the 1D and 3D tapered box model of passive cochlea to investigate the effects of tapered shape on the direct inverse method. It is found that the tapered shape does not have effect on the amplitude of the estimated BM response, but have a slight effect on the phase of the estimated BM response around the characteristic place

The cochlea is close to passive at high sound pressure levels, while it becomes active at low sound pressure levels. Therefore, the direct inverse method should be also tested in an active cochlear model. The Neely and Kim model of the cat cochlea is selected to perform these tests. At first, some important proporties of this model are investigated indicating the fact that the BM response is sharper when the cochlea is active than the passive case. When the cochlea is passive, one pair of poles and one pair of zeros positions are almost coincident in the Neely and Kim model, and the effect of this pole and zero pair are cancelled, so that there is effectively only one pair of poles left. When the cochlea becomes active, the pair of poles those are close to the zeros in the passive cochlear case moves away from those of the zeros, so that there are two distinct pairs of poles and one pair of zeros when the cochlea is active. A new formulation of the BM admittance function is then proposed based on its poles and zeros. It is found that the required parameters (natural frequencies and Q factors of the poles and zeros for the BM admittance) in this function are not entirely constants in the Neely and Kim model, but vary with positions and feedback gains. The direct inverse method is tested using two types of optimization methods. At first, one objective function is tested, V_{BM} is given at fixed frequencies and fixed positions in the Neely and Kim model of cat cochlea, the

amplitude of the estimated result fits well with the “measured” data around the peak area, but the phase of the estimated result is about one cycle less than the “measured” data. Then a multi-objective function method is tested, and it is found that both the amplitude and the phase of the estimated results fit well with the “measured” data, V_{BM} given at fixed frequencies. It was thus found that two objectives optimization method is better than one objective optimization method. If the estimated parameters along the cochlear partition are assumed to be constant, equal to the average values, the new estimated results are in bad agreement with the “measured” data, which reveals that Ω, Q, and m_0 should vary at different positions.

When considering data from measurements, Shera’s inverse method is first tested with the chinchilla data, it was originally developed for and it works successfully to derive the wavenumber. These results show that the real part of the wavenumber starts out small, in the basal region, and increases until it has a peak near the characteristic place, and then decreases again towards the apical locations. The imaginary part of the wavenumber starts out close to zero and becomes negative close to the cut-off region, which confirms that there are active elements in the cochlea. Then the sensitivities of the estimation to assumptions in Shera’s method are investigated. It is shown that different “start” points, truncation points and data smoothing all have effects on the derived wavenumber, which should be carefully considered. Finally, the real and imaginary parts of the wavenumber at different sound pressure levels are investigated. There are, however, no clear indications from these that the cochlea is changing from active to passive with different sound pressure levels. The chinchilla data is also used for the direct inverse method, from which it is found that the amplitude of the estimated BM reponse is in agreement with the measurement data, while the estimated phase has always less cycles than the measured data, due to the noisy data. It should be noted that the BM response calculated using the model is normalized with respect to the stapes velocity, while the chinchilla measurement data are based on the auditory nerve fibre, so that the absolute level of the response is unknown. Then, other sets of available measurement data, from mouse by Lee *et al* (2015) are used. There are four sets of mouse data measured at different characteristic positions. Through the direct inverse method, those estimated amplitude of BM velocity fits very well compared with the measured data along the whole cochlear partition, but the phase is only reasonably fitted with the meausred data. The direct inverse method is then tested, using different passive and active box models with the mouse data. It is found that in the passive models, the amplitudes of estimated responses can match the measured

data from 40 SPL to 80 SPL successfully, but from 10 SPL to 30 SPL, the estimated responses using the passive models can not reach the peak values. For the active box models, 3D fluid coupling is shown to have a significant effect on the estimated results, and improves the estimation, while the tapering do not have significant effect on the estimated results. The estimated values of normalised natural frequency and Q factor with different sound pressure levels show certain variations with varying sound pressured levels. The estimated positions of poles and zeros are then derived, based on the averaged values of estimated parameters, and average values of pole and zeros at four different fixed positions with different sound pressure levels. It can be seen that there are always two pairs of poles and one pairs of zeros, even at high sound pressure levels. The two pairs of poles are close to each other, poles and zeros are always complex values. From 10 SPL to 80 SPL, one pairs of zeros move towards to one pair of poles gradually, so that the cochlea makes the transition from avtive to passive, in a similar way to the Neely and Kim model. The local and coupled response are derived using poles and zeros, which show the variation of from being active to being passive with variation of SPL, wavenumber calculated from the local response shows certification of active element in the micromechanics of cochlea.

6.2. Future work

For the selected five species, more accurate physical parameters could be derived. For instance, the fluid chamber height for human was derived from 0 mm to 26.5 mm, there is still missing data, which leads to error of the estimated data. Also, other data fitting methods, polynomial fitting for instance, could be used to derive the variations of cochlear fluid chamber area and BM width, which can fit measurement data better. More complicated cochlear models could also be investigated to test the direct inverse method. For instance, multiple degree of freedom system or nonlinear systems for the BM admittance could be proposed, which may match the measured data better.

Other active cochlear models, for instance Nobili's model (Nobili *et al.*, 1995), could be selected to investigate the poles and zeros in those models. These active cochlear models could be compared to find difference between them. Other optimization methods should be investigated to try to find the better estimated results, which means that the calculated poles and zeros position can more clearly explain some of the cochlear features .

Other features for the cochlea, for instance, nonlinearity and compression, could also be incorporated with the direct inverse method, to investigate the features of poles and zeros. Other new objective functions, for instance the real and imaginary part of response, could be also used for optimization, to check if better results can be obtained.

More measurement data could be used to find out whether the general trends of the positions of poles and zeros are the same. The nonlinearity, compression, amplifier *etc*, of the cochlea could then be investigated using inverse method, those features can be used to compare with the theoretical reponses of the active cochlear model for the same species, thus validating the cochlear models.

Appendix A.

Certification of equivalence between de Boer's transformation method and Shera's transformation method

If $f_n(x) = f_B e^{-x/\ell}$,

For de Boer's transformation method: Assuming position, *x*, given when measured frequency,

$f = f_n(x) \Rightarrow f = f_B e^{-x/\ell} \Rightarrow x = \ell \ln(f_B / f)$

For Shera's transformation method: the general local scaling symmetry,

$V_{BM}(x, f) = fun(f / CF(x))$, if assuming that $CF(x) = f_B e^{-x/\ell}$ as above. So,

$$\frac{f}{CF(x_0)} = \frac{f_B e^{-x/\ell}}{f_B e^{-x_0/\ell}} = e^{(x_0 - x)\ell} \Rightarrow x = x_0 + \ell \ln(\frac{CF(x_0)}{f}), \text{ but } CF(x_0) = f_B e^{-x/\ell}$$

$$\Rightarrow x = x_0 + \ell \ln(\frac{f_B}{f}) - x_0 \Rightarrow x = \ell \ln(\frac{f_B}{f}) \text{ as above.}$$

Therefore, these two methods are equicalent.

Appendix B.

Procedure of important methods and formulations

B.1. De Boer's first inverse method in the 1D uniform box model

The long-wave model, also known as the 1D model is initially reviewed. The Fourier transforms, $P(k)$ and $V(k)$ of the pressure $p(x)$ and the BM velocity $v_{BM}(x)$ are defined respectively,

$$p(x) = \int_{-\infty}^{\infty} P(k)\exp(-ikx)dk, \tag{B.1}$$

$$v_{BM}(x) = \int_{-\infty}^{\infty} V_{BM}(k)\exp(-ikx)dk. \tag{B.2}$$

the second derivative of $p(x)$ with respect to x has $-k^2P(k)$ as its Fourier transform, therefore the model equation , which is $\frac{d^2}{dx^2}p(x) - \frac{2i\omega\rho}{hz(x)}p(x) = 0$, can be written as

$$\int_{-\infty}^{\infty} k^2P(k)\exp(-ikx)dk = \frac{i\omega\rho}{h}v_{BM}(x). \tag{B.3}$$

from this relation $k^2P(k)$ turns out to be proportional to $V_{BM}(k)$, the Fourier transform of $v_{BM}(x)$. Introduce the function $Q(k)$ by

$$Q(k) = 1/k^2h, \tag{B.4}$$

then $P(k)/Q(k)$ becomes $i\omega\rho$ times $V_{BM}(k)$.

Assume now that the cochlea is excited in such a way that only one wave of the form $\exp(-ikx)$ and unit amplitude exists. The pressure $P(k)$ of this wave is obviously $i\omega\rho$ times $Q(k)$ hence represents the impedance of the oscillating fluid column as seen from the BM, in the case where a wave exists with wavenumber k. This function expresses solely a property of the fluid wave.

The model equation retains the same form

$$\int_{-\infty}^{\infty} \frac{P(k)}{Q(k)} \exp(-ikx)dk = -2i\omega\rho \frac{p(x)}{z_{BM}(x)}, \tag{B.5}$$

in terms of the BM velocity $v_{BM}(x)$, with its Fourier transform $V_{BM}(x)$, the fundamental equation for the model can be formulated as

$$\frac{2i\omega\rho}{Z_{BM}(x)} \int_{-\infty}^{\infty} Q(k) V_{BM}(k) \exp(-ikx)dk = -v_{BM}(x), \tag{B.6}$$

where ω is the radian frequency, ρ the fluid density, $Z_{BM}(x)$ the BM impedance, $V_{BM}(k)$ the Fourier transform of $v_{BM}(x)$, and $Q(k)$ a function that describes the dynamics of the fluid contained in the cochlea channels and thus includes the effects of dimensionality. In the form $2i\omega\rho Q(k)$ the latter function represents the impedance of the fluid when it support a wave with wavenumber *k*. The $Q(k)$ function is analogous to the effective height function used by Steele and his collaborators in their analysis of three-dimensional models (see, e.g., Steel and Taber, 1979, 1981).

In the de Boer/van Bienema method the function $Q(k)$ for the 1D model is approximated by a rational function of *k*, as follows:

$$Q(k) \approx \frac{f_0 \varepsilon}{hk^2}, \tag{B.7}$$

here, ε is the proportion of the width occupied by the BM, *h* the effective height of the channel, f_0 is appropriately chosen dimensionless constant.

The main point in using a rational function like equation (B.7) for $Q(k)$ is that the integral (B.6) reduces to a differential equation when $Q(k)$ is a rational function of *k*. equation (B.6) is first rewritten in the following form as

$$Q(k) = \frac{F_0}{k^2}, \tag{B.8}$$

where $F_0 = \frac{\varepsilon f_0}{h}$.

A new variable $U(k)$ is introduced as

$$U(k) = V(k) \Big/ k^2 . \tag{B.9}$$

According to equations (B.2), (B.8) and (B.9), equation (B.6) reads in terms of the new unknown $V(k)$ as

$$\frac{1}{Z_{BM}(x)} \int_{-\infty}^{\infty} F_0 U(k) e^{-ikx} dx = \frac{i}{2\omega\rho} \int_{-\infty}^{\infty} k^2 U(k) e^{-ikx} dk, \tag{B.10}$$

under the integral sign, a factor *k* can equally well be introduced by taking *i* times the derivative of e^{-ikx} with respect to *x*. Following this idea, the integral equation (B.10) reduces to

$$-\frac{2\omega\rho}{iZ(x)} F_0 u = -\frac{d^2 u}{dx^2}, \tag{B.11}$$

which is recognized to be an ordinary differential equation of the second order. The unknown variable *v* actually *u(x)*, is the Fourier transform of *U(k)*. Once this equation is solved for *u(x)*, it remains to find the BM velocity $v_{BM}(x)$ from the spectral representation, it is easily seen that $v_{BM}(x)$ relates to *u(x)* as

$$v_{BM}(x) = -\frac{d^2 u}{dx^2}. \tag{B.12}$$

Since the same expression appears as the right-hand side of equation (B.11) we can equally well evaluate the left-hand side of that equation to find $v_{BM}(x)$

$$v_{BM}(x) = -\frac{2\omega\rho}{iZ(x)} F_0 u. \tag{B.13}$$

For the inverse solution, first, the "given" $v_{BM}(x)$ is substituted into equation (B.12) and this equation is solved for *u(x)*. The BM impedance $Z_{BM}(x)$ is then derived from $u(x)$ via the equation (B.11).

Equation (B.12) can be solved for $u(x)$ by double integrating $v_{BM}(x)$, which is given by

$$u(x) = -\int_{x_0}^{x} \int_{x_0}^{x'} v_{BM}(x")dx"dx' + v_{10} + v_{00}. \tag{B.14}$$

Here v_{10} and v_{00} re assumed to be zero, $x_0 = x_L$. Therefore, the BM impedance $Z_{BM}(x)$ can be solved, which is given by

$$Z_{BM}(x) = \frac{2\omega\rho}{iv_{BM}(x)} F_0 \int_{x_0}^{x} \int_{x_0}^{x'} v_{BM}(x")dx"dx', \tag{B.15}$$

so

$$Y_{BM}(x) = \frac{1}{Z_{BM}(x)} = \frac{iv_{BM}(x)}{2\omega\rho F_0 \int_{x_0}^{x} \int_{x_0}^{x'} v_{BM}(x")dx"dx'}. \tag{B.16}$$

B.2. De Boer's first inverse method in the 3D uniform box model

For the 3D uniform box model, Q factor has a different form in equation (B.6), as follows:

$$Q(k) \approx \frac{f_0\varepsilon}{hk^2} \frac{1 + b_0k^2h^2}{1 + d_0kh}, \tag{B.17}$$

here, b_0 and d_0 are appropriately chose dimensionless constants.

So,

$$Q(k) = \frac{F_0}{k^2} \frac{1 + B_0k^2}{1 + D_0k}, \tag{B.18}$$

where $B_0 = b_0h^2$, $D_0 = d_0h$

When, the new variable $U(k)$ is equal to

$$U(k) = \left[V(k) \Big/ k^2 \right] (1 + D_0k)^{-1}, \tag{B.19}$$

so that equation (B.6) reads in terms of the new unknown $V(k)$

$$\frac{1}{Z_{BM}(x)} \int_{-\infty}^{\infty} F_0(1 + B_0k^2)U(k)e^{-ikx}dx = \frac{i}{2\omega\rho} \int_{-\infty}^{\infty} k^2(1 + D_0k)U(k)e^{-ikx}dk, \tag{B.20}$$

under the integral sign, a factor k can equally well be introduced by taking i times the derivative of $\exp(-ikx)$ with respect to x following this idea, the integral equation (B.20) reduced to

$$-\frac{2\omega\rho}{iZ(x)}F_0(u-B_0\frac{d^2u}{dx^2})=-\frac{d^2u}{dx^2}-iD_0\frac{d^3u}{dx^3}, \tag{B.21}$$

which is recognized to be an ordinary different equation of the third order, the unknown variable v actually $u(x)$, is the Fourier transform of $U(k)$, once this equation is solved for $u(x)$, it remains to find the BM velocity $v_{BM}(x)$ from the spectral representation, it is easily seen that $v_{BM}(x)$ relates to $u(x)$ as follows.

$$v_{BM}(x)=-\frac{d^2u}{dx^2}-iD_0\frac{d^3u}{dx^3}, \tag{B.22}$$

which is equal to

$$v_{BM}(x)=-\frac{2\omega\rho}{iZ_{BM}(x)}F_0(u-B_0\frac{d^2u}{dx^2}), \tag{B.23}$$

for the inverse solution, first, the "given" $v_{BM}(x)$ is substituted in equation (B.22) and this equation is solved for $u(x)$. The BM impedance $Z_{BM}(x)$ is then derived from $u(x)$ via the equation (B.23).

Equation (B.22) can be solved for $u(x)$ in two stages by introducing the function $u_2(x)$ as the second derivative of $u(x)$:

$$u_2(x)\equiv\frac{d^2u(x)}{dx^2}, \tag{B.24}$$

with this substitution, equation (B.22) becomes a simple first-order differential equation in $u_2(x)$:

$$u_2(x)+iD_0\frac{du_2(x)}{dx}=-v_{BM}(x), \tag{B.25}$$

which can be solved in analytical form, for instance:

$$u_2(x) = \left[u_{20} - \left(\frac{i}{D_0} \right) \int_{x_0}^{x} e^{\frac{-ix'}{D_0}} v_{BM}(x')dx' \right] \times e^{ix/D_0}, \tag{B.26}$$

where, $x_0 = x_L$, u_{20} can also be made zero. Integrating $u_2(x)$ twice, $u(x)$ can be written as follows:

$$u(x) = \int_{x_0}^{x} \int_{x_0}^{x'} u_2(x'')dx''dx' + u_{00} = \int_{x_0}^{x} (x - x')u_2(x')dx' + u_{10}(x - x_0) + u_{00}, \tag{B.27}$$

in this case, u_{00} and u_{10} are made zero.

Therefore, the final form of $Y_{BM}(x)$ is like the following:

$$Y_{BM}(x) = \frac{iv_{BM}(x)}{2\omega\rho F_0 \begin{pmatrix} \int_{x_0}^{x} (x - x') \left[-\left(\frac{i}{D_0} \right) \int_{x_0}^{x} e^{\frac{-ix'}{D_0}} v_{BM}(x')dx' \right] \times e^{ix/D_0} dx' \\ -B_0 \left[-\left(\frac{i}{D_0} \right) \int_{x_0}^{x} e^{\frac{-ix'}{D_0}} v_{BM}(x')dx' \right] \times e^{ix/D_0} \end{pmatrix}}. \tag{B.28}$$

B.3. De Boer's second inverse method

As has been described by de Boer in chapter 1, to prepare for greater generality, there is the reformulated solution in the way described by Allen (1977), Allen and Sondhi (1979), and Mammano and Nobili (1993). First, divide the x-axis into N discrete points x_i ($i = 1, \ldots, N$). The pressure in the fluid $p(x, \omega)$-close to the BM in the upper channel-and the BM velocity $v_{BM}(x, \omega)$ are represented by column vectors $\mathbf{p}$ and $\mathbf{v}$, both of length N. The dydrodynamics of the fluid in the model is described by a matrix $\mathbf{G}$ of size $N \times N$ which represents the Green's function. The pressure $\mathbf{p}$ can then be expressed as

$$\mathbf{p} = \mathbf{i}\omega\rho(\mathbf{G}\mathbf{v} + \mathbf{s}v_{st}), \tag{B.29}$$

here s is a column vector which represents the way the stapes boundary condition expresses itself in the pressure $p(x, \omega)$, and v_{st} is the stapes velocity. for a model of given geometry the matrix $\mathbf{G}$ and s express the hydrodynamics of the fluid constrained as it is by the geometry of the model. furthermore, $\mathbf{G}$ and s incorporate the boundary conditions methioned above in connection with the k domain method. assume further that pressure and velocity are related via the BM impedance, $Z_{BM}(x, \omega)$ as

$$\mathbf{p} = -\frac{1}{2}\mathbf{Z}_{BM}\mathbf{v}, \tag{B.30}$$

where $\mathbf{Z}$ is a diagonal $N \times N$ matrix which has $Z_{BM}(x_i, \omega)$ ($i = 1, \ldots, N$) in its main diagonal. The final equation can given by

$$(i\omega\rho\mathbf{G} + \frac{1}{2}\mathbf{Z}_{BM})\mathbf{v} = -i\omega\rho s v_{st}, \tag{B.31}$$

In 1D uniform box model, $i\omega\rho\mathbf{G} = \mathbf{Z}_{FC}$, equation (B.29) can be rewritten as

$$\mathbf{p} = \mathbf{Z}_{FC}\mathbf{v}, \tag{B.32}$$

where $\mathbf{Z}_{FC}$ is the fluid coupling matrix, which is determined by fluid chamber area. $\mathbf{v}$ is assumed to include the stapes and BM velocity.

Because

$$\mathbf{v} = \mathbf{Y}_{BM}\mathbf{p}, \tag{B.33}$$

if $\mathbf{v}$ is given, the pressure difference can be calculated at first, and then for each element

$$\mathbf{Y}_{BM}(n) = \frac{\mathbf{v}(n)}{\mathbf{p}(n)}. \tag{B.34}$$

B.4. Shera's inverse method

As a motivating example, simple wave propagation in a stretched string is considered first. When a sinusoidal driving force is applied at the left hand side of a semi-infinite, the displacement, $d(x,t)$, can be given by

$$d(x,t) = d_o e^{\gamma x}\cos(\omega t - \kappa x + \phi_o), \tag{B.35}$$

where $\omega = 2\pi f$, d_o and ϕ_o are the initial amplitude and phase. The wavelength, λ, is determined by the propagation coefficient, $\kappa = 2\pi/\lambda$, and the spatial decay of the wave is determined by the gain coefficients, γ, respectively. κ and γ are often combined into a single complex number, k, known as the complex wavenumber, as

$$k \equiv \kappa + i\gamma. \tag{B.36}$$

Initially, we need to find the relation between wavenumber and BM velocity. The one–dimensional wave equation, in terms of the average pressure $\overline{P}$ is given by

$$(\partial_x^2 + k^2)\overline{P} = 0, \tag{B.37}$$

where $k(x,f)$ is complex wavenumber.

The equations for the conservation of fluid mass and momentum can be combined to show that

$$\partial_x^2 \overline{P} = bZ_f V_{BM}, \tag{B.38}$$

where b is the BM width and $Z_f(f)$ is the effective acoustic impedance of the fluid equal to $2i\omega\rho / h$, where h is the effective height of the fluid chambers, combining equations (B.37) and (B.38), gives

$$k^2 \overline{P} = -bZ_f V_{BM}, \tag{B.39}$$

so that

$$\overline{P} = -bZ_f V_{BM} / k^2. \tag{B.40}$$

If the function $V_{BM}(x, f)$ is known, whether by model or by measurement, Equation (56) can be solved for $\overline{P}(x, f)$ by double integration as

$$\overline{P}(x, f) = bZ_f(f)\int_x^L dx' \int_{x'}^L V_{BM}(x'', f)dx'', \tag{B.41}$$

where x' and x'' are dummy integration variables. The constants of integration are chosen to satisfy the boundary conditions (in this case, $\overline{P} = 0$ and $\partial_x \overline{P} = 0$ at the helicotrema, although the physical justification for the latter condition is not clear). Combining equation (B.40) and (B.41), the square of the wavenumber can be expressed as

$$k^2(x, f) = {-V_{BM}(x, f)} \Big/ {\int_x^L dx' \int_{x'}^L V_{BM}(x'', f)dx''}. \tag{B.42}$$

The wavenumber $k(x, f)$ depends only on the given BM response function, $V_{BM}(x)$, and is independent of Z_f and the value of h, the effective height of fluid chamber in the model. In other words, fixing $V_{BM}(x, f)$ yields same wavenumber irrespective of whether the model is everywhere long wave, or short wave, or manifests a transition between the two, as in the real cochlea.

This wavenumber inversion formula indicates how to find the complex wavenumber from the traveling wave. The propagation and gain functions are then found by taking the real and imaginary parts of the wavenumber as

$$\kappa(x, f) = \mathrm{Re}\, k(x, f) \quad \text{and} \quad \gamma(x, f) = \mathrm{Im}\, k(x, f). \tag{B.43}$$

The sign of the square root of k^2 is chosen by assuming that the wave travels forward in the vicinity of its peak. Problems with branch cuts can be minimized by defining the square root as $\sqrt{k^2(x)} = \sqrt{|k^2(x)|}e^{i\theta/2}$, where $\theta(x)$ is the unwrapped phase of $k^2(x)$.

B.5. Far-field pressure in the tapered box model (Ni,2011)

If the areas of the upper fluid chamber, SM and SV, and the lower fluid chamber, ST, vary along the length of the cochlea as $A_1(x)$ and $A_2(x)$, the far-field component of the pressure will be still determined by the continuity and momentum equations. Assuming that the longitudinal fluid velocity in a single chamber, averaged across its cross-sectional area, is $\bar{u}(x)$, and that the radial BM velocity averaged across the width of the chamber is $\bar{v}(x)$, then the continuity equation for this chamber can be written as

$$\frac{\partial}{\partial x}\left[A(x)\bar{u}(x)\right] = W(x)\bar{v}(x), \tag{B.44}$$

where in general the CP width also varies along the cochlear as $W(x)$. This is equivalent to the equation used by Peterson and Bogert (1950), except that the fluid is assumed here to be incompressible.

The momentum equation can also be written in terms of the complex pressure averaged across the cross-sectional area, $\bar{p}(x)$, as

$$\frac{\partial \bar{p}(x)}{\partial x} = -i\omega\rho\bar{u}(x). \tag{B.45}$$

Substituting $\bar{u}(x)$ in equation (B.45) into equation (B.44) gives an expression for $\bar{p}(x)$ in terms of $\bar{v}(x)$ as

$$\frac{\partial}{\partial x}\left[A(x)\frac{\partial \bar{p}(x)}{\partial x} \right] = -i\omega\rho W(x)\bar{v}(x). \tag{B.46}$$

This is an incompressible form of Webster's horn equation, which is described by Fletcher and Rossing (1998), for example.

Applying equation (B.46) to the upper chamber, it can be written in terms of the modal BM velocity, $v(x)$, and the modal pressure $p_1(x)$, by noting that the velocity distribution in the radial direction at position x is equal to $v(x)\psi(y)$, so that

$$\bar{v}(x) = \frac{v(x)}{W(x)}\int_0^{W(x)} \psi(y)\,dy, \tag{B.47}$$

and since, in the far-field limit, the pressure is uniform over the BM, then the definition of the modal pressure gives

$$p_1(x) = \frac{\bar{p}(x)}{W(x)}\int_0^{W(x)} \psi(y)\,dy. \tag{B.48}$$

If the BM velocity is a half sinusoid over a distance B on one side of the fluid chamber, as assumed for the uniform case, then in this case

$$\frac{1}{W(x)}\int_0^{W(x)} \psi(y)dy = \frac{2}{\pi}\sqrt{\frac{2B(x)}{W(x)}}. \tag{B.49}$$

The far-field fluid coupling equation in the upper chamber can thus be written in terms of the modal pressure, and modal velocity as

$$\frac{\partial}{\partial x}\left[A_1(x)\frac{\partial}{\partial x}\left(p_1(x)\sqrt{\frac{W(x)}{B(x)}} \right) \right] = -\frac{8i\omega\rho}{\pi^2} v(x)\sqrt{W(x)B(x)}. \tag{B.50}$$

In general, however, the model pressure in the lower fluid chamber is similarly related to the modal BM velocity by

$$\frac{\partial}{\partial x}\left[A_2(x)\frac{\partial}{\partial x}\left(p_2(x)\sqrt{\frac{W(x)}{B(x)}}\right)\right]=\frac{8i\omega\rho}{\pi^2}v(x)\sqrt{W(x)B(x)}. \tag{B.51}$$

The integral of $i\omega\rho v(x)$ with respect to x is thus equal to both of the expressions below

$$\begin{aligned}&\frac{8i\omega\rho}{\pi^2}\int_0^x v(x')\sqrt{B(x')W(x')}dx'\\&=A_2(x)\frac{\partial}{\partial x}\left(p_2(x)\sqrt{\frac{W(x)}{B(x)}}\right),\\&=-A_1(x)\frac{\partial}{\partial x}\left(p_1(x)\sqrt{\frac{W(x)}{B(x)}}\right)\end{aligned} \tag{B.52}$$

where x' is dummy integration variable, and the fact that both $\partial p_1(x)/\partial x$ and $\partial p_2(x)/\partial x$ are zero when x is equal to zero has been used to eliminate any constants of integration. The pressure gradients in the two chambers are thus related by

$$\frac{\partial}{\partial x}\left(p_2(x)\sqrt{\frac{W(x)}{B(x)}}\right)=-\frac{A_1(x)}{A_2(x)}\frac{\partial}{\partial x}\left(p_1(x)\sqrt{\frac{W(x)}{B(x)}}\right). \tag{B.53}$$

We assume that we can relate the far-field component of the modal pressure difference, $p_F(x)$ equal to $P_1(x)-P_2(x)$, to the modal BM velocity, $v(x)$, via the effective area $A_d(x)$ in the expression

$$\frac{\partial}{\partial x}\left[A_d(x)\frac{\partial}{\partial x}\left(p_F(x)\sqrt{\frac{W(x)}{B(x)}}\right)\right]=-\frac{16i\omega\rho}{\pi^2}v(x)\sqrt{B(x)W(x)}, \tag{B.54}$$

The integral of $v(x)$ thus equal to

$$\begin{aligned}&\frac{8i\omega\rho}{\pi^2}\int_0^x v(x')\sqrt{B(x')W(x')}dx'\\&=-\frac{A_d(x)}{2}\left[\frac{\partial}{\partial x}\left(p_1(x)\sqrt{\frac{W(x)}{B(x)}}\right)-\frac{\partial}{\partial x}\left(p_2(x)\sqrt{\frac{W(x)}{B(x)}}\right)\right].\end{aligned} \tag{B.55}$$

Using equation (B.53) and equation (B.55) to the final form of equation(17) allows the effective area for the pressure difference to be written (Zwislocki, 1953) as the same as equation(1).

An analytic solution to the pressure difference can be obtained for excitation of a single BM element, having a velocity of v_0 from $x_0 - \Delta$ to x_0, by integrating equation (B.54) and using the boundary condition that $\partial p_F(x)/\partial x$ is zero and assuming that $B(x)$ and $W(x)$ are independent of x at $x = 0$ to give

$$\frac{\partial}{\partial x}\left(p_F(x)\sqrt{\frac{W(x)}{B(x)}}\right)\Bigg|_{0 < x < x_0 - \Delta} = 0, \tag{B.56}$$

$$\frac{\partial}{\partial x}\left(p_F(x)\sqrt{\frac{W(x)}{B(x)}}\right)\Bigg|_{x_0 < x < L} = -\frac{16i\omega\rho\Delta v_0\sqrt{B(x)W(x)}}{\pi^2 A_e(x)}v(x). \tag{B.57}$$

The boundary condition that $p_F(x)$ is zero at $x = L$ and the fact that Δ is small compared with L can then be used to integrate these expressions again to give the pressure distribution of the far-field pressure difference as

$$\begin{aligned} p_F(x)\big|_{0<x<x_0-\Delta} &= -16i\omega\rho\Delta v_0\sqrt{\frac{B(x_0)W(x_0)B(x)}{W(x)}}\int_{x_0}^{L}\frac{1}{A_e(x')}dx', \\ p_F(x)\big|_{x_0<x<L} &= -16i\omega\rho\Delta v_0\sqrt{\frac{B(x_0)W(x_0)B(x)}{W(x)}}\int_{x}^{L}\frac{1}{A_e(x')}dx'. \end{aligned} \tag{B.58}$$

If the areas of the fluid chambers in the cochlear models are divided up into N discrete sections, as for the BM, equations (B.51), (B.52) and (B.44) can be used to calculate the effective area for the pressure difference at the n-th discrete element as $A_e(n)$, which is equal to $H_l(n)$ and $W_l(n)$. The integrals in equations (B.58) can be approximated by summations, and the linear approximations for $W(x)$, $H(x)$ and $B(x)$ can be used to give the pressure at the *n-th* element as

$$p_F(n)\big|_{0<n<n_0-1} = -16i\omega\rho\Delta^2 v_0\sqrt{\frac{B_l(n_0)W_l(n_0)B_l(n)}{W_l(n)}}\sum_{n'=n_0}^{N}\frac{1}{H_l^2(n')}, \tag{B.59}$$

$$p_{\mathrm{F}}(n)\big|_{n_0<n<N} = -16i\omega\rho\Delta^2 v_0 \sqrt{\frac{B_l(n_0)W_l(n_0)B_l(n)}{W_l(n)}} \sum_{n'=n}^{N} \frac{1}{H_l^2(n')}, \tag{B.60}$$

where $n_0 = x_0/\Delta$.

The assumed variation of $H_l(x)$, $W_l(x)$ and $B_l(x)$ along the length of the human cochlea, are discussed above. Equations (B.59) and (B.60) can be used to calculate the far-field contribution to the pressure difference in the non-uniform cochlea due to asymmetry in two fluid chambers. These results can be compared with the results for the uniform box model, in which all the geometric parameters are constant by assuming that these constant values are the averages of those, to give the dashed results, which means that equation (B.59) and (B.60) can be simplified into

$$P_F(x)|_{0<x<x_0-\Delta} = 2i\omega\rho\frac{(L-x_0)}{h_{av}}\Delta v_0, \tag{B.61}$$

$$P_F(x)|_{x_0<x<L} = 2i\omega\rho\frac{(L-x)}{h_{av}}\Delta v_0, \tag{B.62}$$

where h_{av} is average value of the effective height, equal to $\frac{\pi^2 W_{av} H_{av}}{8B_{av}}$, W_{av}, H_{av} and B_{av} are the average values of W_l, H_l and B_l.

Appendix C.

Variations of fluid chamber cross-sectional area and BM width from measurement data for other four species

C1. Guinea pig

C1.1. post-processing for the original geometrical data of guinea pig

Figure C.1 shows the variation of scala vestibule (SV), scala tympani (ST), and endolymphatic space-scala media (SM), cross-sectional areas devrived from measurement data for guinea pig, they all decrease along cochlea partition. SV stands for the upper area of the fluid chamber, ST and SM are combined to stand for the lower area of the fluid chamber. Figure C.2 shows the variation of effective area of fluid chamber, calculated using equation (3.1), the square root of this effective area, and the least square fit to this square root. It also shows that the fluid chamber area decreases along cochlear partition.

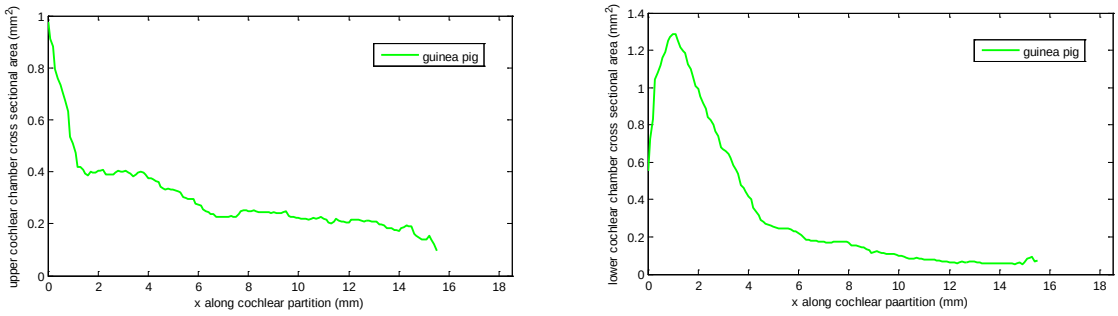

Figure C.1 $A_1(x)$ (upper area) and $A_2(x)$ (lower area) for guinea pig.

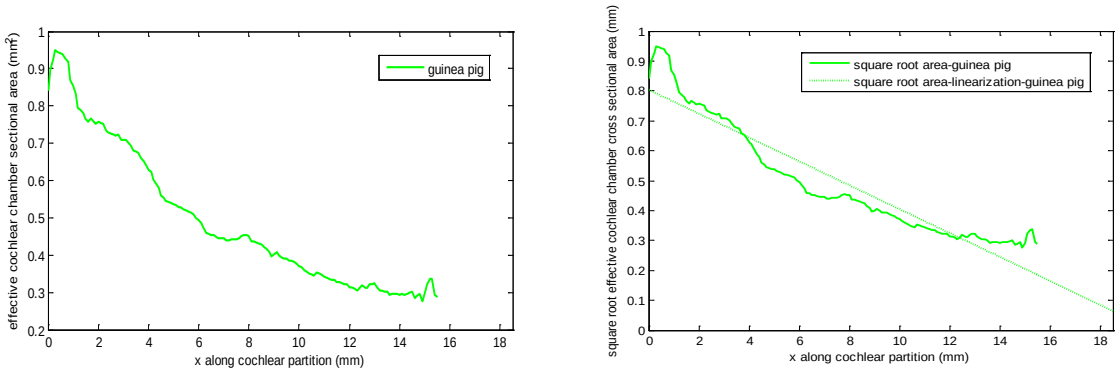

Figure C.2 Effective area of cochlear chamber for guinea pig and its square root (the solid line shows curve for the actual data, the dash line shows a least square fit of a linear variation for the square).

C2. Cat

C2.1. Post-processing for the original geometrical data of cat

Figure C.3 shows variations of the calculated upper and lower fluid chamber area along cochlear partition according to measurement data. Again, the effective area, square root of the effective area, and the least squarefit to the square root of fluid chamber area are shown in Figure C.4.

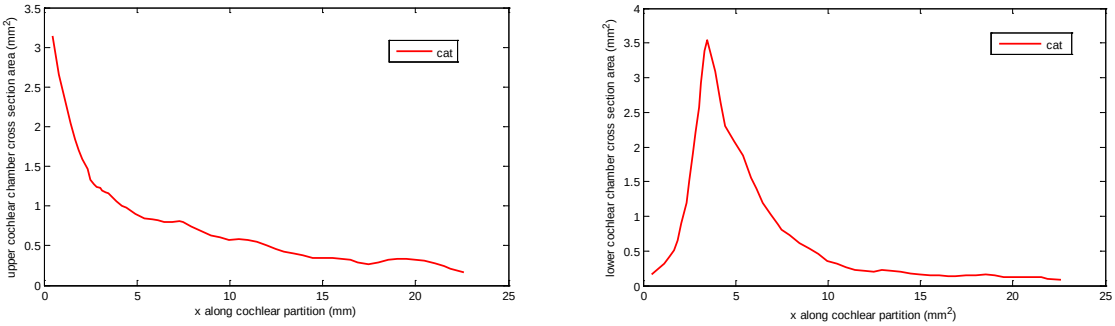

Figure C.3 $A_1(x)$ (upper area) and $A_2(x)$ (lower area) for cat.

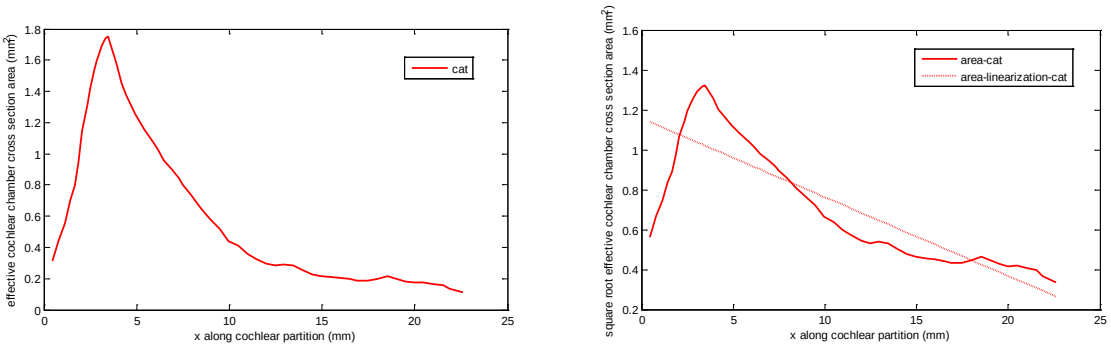

Figure C.4 Effective area of cochlear chamber for cat and its square root (the solid line shows curve for the actual data, the dash line shows a least square fit of a linear variation for the square).

C3. Chinchilla

C3.1. Post-processing for the original geometrical data of chinchilla

Figure C.5 shows variations of the calculated upper and lower fluid chamber area along cochlear partition according to measurement data from Figure C.9. Again, the effective area, square root of the effective area, and the least squarefit to the square root of fluid chamber area are shown in Figure C.6.

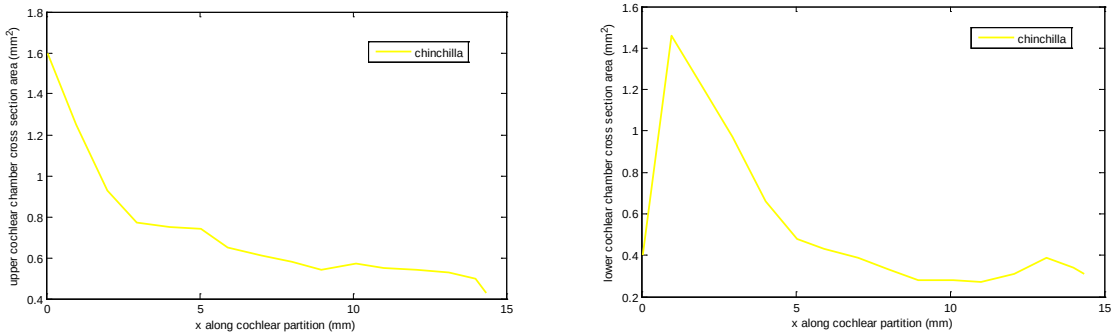

Figure C.5 $A_1(x)$ (upper area) and $A_2(x)$ (lower area) for chinchilla.

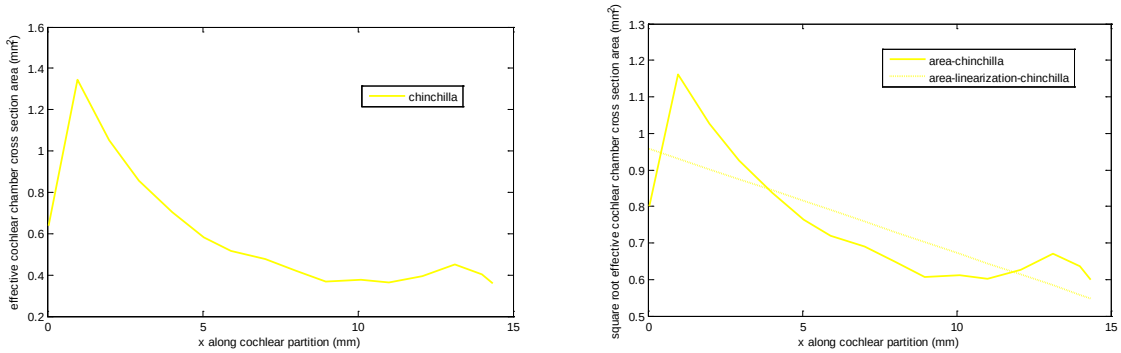

Figure C.6 Effective area of cochlear chamber for chinchilla and its square root (the solid line shows curve for the actual data, the dash line shows a least square fit of a linear variation for the square).

C4. Mouse

C4.1. post-processing for the original geometrical data of chinchilla

Figure C.7 shows variations of the calculated upper and lower fluid chamber area along cochlear partition according to measurement data from FigureA.15. Again, the effective area, square root of the effective area, and the least squarefit to the square root of fluid chamber area are shown in Figure C.8.

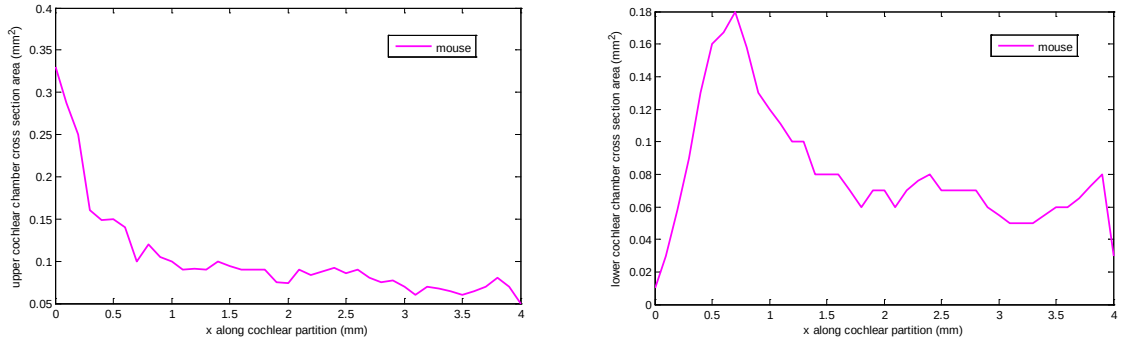

Figure C.7 $A_1(x)$ (upper area) and $A_2(x)$ (lower area) for mouse.

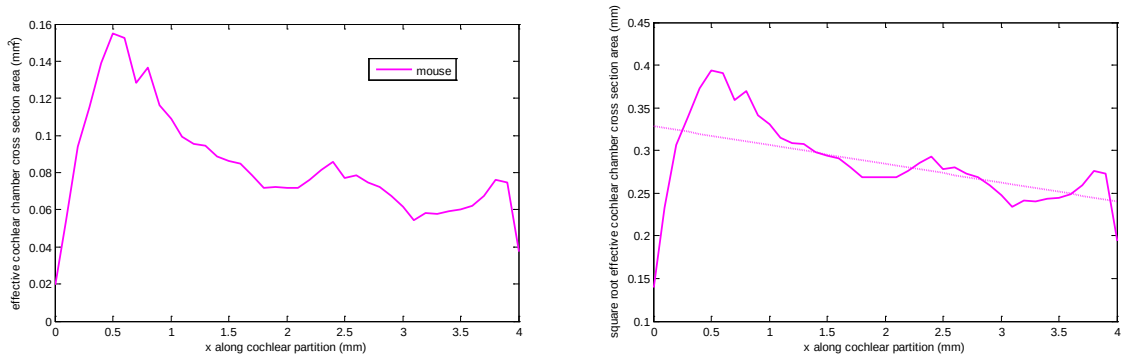

Figure C.8 Effective area of cochlear chamber for mouse and its square root (the solid line shows curve for the actual data, the dash line shows a least square fit of a linear variation for the square).

Some investigated variables

The relationship between BM mass and fluid mass has also been calculated, to investigate the variation of the ratio of the BM mass to the variation of additional fluid mass, given by

$$\frac{\text{BM mass}/area}{\text{Fluid mass}/area} = \frac{m_{3D}(average) + \rho_{BM} T_f(x)}{\rho_f H(x)} = \frac{T_f(x)}{H(x)},$$

although there is a general trend for T/H to increase from bae to apex, the variation is again surprisingly small considering the assumed variation in the overall dimensions of the cochlea, as shown in Figure C.9.

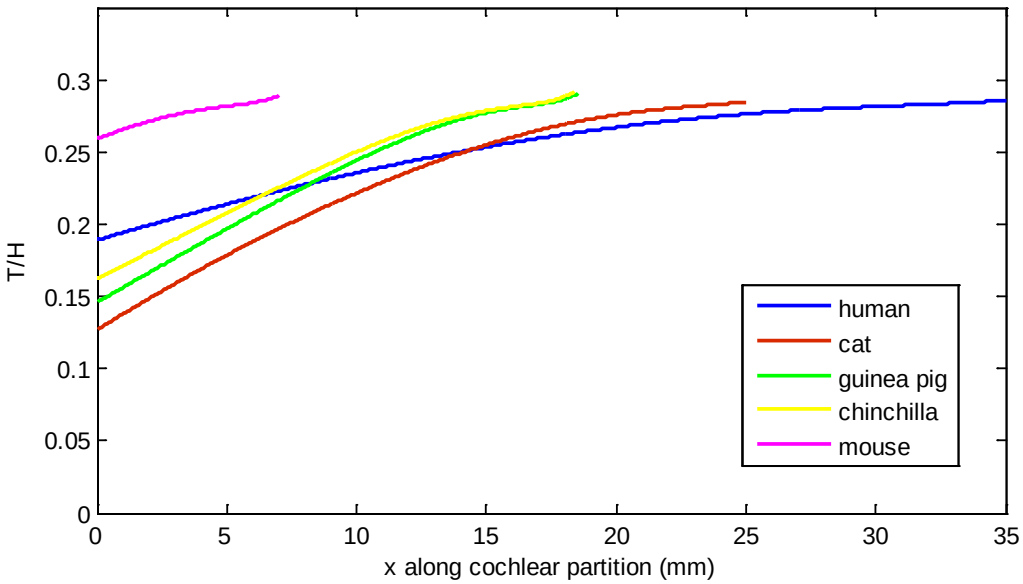

Figure C.9 The ratio of total effective BM thickness to the physical height of the fluid chamber at different positions along the cochlear position in five species.

A non-dimensional parameter introduced by (Zweig el at, 1976) and related to number of cycles of phase lag at the characteristic frequency is given by

$$N_z(x) = \ell \sqrt{\frac{\rho}{8H(x)m(x)}},$$

where ℓ is assumed to be independent of x,

If we write m(x) as $\rho T(x)$, this becomes

$$N_z(x) = \frac{\ell}{\sqrt{8H(x)T(x)}}.$$

It is not clear why the predictions from this theory are greater than the measured values of phase lag below.

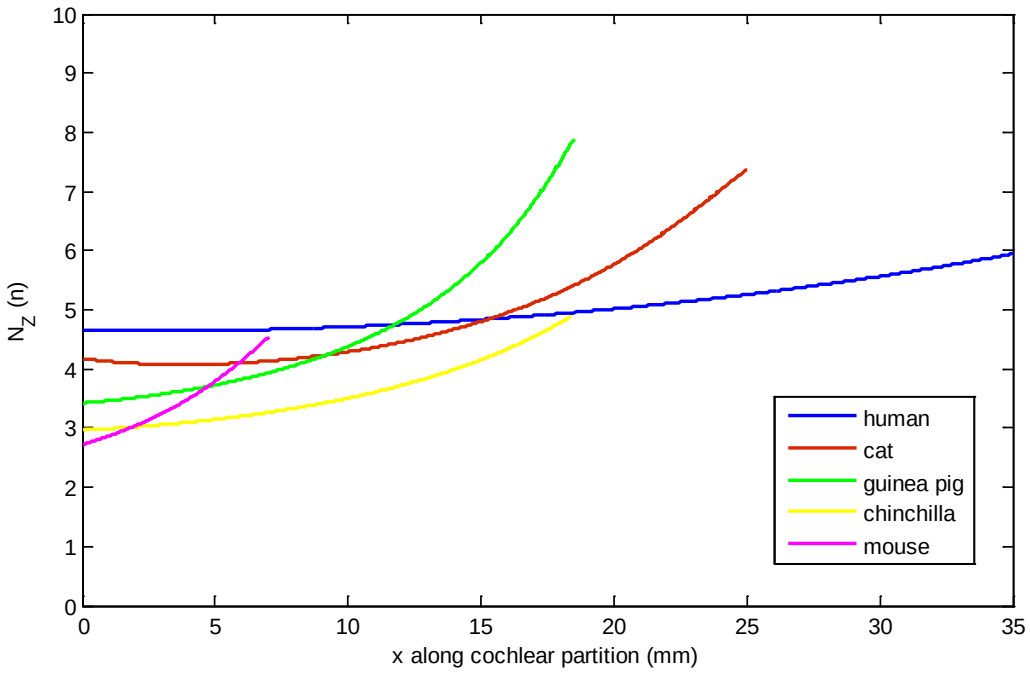

Figure C.10 The number of cycles of phase lag at characteristic frequency for five species.

Appendix D

Comparison of coupled response in different box models

In the uniform and tapered box model, for fixed space, frequencies chosen are both frequencies at 10% and 90% of length, corresponding to basal and apical measurements. 50% of length is also considered. For fixed frequencies, the positions chosen are related to the associated frequencies chosen.

D.1. Coupled responses in the 1D uniform and tapered box model of cochlea for human, cat, guinea pig, chinchilla, and mouse

Figure D.1 to Figure D.5 show the amplitude and phase of BM velocity at three fixed frequencies and thee fixed positions in the 1D uniform and tapered box model of paasive cochlea for human, cat, guinea pig, chinchilla and mouse. Those figures seem to show similar results, the amplitude of the BM velocity in the 1D tapered box model has more dB than the one in the 3D uniform model, this difference become maximum around the peak area, the phase of the BM velocity in the 1D tapered model has more cycles than the one in 1Dthe uniform box model.

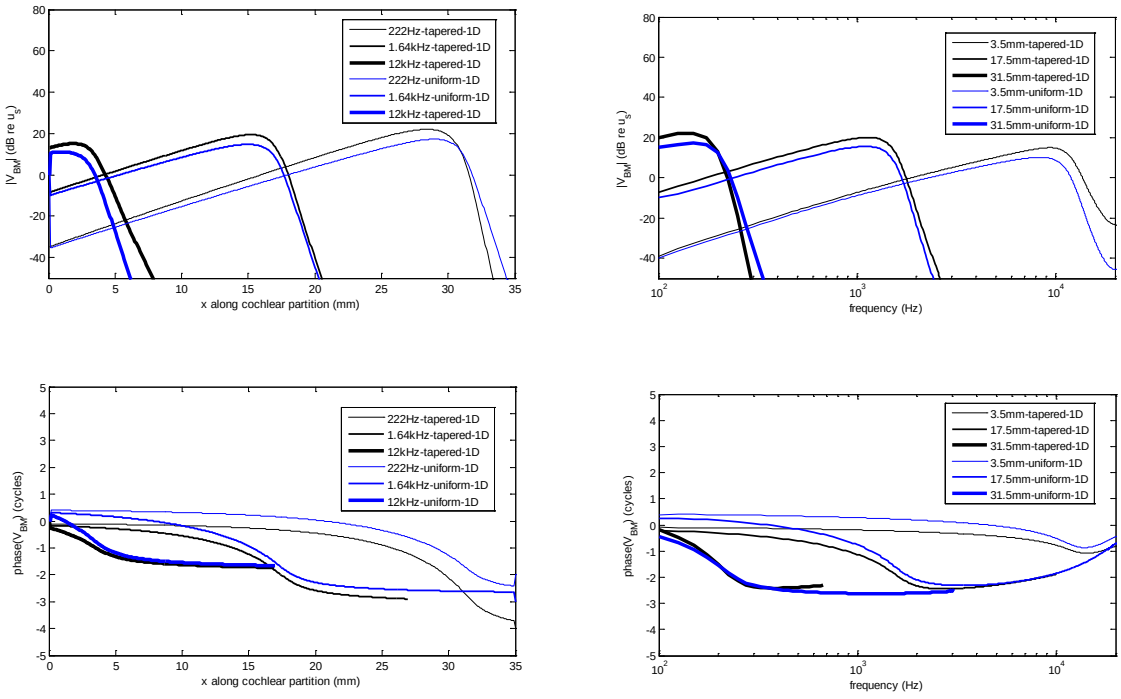

Figure D.1 The calculated magnitude and phase of BM the transverse velocity along cochlear partition at three different frequencies as a function of position and at three different position as a function of frequency in the 1D uniform and 1D tapered box model for the human cochlea.

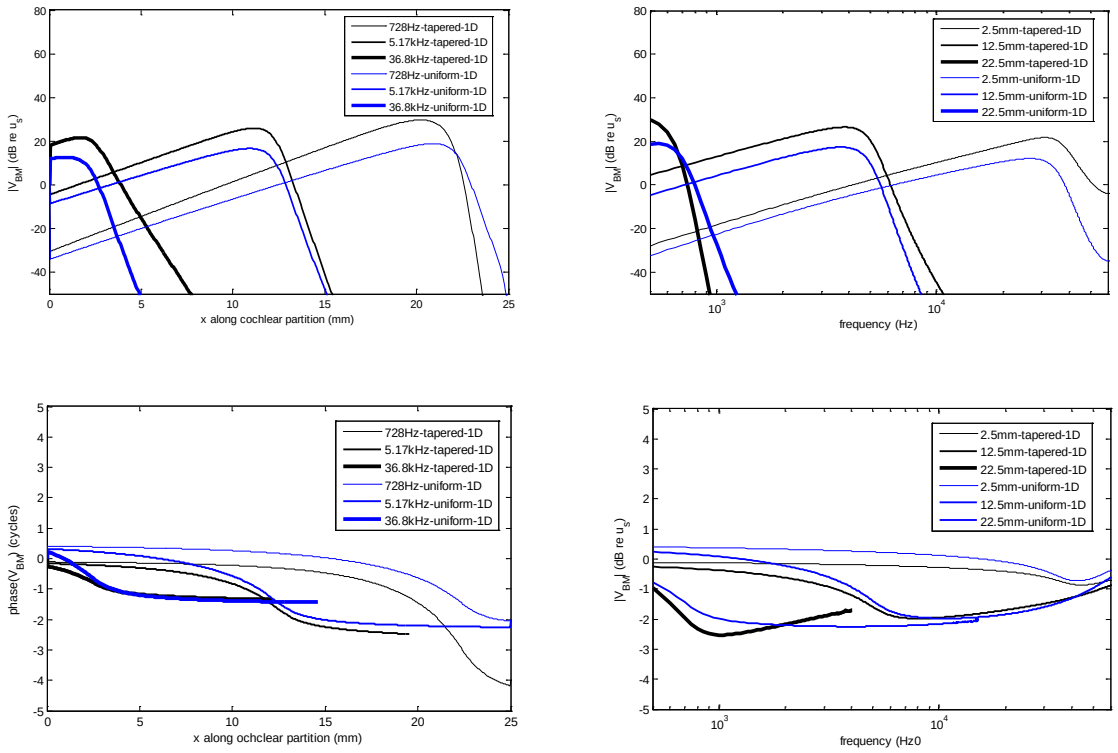

Figure D.2 The magnitude and phase of BM transverse velocity along cochlear partition in three fixed displacement and frequency in 1D uniform and 1D tapered box model for the cat cochlea.

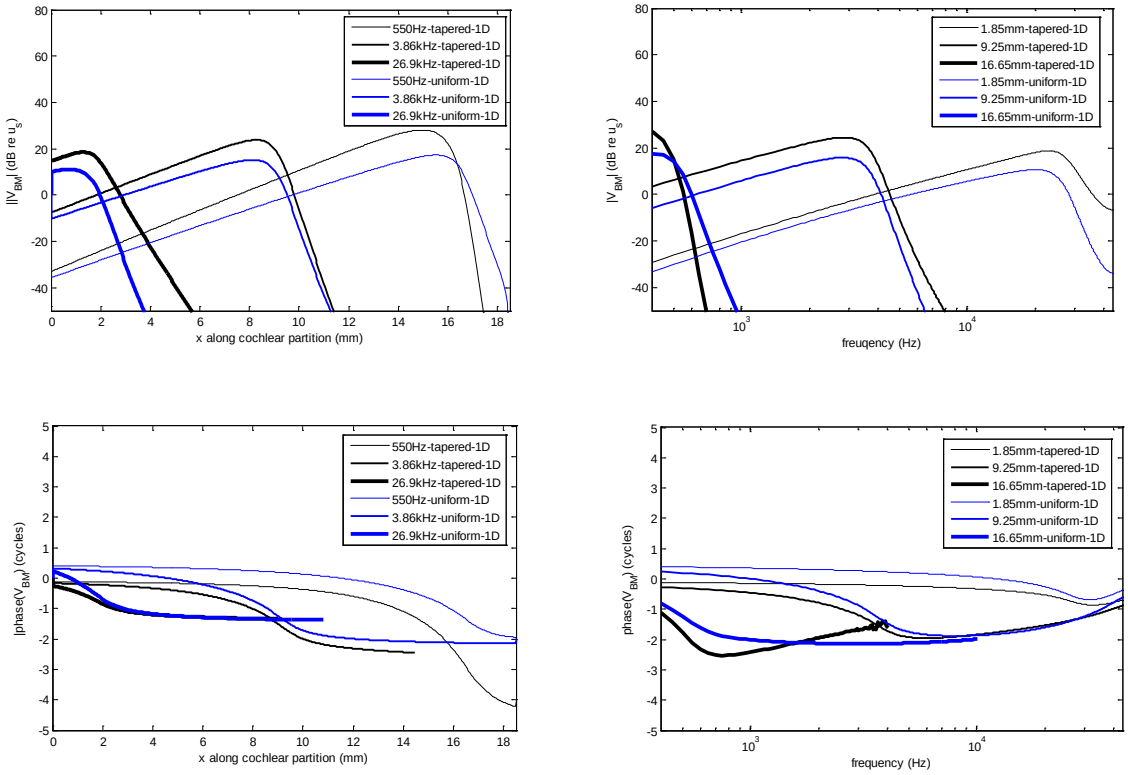

Figure D.3 The magnitude and phase of BM transverse velocity along cochlear partition in three fixed.

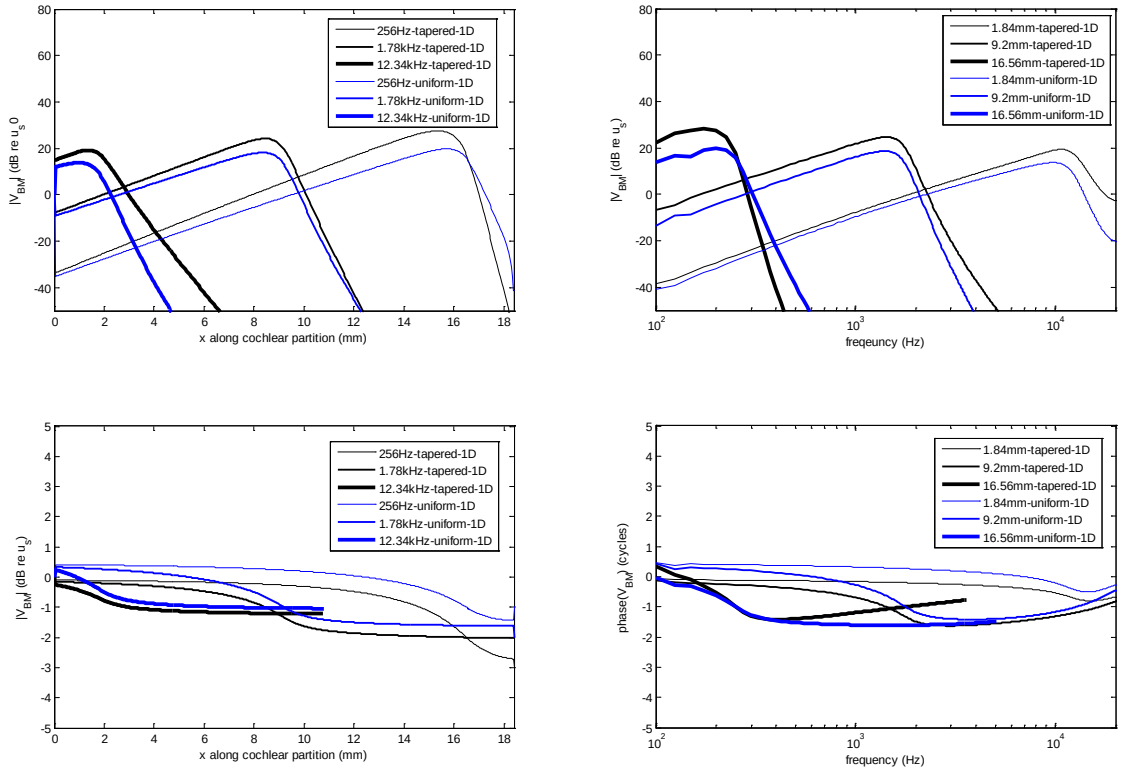

Figure D.4 The magnitude and phase of BM transverse velocity along cochlear partition in three fixed displacement and frequency in 1D uniform and the tapered box model for the chinchilla cochlea.

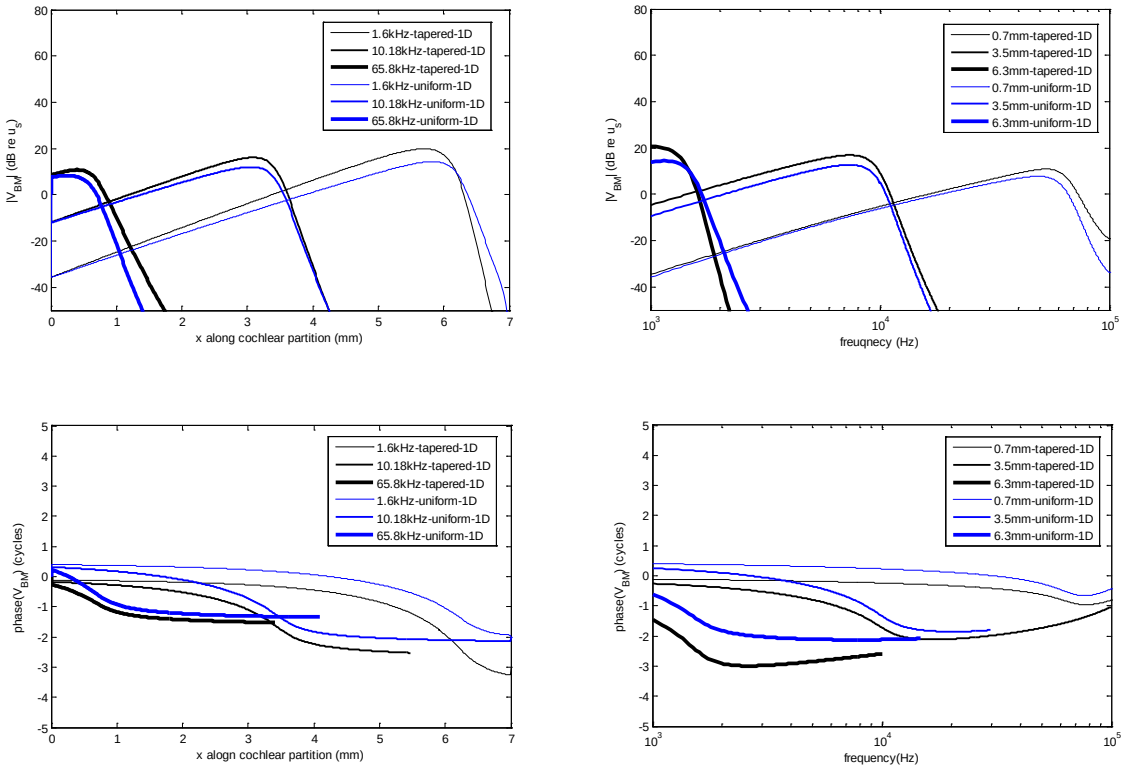

Figure D.5 The magnitude and phase of BM transverse velocity along cochlear partition in three fixed displacement and frequency in 1D uniform and the tapered box model for the mouse cochlea.

D.2. Coupled responses in the 3D uniform and tapered box model of cochlea for human, cat, guinea pig, chinchilla, and mouse

Figure D.6 to Figure D. 10 show the amplitude and phase of BM velocity at three fixed frequencies and thee fixed positions in the 3D uniform and tapered box model of paasive cochlea for human, cat, guinea pig, chinchilla and mouse. Those figures seem to show similar results, the amplitude of the BM velocity in the 3D tapered box model has more dB than the one in the 3D uniform model, this difference become maximum around the peak area, while the phase of the BM velocity in both of the two models seems the same.

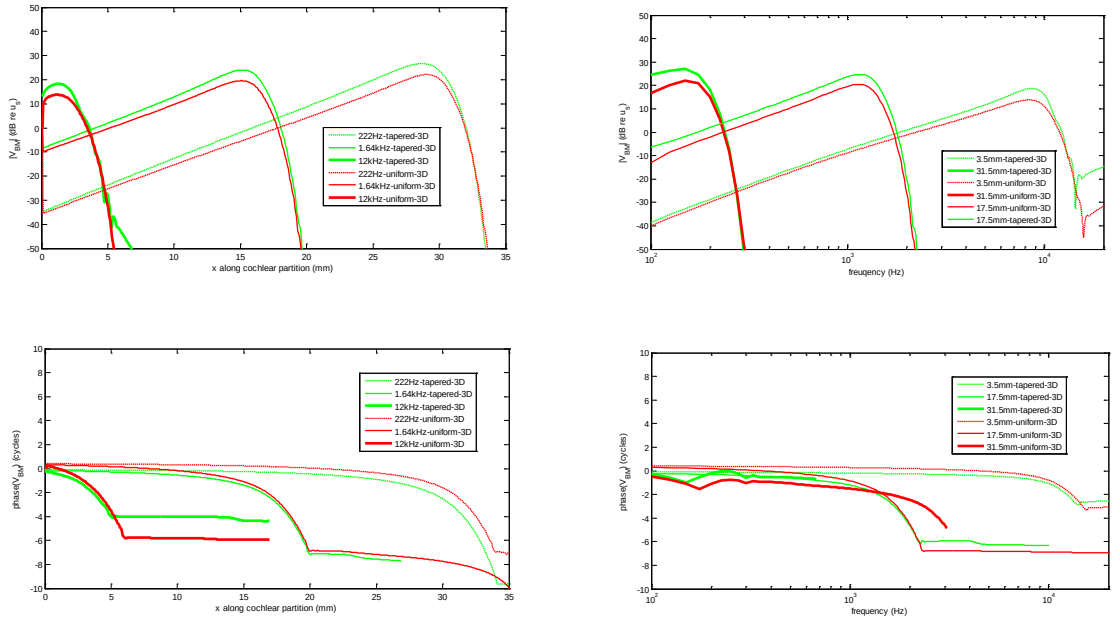

Figure D.6 The magnitude and phase of BM transverse velocity along cochlear partition in three fixed displacement and frequency for uniform (3D) and the tapered (and 3D) chamber in the human cochlea.

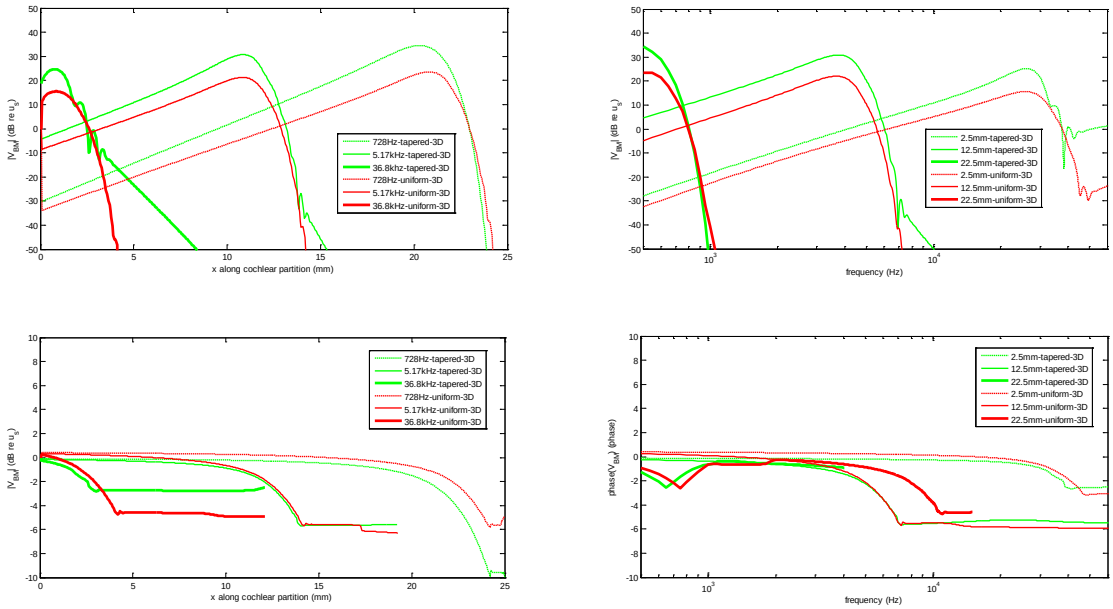

Figure D.7 The magnitude and phase of BM transverse velocity along cochlear partition in three fixed displacement and frequency for uniform (3D) and the tapered (3D) chamber in the cat cochlea.

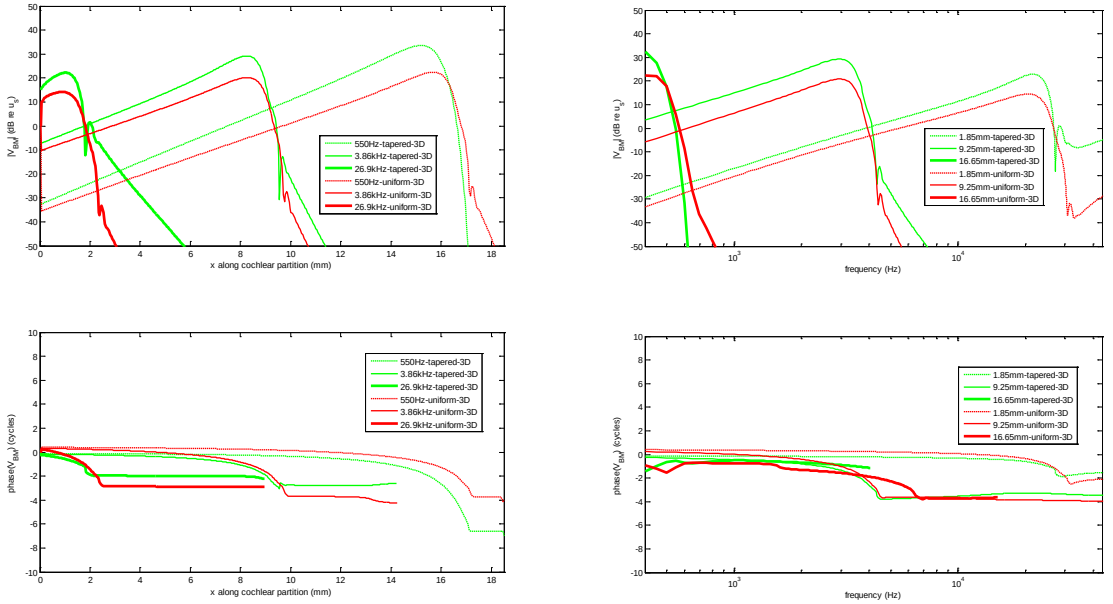

Figure D.8 The magnitude and phase of BM transverse velocity along cochlear partition in three fixed displacement and frequency for uniform (3D) and the tapered (3D) chamber in the guinea pig cochlea.

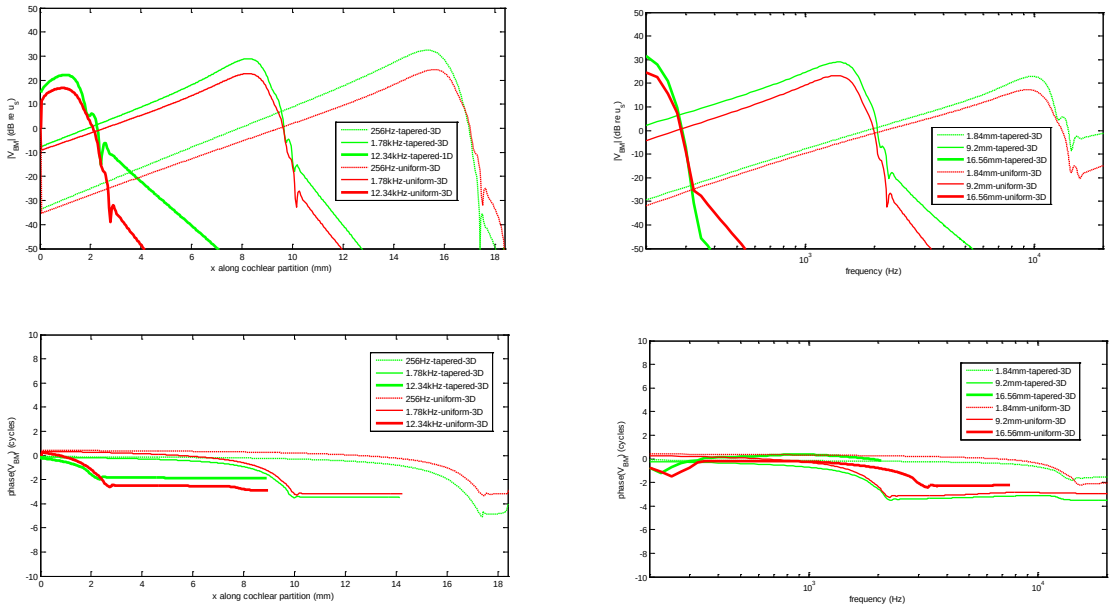

Figure D.9 The magnitude and phase of BM transverse velocity along cochlear partition in three fixed displacement and frequency for uniform (3D) and the tapered (3D) chamber in the chinchilla cochlea.

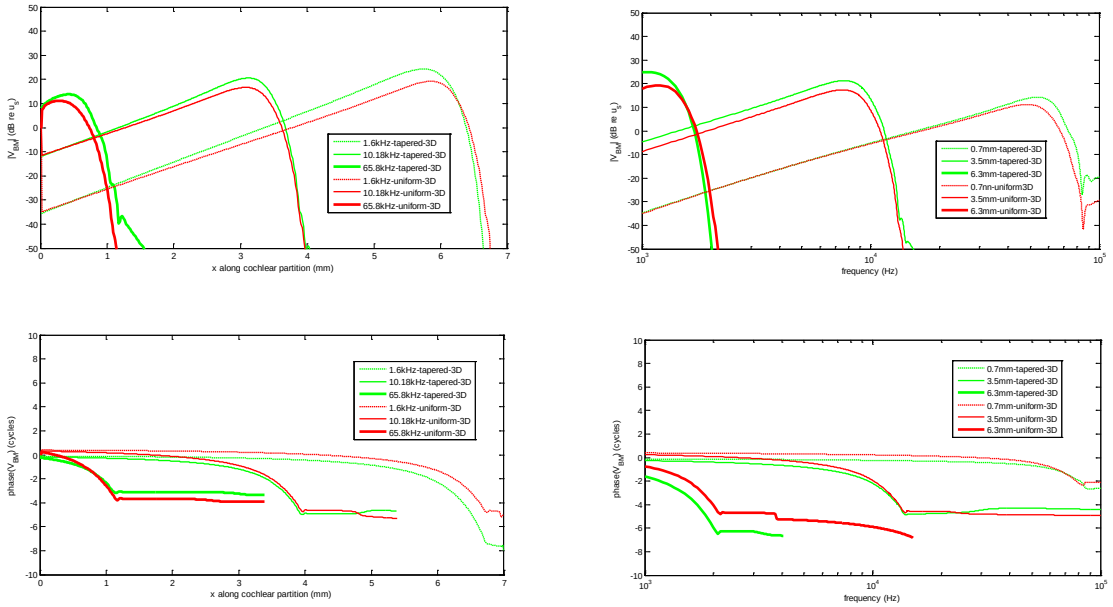

Figure D.10 The magnitude and phase of BM transverse velocity along cochlear partition in three fixed displacement and frequency for uniform (3D) and the tapered (3D) chamber in the mouse cochlea.

Appendix E.

Effect of constant estimated parameters

Section 4.2 and 4.3 have estimated the BM response using the "direct" inverse method with genetic algorithm of one objective optimization and two objectives optimization; the parameters are estimated as well. From those parameters, we can see that Ω and Q vary along each characteristic position. Now, if Ω and Q are fixed to certain values and assumed to be constants along each characteristic position, this effect on the coupled response will be investigated here.

Initially, the estimated parameters derived from V_{BM} at fixed frequencies using the direct inverse method with genetic algorithm of one objective optimization are used, the average values of Ω and Q at four fixed frequencies are calculated. Then, $\hat{V}_{BM}$ combined with V_{BM} are shown in Figure E.1.

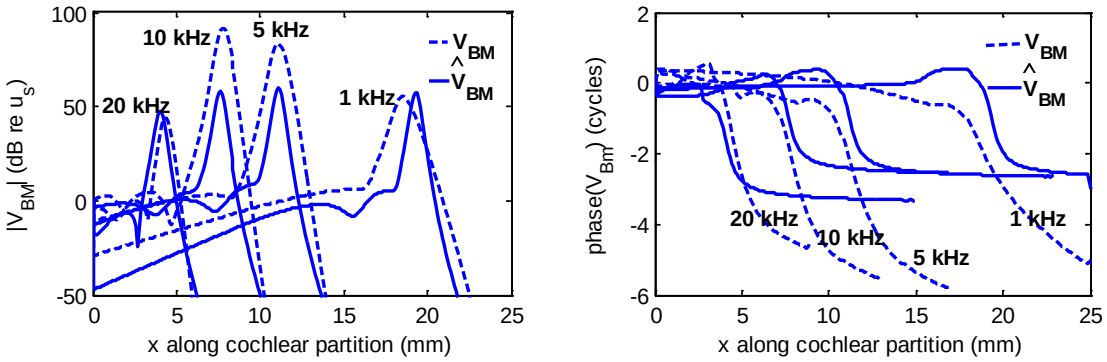

Figure E. 1 Comparison of amplitude and phase between $\hat{V}_{BM}$ using average values and V_{BM} given at fixed frequencies of one objective optimization.

Figure E.1 shows that the amplitude of $\hat{V}_{BM}$ does not fit well with V_{BM} except for the one at 20 kHz, while the comparison of phase between $\hat{V}_{BM}$ and V_{BM} is similar as Figure 4.9.

Table E.1 Average values of Ω_1, Q_1, Ω_2, Q_2, Ω_3, Q_3, m_0 at fixed frequencies in Table 4.3.

One objective genetic algorithm (fixed frequencies)							
Condition	Ω_1	Q_1	Ω_2	Q_2	Ω_3	Q_3	m_0
Average value	0.35	5.50	0.75	5.28	0.73	5.37	0.43

Then, the estimated parameters derived from V_{BM} at fixed frequencies using the direct inverse method with genetic algorithm of two objectives optimization are used, the average values of Ω and Q at four fixed frequencies are calculated. Then, $\hat{V}_{BM}$ combined with V_{BM} is shown in Figure E.2.

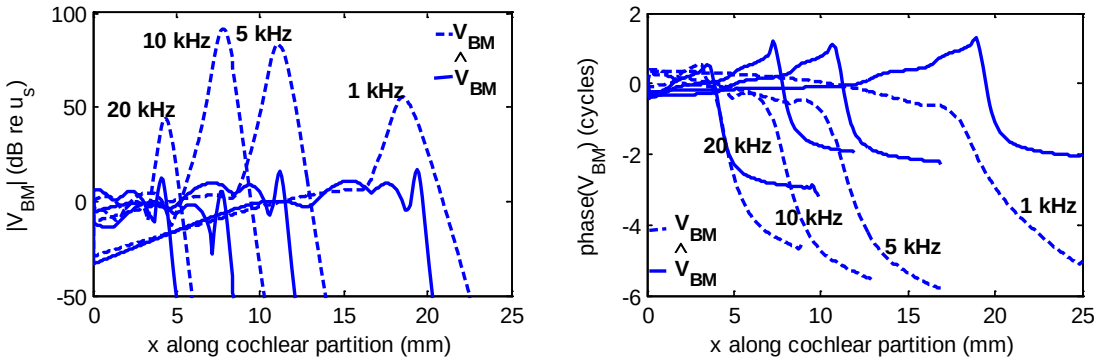

Figure E.2 Comparison of amplitude and phase between $\hat{V}_{BM}$ using average values and V_{BM} given at fixed frequencies with the two objectives optimization.

Figure E.2 shows that the amplitude of $\hat{V}_{BM}$ fits worse compared with V_{BM} .

Table E.2 Average values of Ω_1, Q_1, Ω_2, Q_2, Ω_3, Q_3, m_0 at fixed frequencies in Table 4.5.

Two objective genetic algorithm (fixed frequencies)							
Condition	Ω_1	Q_1	Ω_2	Q_2	Ω_3	Q_3	m_0
Average value	0.44	6.25	0.72	5.17	0.78	5.74	0.17

If the estimated parameters along the cochlear partition are assumed to be constant, equal to the average values, the new estimated results are in bad agreement with the “measured” data, which reveals that Ω, Q, and m_0 should vary at different positions.

Appendix F.

Trend lines of variations of wavenumber at other ranges of characteristic frequencies

Figure F.1 shows variations of $\mathrm{Re}(\hat{k})$ and $\mathrm{Im}(\hat{k})$ estimated from BM velocity measurement data at fixed characteristic frequencies, $CF(x_0)$, from 10 kHz to 16 kHz in the 13 Wiener kernel files. One of the distribution lines for $\mathrm{Re}(\hat{k})$ and $\mathrm{Im}(\hat{k})$,respectively, is selected by eye as the trend line in the range 10-16 kHz, which expresses the similar features of wavenumber for the active cochlea as the main text.

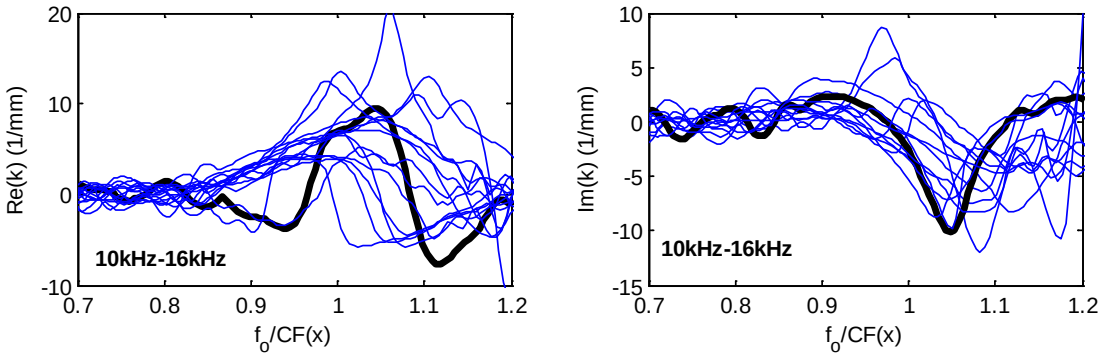

Figure F.1 Real and imaginary parts of wavenumber functions derived from all 13 Wiener kernels with CFs in the range 10-16 kHz. Blue lines shows individual functions $\mathrm{Re}(\hat{k})$ and $\mathrm{Im}(\hat{k})$; black lines show rends obtained by selecting a line that shows the mean behaviour roughly.

Figure F.2 shows variations of $\mathrm{Re}(\hat{k})$ and $\mathrm{Im}(\hat{k})$ estimated from BM velocity measurement data at fixed characteristic frequencies, $CF(x_0)$, from 5 kHz to 8 kHz in the 29 Wiener kernel files. One of the distribution lines for $\mathrm{Re}(\hat{k})$ and $\mathrm{Im}(\hat{k})$,respectively, is selected by eye as the trend line in the range 5-8 kHz, which expresses the similar features of wavenumber for the active cochlea as the main text.

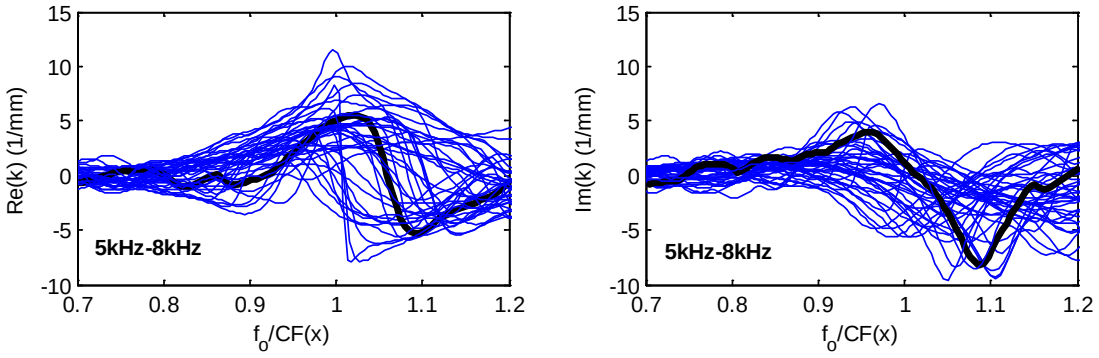

Figure F.2 Real and imaginary parts of wavenumber functions derived from all 29 Wiener kernels with CFs in the range 5-8 kHz. Blue lines shows individual functions $\mathrm{Re}(\hat{k})$ and $\mathrm{Im}(\hat{k})$; black lines show rends obtained by selecting a line that shows the mean behaviour roughly.

Figure F.3 shows variations of $\mathrm{Re}(\hat{k})$ and $\mathrm{Im}(\hat{k})$ estimated from BM velocity measurement data at fixed characteristic frequencies, $CF(x_0)$, from 2 kHz to 5 kHz in the 23 Wiener kernel files. One of the distribution lines for $\mathrm{Re}(\hat{k})$ and $\mathrm{Im}(\hat{k})$,respectively, is selected by eye as the trend line in the range 2-5 kHz, which expresses the similar features of wavenumber for the active cochlea as the main text.

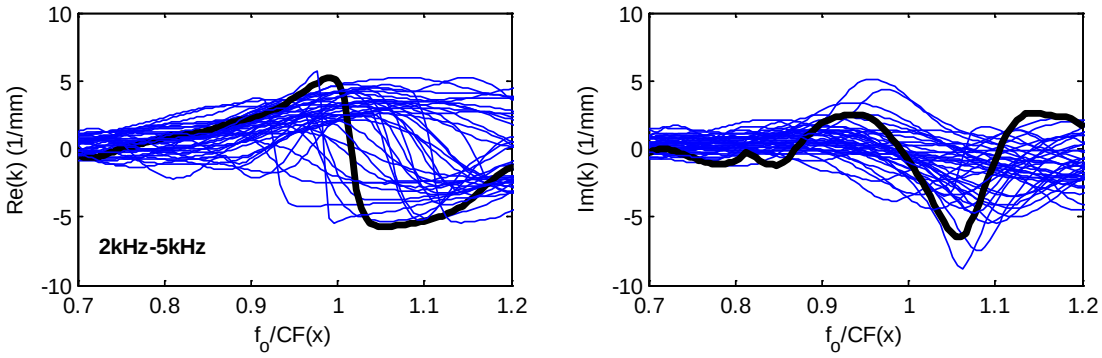

Figure F.3 Real and imaginary parts of wavenumber functions derived from all 23 Wiener kernels with CFs in the range 2-5 kHz. Blue lines shows individual functions $\mathrm{Re}(\hat{k})$ and $\mathrm{Im}(\hat{k})$; black lines show rends obtained by selecting a line that shows the mean behaviour roughly.

Figure F.4 shows variations of $\mathrm{Re}(\hat{k})$ and $\mathrm{Im}(\hat{k})$ estimated from BM velocity measurement data at fixed characteristic frequencies, $CF(x_0)$, from 100 Hz to 2 kHz in the 22 Wiener kernel files. One of the distribution lines for $\mathrm{Re}(\hat{k})$ and $\mathrm{Im}(\hat{k})$,respectively, is selected by eye as the trend line in the range 100 Hz-2 kHz. Although, this figure shows the main features of wavenumber for active cochlea, they accur around 1.5 ($f_0 / CF(x)$), not around peak area, which causes an error in this case.

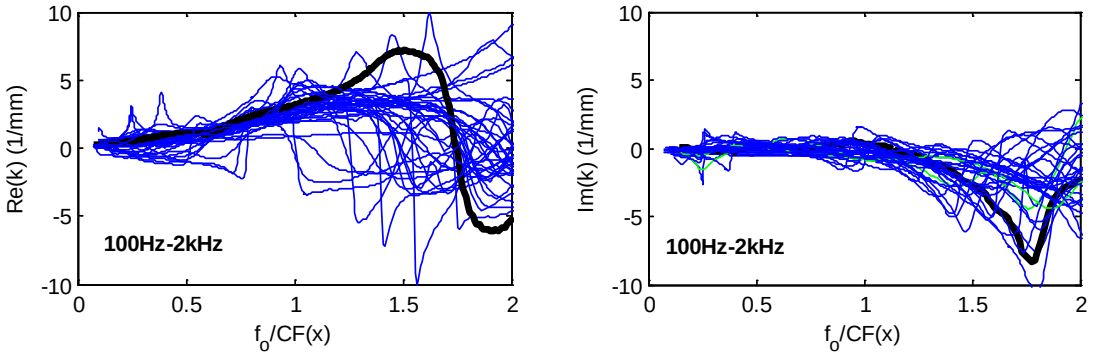

Figure F.4 Real and imaginary parts of wavenumber functions derived from all 22 Wiener kernels with CFs in the range 100 Hz-2 kHz. Blue lines shows individual functions $\mathrm{Re}(\hat{k})$ and $\mathrm{Im}(\hat{k})$; black lines show rends obtained by selecting a line that shows the mean behaviour.

Appendix G

Estimates of wavenumber at different sound levels at other characteristic frequencies

Three Wiener kernels are collected at the same place, $CF(x_0)$=11 kHz, with SPLs of 40, 60, 70 dB, respectively. The original data in time domain and Fourrier transform of the original data in frequency domain along the BM are shown in Figures G.1 and G.2.

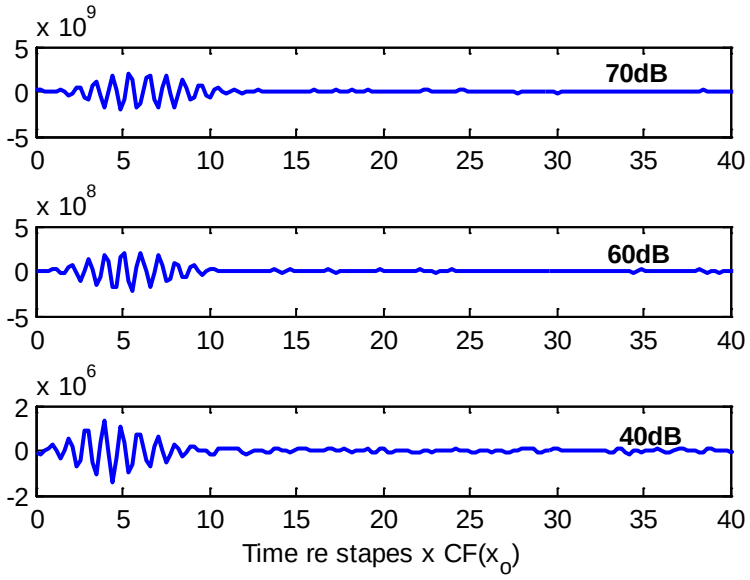

Figure G.1 Auditory-nerve based estimate of the BM click response, $v_{BM}(x_0,t)$, at the cochlear partition, x_0, tuned to approximately 11 kHz in chinchilla at different SPLs of 70, 60, 40 dB, respectively.

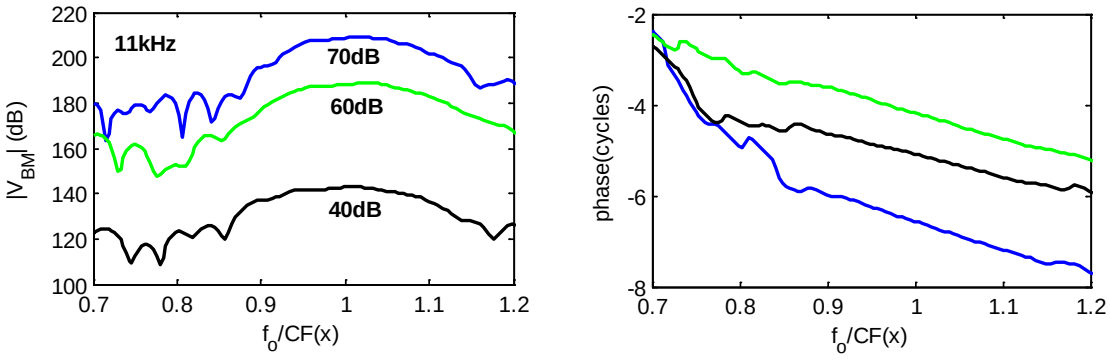

Figure G.2 The amplitude and phase of the BM response at a fixed frequency are converted from them at a fixed position ($CF(x_0)$ =11 kHz), which are obtained from Fourier transform of $V_{BM}(x_0,t)$ and plotted against $f_0 / CF(x)$ at different SPLs of 70, 60, 40 dB, respectively.

$\mathrm{Re}(\hat{k})$ and $\mathrm{Im}(\hat{k})$ can then be calculated at the same place but at both low and high levels, in order to investigate the variation in $\mathrm{Re}(\hat{k})$ and $\mathrm{Im}(\hat{k})$ from active cochlea to passive cochlea. However, it is difficult to discern any particular trend at $CF(x_0)$=11 kHz with SPLs in this case, as shown in Figure G.3.

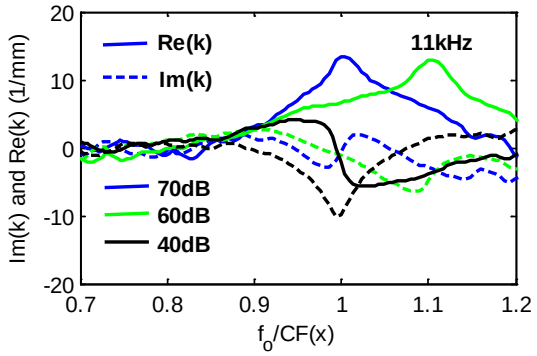

Figure G.3 The real and imaginary parts of wavenumber functions are plotted against the generalized scaling variable using solid (real part) and dash (imaginary part) lines, respectively, the functions $\mathrm{Re}(\hat{k})$ and $\mathrm{Im}(\hat{k})$ were obtained by using the inverse method at the certain frequency place, which is 11 kHz for different SPLs of 70, 60, 40 SPL, respectively. $CF(x) = f_B e^{-x/\ell}$, where f_B =20 kHz, x=18.4 mm, ℓ =3.8 mm (the 178th, 179th, 180th files are selected in FSVs.mat file).

Four Wiener kernels are collected at the same place, $CF(x_0)$=9.6 kHz, with SPLs of 40, 50, 60, 80 dB, respectively. The original data in time domain and Fourrier transform of the original data in frequency domain along the BM are shown Figures G.4 in and G.5.

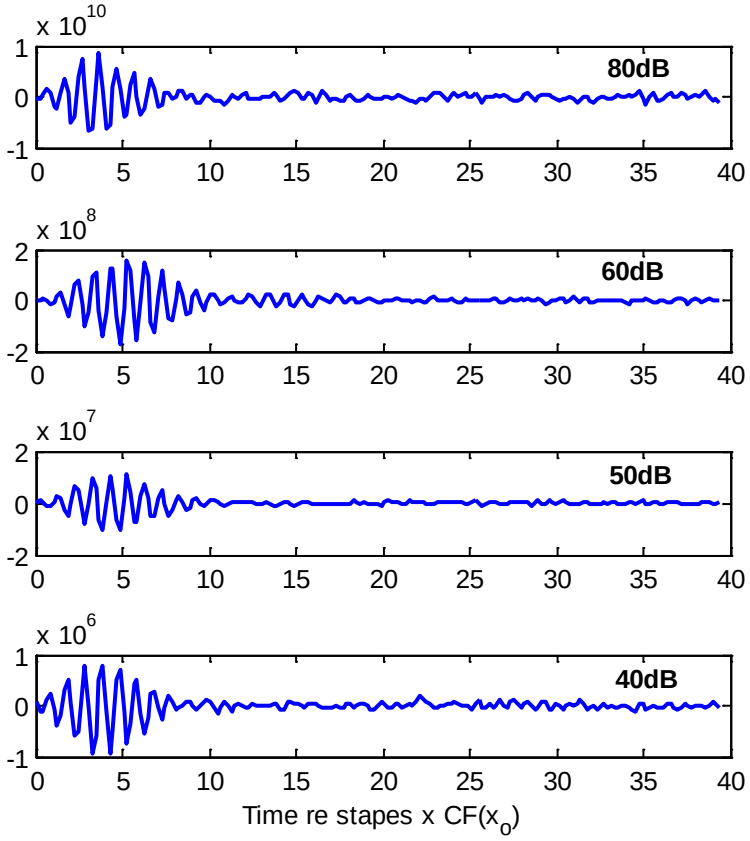

Figure G.4 Auditory-nerve based estimate of the BM click response, $v_{BM}(x_0,t)$, at the cochlear partition, x_0, tuned to approximately 9.6 kHz in chinchilla at different SPLs of 80, 60, 50, 40 dB, respectively.

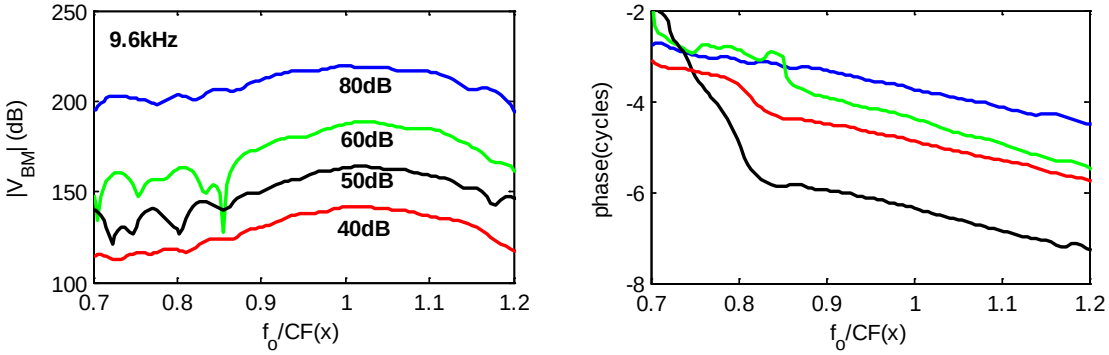

Figure G.5 The amplitude and phase of the BM response at a fixed frequency are converted from them at a fixed position ($CF(x_0)$ =9.6 kHz), which are obtained from Fourier transform of $V_{BM}(x_0,t)$ and plotted against $f_0 / CF(x)$ at at different SPLs of 80, 60, 50, 40 dB, respectively.

$\mathrm{Re}(\hat{k})$ and $\mathrm{Im}(\hat{k})$ can then be calculated at the same place but at both low and high levels, in order to investigate the variation in $\mathrm{Re}(\hat{k})$ and $\mathrm{Im}(\hat{k})$ from active cochlea to passive cochlea. However, it is difficult to discern any particular trend at $CF(x_0)$ =9.6 kHz with SPLs, as shown in Figure G.6.

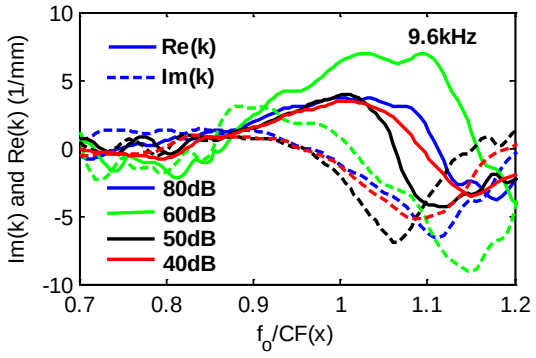

Figure G.6 The real and imaginary parts of wavenumber functions are plotted against the generalized scaling variable using solid (real part) and dash (imaginary part) lines, respectively, the functions Re($\hat{k}$) and Im($\hat{k}$) were obtained by using the inverse method at the certain frequency place,, which is 9.6 kHz, for different SPLs of 65, 60, 50, 40, 30 dB, respectively. $CF(x) = f_B e^{-x/\ell}$, where f_B=20 kHz, x=18.4 mm, ℓ=3.8 mm (the 170th, 171^{h}, 172^{h}, 173^{h} files are selected in FSVs.mat file).

Four Wiener kernels are collected at the same place, $CF(x_0)$=8.4 kHz, with SPLs of 70, 80, 90 dB, respectively. The original data in time domain and Fourrier transform of the original data in frequency domain along the BM are shown in Figures G.7 and G.8.

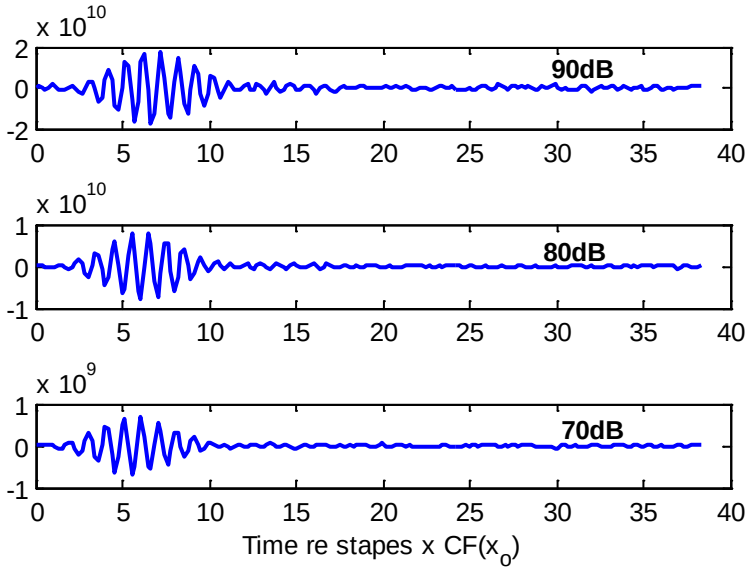

Figure G.7 Auditory-nerve based estimate of the BM click response, $v_{BM}(x_0,t)$, at the cochlear partition, x_0, tuned to approximately 8.4 kHz in chinchilla at different SPLs of 80, 60, 50, 40 dB, respectively.

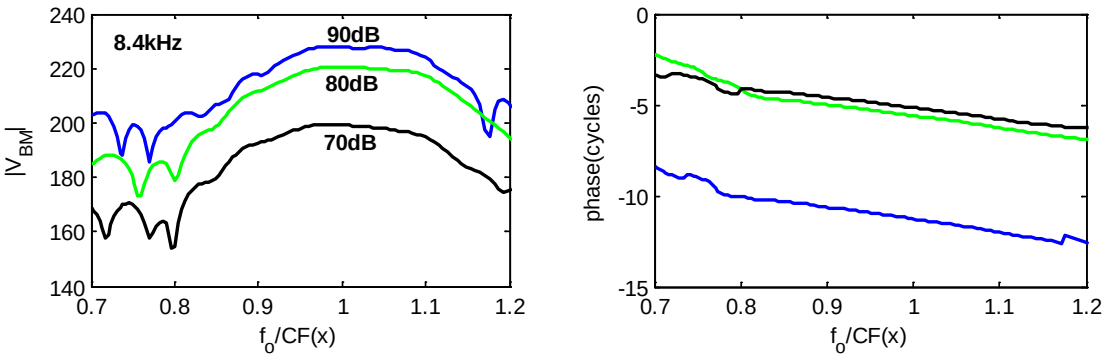

Figure G.8 The amplitude and phase of the BM response at a fixed frequency are converted from them at a fixed position ($CF(x_0)$ =8.4 kHz), which are obtained from Fourier transform of $V_{BM}(x_0,t)$ and plotted against $f_0 / CF(x)$ at different SPLs of 90, 80, 70 dB, respectively.

$\mathrm{Re}(\hat{k})$ and $\mathrm{Im}(\hat{k})$ can then be calculated at the same place but at both low and high levels, in order to investigate the variation in $\mathrm{Re}(\hat{k})$ and $\mathrm{Im}(\hat{k})$ from active cochlea to passive cochlea. However, it is difficult to discern any particular trend at $CF(x_0)$ =8.4 kHz with SPLs, as shown in Figure G.9.

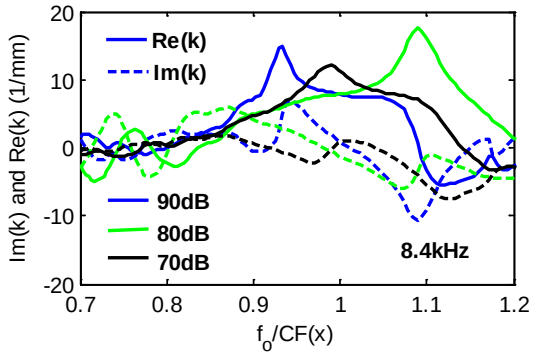

Figure G.9 The real and imaginary parts of wavenumber functions are plotted against the generalized scaling variable using solid (real part) and dash (imaginary part) lines, respectively, the functions $\mathrm{Re}(\hat{k})$ and $\mathrm{Im}(\hat{k})$ were obtained by using the inverse method at the certain frequency place, which is 8.4 kHz, for different SPLs of 65, 60, 50, 40, 30 dB, respectively. $CF(x) = f_B e^{-x/\ell}$, where f_B =20 kHz, x=18.4 mm, ℓ =3.8 mm (the 157th, 158th, 159th files are selected in FSVs.mat file).

Four Wiener kernels are collected at the same place, $CF(x_0)$ =5.1 kHz, with SPLs of 40, 50, 60, 70 dB, respectively. The original data in time domain and Fourrier transform of the original data in frequency domain along the BM are shown in Figures G.10 and G.11.

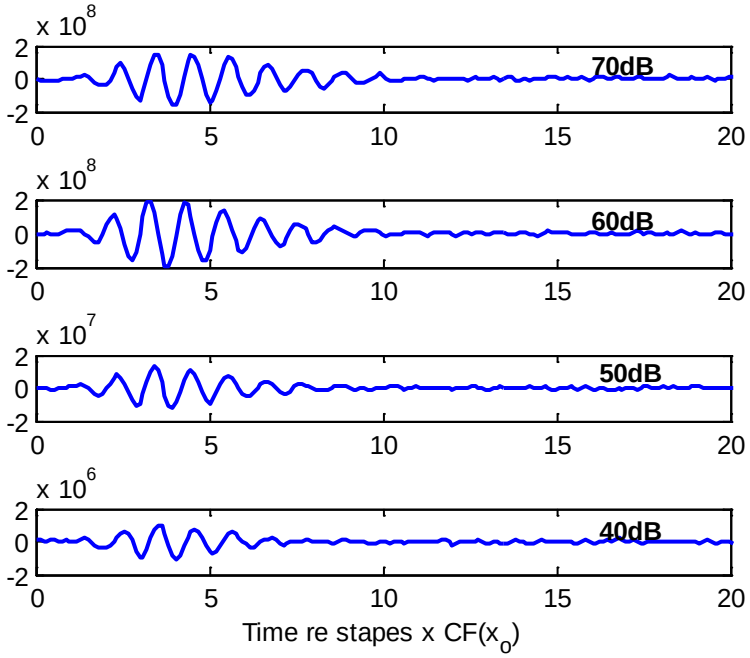

Figure G.10 Auditory-nerve based estimate of the BM click response, $v_{BM}(x_0,t)$, at the cochlear partition, x_0, tuned to approximately 5.1 kHz in chinchilla at different SPL of 70, 60, 50, 40 dB, respectively.

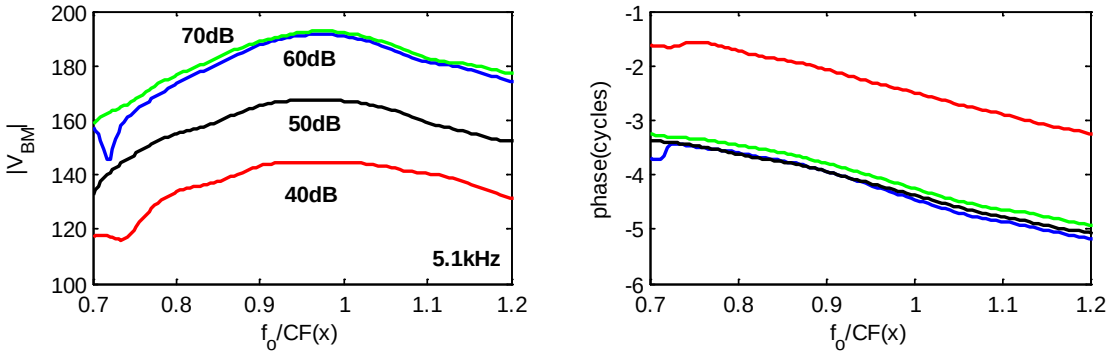

Figure G.11 The amplitude and phase of the BM response at a fixed frequency are converted from them at a fixed position ($CF(x_0)$=5.1 kHz), which are obtained from Fourier transform of $V_{BM}(x_0,t)$ and plotted against $f_0 / CF(x)$ at different SPLs of 70, 60, 50, 40 dB, respectively.

$\mathrm{Re}(\hat{k})$ and $\mathrm{Im}(\hat{k})$ can then be calculated at the same place but at both low and high levels, in order to investigate the variation in $\mathrm{Re}(\hat{k})$ and $\mathrm{Im}(\hat{k})$ from active cochlea to passive cochlea. However, it is difficult to discern any particular trend at $CF(x_0)$=5.1 kHz with SPLs, as shown in Figure G.12.

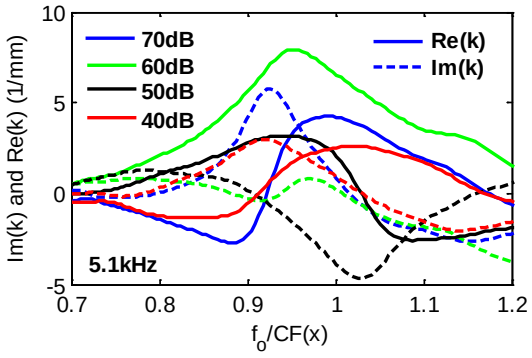

Figure G.12 The real and imaginary parts of wavenumber functions are plotted against the generalized scaling variable using solid (real part) and dash (imaginary part) lines, respectively, the functions Re($\hat{k}$) and Im($\hat{k}$) were obtained by using the inverse method at the certain frequency place, which is 5.1 kHz, for different SPLs of 65, 60, 50, 40, 30 dB, respectively. $CF(x) = f_B e^{-x/\ell}$, where f_B=20 kHz, x=18.4 mm, ℓ=3.8 mm (the 104th, 106th, 108th, 109^{h} files are selected in FSVs.mat file).

Four Wiener kernels are collected at the same place, $CF(x_0)$=5 kHz, with SPLs of 59, 69, 74.5, 79 dB, respectively. The original data in time domain and Fourrier transform of the original data in frequency domain along the BM are shown in Figure G.13 and Figure G.14.

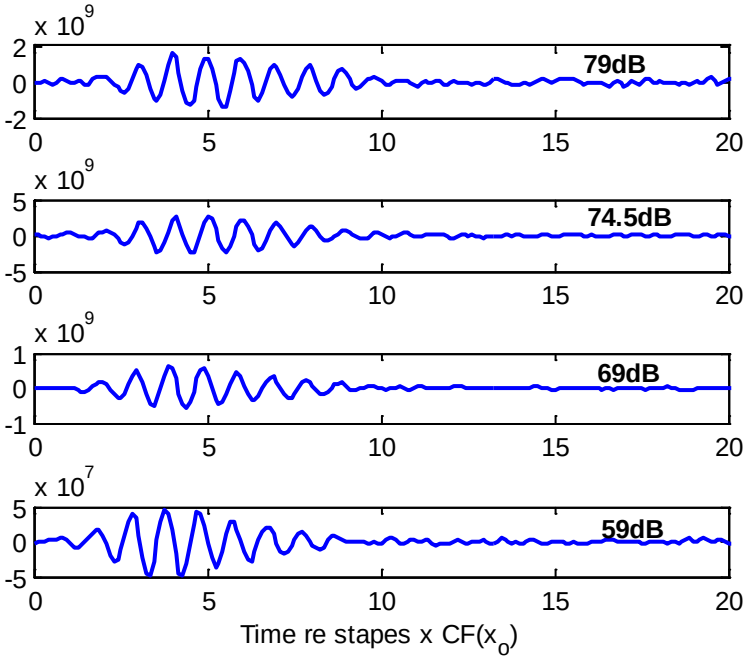

Figure G.13 Auditory-nerve based estimate of the BM click response, $v_{BM}(x_0,t)$, at the cochlear partition, x_0, tuned to approximately 5 kHz in chinchilla at different SPLs of 79, 74.5, 69, 59 dB, respectively.

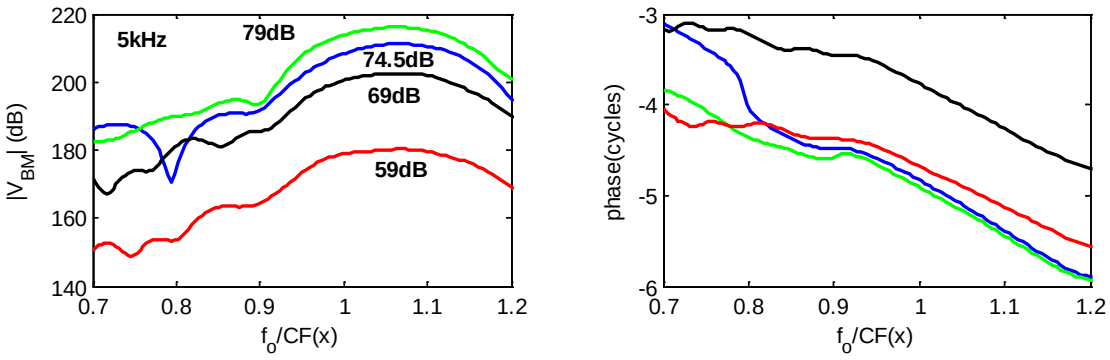

Figure G.14 The amplitude and phase of the BM response at a fixed frequency are converted from them at a fixed position ($CF(x_0)$=5 kHz), which are obtained from Fourier transform of $V_{BM}(x_0,t)$ and plotted against $f_0 / CF(x)$ at different SPLs of 79, 74.5, 69, 59 dB, respectively.

$\mathrm{Re}(\hat{k})$ and $\mathrm{Im}(\hat{k})$ can then be calculated at the same place but at both low and high levels, in order to investigate the variation in $\mathrm{Re}(\hat{k})$ and $\mathrm{Im}(\hat{k})$ from active cochlea to passive cochlea. However, it is difficult to discern any particular trend at $CF(x_0)$=5 kHz with SPLs, as shown in Figure G.15.

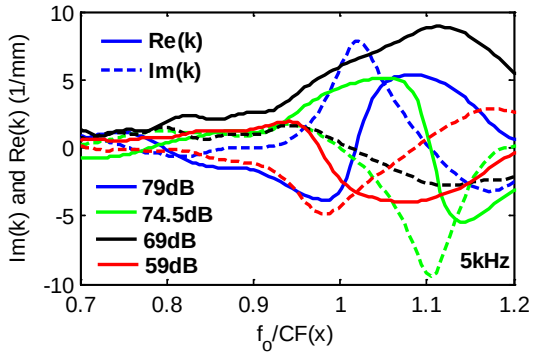

Figure G.15 The real and imaginary parts of wavenumber functions are plotted against the generalized scaling variable using solid (real part) and dash (imaginary part) lines, respectively, the functions $\mathrm{Re}(\hat{k})$ and $\mathrm{Im}(\hat{k})$ were obtained by using the inverse method at the certain frequency place, which is 5 kHz, for different SPLs of 65, 60, 50, 40, 30 dB, respectively. $CF(x) = f_B e^{-x/\ell}$, where f_B=20 kHz, x=18.4 mm, ℓ=3.8 mm (the 100th, 101th, 102th, 103th files are selected in FSVs.mat file).

Appendix H.

Estimated results with one objective optimization (NMSE for complex BM velocity)using mouse data

Initially, 1D uniform box model of active cochlea is used to estimate parameter at CFs of 9.325, 9.87, 10.6 and 11.3 kHz and SPLs of 10, 20, 30, 40, 50, 60, 70 and 80 dB fitting to the mouse data by Lee *er al.* (2015), as shown in Figures H.1, H.2, H.3 and H.4. It can be seen from those figures that both of amplitudes and phases of estimated BM response fit well to mouse data from SPL of 10 dB to 40 dB, but the amplitudes of estimated BM response decrease faster than mouse data after characteristic position, this gap increase gradually from SPL of 50 dB to 80 dB, the estimated phases are still in good agreement with mouse data from SPL of 50 dB to 80 dB, although the cycles of estimated phase decrease.

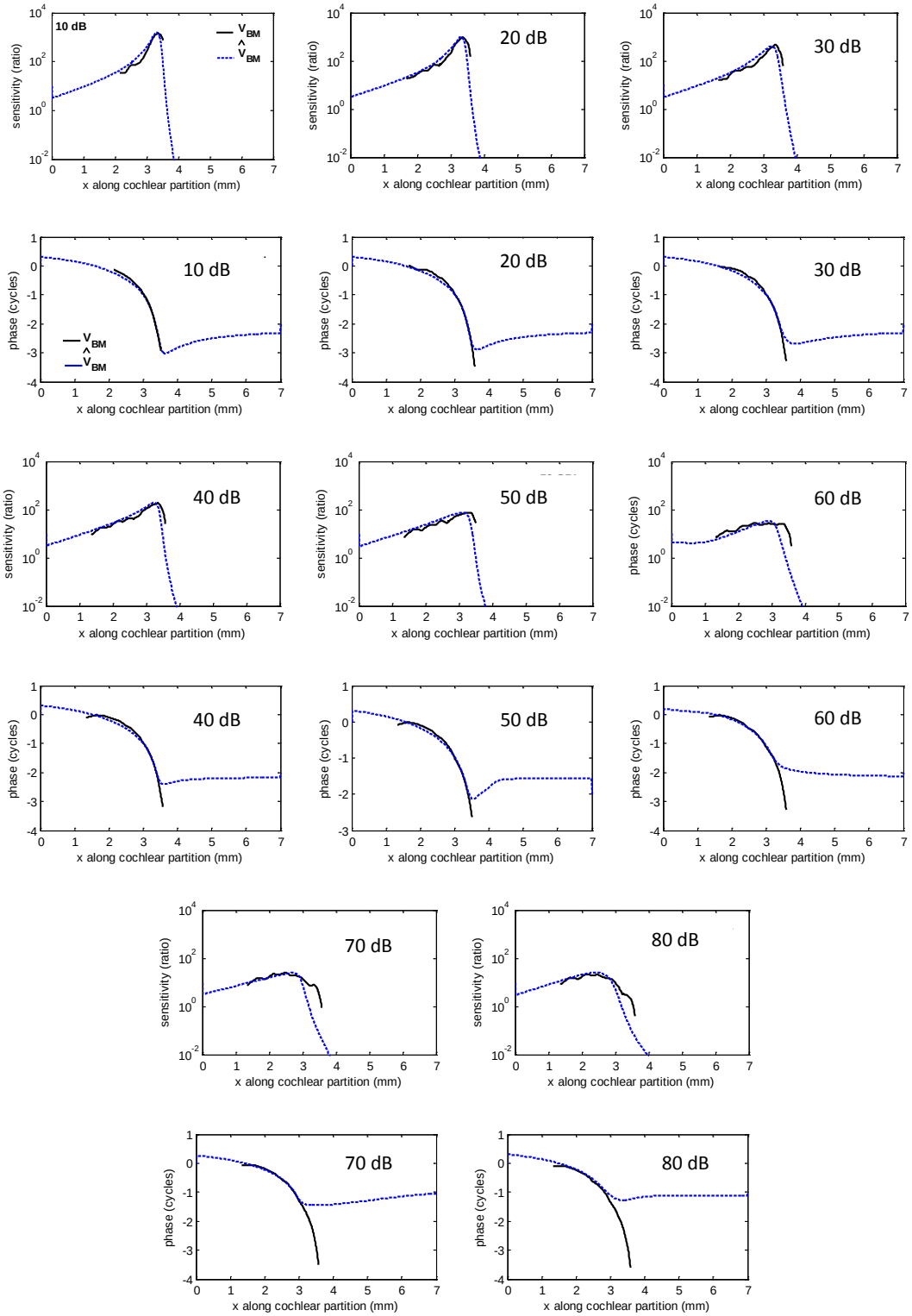

Figure H.1 Comparison between the magnitudes and phases of the BM responses measured by Lee *et al*. (2015) for a CF of 9.325 kHz and SPLs of 10, 20, 30, 40, 50, 60 ,70, and 80 dB, black lines, and the responses of a model with second order micromechanics and 1D fluid coupling, obtained using single objective optimisation to identify the micromechanical poles and zeros, blue lines

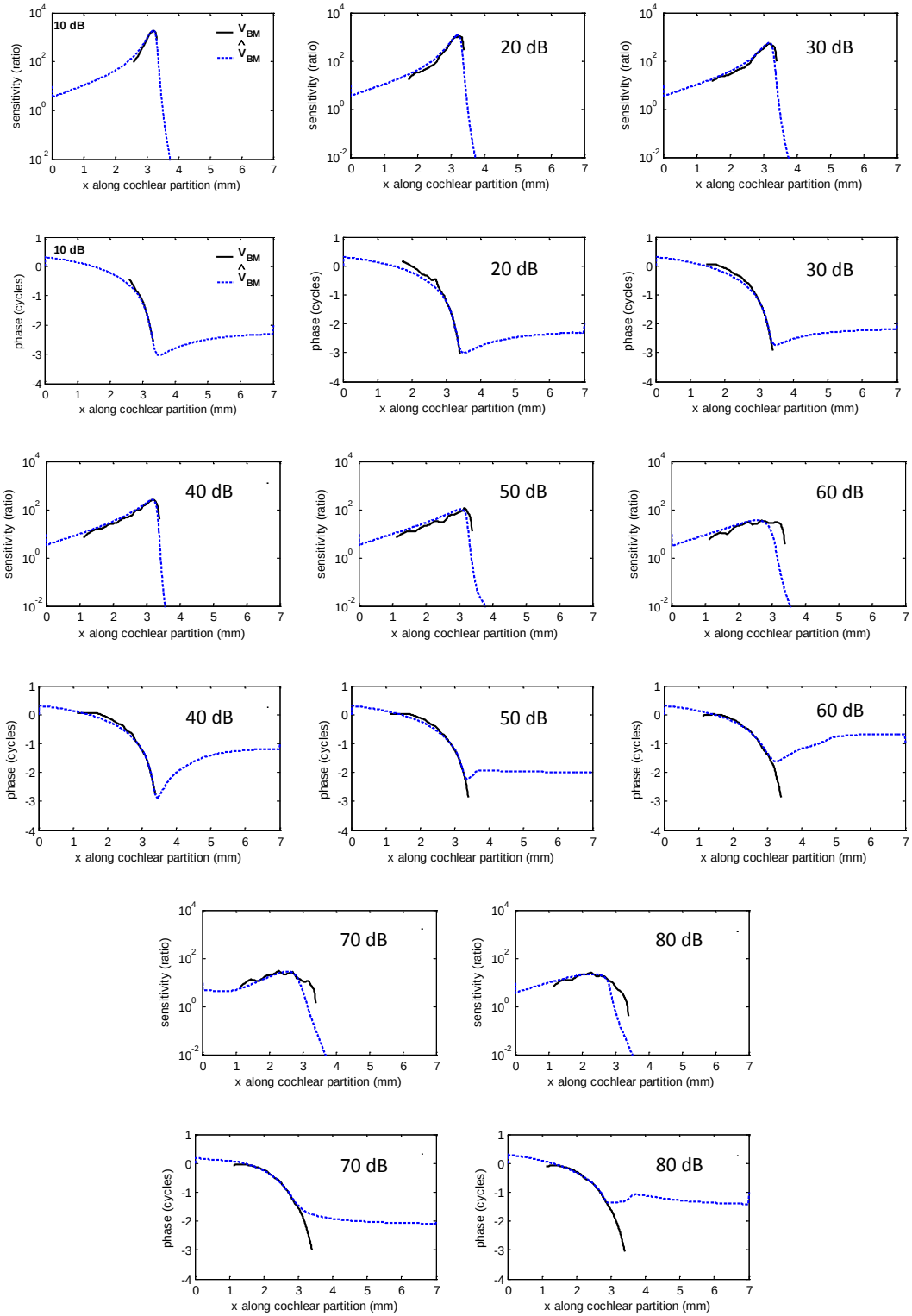

Figure H.2 Comparison between the magnitudes and phases of the BM responses measured by Lee *et al*. (2015) for a CF of 9.87 kHz and SPLs of 10, 20, 30, 40, 50, 60 ,70, and 80 dB, solid lines, and the responses of a model with second order micromechanics and 1D fluid coupling, obtained using single objective optimisation to identify the micromechanical poles and zeros, dashed lines

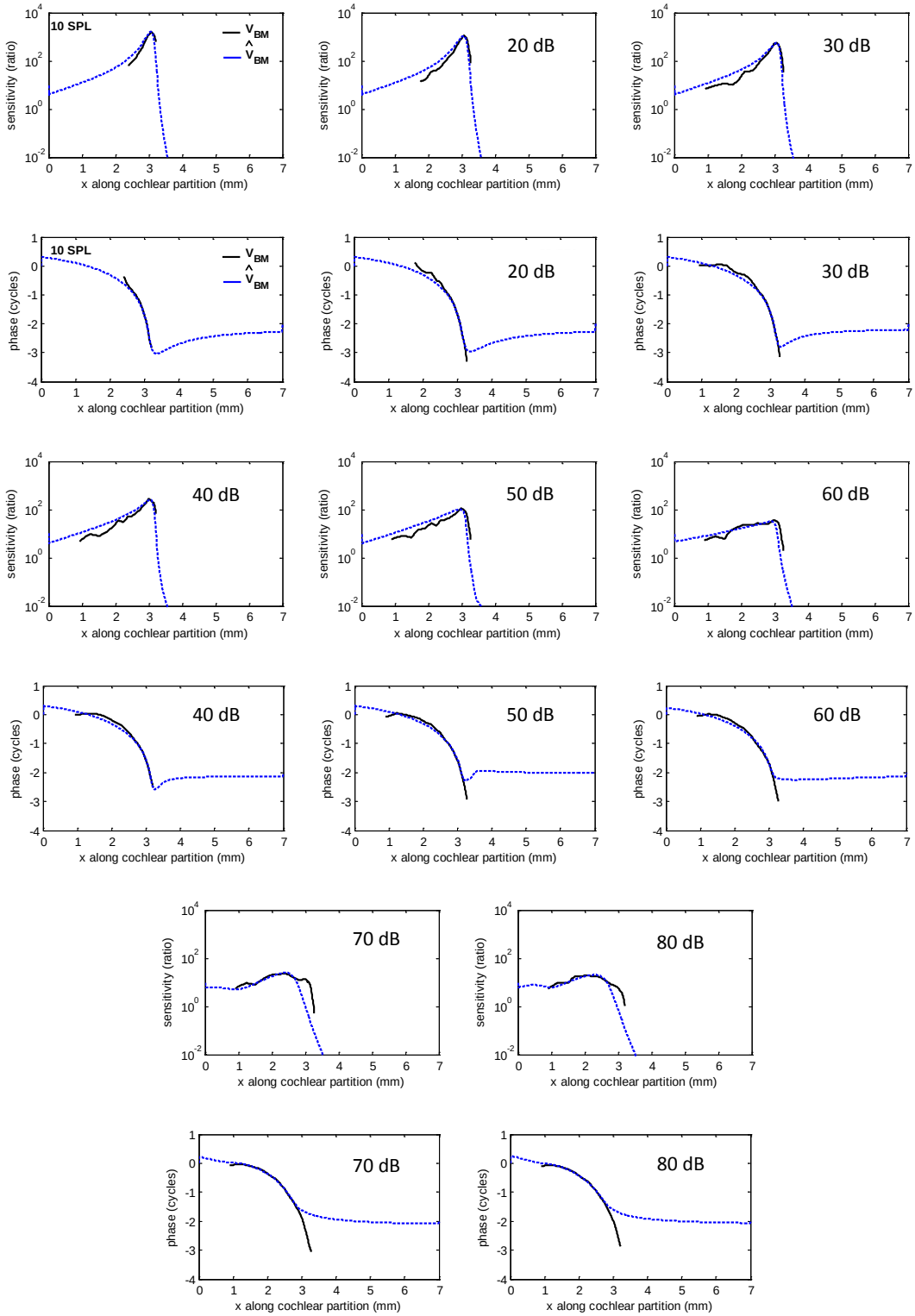

Figure H.3 Comparison between the magnitudes and phases of the BM responses measured by Lee *et al*. (2015) for a CF of 10.6 kHz and SPLs of 10, 20, 30, 40, 50, 60 ,70, and 80 dB, solid lines, and the responses of a model with second order micromechanics and 1D fluid coupling, obtained using single objective optimisation to identify the micromechanical poles and zeros, dashed lines

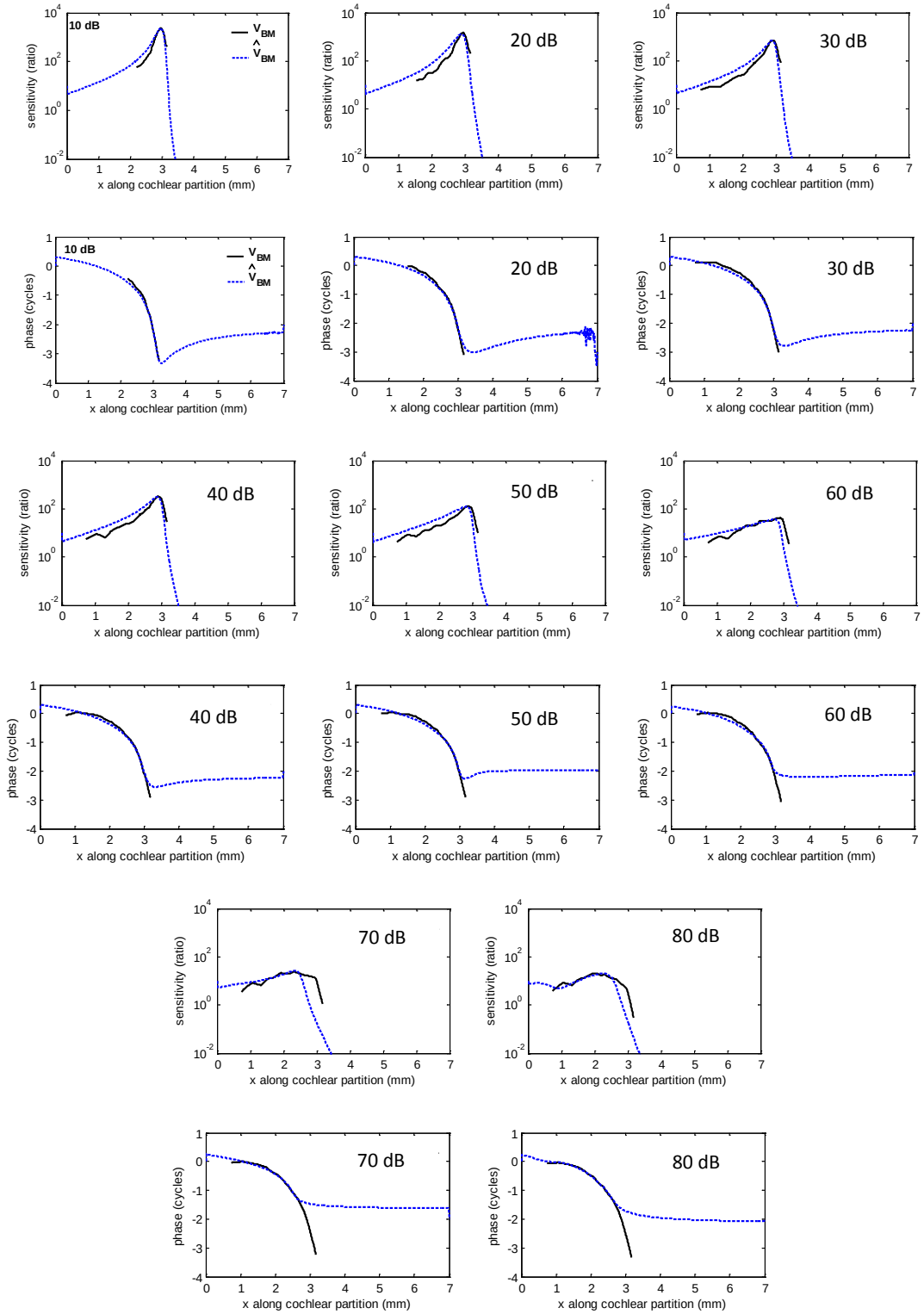

Figure H.4 Comparison between the magnitudes and phases of the BM responses measured by Lee *et al*. (2015) for a CF of 11.3 kHz and SPLs of 10, 20, 30, 40, 50, 60 ,70, and 80 dB, solid lines, and the responses of a model with second order micromechanics and 1D fluid coupling, obtained using single objective optimisation to identify the micromechanical poles and zeros, dashed lines

The variations of the estimated parameters with different SPL excitation levels at each fixed position for the mouse data optimized to give the smallest NMSE for amplitude are listed in Table H.1, and these parameters are also shown in Figure H.5 as a function of excitation level.

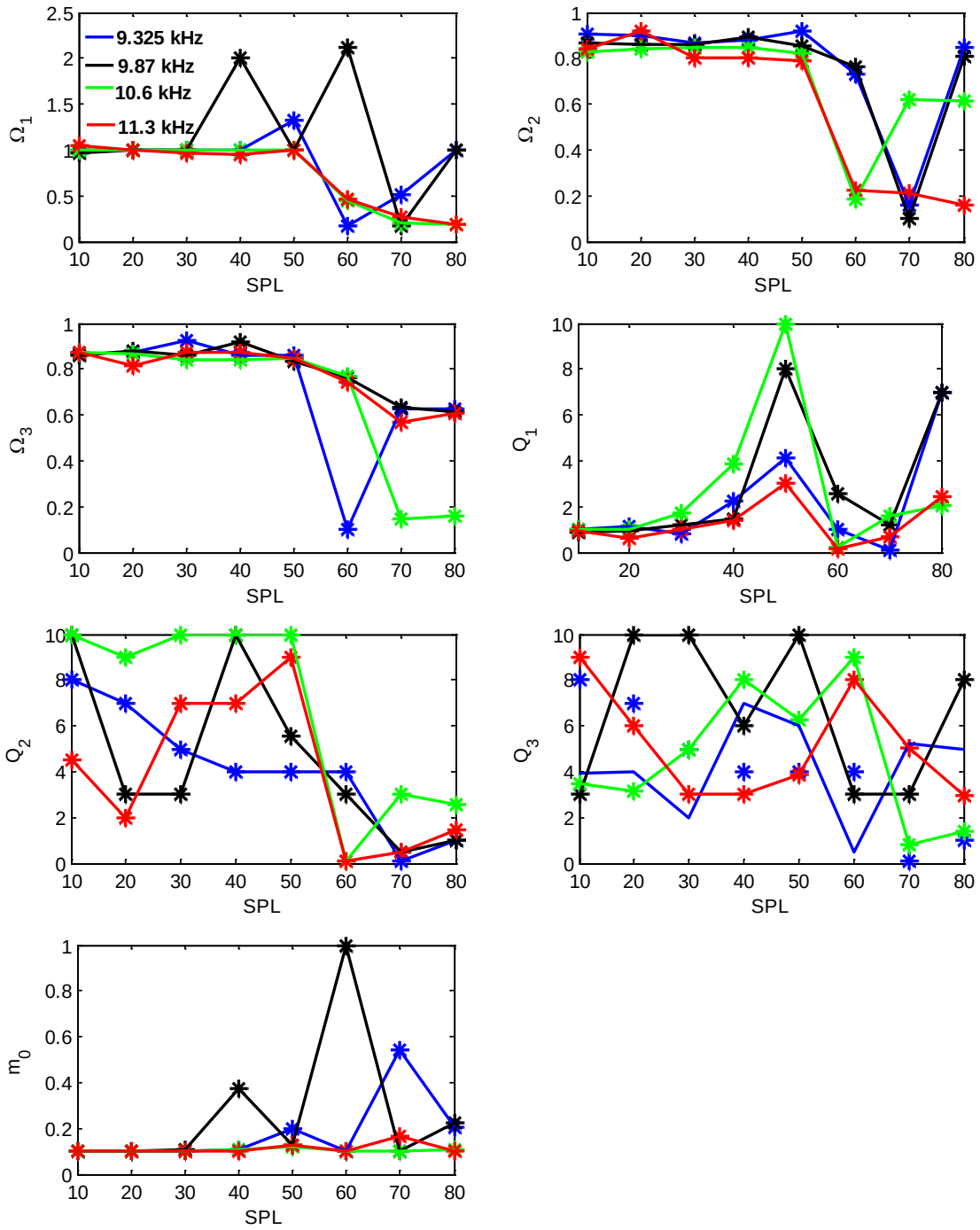

Figure H.5 parameter distributions obtained using single objective optimisation to identify the micromechanical poles and zeros

Average values of estimated parameters are calculated shown in Figure H.6, they do not show certain distribution trend along SPL, same as described in Chapter 5.

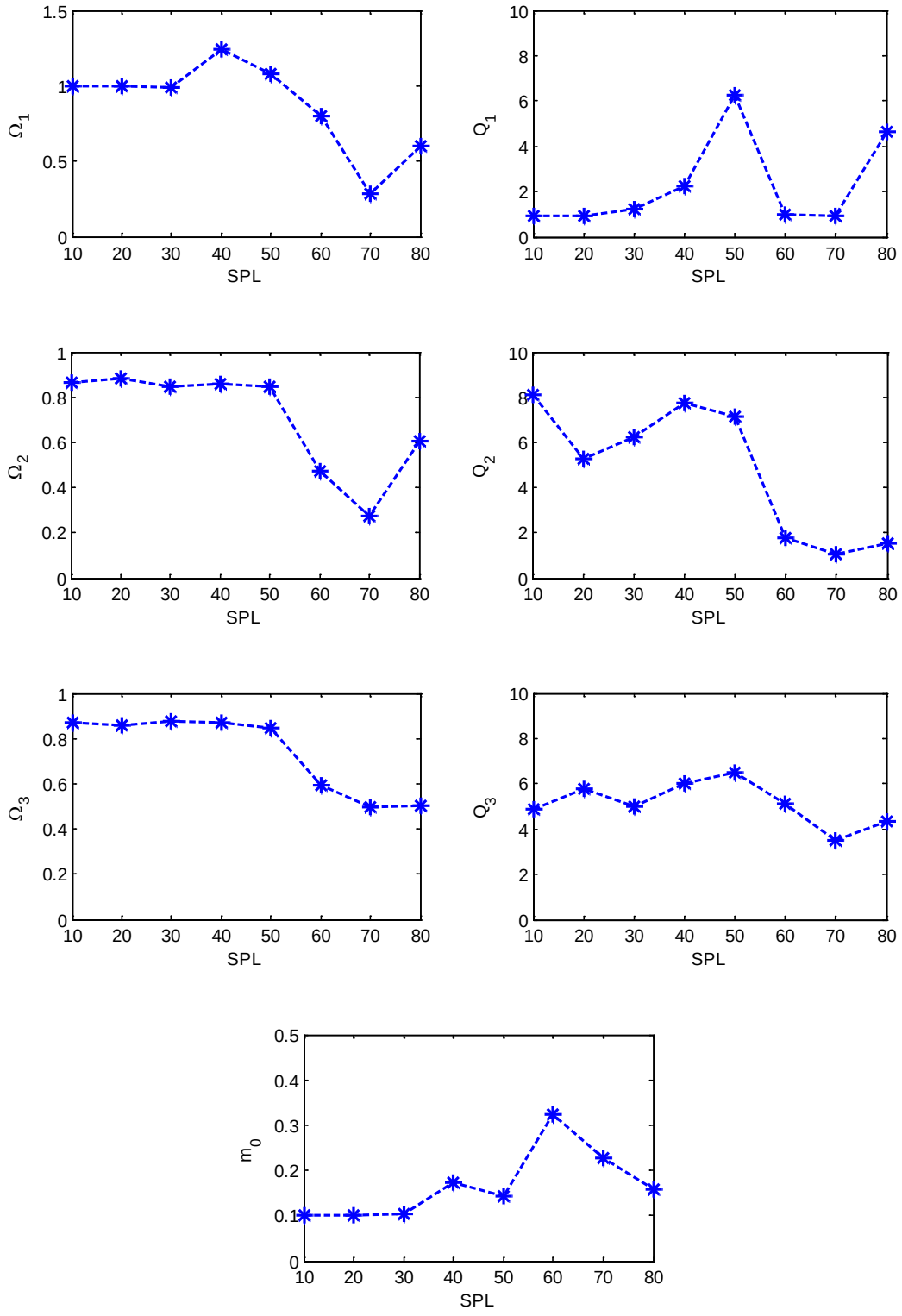

Figure H.6 Variations of average values of estimated parameters along SPL.

Those average values of parameters are then used to calculate the real and imaginary part of poles and zeros, as shown in Figure H. 6. It is shown in Figure H.6 that there are no certain trends for the variations of real and imaginary part of poles and zeros with variation of SPLs, as the same description in Chapter 5.

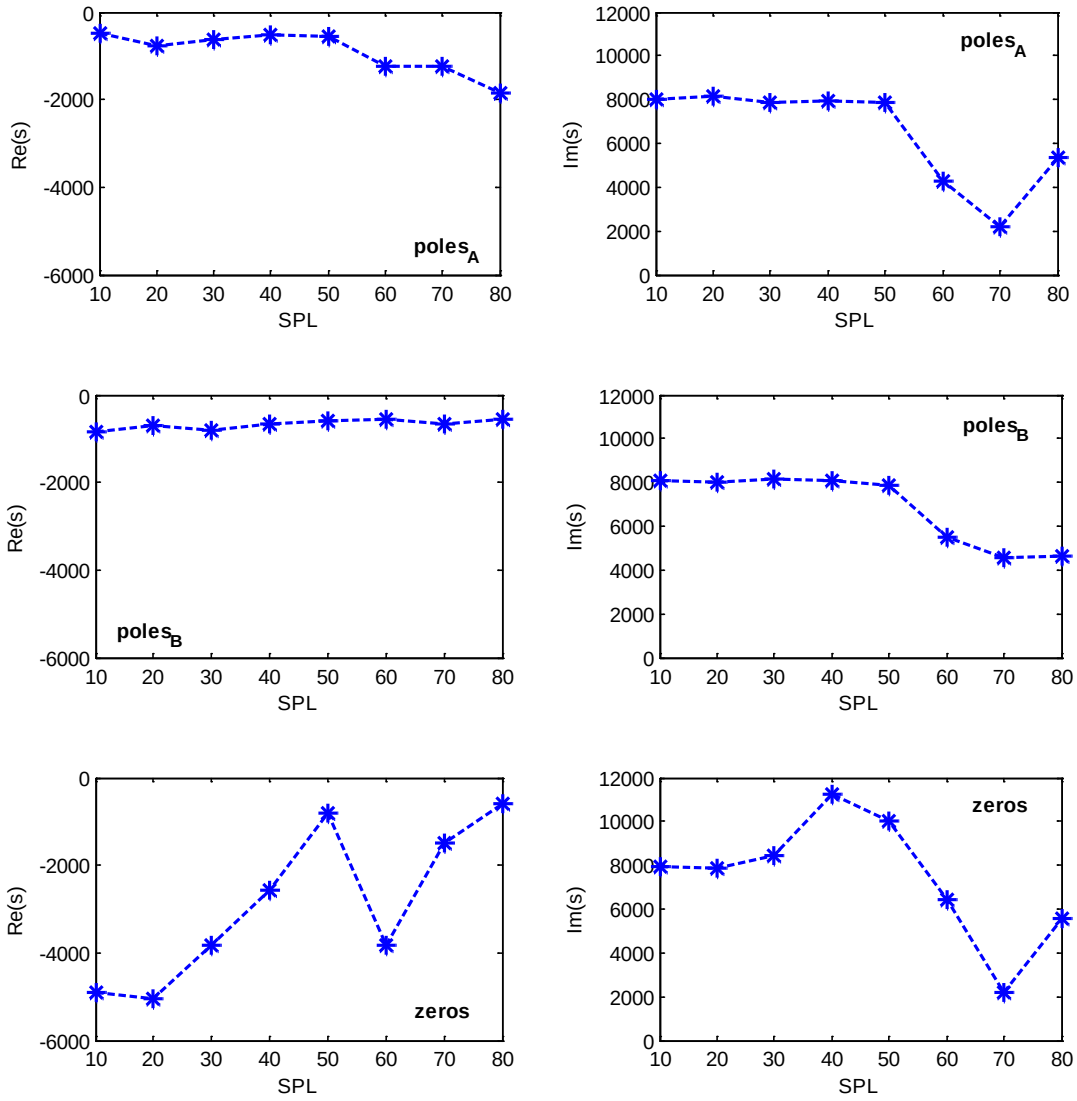

Figure H.7 Real and imaginary part of poles and zeros obtained from average values of eatimated parameter shown in Figure H. 6 along SPL.

The average values of estimated parameters are then used to determine the positions of the poles and zeros, as shown in Figure H.8. Positions of poles and zeros at each SPL show the similar situations described in Chapter 5. Two pairs of poles are always close to each other, and poles and zeros are always complex values. One pairs of zeros seems to move towards to one pairs of poles, so that the cochlea becomes from active to passive.

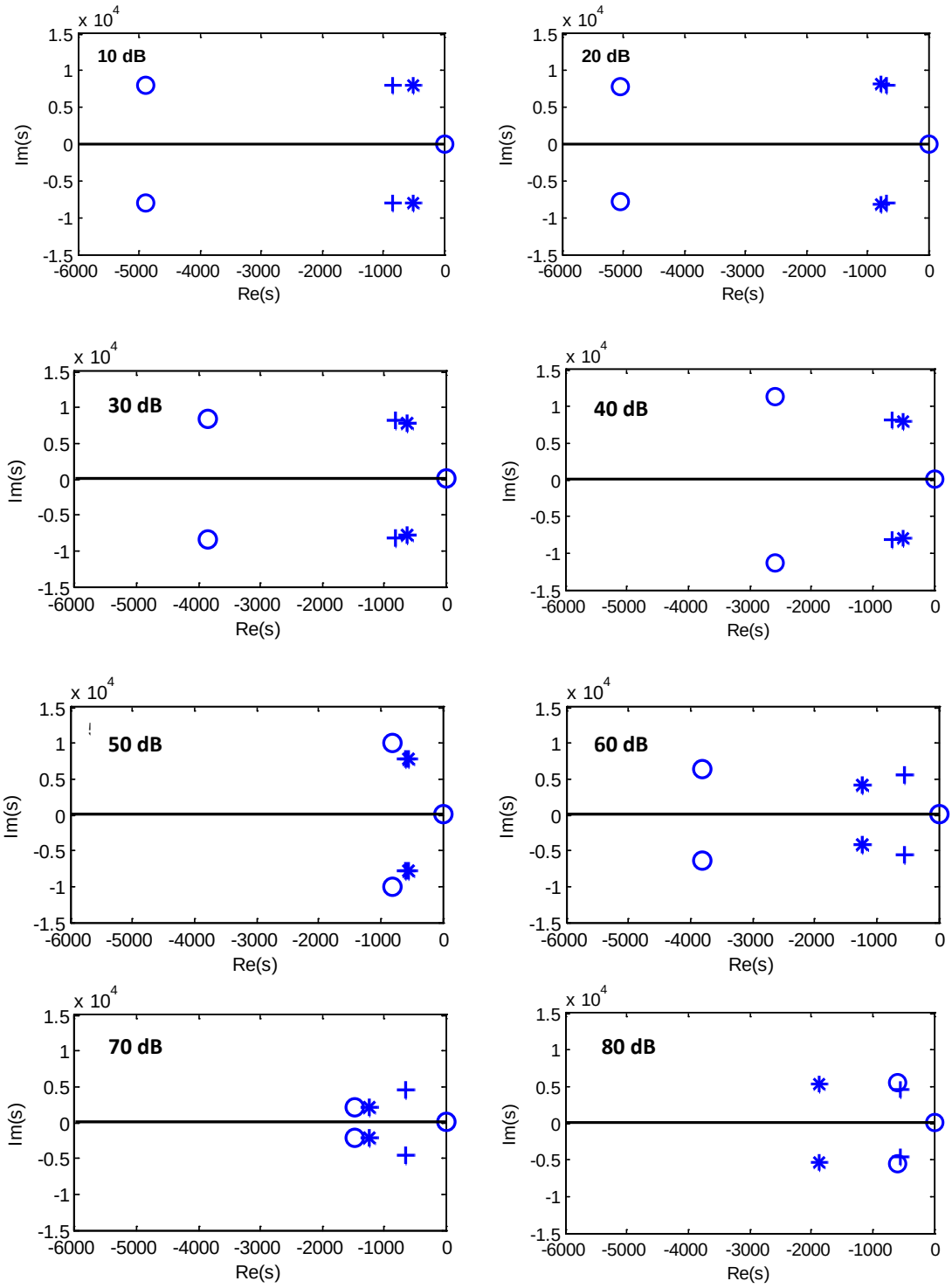

Figure H.8 Positions of the poles and zeros in the second order micromechanical models fitted to the data of Lee *et al.* (2015) at different levels of excitation.

Due to the reason that the varaitions of average values of parameters, and real and imaginary part of poles and zeros calculated using those average values ado not show certain distribution trends, the average values of real and imaginary part of poles and zeros using the estimated parameters at CF(x_0)=9.325, 9.87, 10.6 and 11.3 kHz and each set of these values at each characteristic position should be considered, as shown in Figure H.9.

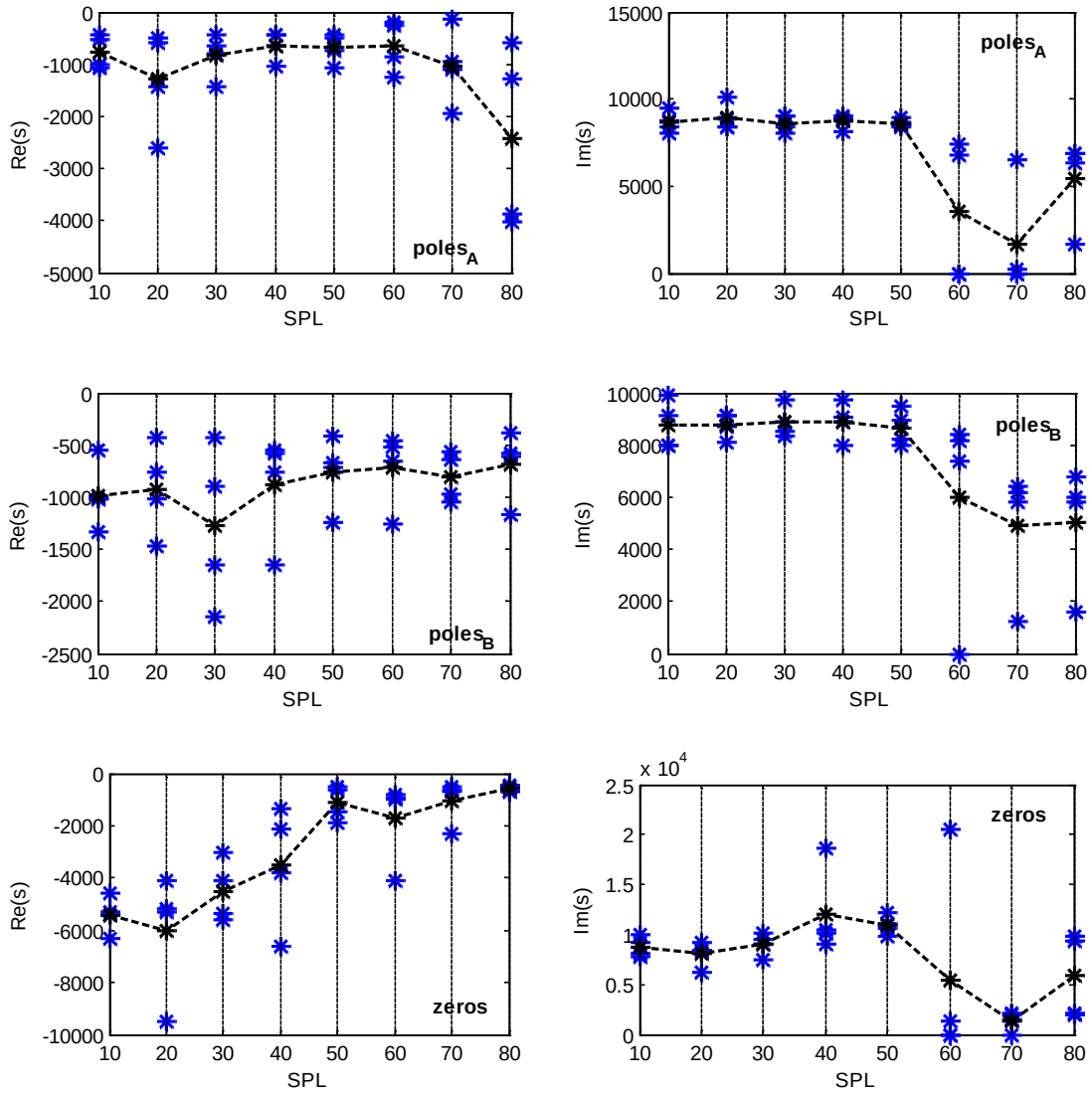

Figure H.9 Comparison of variations of real and imaginary part of poles and zeros at CF(x_0)=9.325, 9.87, 10.6 and 11.3 kHz with SPLs, and variation anf average values of real and imaginary part of poles and zeros for the four characteristic positions with SPLs.

Figure H.9 seems to show the reasonable distribution trends of variations of real and imaginary part of poles and zeros for the four characteristic positions. Those average values are used to calculate the positions of poles and zeros at each SPL shown in Figure H.10. Two pairs of poles are always close to each other, and poles and zeros are always complex values, one pairs of zeros move towards to original spot and one pairs of poles, so that the cochlea becomes from avtive to passive.

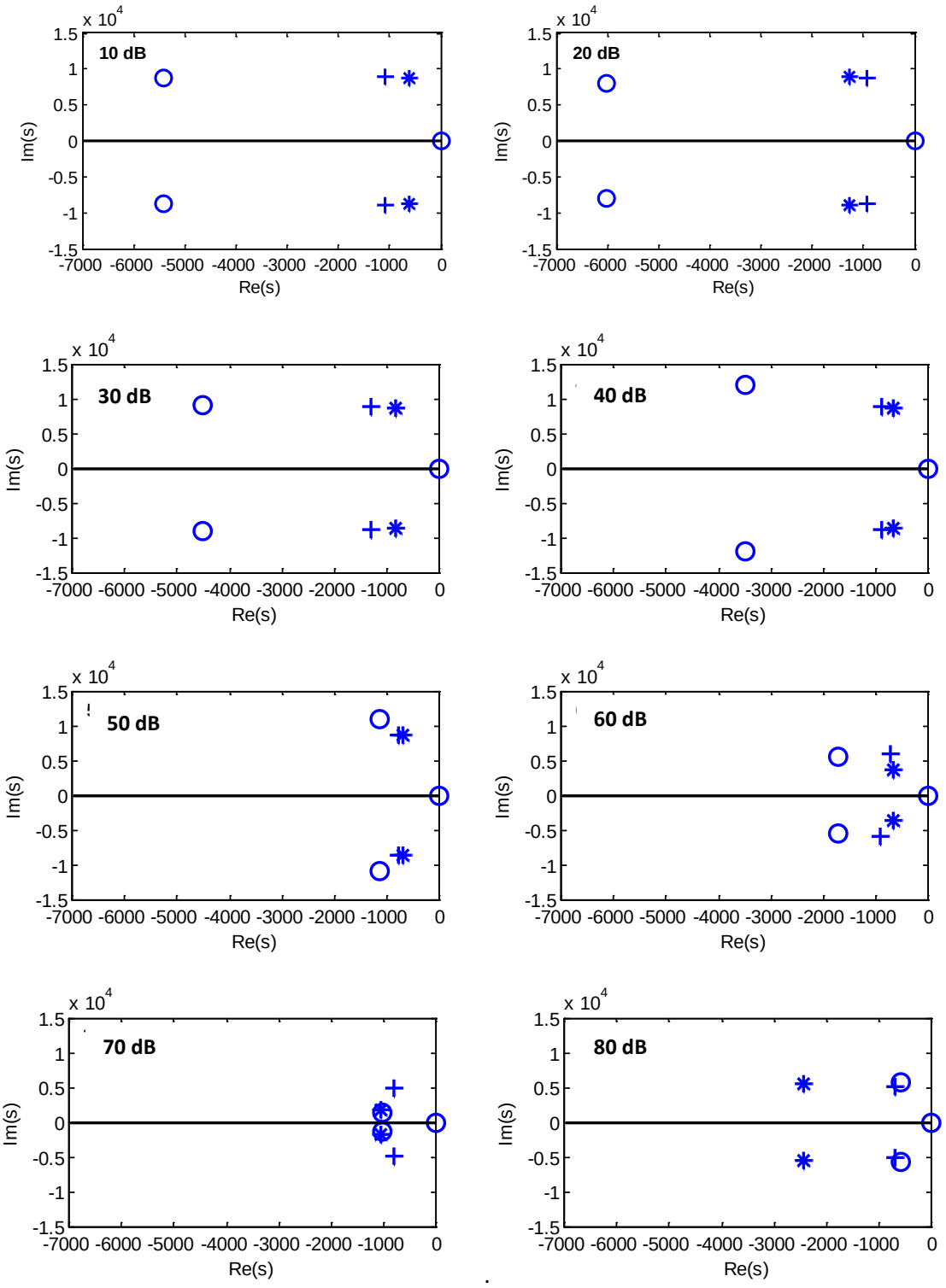

Figure H.10 Positions of poles and zeros at each SPL, oatained from the average values of real and imaginary part of poles and zeros for the four characteristic positions.

Those average values of poles and zeros are chosen to reconstruct the local frequency response, $\hat{Y}_{BM}(i\omega, x_0)$, as shown in FigureH.11, thus the coupled frequency response, $\hat{V}_{BM}(i\omega, x_0)$, can be calculated using the 1D uniform box model with this local response,

$\hat{Y}_{BM}(i\omega, x)$, as shown in Figure H.12, the local and coupled response are similar as those described in Chapter 5.

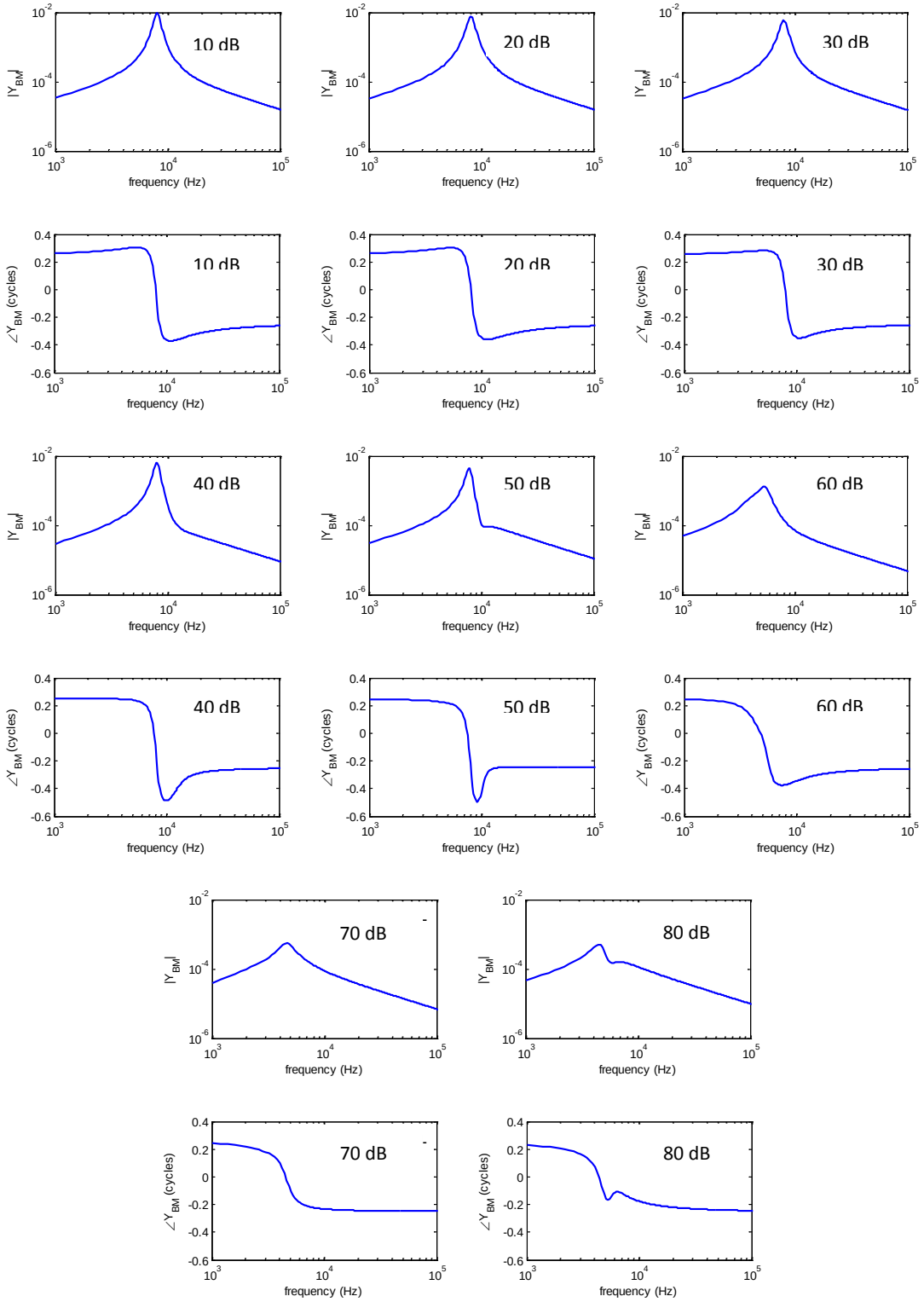

Figure H.11 The magnitude and phase of the BM admittance calculated using the pole and zero locations shown in Figure H. 10.

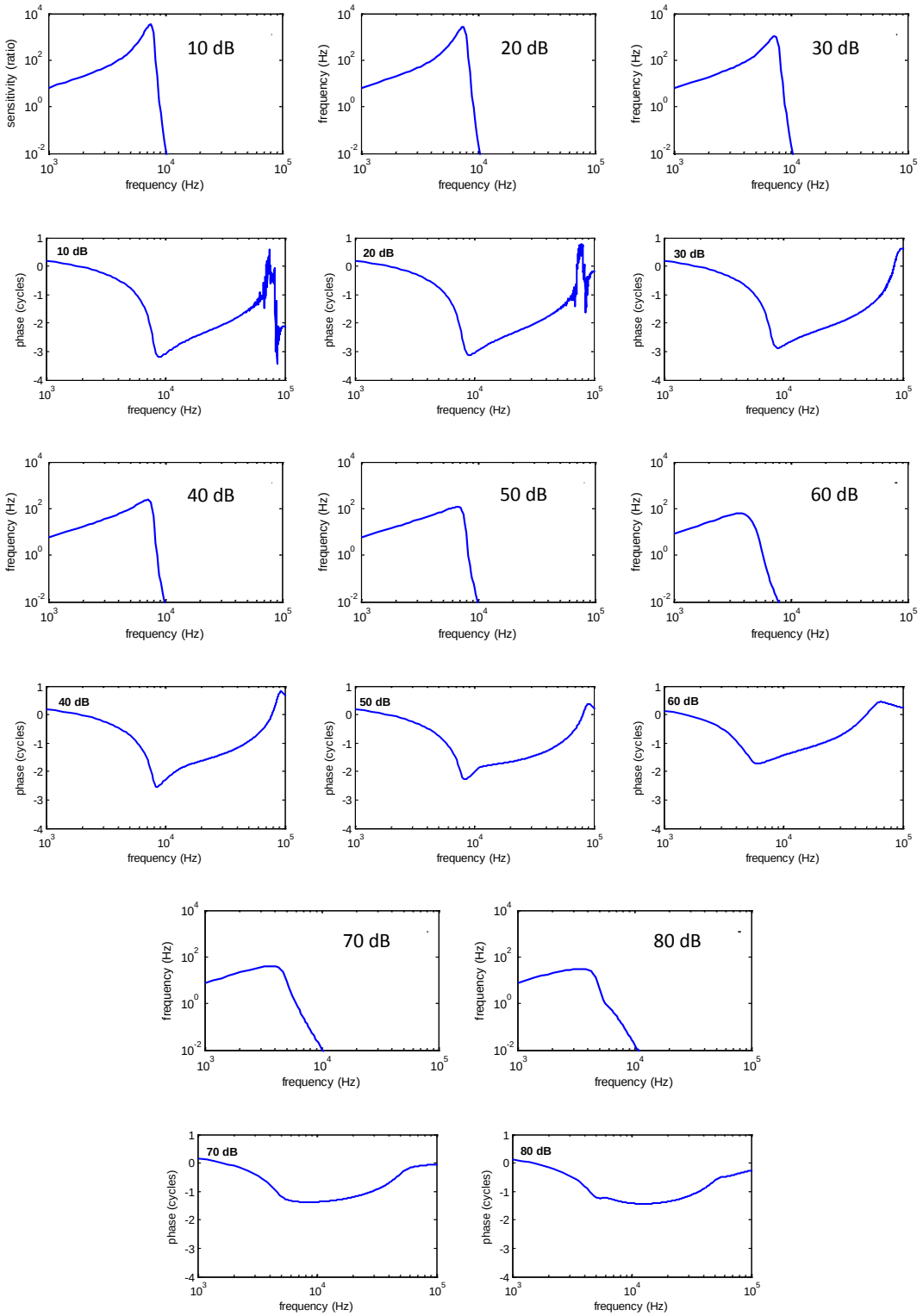

Figure H.12 The magnitude and phase of the coupled responses of the cochlea, calculated using the box model with the distribution of BM admittance (second order micromechanics), as shown in Figure H.11.

The reconstructed wavenumber can also be calculated, as shown in Figure H.13. It shows the similar results as those described in Chapter 5.

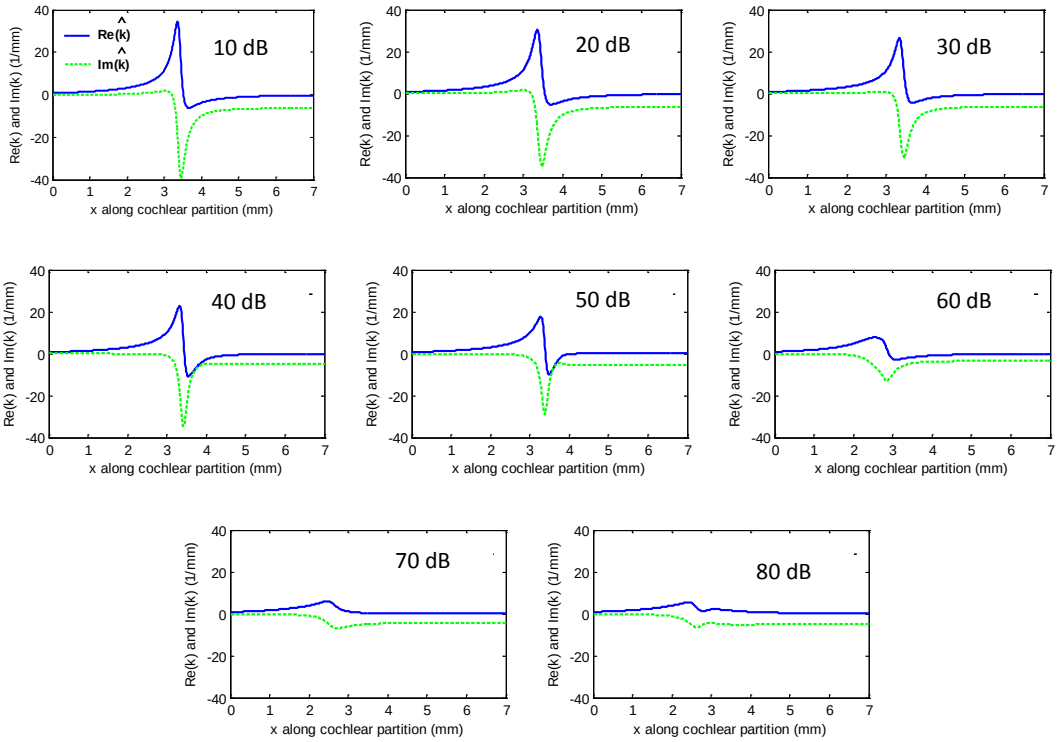

Figure H.13 Real (blue solid lines) and imaginary (green dash lines) part of the wavenumber distribution along cochlear partition calculated using the distribution of BM admittance shown in Figure H.11.

Finally, passive model fitting to the passive response and the effect of 3D fluid coupling on the optimization are also investigated in Figures H.14, H.15 and H.16. They show the similar effect as those described in Chapter 5. The passive model can only fit to mouse data from SPL of 40 dB to 80 dB, and 3D fluid coupling can improve the eatimated results. The estimated parameter and NMSE for complex BM velocity are listed in Tables H.1, H.2 and H. 3. The average values of NMSE in each case are also calculated, as listed in Table H.4, it can be found that the model with second order micromechanics shows better results than the model with first order micromechanics, and 3D fluid coupling shows better results than the 1D fluid coupling.

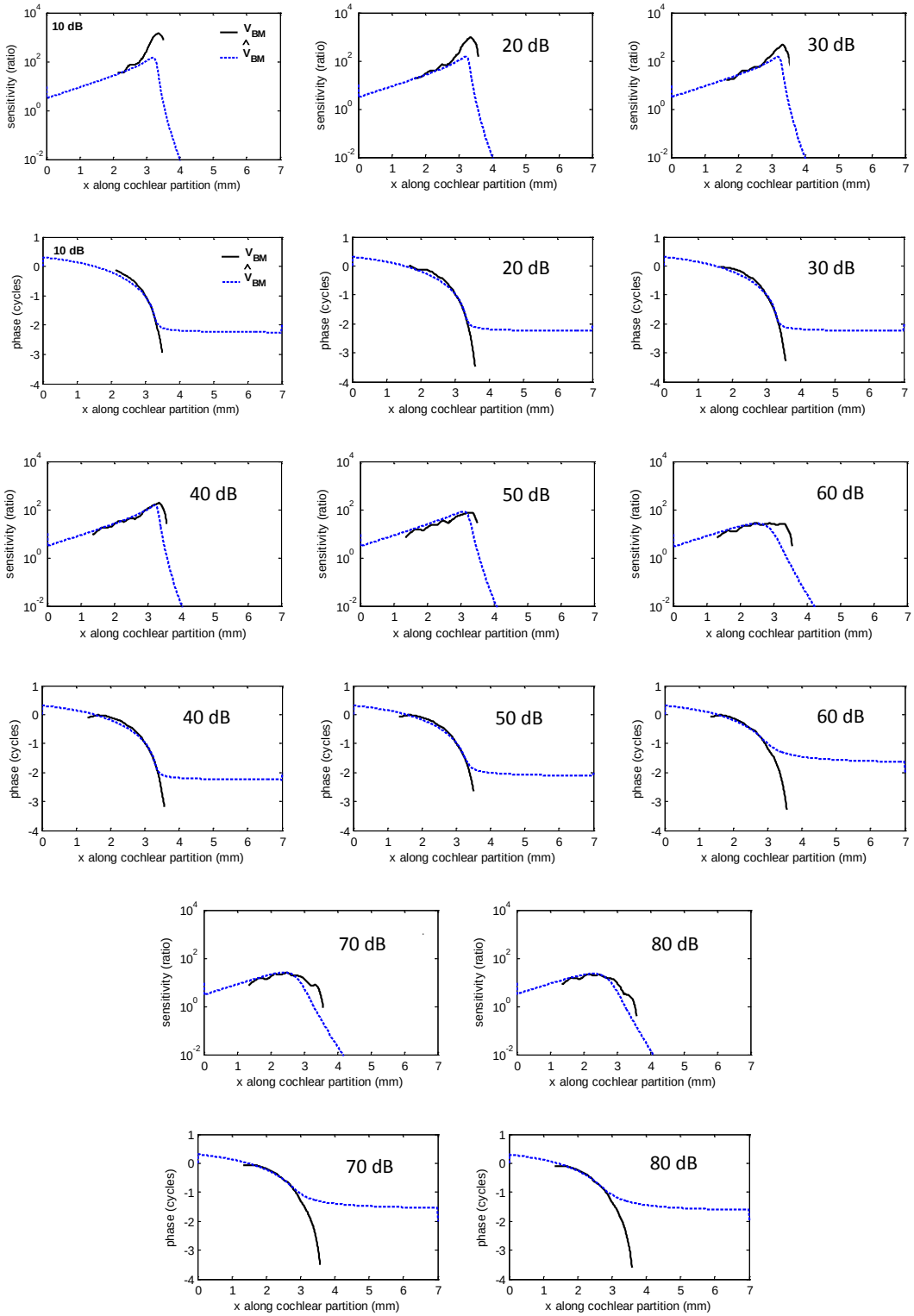

Figure H.14 Comparison between the magnitudes and phases of the BM responses measured by Lee *et al*. (2015) for a CF of 9.325 kHz and SPLs of 10, 20, 30, 40, 50, 60 ,70, and 80 dB, solid lines, and the responses of a model with first order micromechanics and 1D fluid coupling, obtained using single objective optimisation to identify the micromechanical poles and zeros, dashed lines

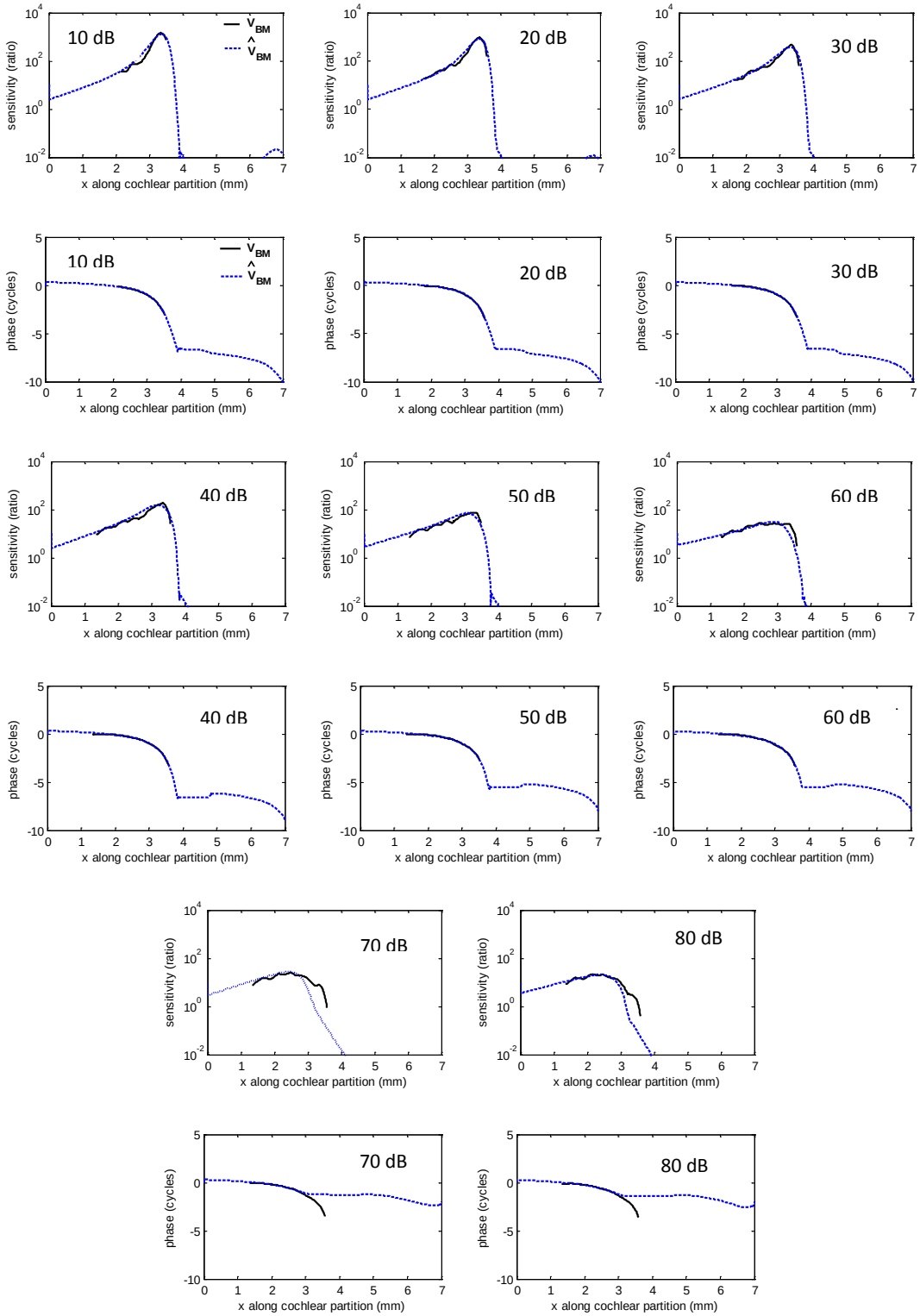

Figure H.15 Comparison between the magnitudes and phases of the BM responses measured by Lee *et al*. (2015) for a CF of 9.325 kHz and SPLs of 10, 20, 30, 40, 50, 60 ,70, and 80 dB, solid lines, and the responses of a model with second order micromechanics and 3D fluid coupling, obtained using single objective optimisation to identify the micromechanical poles and zeros, dashed lines

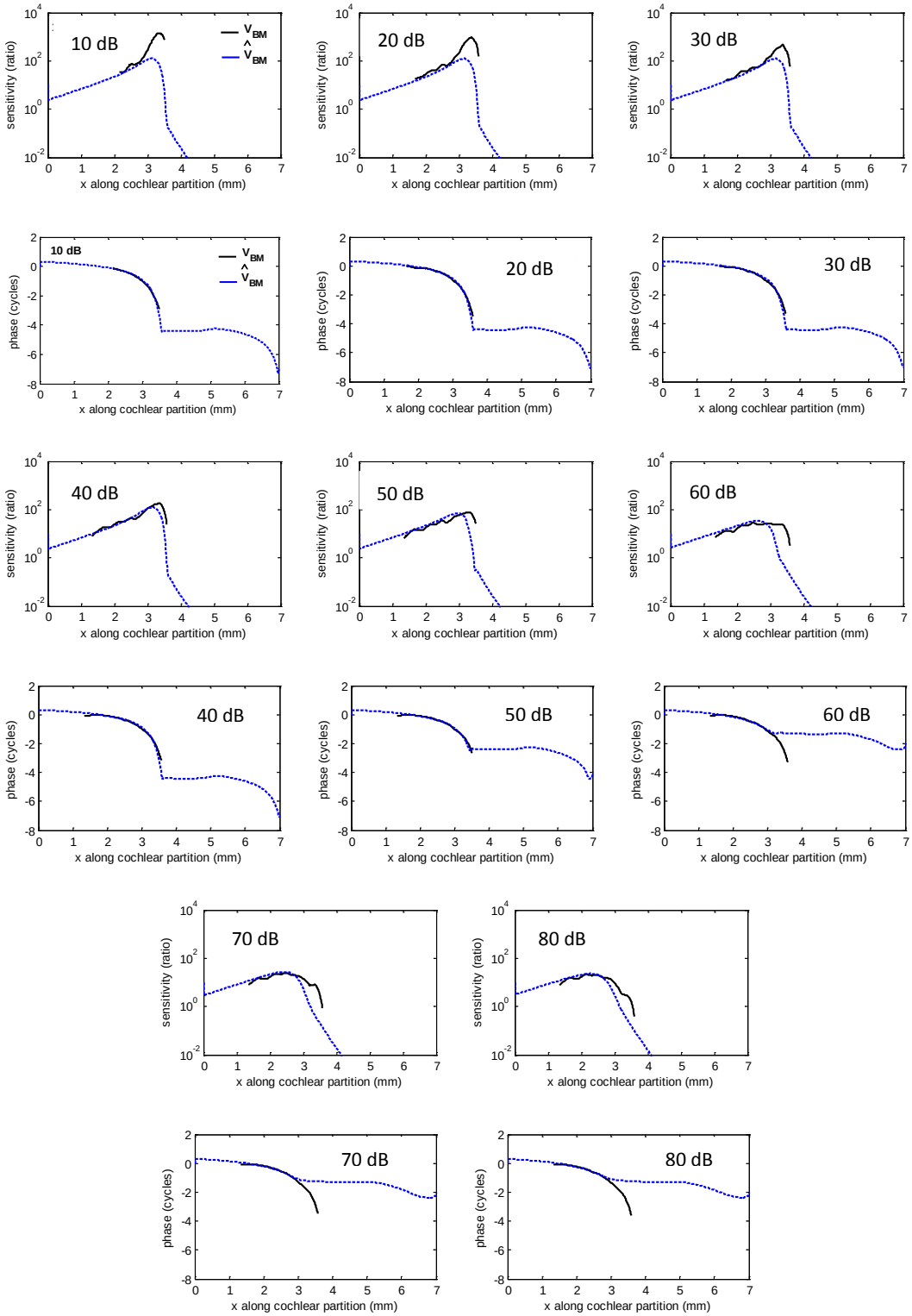

Figure H.16 Comparison between the magnitudes and phases of the BM responses measured by Lee *et al*. (2015) for a CF of 9.325 kHz and SPLs of 10, 20, 30, 40, 50, 60 ,70, and 80 dB, solid lines, and the responses of a model with first order micromechanics and 3D fluid coupling, obtained using single objective optimisation to identify the micromechanical poles and zeros, dashed lines.

Appendix H

Table H.1 The estimated parameters for the zero, Ω_1 and Q_1, and the poles, Ω_2, Ω_3, Q_2 and Q_3 of the micromechanical model obtained in the 1D uniform box model of active cochlea for different characteristic positions with mouse data, together with the normalised mean square error, NMSE, for complex BM response.

1D uniform box model of active cochlea									
Condition		Ω_1	Q_1	Ω_2	Q_2	Ω_3	Q_3	m_0	NMSE
Measurement data Mouse CF(x_0)=9.325 kHz SPL	10 SPL	1.00	1.01	0.91	8.00	0.87	4.00	0.10	0.13
	20 SPL	1.00	1.14	0.90	7.00	0.88	4.00	0.10	0.16
	30 SPL	1.00	0.83	0.87	5.00	0.92	2.00	0.10	0.29
	40 SPL	1.00	2.21	0.88	4.00	0.86	7.00	0.11	0.23
	50 SPL	1.32	4.13	0.92	4.00	0.86	6.00	0.20	0.29
	60 SPL	0.17	1.00	0.73	3.98	0.10	0.47	0.10	0.21
	70 SPL	0.51	0.10	0.16	0.10	0.63	5.25	0.54	0.10
	80 SPL	1.00	7.00	0.85	1.02	0.63	5.00	0.21	0.08
Average NMSE									0.19
Measurement data Mouse CF(x_0)=9.87 kHz SPL	10 SPL	0.97	0.88	0.87	10.00	0.86	3.00	0.10	0.05
	20 SPL	1.00	0.96	0.86	3.00	0.88	10.00	0.10	0.14
	30 SPL	1.00	1.21	0.86	3.00	0.86	10.00	0.11	0.13
	40 SPL	2.00	1.49	0.89	10.00	0.92	6.00	0.37	0.10
	50 SPL	1.00	8.00	0.85	5.58	0.83	10.00	0.12	0.27
	60 SPL	2.12	2.54	0.76	3.00	0.76	3.00	0.99	0.30
	70 SPL	0.17	1.23	0.10	0.51	0.64	3.00	0.10	0.10
	80 SPL	1.00	7.00	0.81	0.99	0.61	8.00	0.22	0.10
Average NMSE									0.15
Measurement data Mouse CF(x_0)=10.6 kHz SPL	10 SPL	1.00	1.00	0.83	10.00	0.87	3.45	0.10	0.11
	20 SPL	1.00	1.00	0.84	9.00	0.87	3.13	0.10	0.09
	30 SPL	1.00	1.75	0.85	10.00	0.84	5.00	0.10	0.07
	40 SPL	1.00	3.85	0.85	10.00	0.84	8.00	0.11	0.11
	50 SPL	1.00	10.00	0.82	10.00	0.84	6.24	0.12	0.27
	60 SPL	0.45	0.20	0.18	0.10	0.77	9.00	0.10	0.28
	70 SPL	0.20	1.60	0.62	3.00	0.15	0.81	0.10	0.12
	80 SPL	0.19	2.05	0.61	2.56	0.16	1.40	0.10	0.07
Average NMSE									0.14

Appendix H

1D uniform box model of active cochlea									
Condition		Ω_1	Q_1	Ω_2	Q_2	Ω_3	Q_3	m_0	NMSE
Measurement data Mouse CF(x_0)=11.3 kHz SPL	10 SPL	1.04	0.93	0.84	4.50	0.88	9.00	0.10	0.08
	20 SPL	1.00	0.60	0.92	2.00	0.81	6.00	0.10	0.20
	30 SPL	0.97	1.03	0.80	7.00	0.88	3.00	0.10	0.11
	40 SPL	0.95	1.41	0.80	7.00	0.87	3.00	0.10	0.15
	50 SPL	1.00	3.00	0.79	9.00	0.84	3.85	0.12	0.25
	60 SPL	0.46	0.18	0.22	0.10	0.74	8.00	0.10	0.30
	70 SPL	0.27	0.68	0.21	0.49	0.57	5.04	0.16	0.22
	80 SPL	0.19	2.45	0.16	1.49	0.61	2.95	0.10	0.08
Average NMSE									0.17

Table H.2 The estimated parameters for the zero, and, and the poles,and of the micromechanical model obtained in the 1D uniform box model for the passive cochlea at CF(x_0) = 9.325 kHz, together with the normalised mean square error, NMSE, for complex BM response.

CF(x_0)=9.325 kHz				
1D uniform box model of passive cochlea				
condition	Ω	Q	m_0	NMSE
10S PL	0.79	10.00	0.10	0.88
20 SPL	0.81	10.00	0.10	0.81
30 SPL	0.80	10.00	0.10	0.60
40 SPL	0.81	10.00	0.10	0.33
50 SPL	0.78	5.60	0.11	0.38
60 SPL	0.64	2.00	0.18	0.41
70 SPL	0.58	2.00	0.20	0.20
80 SPL	0.57	1.75	0.18	0.14
Average NMSE				0.47

Table H.3 The estimated parameters for the zero, and, and the poles,and of the micromechanical model obtained in the 3D uniform box model for the passive and active cochlea at CF(x0) = 9.325 kHz, together with the normalised mean square error, NMSE, for complex BM response.

CF(x_0)=9.325 kHz								
3D uniform box model of active cochlea								
condition	Ω_1	Q_1	Ω_2	Q_2	Ω_3	Q_3	m_0	NMSE
10 SPL	2.50	0.30	2.00	3.00	1.21	1.32	0.10	0.03
20 SPL	2.41	0.45	1.17	1.70	2.00	8.00	0.10	0.05
30 SPL	2.50	0.61	1.24	2.00	1.90	8.00	0.10	0.05
40 SPL	1.50	0.10	1.20	0.14	1.22	10.00	0.10	0.09
50 SPL	1.50	0.10	1.22	10.00	1.04	0.12	0.10	0.11
60 SPL	1.08	0.10	1.30	10.00	0.50	0.10	0.10	0.15
70 SPL	1.50	1.00	1.03	1.26	0.98	1.50	0.16	0.17
80 SPL	0.94	0.10	0.55	0.12	1.12	1.50	0.10	0.08
Average NMSE								0.09

3D uniform box model of passive cochlea				
condition	Ω	Q	m_0	NMSE
10S PL	1.00	10.00	0.10	0.87
20 SPL	1.01	10.00	0.10	0.81
30 SPL	1.02	10.00	0.10	0.63
40 SPL	1.01	10.00	0.10	0.41
50 SPL	0.99	4.52	0.10	0.39
60 SPL	0.92	1.94	0.10	0.34
70 SPL	0.84	1.56	0.10	0.17
80 SPL	0.81	1.29	0.10	0.13
Average NMSE				0.47

Table H.4 Average values of NMSE in each case.

CF(x_0)=9.325 kHz		
Average value of NMSE		
condition	1D uniform model	3D uniform model
1 degree of freedom	0.47	0.47
2 degree of freedom	0.19	0.09

Reference

Allen, J. B. (1977). "Two-dimensional cochlear fluid model: New results," The Journal of the Acoustical Society of America, 61, 110-119.

Allen, J. B., & Sondhi, M. M. (1979). Cochlear macromechanics: Time domain solutions. The Journal of the Acoustical Society of America, 66(1), 123-132.

Allen, J. B. (1980). Cochlear micromechanics—a physical model of transduction. The Journal of the Acoustical Society of America, 68(6), 1660-1670.

Allen, J. B., & Fahey, P. F. (1992). Using acoustic distortion products to measure the cochlear amplifier gain on the basilar membrane. The Journal of the Acoustical Society of America, 92(1), 178-188.

Allen, J. B., & Fahey, P. F. (1993). A second cochlear-frequency map that correlates distortion product and neural tuning measurements. The Journal of the Acoustical Society of America, 94(2), 809-816.

Bekesy, G. von (1960). "Experiments in Hearing," (McGraw Hill, New York).

Wen, Bo. "Modeling the nonlinear active cochlea: Mathematics and analog VLSI." (2006).

Cai, H., Manoussaki, D., & Chadwick, R. (2005). Effects of coiling on the micromechanics of the mammalian cochlea. Journal of the Royal Society Interface, 2(4), 341-348.

Cannell, J. K. (1969). "Cochlear Models," Ph.D, thesis, University of Warwick, Coventry, England.

Steele, C. R., & Zais, J. G. (1985). Effect of coiling in a cochlear model. The Journal of the Acoustical Society of America, 77(5), 1849-1852.

Dallos, P., and Fakler, B. (2002) "Prestin, a New Type of Motor Protein," Nature Reviews Molecular Cell Biology, 3, pp, 104-111.

De Boer, E., & De Jongh, H. R. (1978). On cochlear encoding: Potentialities and limitations of the reverse-correlation technique. The Journal of the Acoustical Society of America, 63(1), 115-135.

de Boer, E. (1980). Auditory physics. Physical principles in hearing theory. I.Physics reports, 62(2), 87-174.

de Boer, E. (1981). Digital solution of cochlear mechanics problems. The Journal of the Acoustical Society of America, 69(5), 1369-1373.

de Boer, E. (1981) "Short waves in three-dimensional cochlea models: Solution for a 'block' model, " Hearing Reseach, 4(1), 53-77.

de Boer, E., & van Bienema, E. (1982). Solving cochlear mechanics problems with higher-order differential equations. The Journal of the Acoustical Society of America, 72(5), 1427-1434.

de Boer, E. (1983). No sharpening? A challenge for cochlear mechanics. The Journal of the Acoustical Society of America, 73(2), 567-573.

de Boer, E. (1983). Power amplification in an active model of the cochlea—Short-wave case. The Journal of the Acoustical Society of America, 73(2), 577-579.

de Boer, E., & Kruidenier, C. (1990). On ringing limits of the auditory periphery.Biological cybernetics, 63(6), 433-442.

de Boer, E. (1991) "Auditory Physics. Physical principle in hearing theory III," Physics Report (Review Section of Physics Letters) 203. No.3 125-231. North-Holland.

de Boer, E. (1991) "On mechanical excitation of hair-cell stereocilia in the cochlea, " in Auditory Physiology and Perception, edited by Y. Cazals, L. Demany, and K. Horner (Pergamon, Oxford), pp, 93-99.

de Boer, E. (1993). "The sulcus connection. On a mode of participation of outer hair cells in cochlear mechanicsa), " The Journal of the Acoustical Society of America, 93(5), 2845-2859.

de Boer, E. (1995). "The 'inverse problem' solved for a three-dimensional model of the cochlea. I. Analysis, " The Journal of the Acoustical Society of America,98(2), 896-903.

de Boer, E. (1995). "The 'inverse problem'solved for a three-dimensional model of the cochlea. II. Application to experimental data sets, " The Journal of the Acoustical Society of America, 98(2), 904-910.

de Boer, E. (1996) Mechanics of the cochlea: Modelling efforts, in The cochlea, edited by Dallos, P., et al., Springer, New York, 258-317.

de Boer, E. (1997). Classical and non-classical models of the cochlea. The Journal of the Acoustical Society of America, 101(4), 2148-2150.

de Boer, E. (1997). Connecting frequency selectivity and nonlenearity for models of the cochlea. Auditory neuroscience, 3(4), 377-388.

de Boer, E., & Nuttall, A. L. (1997). "The mechanical waveform of the basilar membrane. I. Frequency modulations ("glides") in impulse responses and cross-correlation functions, " The Journal of the Acoustical Society of America, 101(6), 3583-3592.

de Boer, E. (1998) "A method for forward and inverse solutions of a three-dimensional model of the cochlea," The Journal of the Acoustical Society of America, 103(6), 3725-3728.

de Boer, E., & Nuttall, A. L. (2000). "The mechanical waveform of the basilar membrane. II. From data to models—and back," The Journal of the Acoustical Society of America, 107(3), 1487-1496.

de Boer, E., & Nuttall, A. L. (2000). "The mechanical waveform of the basilar membrane. III. Intensity effects," The Journal of the Acoustical Society of America, 107(3), 1497-1507.

de Boer, Egbert, and Alfred L. Nuttall. (2002) "The mechanical waveform of the basilar membrane. IV. Tone and noise stimuli." The Journal of the Acoustical Society of America 111.2: 979-989.

de Boer, E., & Nuttall, A. L. (1999). "The 'inverse problem' solved for a three-dimensional model of the cochlea. III. Brushing-up the solution method, " The Journal of the Acoustical Society of America, 105(6), 3410-3420.

de Boer, E. and Viergever, M. A. (1982). "Validity of the Liouville-Green (or WKB) method for cochlear mechanics, " Hearing Research, 8(2), 131-155.

Deb, K., 2001. Multi-objective optimization using evolutionary algorithms(Vol. 16). John Wiley & Sons.

Diependaal, R. J. (1988). Nonlinear and active cochlear models: analysis and solution methods (Doctoral dissertation, TU Delft, Delft University of Technology).

Diependaal, Rob J., Max A. Viergever, and Egbert de Boer. "Are active elements necessary in the basilar membrane impedance?." The Journal of the Acoustical Society of America 80.1 (1986): 124-132.

Diependaal, R. J., de Boer, E., & Viergever, M. A. (1987). "Cochlear power flux as an indicator of mechanical activity, " The Journal of the Acoustical Society of America, 82(3), 917-926.

Dong, W., & Olson, E. S. (2009). In vivo impedance of the gerbil cochlear partition at auditory frequencies. Biophysical journal, 97(5), 1233-1243.

Evolutionary multiobjective optimization: theoretical advances and applications. Springer, 2005.

Elliott, S. J., Lineton, B., and Ni, G. (2011a). "Fluid coupling between the elements in a discrete model of cochlear mechanics," in ISVR Technical Memorandum 990 (ISVR, University of Southampton, Southampton, UK), pp. 1-97.

Elliott, S. J., Lineton, B., and Ni, G. (2011b). "Fluid coupling in a discrete model of cochlear mechanics," The Journal of the Acoustical Society of America, 130, 1441-1451.

Fernández, C. (1952). Dimensions of the cochlea (guinea pig). The Journal of the Acoustical Society of America, 24(5), 519-523.

Geisler, C. D. (1991). "A cochlear model using feedback from motile outer hair cells," Hearing research, 54(1), 105-117.

Geisler, C. D. (1993). "A realizable cochlear model using feedback from motile outer hair cells, " Hearing research, 68(2), 253-262.

Geisler, C. D. (1998). "From sound to synapse: physiology of the mammalian ear, " Oxford University Press.

Greenwood, D. D. (1990). “A cochlear frequency-position function for several species—29 years later.” The Journal of the Acoustical Society of America,87(6), 2592-2605.

Hall, J. L. (1974). "Two-Tone distortion products in a non-linear model of the basilar membrane," The Journal of the Acoustical Society of America, 56, 1818-1828.

Helmoltz, H. F. von (1874). Theorie Physiologique de la Musique, Masson G. Ed., Paris.

Helmholtz, H. v. (1862). Die Lehre von den Tonempfindungen, als physiologische Grundlage fur die Theorie der Musik. Braunschweig.

Hubbard, A. (1993). "A traveling-wave amplifier model of the cochlea, " Science,259(5091), 68-71.

Johnstone, B. M., and Boyle, A. J. F. (1967). "Basilar Membrane Vibrations Examined with the Mossbauer Technique," Science, 158, 389-390.

Kates, J. M. (1993). Accurate tuning curves in a cochlear model. Speech and Audio Processing, IEEE Transactions on, 1(4), 453-462.

Kemp, D. T. (1978). "Stimulated acoustic emissions from within the human auditory system," The Journal of the Acoustical Society of America, 64(5), 1386-1391.

Kim, N., Homma, K., and Puria, S. (2011). "Inertial bone conduction: symmetric and anti-symmetric components," Journal of the Association for Research in Otolaryngology : JARO 12, 261-279.

Kim, D. O., Molnar, C. E., and Pfeiffer, R. R. (1973). "A system of Non-Linear Differential Equations Modeling Basilar Membrane Motion," The Journal of the Acoustical Society of America, 54, 1517-1529.

Kim, D. O., Molnar, C. E., & Matthews, J. W. (1980). "Cochlear mechanics: nonlinear behavior in two-tone responses as reflected in cochlear-nerve-fiber responses and in ear-canal sound pressure," The Journal of the Acoustical Society of America, 67(5), 1704-1721.

Kolston, P. J., Viergever, M. A., de Boer, E., & Diependaal, R. J. (1989). Realistic mechanical tuning in a micromechanical cochlear model. The Journal of the Acoustical Society of America, 86(1), 133-140.

Kolston, P. J. (2000). The importance of phase data and model dimensionality to cochlear mechanics. Hearing research, 145(1), 25-36.

Ku, E. M. (2008). "Modelling the human cochlear amplifier," Ph.D, thesis, University of Southampton, England.

Lee, H.Y., Raphael, P.D., Park, J., Ellerbee, A.K., Applegate, B.E. and Oghalai, J.S., 2015. Noninvasive in vivo imaging reveals differences between tectorial membrane and basilar membrane traveling waves in the mouse cochlea. Proceedings of the National Academy of Sciences, 112(10), pp.3128-3133

Mandal, S., Zhak, S. M., & Sarpeshkar, R. (2009). A bio-inspired active radio-frequency silicon cochlea. Solid-State Circuits, IEEE Journal of, 44(6), 1814-1828.

Manoussaki, D., & Chadwick, R. S. (2000). Effects of geometry on fluid loading in a coiled cochlea. SIAM Journal on Applied Mathematics, 61(2), 369-386.

Mammano, F., and Nobili, R. (1993). "Biophysics of the cochlea: Linear approximation," The Journal of the Acoustical Society of America, 93, 3320-3332.

Marquardt, D.W., 1963. An algorithm for least-squares estimation of nonlinear parameters. Journal of the society for Industrial and Applied Mathematics, 11(2), pp.431-441.

Neely, S. T., & Kim, D. O. (1983). An active cochlear model showing sharp tuning and high sensitivity. Hearing Research, 9(2), 123-130.

Neely, S. T., and Kim, D. O. (1986). "A model for active elements in cochlear biomechanics," The Journal of the Acoustical Society of America, 79 (5), 1472-1480.

Neely, S. T. (1978). "Mathematical Models the Mechanics of the Cochlea," Ph.D, thesis, Califoniss Institute of Technology.

Neely, S. T. (1993). "A model of cochlear mechanics with outer hair cell motility, " The journal of the acoustical society of America, 94(1), 137-146.

Ni, G. (2012). "Fluid coupling and waves in the cochlea," in ISVR (University of Southampton, Southampton), p. 215.

Nobili, R., & Mammano, F. (1996). Biophysics of the cochlea II: Stationary nonlinear phenomenology. The Journal of the Acoustical Society of America,99(4), 2244-2255.

Nobili, R., Vetešnik, A., Turicchia, L., & Mammano, F. (2003). Otoacoustic emissions from residual oscillations of the cochlear basilar membrane in a human ear model. Journal of the Association for Research in Otolaryngology,4(4), 478-494.

Nobili, R., Vetešník, A., Turicchia, L., & Mammano, F. (2003). Otoacoustic emissions simulated in the time domain by a hydrodynamic model of the human cochlea. Biophysics of the Cochlea: From Molecules to Models. Singapore: World Scientific, 524-530.

Nuttall, A.L. and Dolan, D.F., 1996. Steady-state sinusoidal velocity responses of the basilar membrane in guinea pig. The Journal of the Acoustical Society of America, 99(3), pp.1556-1565.

Olson, E. S. (2001). Intracochlear pressure measurements related to cochlear tuning. The Journal of the Acoustical Society of America, 110(1), 349-367.

Parthasarathi, A. A., Grosh, K., & Nuttall, A. L. (2000). Three-dimensional numerical modeling for global cochlear dynamics. The Journal of the Acoustical Society of America, 107(1), 474-485.

Peterson, L. C., and Bogert, B. P. (1950). "A dynamical theory of the cochlea," The Journal of the Acoustical Society of America, 22, 369-381.

Pickles, J. O., (2008). "An Introduction to the Physiology of Hearing," 3rd edn (Bingley: Emerald).

Rasetshwane, D. M., & Neely, S. T. (2011). Inverse solution of ear-canal area function from reflectance. The Journal of the Acoustical Society of America,130(6), 3873-3881.

Ramamoorthy, S., Deo, N. V. and Grosh, K., (2007). "A mechano - electro - acoustical model for the cochlea: response to acoutic stimuli," The Journal of the Acoustical Society of America, 121, 2758.

Recio-Spinoso, A., Temchin, A. N., van Dijk, P., Fan, Y. H., & Ruggero, M. A. (2005). Wiener-kernel analysis of responses to noise of chinchilla auditory-nerve fibers. Journal of neurophysiology, 93(6), 3615-3634.

Rhode, W. S. (1971). "Observations of the VIBRATION OF THE Basilar Membrane Using the Mossbauer Technique," The Journal of the Acoustical Society of America 49, 1218-1231.

Rhode, W. S., and Robles, L. (1974) "Evidence from Mossbauer Experiments for Non-Linear Vibration in the Cochlea,"The Journal of the Acoustical Society of America, 55, 588-596.

Robles, L., & Ruggero, M. A. (2001). Mechanics of the mammalian cochlea. Physiological reviews, 81(3), 1305-1352.

Salt, A. N. (1995)."Cochlear Fluid Research Laboratory."Available: http://oto2.wustl.edu/cochlea/. Last accessed 23th Feb 2014.

Sellick, P.M., Patuzzi, R.M.J.B. and Johnstone, B.M., 1982. Measurement of basilar membrane motion in the guinea pig using the Mössbauer technique. The journal of the acoustical society of America, 72(1), pp.131-141.

Shera, C. A., & Zweig, G. (1991). A symmetry suppresses the cochlear catastrophe. The Journal of the Acoustical Society of America, 89(3), 1276-1289.

Shera, Christopher A. (1992) Listening to the ear. Dissertation (Ph.D.), California Institute of Technology.

Shera, C. A. (2001). "Intensity-invariance of fine time structure in basilar-membrane click responses: Implications for cochlear mechanics, " The Journal of the Acoustical Society of America, 110(1), 332-348.

Shera, C. A., Tubis, A., & Talmadge, C. L. (2004). Do forward-and backward-traveling waves occur within the cochlea? Countering the critique of Nobili et al.Journal of the Association for Research in Otolaryngology, 5(4), 349-359.

Shera, C. A., Tubis, A., & Talmadge, C. L. (2005). "Coherent reflection in a two-dimensional cochlea: Short-wave versus long-wave scattering in the generation of reflection-source otoacoustic emissions," The Journal of the Acoustical Society of America, 118(1), 287-313.

Shera, C. A. (2007). "Laser amplification with a twist: Traveling-wave Propagation and gain functions from throughout the cochlea," The Journal of the Acoustical Society of America, 122(5), 2738-2758.

Steele, C. R. (1974). "Behavior of the basilar membrane with pure-tone excitation," The Journal of the Acoustical Society of America, 55(1), 148-162.

Steele, C. R. and Miller, C. E. (1980). "An improved WKB calculation for a two-dimensional cochlear model, " The Journal of the Acoustical Society of America, 68(1), 147-148.

Steele, C. R., and Taber, L. A. (1979). "Comparison of WKB and finite difference calculations for a two-dimensional cochlear mmodel," The Journal of the Acoustical Society of America, 65(4),1001-1006.

Steele, C. R., and Taber, L. A. (1979). "Comparison of WKB calculations and experimental results for three-dimensional cochlear models," The Journal of the Acoustical Society of America, 65, 1007-1018.

Steele, C. R., & Zais, J. G. (1985). Effect of coiling in a cochlear model. The Journal of the Acoustical Society of America, 77(5), 1849-1852.

Taber, L. A. and Steele, C. R. (1981). "Cochlear model including three-dimensional fluid and four modes of partition flexibility," The Journal of the Acoustical Society of America, 70(2), 426-436.

Temchin, A. N., Recio-Spinoso, A., van Dijk, P., & Ruggero, M. A. (2005). Wiener kernels of chinchilla auditory-nerve fibers: verification using responses to tones, clicks, and noise and comparison with basilar-membrane vibrations. Journal of neurophysiology, 93(6), 3635-3648.

van Dijk, P., Wit, H. P., Segenhout, J. M., & Tubis, A. (1994). Wiener kernel analysis of inner ear function in the American bullfrog. The Journal of the Acoustical Society of America, 95(2), 904-919.

Vetešník, A., & Nobili, R. (2006). The approximate scaling law of the cochlea box model. Hearing research, 222(1), 43-53.

Von Békésy, G. (1960). Experiments in hearing (Vol. 8). E. G. Wever (Ed.). New York: McGraw-Hill.

Wen, B. and Boahen, K., 2009. A silicon cochlea with active coupling.Biomedical Circuits and Systems, IEEE Transactions on, 3(6), pp.444-455.

Wang, Y., Steele, C. R., & Puria, S. (2016). Cochlear Outer-Hair-Cell Power Generation and Viscous Fluid Loss.Scientific reports,6.

Yoon, Y.J., Steele, C.R. and Puria, S., (2011). Feed-forward and feed-backward amplification model from cochlear cytoarchitecture: an interspecies comparison. Biophysical journal, 100(1), pp.1-10.

Zweig, G., Lipes, R. and Pierce, J. R. (1976). "The cochlear compromise," The Journal of the Acoustical Society of America, 59(4), 975-982.

Zweig, G. (1991). "Finding the impedance of the organ of Corti, " The Journal of the Acoustical Society of America, 89(3), 1229.

Zweig, G. (1997). Wavelet transforms as solutions of partial differential equations (No. LA-UR--97-3514). Los Alamos National Lab., NM (United States).

Zwislocki, J. (1948). "Theorie der Schneckenmechanik: Qualitative und quantitative Analyse," Acta Otolaryngol. Suppl. 72, 1-76.